Measurement of time-dependent CP asymmetry parameters in $B^0 \to \eta' K_S$ decays

DISSERTATION
Presented in Partial Fulfillment of the Requirements for the Degree of Doctor of Science in the Graduate School of Osaka University

Koji Hara
Osaka University
May 2003

Abstract

We present a measurement of CP asymmetry parameters in $B^0 \to \eta' K_S$ decays based on a 78 fb^{-1} data sample collected at the $\Upsilon(4S)$ resonance with the Belle detector at the KEKB asymmetric-energy e^+e^- collider. We reconstruct one neutral B meson as a $B^0 \to \eta' K_S$ CP eigenstate and identify the flavor of the accompanying B meson from inclusive properties of its decay products. Using 294 candidate events, we extract CP asymmetry parameters with an unbinned maximum likelihood fit to the distribution of the time intervals between the two B meson decay points. We obtain

$$\mathcal{A}_{\eta' K_S} = 0.30^{+0.20}_{-0.21}(\text{stat})^{+0.06}_{-0.04}(\text{syst}),$$
$$\mathcal{S}_{\eta' K_S} = 0.61^{+0.31}_{-0.35}(\text{stat})^{+0.06}_{-0.07}(\text{syst}).$$

The result is consistent with the Standard Model expectation at the 68% confidence level. We give model independent constraints on CP phases and size of new physics decay amplitude. This is the first measurement of CP violation phases in the $b \to sq\overline{q}$ transition that provides model independent constraints on new physics beyond the Standard Model with negligibly small theoretical uncertainties.

Acknowledgment

First, I would like to thank my advisor, Prof. Taku Yamanaka, for giving me a chance on a research in high energy physics in such a great place.

I am deeply thankful to Prof. Yorikiyo Nagashima for introducing me to the world of high energy physics.

I express my gratitude to Dr. T. Hara for teaching me the basis of high energy physics and amusing me by great jokes for six years in Yamanaka and Nagashima lab.

My thanks go to all the members of the Belle flavor tagging and CP fit group for their help and valuable suggestions. I am specially grateful to Prof. Y. Sakai, Dr. K. Sumisawa, Dr. T. Kawasaki, Dr. H. Kakuno, Dr. C. Brendan, Dr. H. Hamasaki, Dr. J. Suzuki, Dr. J. Tanaka, Dr. T. Higuchi, Dr. M. Yokoyama, Dr. T. Tomura and Dr. T. Nakadaira. I am deeply grateful to Mr. K.-F. Chen for his great help in the $B^0 \to \eta' K_S$ analysis.

I owe thanks to all the member of the Belle SVD groups for generous cooperation. I am specially thankful to Prof. J. Haba, Dr. M. Tanaka, Dr T. Tsuboyama, Dr. Y. Yamada, Dr. T. Kawasaki, Dr. J. Kaneko for their supports in the Tsukuba-B4 work.

I also owe a lot to the members of the Yamanaka and Nagashima Group at Osaka University for the good companionship and encouragement. Mr. T. Hojo has given me a great deal of help to proceed in my research. I am very much thankful to my colleagues Dr. K. Nitta, Mr. K. Manabe, Mr. H. Miyake and Mr. K. Kotera for their kindness and friendship. I also thank to my colleagues Mr. K. Sakashita, Mr T. Ikei, Mr. T. Oba, Mr. B. Takeshita, Mr. Y. Tamai, Ms. Y. Ikemoto, Mr Y. Shibata and Mr. E. Tanaka. I enjoyed the life at the university with them.

I wish to express my appreciation to Dr. S. Nishida, Dr. J. Zhang and Mr. N. Abe for their friendship and help in the Tsukuba life.

I am very indebted to secretaries of Yamanaka and Nagashima laboratories: Ms. S. Tsuzuki and Ms. N. Sugimoto for their help.

I also would like to thank all the members of the BELLE collaboration and the KEKB accelerator group for keeping the experiment stable and providing excellent data.

At the last, I would like to express my special thanks to Prof. Masashi Hazumi. Without his precious advise and discussion with him, this thesis work wouldn't have finished.

Contents

List of Figures

List of Tables

Chapter 1

Introduction

One of the ultimate challenges in modern science is to understand the fundamental elements of our world. To give an answer to this problem, many studies have been carried out both by experimental and theoretical particle physicists. The standard model (SM) of particle physics has been constructed through these efforts. Almost all the known phenomena of the elemental particles measured so far are explained by the SM. However, there are many unresolved problems that cannot be answered by the SM. For example, we do not know why the electric charge is quantized. It is generally believed that there still exists some hidden new physics beyond the SM. Therefore, the current main theme of experimental particle physicists is to test the SM much more precisely and to find a phenomenon beyond the SM.

For this purpose, violation of CP symmetry, the difference between matter and anti-matter in other words, provides one of the best testing grounds [1]. In the SM, the origin of CP violation is explained by only one parameter. In contrast, expansions of the SM often yield more sources of CP violation and make the observable CP asymmetry deviate from the SM prediction due to the new CP-violating phases. CP violation beyond the SM is also desired in cosmology. It has been pointed out that CP violation in the SM is too small to generate our matter-dominant universe [2]. CP violation had only been observed in the neutral K meson system over 30 years [3–7]. In 2001, two new B factories, Belle and BaBar, have observed CP violation in neutral B mesons decaying into $J/\psi K_S$ and other $c\overline{c}K^{(*)0}$ modes [8, 9]. Their improved measurements in 2002 [10, 11] agree with the SM constraint from other measurements very well. It strongly suggests that the SM is the dominant source of CP violation in the quark sector. Therefore, to test the SM further and to search for new physics effects, it is a good strategy to study rare decays in which the SM effect is small and the effect of new physics can be large.

In this thesis, we describe a measurement of time-dependent CP asymmetry parameters in $B^0 \to \eta' K_S$[1] decays, which is one of the best ways to search for a new source of CP violation. If there is a difference of CP asymmetry parameters between $B^0 \to J/\psi K_S$ and $B^0 \to \eta' K_S$, it is a manifestation of new physics.

In this introduction, we first explain the reason why the $B^0 \to \eta' K_S$ decays are suited

[1]Throughout this thesis, the inclusion of the charge conjugate mode decay is implied unless otherwise stated.

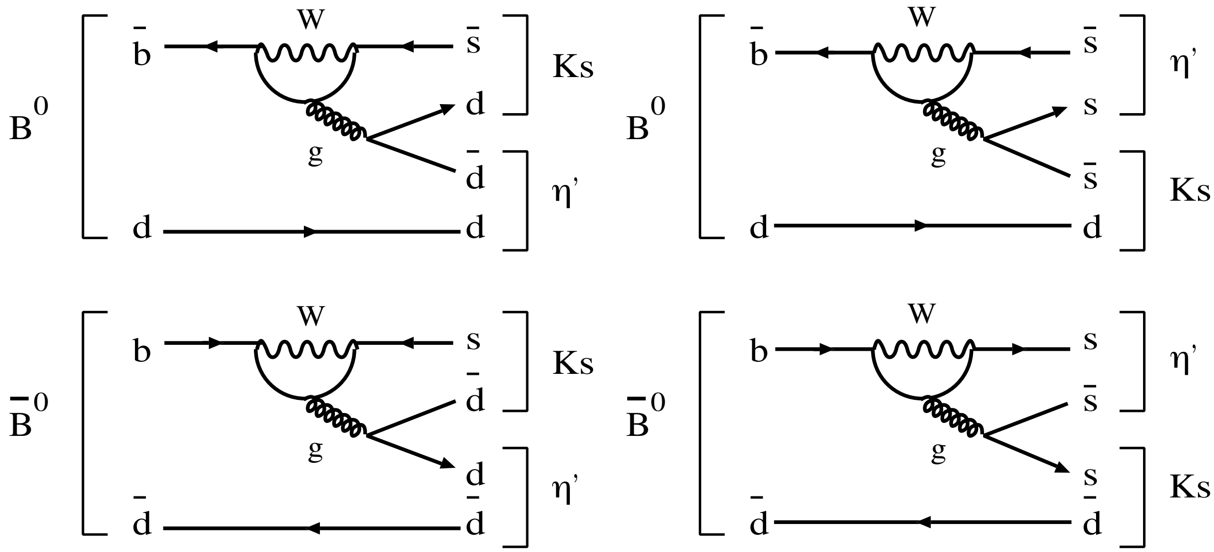

Figure 1.1: *The penguin diagrams of $B^0(\overline{B}^0) \to \eta' K_S$ decays.*

for new physics searches. We then describe CP violation in $B^0 \to \eta' K_S$ decays and how the new physics effects appears.

1.1 $B^0 \to \eta' K_S$ decay

The $\eta' K_S$ state is a CP eigenstate with an eigenvalue -1. Both B^0 and $\overline{B}^0$ can decay into $\eta' K_S$ through a transition of a b quark to an s quark. Since this transition changes the quark flavor but does not change the electric charge, it is called a flavor-changing neutral current (FCNC) transition. In the SM, since the FCNC transition cannot occur directly, it proceeds through loop diagrams shown in Figure 1.1, which are often called penguin diagrams. Such loop diagrams are expected to be sensitive to new physics because heavy particles beyond the SM can contribute via additional loop diagrams.

Among several B^0 meson decay modes that can be used to study CP asymmetries in the $b \to sq\overline{q}$ hadronic penguin process, the $B^0 \to \eta' K_S$ decay is the best from an experimental point of view. Table 1.1 shows B^0 meson decay modes governed by the $b \to sq\overline{q}$ process. The third column is a usable decay mode for reconstruction at a reasonable background level and the fourth column is a product of branching fractions of daughter particles decays. The $B^0 \to \eta' K_S$ decay has the largest product branching fraction among them and thus allows the most precise measurement. As for K^0, we can identify K_S cleanly by $K_S \to \pi^+\pi^-$ decay with an isolated decay vertex. We will not use K_L because most of them do not decay within the detector, and they must be detected as neutral hadronic showers which suffer from large background contamination.

There is a hint of new physics effect in $B^0 \to \eta' K$ decays. CLEO [12, 13], BaBar [14] and Belle [15] experiments have measured the branching fractions of $B \to \eta' K$ decays. Table 1.2 shows the world average [16] of the measurements together with the theoret-

Decay mode	Branching fraction	Daughter decay	Product BF
$\eta' K^0$	$(5.8^{+1.4}_{-1.3}) \times 10^{-5}$	$\eta' \to \rho^0\gamma$, $\rho^0 \to \pi^+\pi^-$	2.8×10^{-5}
		$\eta' \to \eta\pi^+\pi^-$, $\eta \to \gamma\gamma$	
ηK^0	$< 9.3 \times 10^{-5}$		
ϕK^0	$(0.81^{+0.32}_{-0.26}) \times 10^{-5}$	$\phi \to K^+K^-$	0.4×10^{-5}
ωK^0	$< 1.3 \times 10^{-5}$		
$\pi^0 K^0$	$(1.07^{+0.27}_{-0.25}) \times 10^{-5}$	$\pi^0 \to \gamma\gamma$	1.1×10^{-5}
$\rho^0 K^0$	$< 3.9 \times 10^{-5}$		

Table 1.1: *B^0 meson decay modes governed by the $b \to sq\overline{q}$ hadronic penguin process. The third column is a usable decay mode for reconstruction. The fourth column is a product branching fraction of daughter branching fractions.*

	Experimental result [16]	Theory [17–20]
$B^+ \to \eta' K^+$	$(7.5 \pm 0.7) \times 10^{-5}$	2.1-5.3 $\times 10^{-5}$
$B^0 \to \eta' K^0$	$(5.8^{+1.4}_{-1.3}) \times 10^{-5}$	2.0-5.0 $\times 10^{-5}$

Table 1.2: *Branching fractions of $B \to \eta' K$ decays.*

ical calculation [17–20]. The experimental result is higher than theoretical calculations. The semi-inclusive branching fraction of $B \to \eta' X_s$ decays has been measured to be $6.2 \pm 1.6(stat.) \pm 1.3(syst.)^{+0.0}_{-0.5}(bkg.)$ for $2.0 < p_{\eta'} < 2.7$ [21] by CLEO experiment. It is also higher than the theoretical calculation [22]. These discrepancies have not been explained yet and are possibly an indication of the existence of new physics beyond the SM. Since there are large theoretical uncertainties in the estimation of branching fractions, an independent and clean test is being awaited.

The measurement of the time-dependent CP asymmetry in $B^0 \to \eta' K_S$ provides such a test of the SM without relying on the theoretical calculation of the branching fraction. The time-dependent CP asymmetry is defined as an asymmetry between partial decay rate of B^0 and $\overline{B}^0$ at time t. It is given by

$$a_{\eta' K_S} \equiv \frac{\Gamma(\overline{B}^0(t) \to \eta' K_S) - \Gamma(B^0(t) \to \eta' K_S)}{\Gamma(\overline{B}^0(t) \to \eta' K_S) + \Gamma(B^0(t) \to \eta' K_S)}. \tag{1.1}$$

We explain how this asymmetry is sensitive to new physics and is independent of theoretical uncertainty of the branching fraction calculation in the next section.

1.2 CP Violation in $B^0 \to \eta' K_S$

In this section, we explain CP violation in $B^0 \to \eta' K_S$ in the SM and effect of new physics beyond the SM. First, we explain general phenomenology of CP violation in B decays briefly, and describe the case of the $B^0 \to \eta' K_S$ decay.

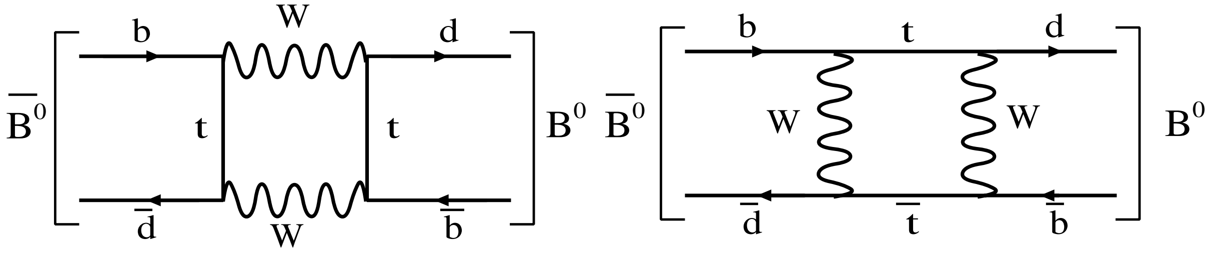

Figure 1.2: *The box diagrams responsible for $B^0 - \overline{B}^0$ mixing.*

1.2.1 Phenomenology of CP violation in B decays

Time Evolution of Neutral B Mesons

B^0 and $\overline{B}^0$ can mix through second order weak interactions known as the "box diagrams" shown in Figure 1.2. Therefore, neutral B meson state evolves as the admixture $a(t)|B^0\rangle + b(t)|\overline{B}^0\rangle$ and oscillates between B^0 and $\overline{B}^0$. The behavior is governed by the time-dependent Schrödinger equation

$$i\frac{d}{dt}\begin{pmatrix} a(t) \\ b(t) \end{pmatrix} = \mathcal{H}\begin{pmatrix} a(t) \\ b(t) \end{pmatrix}. \tag{1.2}$$

The matrix $\mathcal{H}$ is written as

$$\mathcal{H} = \mathbf{M} - \frac{i}{2}\mathbf{\Gamma} = \begin{pmatrix} M_{11} - \frac{i}{2}\Gamma_{11} & M_{12} - \frac{i}{2}\Gamma_{12} \\ M_{12} - \frac{i}{2}\Gamma_{12} & M_{22} - \frac{i}{2}\Gamma_{22} \end{pmatrix}, \tag{1.3}$$

where, $\mathbf{M}$ and $\mathbf{\Gamma}$ are Hermitian matrices, which are called the mass and decay matrices, respectively. CPT invariance requires $M_{11} = M_{22} \equiv M$ and $\Gamma_{11} = \Gamma_{22} \equiv \Gamma$, where M and Γ are the mass and decay width of the flavor eigenstates, B^0 and $\overline{B}^0$.

The two mass eigenstates, B_1 and B_2, can be written as

$$\begin{aligned} B_1 &= p|B^0\rangle + q|\overline{B}^0\rangle, \\ B_2 &= p|B^0\rangle - q|\overline{B}^0\rangle, \end{aligned} \tag{1.4}$$

where

$$\frac{q}{p} = \sqrt{\frac{M_{12}^* - \frac{i}{2}\Gamma_{12}^*}{M_{12} - \frac{i}{2}\Gamma_{12}}}. \tag{1.5}$$

The time evolution of these states is given by

$$\begin{aligned} |B_1(t)\rangle &= e^{-iM_1 t}e^{-\frac{\Gamma_1 t}{2}}|B_1(0)\rangle, \\ |B_2(t)\rangle &= e^{-iM_2 t}e^{-\frac{\Gamma_2 t}{2}}|B_2(0)\rangle, \end{aligned} \tag{1.6}$$

where $M_{1(2)}$ and $\Gamma_{1(2)}$ are the mass and decay width of $B_{1(2)}$ given by

$$\begin{aligned} M_1 - \frac{i}{2}\Gamma_1 &= M - \frac{i}{2}\Gamma + \frac{q}{p}(M_{12} - \frac{i}{2}\Gamma_{12}), \\ M_2 - \frac{i}{2}\Gamma_2 &= M - \frac{i}{2}\Gamma - \frac{q}{p}(M_{12} - \frac{i}{2}\Gamma_{12}). \end{aligned} \tag{1.7}$$

When $|q/p| \simeq 1$ holds, B_1 and B_2 states correspond to CP eigenstates with eigenvalues $+1$ and -1, respectively. Neglecting the CP violation in the decay, B_1 cannot decay into $CP = -1$ states and vice versa. In the neutral K meson system, corresponding K_1 and K_2 have significantly different decay widths, because of the light K meson mass: the phase space between K_1 to $\pi\pi$ ($CP = +1$) and K_2 to $\pi\pi\pi$ ($CP = -1$) decays are significantly different. In contrast, the neutral B meson mass is heavy enough to reduce such an effect to a level of $(\Gamma_1 - \Gamma_2)/\Gamma \sim \mathcal{O}(10^{-3})$. Therefore, we set $\Gamma_1 = \Gamma_2 = \Gamma$. The time evolution of initially pure B^0 or $\overline{B}^0$ states are obtained from equation (1.4) and (1.6) as:

$$\begin{aligned} |B^0(t)\rangle &= f_+(t)|B^0\rangle + \frac{q}{p} f_-(t)|\overline{B}^0\rangle, \\ |\overline{B}^0(t)\rangle &= \frac{p}{q} f_-(t)|B^0\rangle + f_+(t)|\overline{B}^0\rangle, \end{aligned} \tag{1.8}$$

where

$$f_\pm(t) = \frac{1}{2} e^{-i(M-\frac{i}{2}\Gamma)t}(1 \pm e^{-i\Delta m_d t}). \tag{1.9}$$

The $\Delta m_d \equiv M_2 - M_1$ is the mass difference of the two mass eigenstates and determines the oscillation frequency between B^0 and $\overline{B}^0$.

B Meson Decays into a CP Eigenstate

Now we consider decays of neutral B mesons into a CP eigenstate, f_{cp}. The amplitudes for these processes are defined as

$$\begin{aligned} A(f_{CP}) &\equiv \langle f_{CP}|\mathcal{H}_W|B^0\rangle, \\ \overline{A}(f_{CP}) &\equiv \langle f_{CP}|\mathcal{H}_W|\overline{B}^0\rangle. \end{aligned} \tag{1.10}$$

Here, it is essential that both B^0 and $\overline{B}^0$ can decay into f_{CP} and interfere. For convenience we introduce the ratio of two amplitudes:

$$\begin{aligned} \overline{\rho}(f_{CP}) &\equiv \frac{\overline{A}(f_{CP})}{A(f_{CP})}, \\ \rho(f_{CP}) &\equiv \frac{A(f_{CP})}{\overline{A}(f_{CP})}. \end{aligned} \tag{1.11}$$

Using equations (1.8), (1.10) and (1.11), the time-dependent decay rates of initially pure B^0 or $\overline{B}^0$ states become

$$\begin{aligned} \Gamma(B^0(t) \to f_{CP}) = e^{-\Gamma t}|A^2| &\left[\frac{1+\cos\Delta m_d t}{2} + \left|\frac{q}{p}\right|^2 |\overline{\rho}(f_{CP})|^2 \frac{1-\cos\Delta m_d t}{2} \right. \\ &\left. - \operatorname{Im}\left[\left(\frac{q}{p}\right) \overline{\rho}(f_{CP}) \right] \sin\Delta m t \right] \\ \Gamma(\overline{B}^0(t) \to f_{CP}) = e^{-\Gamma t}|\overline{A}^2| &\left[\frac{1+\cos\Delta m_d t}{2} + \left|\frac{p}{q}\right|^2 |\rho(f_{CP})|^2 \frac{1-\cos\Delta m_d t}{2} \right. \\ &\left. - \operatorname{Im}\left[\left(\frac{p}{q}\right) \rho(f_{CP}) \right] \sin\Delta m t \right] \end{aligned} \tag{1.12}$$

In the neutral B meson system, $|q/p| \simeq 1$ is a good approximation to less than $\mathcal{O}(10^{-2})$. Introducing

$$\lambda_{CP} \equiv \frac{q}{p}\overline{\rho}(f_{CP}), \tag{1.13}$$

the decay rates are written as

$$\begin{aligned}
\Gamma(B^0(t) \to f_{CP}) &= e^{-\Gamma t}|A|^2 \left[1 - \frac{|\lambda_{CP}|^2 - 1}{|\lambda_{CP}|^2 + 1}\cos\Delta m_d t - \frac{2\,\mathrm{Im}\,\lambda_{CP}}{|\lambda_{CP}|^2 + 1}\sin\Delta m_d t\right] \\
\Gamma(\overline{B}^0(t) \to f_{CP}) &= e^{-\Gamma t}|A|^2 \left[1 + \frac{|\lambda_{CP}|^2 - 1}{|\lambda_{CP}|^2 + 1}\cos\Delta m_d t + \frac{2\,\mathrm{Im}\,\lambda_{CP}}{|\lambda_{CP}|^2 + 1}\sin\Delta m_d t\right]
\end{aligned} \tag{1.14}$$

The time-dependent CP asymmetry is then defined by

$$\begin{aligned}
a_{f_{CP}} \equiv& \frac{\Gamma(\overline{B}^0(t) \to f_{CP}) - \Gamma(B^0(t) \to f_{CP})}{\Gamma(\overline{B}^0(t) \to f_{CP}) + \Gamma(B^0(t) \to f_{CP})} \\
=& \frac{(|\lambda_{CP}|^2 - 1)\cos\Delta m_d t + 2\,\mathrm{Im}\,\lambda_{CP}\sin\Delta m_d t}{|\lambda_{CP}|^2 + 1} \\
\equiv& \mathcal{A}\cos\Delta m_d t + \mathcal{S}\sin\Delta m_d t,
\end{aligned} \tag{1.15}$$

where we define

$$\begin{aligned}
\mathcal{A} &\equiv \frac{|\lambda_{CP}|^2 - 1}{|\lambda_{CP}|^2 + 1}, \\
\mathcal{S} &\equiv \frac{2\,\mathrm{Im}\,\lambda}{1 + |\lambda_{CP}|^2}.
\end{aligned} \tag{1.16}$$

The values of CP asymmetry parameter $\mathcal{A}$ and $\mathcal{S}$ are limited within a circle, $\mathcal{A}^2 + \mathcal{S}^2 \leq 1$, by definition. We can see that CP violation arises when $|\lambda_{CP}| \neq 1$ or $\mathrm{Im}\,\lambda_{CP} \neq 0$. The former means that the decay amplitudes are different, i.e. $|A(f_{CP})| \neq |\overline{A}(f_C P)|$. This type is called direct CP violation. The latter is realized when there is a phase difference between the decay and the mixing even if $|A(f_{CP})| = |\overline{A}(f_C P)|$ and $|q/p| = 1$ hold. This type is called mixing-induced CP violation.

In the next subsection, we describe the case of $B^0 \to \eta' K_S$ decays in the SM.

1.2.2 CP Violation in the Standard Model

Cabibbo-Kobayashi-Maskawa Matrix

In the SM, CP violation is explained by the quark mixing matrix of the charged current weak interaction introduced by Kobayashi and Maskawa [23].

$$\mathbf{V} = \begin{pmatrix} V_{ud} & V_{us} & V_{ub} \\ V_{cd} & V_{cs} & V_{cb} \\ V_{td} & V_{ts} & V_{tb} \end{pmatrix}. \tag{1.17}$$

The matrix elements are parametrized by three real parameters and a complex phase. The complex phase introduces CP violation to the SM. It is convenient to write the matrix

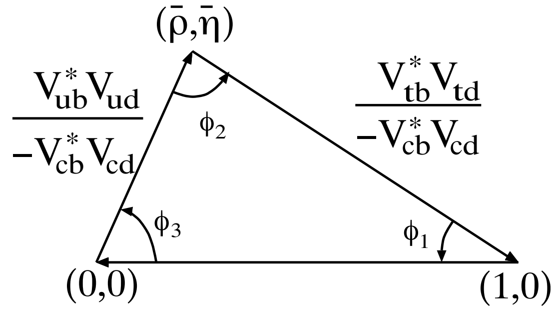

Figure 1.3: *The unitarity triangle.*

in Wolfenstein parametrization [24] which is an expansion in powers of sine of Cabibbo angle, $\lambda \equiv \sin\theta_c \simeq 0.22$:

$$\begin{pmatrix} V_{ud} & V_{us} & V_{ub} \\ V_{cd} & V_{cs} & V_{cb} \\ V_{td} & V_{ts} & V_{tb} \end{pmatrix} = \begin{pmatrix} 1-\frac{1}{2}\lambda^2 & \lambda & A\lambda^3(\rho - i\eta) \\ -\lambda & 1-\frac{1}{2}\lambda^2 & A\lambda^2 \\ A\lambda^3(1-\rho-i\eta) & -A\lambda^2 & 1 \end{pmatrix} + \mathcal{O}(\lambda^4), \tag{1.18}$$

where A, ρ and η are real parameters of order unity.

The unitarity of the CKM matrix imposes relations between the matrix elements. An important equation among such relations for the discussion here is

$$V_{ub}^* V_{ud} + V_{cb}^* V_{cd} + V_{tb}^* V_{td} = 0. \tag{1.19}$$

This relation can be visualized as a triangle in the complex plane. Figure 1.3 shows the unitarity triangle, where three angles, $\overline{\rho}$ and $\overline{\eta}$ are defined as:

$$\begin{aligned} \phi_1 &\equiv \pi - \arg\left(\frac{-V_{tb}^* V_{td}}{-V_{cb}^* V_{cd}}\right), \\ \phi_2 &\equiv \arg\left(\frac{V_{tb}^* V_{td}}{-V_{ub}^* V_{ud}}\right), \\ \phi_3 &\equiv \arg\left(\frac{V_{ub}^* V_{ud}}{-V_{cb}^* V_{cd}}\right), \\ \overline{\rho} &\equiv \left(1 - \frac{\lambda^2}{2}\right)\rho, \\ \overline{\eta} &\equiv \left(1 - \frac{\lambda^2}{2}\right)\eta. \end{aligned} \tag{1.20}$$

CP asymmetry parameters in $B^0 \to \eta' K_S$ decays

We now describe CP asymmetry parameter $\mathcal{A}_{\eta' K_S}$ and $\mathcal{S}_{\eta' K_S}$ in terms of the CKM matrix elements. The main contribution to the box diagrams of B^0-$\overline{B}^0$ mixing in Figure 1.2 is the top quark because of its heavy mass, and the CKM matrix elements contributing to the mixing are $V_{tb}V_{td}^*$ on the vertices of the box diagrams. Theoretical calculations [25–28] on M_{12}, Γ_{12} and their ratio yield:

$$\begin{aligned} M_{12} &\propto (V_{tb}V_{td}^*)^2 m_t^2, \\ \Gamma_{12} &\propto (V_{tb}V_{td}^*)^2 m_b^2, \\ \left|\frac{\Gamma_{12}}{M_{12}}\right| &\simeq \frac{m_b^2}{m_t^2} \simeq 10^{-3}, \end{aligned} \tag{1.21}$$

where m_b is the bottom quark mass and m_t is the top quark mass. Using (1.5) and (1.21), the q/p becomes

$$\begin{aligned} \frac{q}{p} &= \sqrt{\frac{M_{12}^*}{M_{12}}} + \mathcal{O}\left(\frac{\Gamma_{12}}{M_{12}}\right), \\ &\simeq \frac{V_{tb}^*V_{td}}{V_{tb}V_{td}^*}. \end{aligned} \tag{1.22}$$

As for the decay of $B^0 \to \eta' K_S$, the main contribution comes from the penguin diagrams shown in Figure 1.1. The decay amplitude is written as

$$A(\eta' K_S) = V_{tb}^* V_{ts} P_t + V_{cb}^* V_{cs} P_c + V_{ub}^* V_{us} P_u \tag{1.23}$$

where P_i $(i = u, c, t)$ are the amplitudes apart from the explicitly shown CKM factors. The amplitude $\overline{A}$ is given by the complex conjugate CKM matrix elements and the same P_i terms. Using the unitarity of the CKM matrix, $V_{tb}^*V_{ts} + V_{cb}^*V_{cs} + V_{ub}^*V_{us} = 0$ holds, and the amplitude becomes

$$A(\eta' K_S) = V_{cb}^* V_{cs}(P_c - P_t) + V_{ub}^* V_{us}(P_u - P_t). \tag{1.24}$$

Compared to the first term, the second term is suppressed by $V_{ub}^*V_{us}/V_{cb}^*V_{cs} \simeq \lambda^2$ and is negligible. There is also a contribution from a tree diagram shown in Figure 1.4. This contribution is also suppressed by $V_{ub}V_{us}^*/(V_{cb}^*V_{cs}) \simeq \lambda^2$ compared to the penguin amplitude. In addition, it has a color suppression, and the tree contribution becomes less than a few % level [29–31]. Consequently, the decay amplitudes A and $\overline{A}$ are written as:

$$\begin{aligned} A(\eta' K_S) &\simeq V_{cb}^* V_{cs}(P_c - P_t), \\ \overline{A}(\eta' K_S) &\simeq -V_{cb} V_{cs}^*(P_c - P_t), \end{aligned} \tag{1.25}$$

where a minus sign of $\overline{A}$ comes from the eigenvalue $CP(\eta' K_S) = -1$. The P_c and the P_t have large hadronic uncertainty which appears as the theoretical uncertainty of the branching fraction in Table 1.2. The uncertainty, however, does not affect CP asymmetry, because the term $(P_c - P_t)$ cancels in $\overline{\rho}(\eta' K_S) = \overline{A}/A$. The $\overline{\rho}(\eta' K_S)$ is written only with CKM matrix elements as,

$$\overline{\rho}(\eta' K_S) \simeq -\frac{V_{cb}V_{cs}^*}{V_{cb}^*V_{cs}}. \tag{1.26}$$

It leads to $|\rho(\eta' K_S) = 1|$ up to a few % uncertainty, and the direct CP violation term $\mathcal{A}_{\eta' K_S}$ becomes zero.

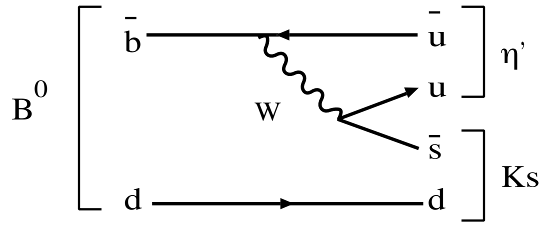

Figure 1.4: *The CKM and color suppressed tree diagram of $B^0 \to \eta' K_S$ decay.*

In addition to the two terms described above, there is an additional term due to K^0-$\overline{K}^0$ mixing expressed as

$$\left(\frac{q}{p}\right)_K = \frac{V_{cs}V_{cd}^*}{V_{cs}^*V_{cd}}, \tag{1.27}$$

because we require K_S in the final state.

Finally, we find

$$\lambda_{\eta' K_S} = -\frac{V_{tb}^*V_{td}}{V_{tb}V_{td}^*}\frac{V_{cs}V_{cd}^*}{V_{cs}^*V_{cd}}\frac{V_{cb}V_{cs}^*}{V_{cb}^*V_{cs}} = -e^{-2i\phi_1}. \tag{1.28}$$

Therefore, within the SM, CP asymmetry parameters become

$$\begin{aligned} \mathcal{A}_{\eta' K_S} &\simeq 0, \\ \mathcal{S}_{\eta' K_S} &\simeq \sin 2\phi_1, \end{aligned} \tag{1.29}$$

and the CP asymmetry is given by

$$a_{\eta' K_S} = \sin 2\phi_1 \sin \Delta m_d t, \tag{1.30}$$

with a few % uncertainty.

1.2.3 CP Violation in New Physics Beyond the Standard Model

The effect of new physics beyond the SM contributes in additional loop diagrams in the $b \to s q\overline{q}$ transition. This changes the decay amplitudes to

$$\begin{aligned} A &= |A_{\rm SM}|e^{i\phi_{\rm SM}}e^{i\delta_{\rm SM}} + |A_{\rm NP}|e^{i\phi_{\rm NP}}e^{i\delta_{\rm NP}}, \\ \overline{A} &= -\left(|A_{\rm SM}|e^{-i\phi_{\rm SM}}e^{i\delta_{\rm SM}} + |A_{\rm NP}|e^{-i\phi_{\rm NP}}e^{i\delta_{\rm NP}}\right), \end{aligned} \tag{1.31}$$

where $A_{\rm SM(NP)}$ is the amplitude of the SM (new physics), $\phi_{\rm SM(NP)}$ is the CP violating phase and $\delta_{\rm SM(NP)}$ is the CP invariant strong phase. In the case of the $B^0 \to \eta' K_S$ decay, equation (1.18) and (1.25) show that CKM matrix elements in the decay amplitude are real up to λ^3. Therefore, $\phi_{SM} = 0$ holds. Consequently, CP asymmetry parameters are changed [32] from (1.29) to

$$\begin{aligned}
\mathcal{A}_{\eta' K_S} &= -\frac{2\frac{|A_{NP}|}{|A_{SM}|}\sin\delta_{12}\sin\phi_{NP}}{1+2\frac{|A_{NP}|}{|A_{SM}|}\cos\delta_{12}\cos\phi_{NP}+\left(\frac{|A_{NP}|}{|A_{SM}|}\right)^2}, \\
\mathcal{S}_{\eta' K_S} &= \frac{\sin 2\phi_1 + 2\frac{|A_{NP}|}{|A_{SM}|}\cos\delta_{12}\sin(\phi_{NP}+2\phi_1)+\left(\frac{|A_{NP}|}{|A_{SM}|}\right)^2\sin(2\phi_{NP}+2\phi_1)}{1+2\frac{|A_{NP}|}{|A_{SM}|}\cos\delta_{12}\cos\phi_{NP}+\left(\frac{|A_{NP}|}{|A_{SM}|}\right)^2},
\end{aligned} \tag{1.32}$$

where $\delta_{12} \equiv \delta_{SM} - \delta_{NP}$. The CP asymmetry parameters can deviate from the SM expectation depending on three parameters: $|A_{NP}|/|A_{SM}|$, δ_{12} and ϕ_{NP}. Currently, there are no model independent constraint on these three new physics parameters. By measuring the CP asymmetry parameters and comparing it to the SM expectation, we can search for evidence of new physics or constrain these three parameters.

As an example of new physics, we briefly explain the supersymmetry (SUSY)-based models. In the SUSY model, penguin diagrams with intermediate gluinos $\tilde{g}$ and squarks ($\tilde{b}$ and $\tilde{s}$) contribute to the $b \to sq\overline{q}$ process. Figure 1.5 shows an example in which right-handed squarks couple with quarks. The $(\delta^d_{RR})_{23}$ is the mass insertion parameter that

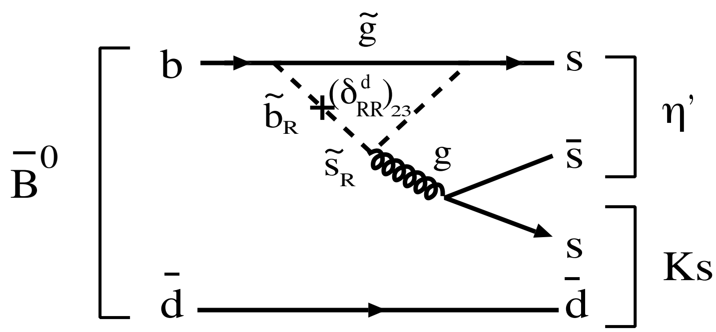

Figure 1.5: *The gluino-squark penguin diagrams of $B^0 \to \eta' K_S$ decay in the SUSY model.*

express the right-right squark mixing term. There are also other three left-right combinations: $(\delta^d_{LR})_{23}$, $(\delta^d_{RL})_{23}$ and $(\delta^d_{LL})_{23}$. These four $(\delta^d)_{23}$ factors determine the size of each decay amplitude and introduce CP violating phases. These additional loop contributions can also carry different CP invariant phases from the SM. The $(\delta^d_{LR})_{23}$ and $(\delta^d_{RL})_{23}$ are strongly constrained to be $\mathcal{O}(10^{-2})$ by $B \to X_s\gamma$ branching fraction [33,34], while $(\delta^d_{LL})_{23}$ and $(\delta^d_{RR})_{23}$ are constrained much weakly by experiments; values less than unity are all allowed at present. There are two SUSY based models which suggest large $(\delta^d_{RR})_{23}$:

- Supersymmetry (SUSY) Models with Abelian Horizontal Symmetry [35,36]
  This model correlates the quark mass hierarchy with the flavor mixing hierarchy which is determined by powers of the CKM parameter λ. Assuming the degenerate

squark masses, this provides a large mixing in the right handed squarks and gives [37]

$$|(\delta^d_{RR})_{23}| \sim \frac{m_s/m_b}{|V_{cb}|} = \mathcal{O}(1). \tag{1.33}$$

- SUSY Grand Unified Theory [38, 39]
  The atmospheric neutrino oscillation, which is observed recently [40], requires large mixing between ν_μ and ν_τ. In this model, due to the unification, the neutrino mixing is related to the $\tilde{b}_R$-$\tilde{s}_R$ mixing, and $|(\delta^d_{RR})_{23}|$ becomes ~ 0.5.

These models suggest large contributions to the decay amplitude, while their CP phases are unknown. Therefore, the CP asymmetry parameters can deviate significantly from the SM and can be observed by our measurement.

1.2.4 Comparison with the $B^0 \to J/\psi K_S$

The $B^0 \to J/\psi K_S$ and other $c\bar{c}K^{(*)0}$ decays provide the CP asymmetry parameter $\sin 2\phi_1$ with very small hadronic uncertainties. The difference from the $B^0 \to \eta' K_S$ decay is that $B^0 \to J/\psi K_S$ decay occurs through a tree diagram as shown in Figure 1.6 and contribution from a penguin diagram is negligible. Therefore, $B^0 \to J/\psi K_S$ is unlikely to receive new

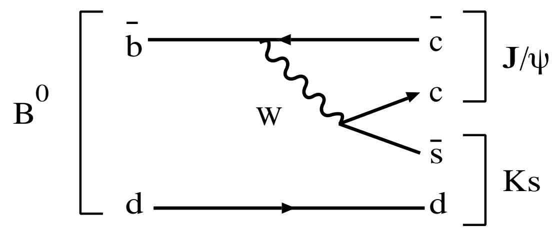

Figure 1.6: *The diagram of $B^0 \to J/\psi K_S$ decay*

physics effects. CP violation in these decays has already been observed, and $\sin 2\phi_1$ is measured to a 10% accuracy [10, 11]. The measured results are in good agreement with the SM expectation from other measurements of the CKM matrix elements as shown in Figure 1.7 [41]. Therefore, we can regard the $\sin 2\phi_1$ measured by $B^0 \to J/\psi K_S$ as the value for the SM.

If the $\sin 2\phi_1$ measured by $B^0 \to \eta' K_S$ decay is different from the $\sin 2\phi_1$ measured by $B^0 \to J/\psi K_S$, then it will be a clear evidence for new physics, independent of theoretical models.

1.3 Previous Experimental Results

The SM CP asymmetry parameter $\sin 2\phi_1$ has been measured with $B^0 \to J/\psi K_S$ and other $c\bar{c}K^{(*)0}$ decays by OPAL [42], ALEPH [43], CDF [44], BaBar [9, 11] and Belle [8, 10]. Table 1.3 shows their results. The present world average value is [37]

$$\sin 2\phi_1 = 0.734 \pm 0.054. \tag{1.34}$$

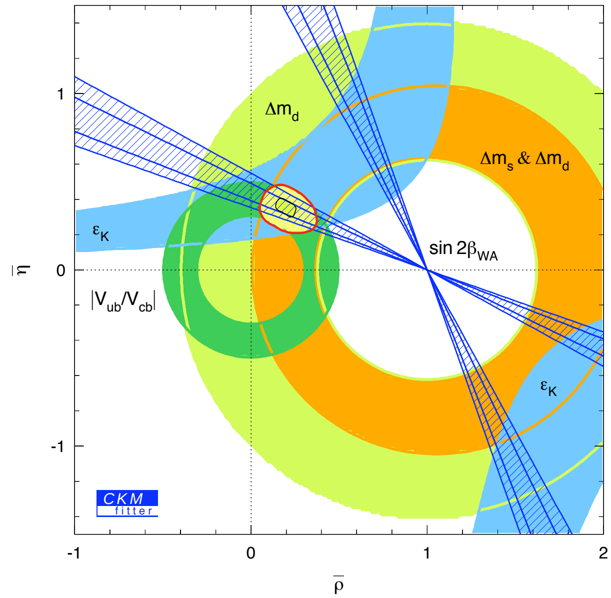

Figure 1.7: *The constraint on* $\overline{\rho}$-$\overline{\eta}$ *plane from neutral* B *meson mixings*(Δm_d *and* Δm_s), $|V_{ub}/V_{cb}|$ *and the* CP *violation in neutral* K *meson*(ϵ_K) *with the* $\sin 2\phi_1$(=$\sin 2\beta_{WA}$) *measured by* $B^0 \to J/\psi K_S$ *and other* $c\overline{c}K^{(*)0}$ *decays overlaid.*

The CP asymmetry parameters in $B^0 \to \eta' K_S$ decays have been measured by Belle using the data that corresponds to an integrated luminosity of 41.8fb^{-1} [45]. The results are:

$$\begin{aligned} \mathcal{A}_{\eta' K_S} &= 0.13 \pm 0.32(stat)^{+0.09}_{-0.06}(syst), \\ \mathcal{S}_{\eta' K_S} &= 0.28 \pm 0.55(stat)^{+0.07}_{-0.08}(syst). \end{aligned} \tag{1.35}$$

Experiment	$\sin 2\phi_1$
OPAL [42]	$3.2^{+1.8}_{-2.0} \pm 0.5$
ALEPH [43]	$0.84^{+0.82}_{-1.02} \pm 0.16$
CDF [44]	$0.79^{+0.41}_{-0.44}$
BaBar [11]	$0.741 \pm 0.067 \pm 0.034$
Belle [10]	$0.719 \pm 0.074 \pm 0.035$

Table 1.3: *The experimental results of* $\sin 2\phi_1$ *measurements with* $B^0 \to J/\psi K_S$ *and* $c\overline{c}K^{(*)0}$ *decays. The first error is statistical and the second is systematic, except for the CDF result. The errors of the CDF result include both statistical and systematic.*

1.4 Goal of This Thesis

In this thesis, we report the improved measurement of CP asymmetry parameters in $B^0 \to \eta' K_S$ at the Belle experiment. Since the statistical uncertainties of the previous result [45] are still large, it is important to measure the CP asymmetry parameters with much larger data sample. The analysis is based on a 78fb^{-1} data sample, which is about twice as large as the sample used for the previous result [45]. We also introduce several improvements in the analysis methods. We compare our result to the SM expectation and discuss the possibility of existence of new physics.

In the next chapter, we explain the principle of the measurement. In Chapter 3, we describe the experimental apparatus: the Belle detector and the KEKB e^+e^- asymmetric collider. In Chapter 4, we describe the $B^0 \to \eta' K_S$ event selection. In Chapter 5 we extract the CP asymmetry parameters from the selected candidate events. In Chapter 6, we discuss our result. In Chapter 7, the conclusion is given.

Chapter 2

Principle of the Measurement

In this chapter, we describe how to measure the CP asymmetry parameters in $B^0 \to \eta' K_S$ decays with the process $e^+e^- \to \Upsilon(4S) \to B^0\overline{B}^0$ at the Belle experiment.

2.1 CP Asymmetry Measurement with $B^0\overline{B}^0$ Pairs from $\Upsilon(4S)$ decays

At the Belle experiment, B mesons are produced through the $e^+e^- \to \Upsilon(4S) \to B\overline{B}$ process. The mass of $\Upsilon(4S)$, which is a bound state of a b quark and a $\overline{b}$ quark, is 10.58 GeV/c^2. The value is just above the B meson pair production threshold $5.28\text{GeV}/c^2 \times 2 = 10.56\text{GeV}/c^2$. Thus the $\Upsilon(4S)$ meson decays nearly 100% into $B^0\overline{B^0}$ or B^+B^- with almost the same branching fraction. The Belle experiment has the special feature that the $B^0\overline{B}^0$ pair is produced with the Lorentz boost of $\beta\gamma = 0.425$ by an asymmetric collision of a positron and an electron with energy of 3.5 GeV and 8 GeV, respectively. To measure time-dependent CP asymmetry parameters, we need to determine the initial flavor of B meson and the decay time. The boosted $B^0\overline{B}^0$ pair has a characteristic feature suitable for these measurement.

A $B^0\overline{B}^0$ pair from $\Upsilon(4S)$ is produced as a C-odd state. Although $B^0 - \overline{B}^0$ oscillation then starts, the state preserves the C-odd configuration and is not allowed to be B^0B^0 or $\overline{B}^0\overline{B}^0$. The time evolution of the pair is given by

$$\begin{aligned} |\Psi(t)\rangle &= e^{-t/\tau_{B^0}}|\Psi(t=0)\rangle, \\ |\Psi(t=0)\rangle &= \frac{1}{\sqrt{2}}[|B^0(\vec{k})\overline{B}^0(-\vec{k})\rangle - |B^0(-\vec{k})\overline{B}^0(\vec{k})\rangle], \end{aligned} \tag{2.1}$$

where τ_{B^0} is the lifetime of the neutral B meson, and $\vec{k}$ and $-\vec{k}$ are the B mesons' momenta in the $\Upsilon(4S)$ center of mass system. This coherence is preserved until one B meson decays. Hence, if we detect a decay of one of the B meson pair, which we call B_{tag}, and tag its flavor from the decay product at the time t_{tag}, we can determine the flavor of the other B meson, which we call B_{CP}, to be the opposite flavor of B_{tag} at t_{tag}. We then

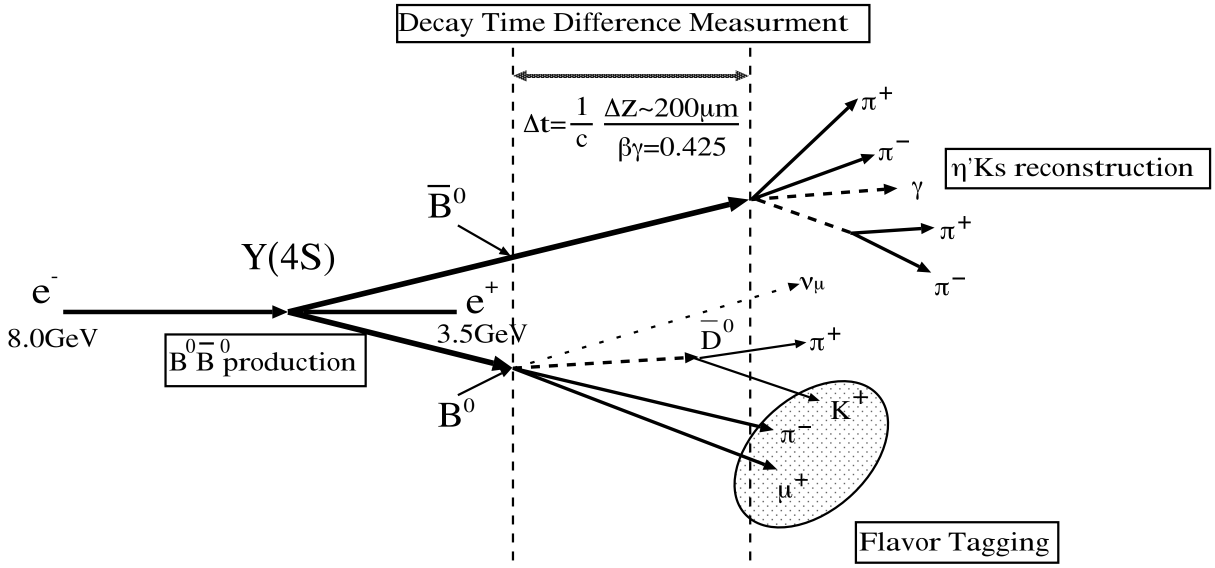

Figure 2.1: *The schematic picture of the experiment.*

detect B_{CP} decay into $\eta' K_S$ at the time t_{CP} by a probability given by

$$\mathcal{P}(q, \Delta t; \mathcal{A}_{\eta' K_S}, \mathcal{S}_{\eta' K_S}) = \frac{e^{-\frac{|\Delta t|}{\tau_{B^0}}}}{4\tau_{B^0}} [1 + q(\mathcal{A}_{\eta' K_S} \cos \Delta m_d \Delta t + \mathcal{S}_{\eta' K_S} \sin \Delta m_d \Delta t)], \tag{2.2}$$

where $\Delta t \equiv t_{CP} - t_{tag}$ and q denotes the flavor of B_{tag}: $q = +1$ corresponds to $B_{tag} = B^0$ and $q = -1$ corresponds to $B_{tag} = \overline{B}^0$. The CP asymmetry becomes

$$\begin{aligned} a_{\eta' K_S} &= \frac{\mathcal{P}(q = 1, \Delta t; \mathcal{A}_{\eta' K_S}, \mathcal{S}_{\eta' K_S}) - \mathcal{P}(q = -1, \Delta t; \mathcal{A}_{\eta' K_S}, \mathcal{S}_{\eta' K_S})}{\mathcal{P}(q = 1, \Delta t; \mathcal{A}_{\eta' K_S}, \mathcal{S}_{\eta' K_S}) + \mathcal{P}(q = -1, \Delta t); \mathcal{A}_{\eta' K_S}, \mathcal{S}_{\eta' K_S}} \\ &= \mathcal{A}_{\eta' K_S} \cos \Delta m_d \Delta t + \mathcal{S}_{\eta' K_S} \sin \Delta m_d \Delta t. \end{aligned} \tag{2.3}$$

The probability (2.2) is normalized in $-\infty < \Delta t < +\infty$. Although the explanation above is only for the case of $\Delta t \geq 0$, the equation also holds for $\Delta t < 0$. Interference of the decay of B_{CP} and the mixing of B_{tag} causes the CP asymmetry in the case of $\Delta t < 0$.

Considering the discussion above, experimentally necessary information to measure CP asymmetry parameters is summarized as follows:

- Reconstruction of B_{CP} decays into $\eta' K_S$,
- Measurement of decay time difference Δt between B_{CP} and B_{tag},
- Flavor tagging of B_{tag}.

These are shown schematically in Figure 2.1. The boosted $B\overline{B}^0$ pair plays an important role for the Δt measurement. Although the $\tau_{B^0} \sim 1.5$ ps is too short for a direct measurement, thanks to the Lorentz boost, we can measure the Δt as the distance of the B meson vertices. Since B mesons are nearly at rest in the $\Upsilon(4S)$ center of mass system, they fly along the electron beam direction and make decay vertices with an average distance of $\beta\gamma c\tau_{B^0} \sim 200\mu$m. The Δt is determined from the distance to be

$$\Delta t \simeq \frac{z_{CP} - z_{tag}}{\beta\gamma c} \tag{2.4}$$

where the z axis is defined to be anti-parallel to the positron beam direction, z_{CP} is the z position of the B_{CP} decay vertex and z_{tag} is the z position of the B_{tag} decay vertex. We can measure the Δz by using micro-strip silicon detectors with a spatial resolution better than 200 μm .

We explain the remaining two items and an extraction of CP asymmetry parameters from reconstructed events in the following sections.

2.2 $B_{CP} \to \eta' K_S$ Reconstruction

To maximize the sensitivity of the measurement, we need to collect $B^0 \to \eta' K_S$ decays as many as possible while keeping a small background fraction. As shown in Table 1.2, the branching fraction of the $B^0 \to \eta' K_S$ decay is $\mathcal{O}(10^{-5})$. Therefore, we need to produce a large number of B mesons. At the Belle experiment, the e^+e^- collisions with the world leading high luminosity of the KEKB collider have already accumulated $\sim 10^8$ $B\overline{B}$ pairs, which enable us to study $B^0 \to \eta' K_S$ decays. We reconstruct $\eta' K_S$ decays from the η' decaying into $\rho^0\gamma, \rho \to \pi^+\pi^-$ and $\eta\pi^+\pi^-, \eta \to \gamma\gamma$ and the K_S decaying into $\pi^+\pi^-$.

Background sources for $B^0 \to \eta' K_S$ decays are divided into two classes:

- Background from $B\overline{B}$ events,
- Background from $e^+e^- \to q\overline{q}(q = u, d, s, c)$ continuum events.

The background fraction from $B\overline{B}$ decays is small because the narrow width of η' reduces fake η' candidates and higher momenta of η' and K_S due to the two-body decay kinematics suppress the background from multi-body B decays.

On the other hand, particles from continuum events have higher momenta that can mimic $B^0 \to \eta' K_S$ decay. Also the cross section of the continuum process is about three times as large as the cross section of the $\Upsilon(4S)$ resonance. To suppress the continuum background, a difference in the event shape between the continuum and $B\overline{B}$ events is used. Figure 2.2 is a rough sketch of their event shapes. The continuum event consists of two jets and is collinear in the center of mass system. On the other hand, because $B\overline{B}$ pairs are nearly at rest in the center of mass system, their decay products are spherical.

2.3 Flavor Tagging

For the flavor tagging, relations between the flavor and charge of the decay products are used. In particular, the following lepton and kaon are important.

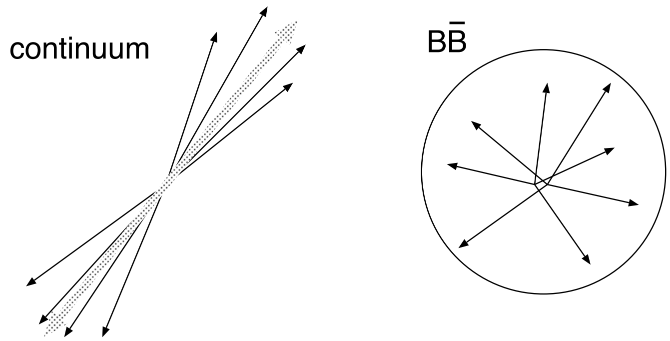

Figure 2.2: *Event shape of continuum (left) and $B\overline{B}$ events (right) in the center of mass system.*

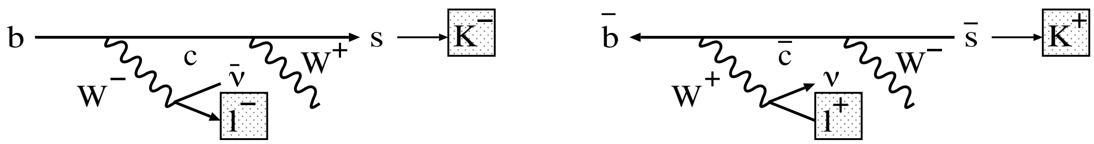

Figure 2.3: *The flavor specific decays of $b(\overline{b})$ into lepton or charged kaon.*

- The charge of leptons from semi-leptonic decays of B meson. As shown in Figure 2.3, the charge of leptons is correlated with the flavor of the primary b quarks.
- The strangeness from the cascade decay $b \to c \to s$. As also shown in Figure 2.3, the charge of K meson is correlated with the b quark flavor.

Because the branching fractions of inclusive $B^0 \to l^+X$ and $B^0 \to K^+X$ decays are about 20% and 80%, respectively, tagging with leptons and kaons is important. We need good particle identification capability to distinguish $e^\pm, \mu^\pm$ and $K^\pm$ from other particles, especially from $\pi^\pm$.

2.4 Extraction of CP Asymmetry Parameters

CP asymmetry parameters are extracted from the Δt distribution of reconstructed events. The measured Δt distribution is diluted by three sources: wrong flavor tagging, background contamination and Δt resolution. Figure 2.4 shows the dilution effect to the Δt distribution and CP asymmetry assuming the wrong tag probability of 20%, 50% background contamination and the Δt resolution of 200 μm. These values are typical for $B^0 \to \eta' K_S$. A Gaussian with rms of 1 ps is used for the Δt shape of the background. We can see that the proper evaluation of the wrong tag probability, the background and the Δt resolution is essential to extract correct CP asymmetry parameters without any bias.

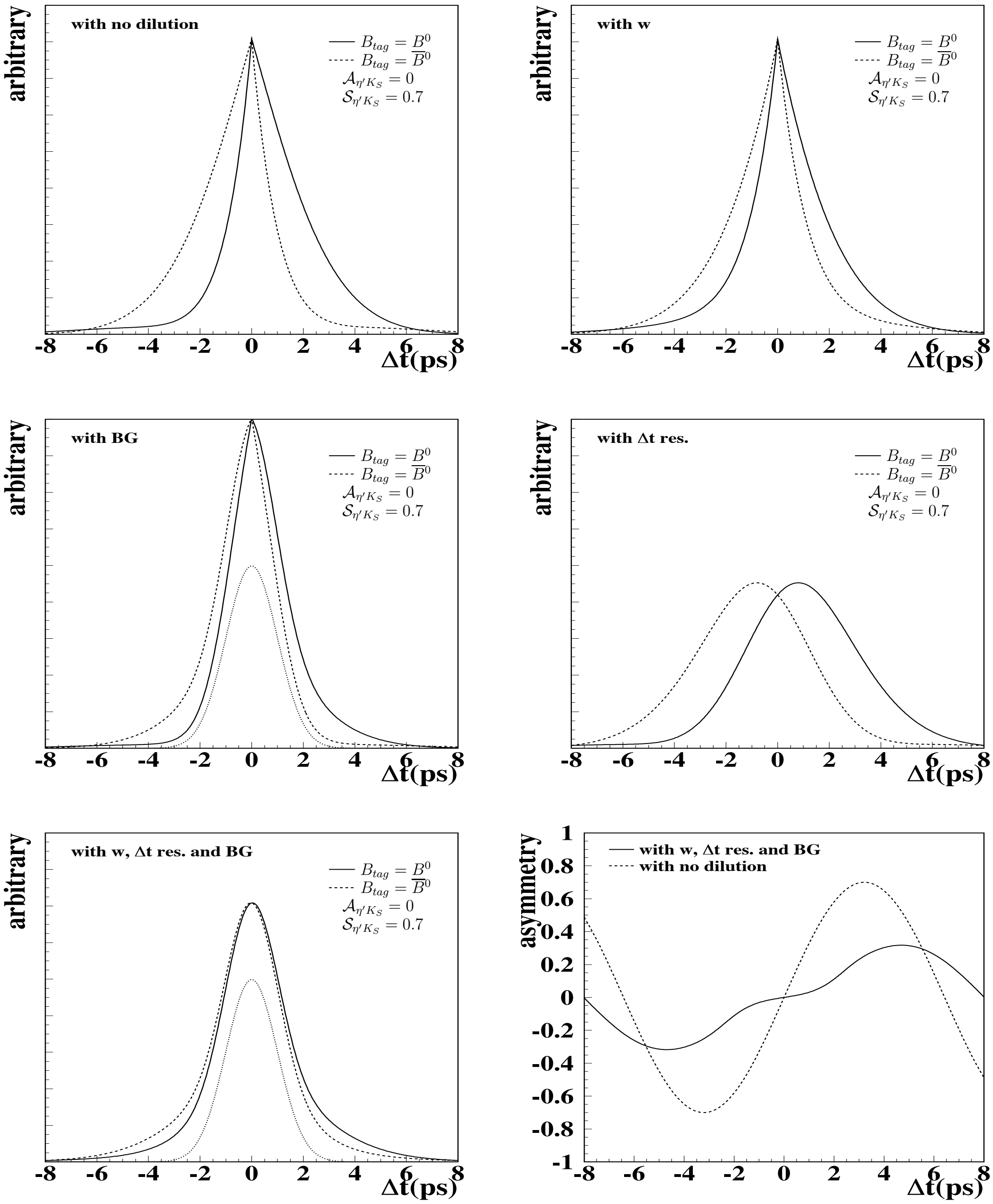

Figure 2.4: *Examples of* Δt *distributions and asymmetries with various experimental dilutions. Input* CP *asymmetry parameters are* $\mathcal{A}_{\eta' K_S} = 0$ *and* $\mathcal{S}_{\eta' K_S} = 0.7$*: The* Δt *distribution with no dilution (upper left), with the wrong tag probability of 20 % (upper right), with 50% background contamination, with the* Δt *resolution of* 200 μm *(middle right), with these three dilutions simultaneously (lower left), and the* CP *asymmetry with and without the dilutions (lower right). For the* Δt *distribution, the solid line shows* $B_{tag} = \overline{B}^0$ *and the dashed line shows* $B_{tag} = B^0$*. The dotted line shows the background* Δt *shape represented by a Gaussian with rms of 1 ps. For the* CP *asymmetry, the solid line shows the diluted asymmetry with these three sources and the dashed line shows asymmetry with no dilution.*

The dilution also affects the statistical significance of measured CP asymmetry parameters. The proper evaluation of the wrong tag probability, the background and the Δt resolution improves the statistical significance.

Neglecting the difference in the Δt shape and the flavor tagging efficiency between the signal and the background, the measured CP asymmetry is expressed as

$$a_{meas} \sim f_{sig}(1-2w)d_{\Delta t}\, a_{\eta' K_S}, \tag{2.5}$$

where a_{meas} is the measured CP asymmetry, $f_{sig} \equiv S/(S+B)$ is a fraction of signal events (S) in the the sum of signal and background events (B), $1-2w$ is a dilution due to a probability of wrong flavor tagging w, and $d_{\Delta t}$ denotes a dilution due to Δt resolution. The statistical error of the measured asymmetry δa_{meas} is proportional to $1/\sqrt{N}$, where N is the number of reconstructed and flavor tagged events. The N is given by $(S+B)\epsilon_{tag}$, where ϵ_{tag} is the flavor tagging efficiency. From (2.5), the statistical error of the true asymmetry $\delta a_{\eta' K_S}$ is calculated to be:

$$\begin{aligned} \delta a_{\eta' K_S} &\sim \delta a_{meas}\,[f_{sig}(1-2w)d_{\Delta t}]^{-1} \\ &\propto \left[\sqrt{(S+B)\epsilon_{tag}}\frac{S}{S+B}(1-2w)d_{\Delta t}\right]^{-1} \\ &= \left[\frac{S}{\sqrt{S+B}}\sqrt{\epsilon_{tag}(1-2w)^2}\,d_{\Delta t}\right]^{-1}. \end{aligned} \tag{2.6}$$

Two factors, $S/\sqrt{S+B}$ and $\epsilon_{tag}(1-2w)^2$, represent the effect of dilution due to background and flavor tagging, respectively. The first factor, $S/\sqrt{S+B}$, is a figure of merit of $\eta' K_S$ reconstruction. The $\epsilon_{tag}(1-2w)^2$ is called the effective tagging efficiency. By the proper evaluation of the background fractions, the wrong tag fractions and the Δt resolution, we can improve these factors by classifing events into several categories that have different background fraction, wrong tag probability or Δt resolution. For example, if we divide events into two subsamples that have different background levels, the total figure of merit (FOM) is given by the quadratic sum of two subsamples and is greater than that without dividing into subsamples. It is expressed as

$$\begin{aligned} \sqrt{\frac{S_1^2}{S_1+B_1}+\frac{S_2^2}{S_2+B_2}} &= \sqrt{\frac{(S_1+S_2)^2}{S_1+S_2+B_1+B_2}+\frac{S_1^2S_2^2(B_1/S_1-B_2/S_2)^2}{(S_1+B_1)(S_2+B_2)(S_1+S_2+B_1+B_2)}} \\ &= \sqrt{\frac{S^2}{S+B}+(\mathrm{FOM}_1\times\mathrm{FOM}_2)^2\frac{(B_1/S_1-B_2/S_2)^2}{S+B}} \\ &\geq \frac{S}{\sqrt{S+B}}, \end{aligned} \tag{2.7}$$

where $S_{1,2}$ and $B_{1,2}$ are the number of signal and background events of two subsamples, respectively. The total FOM is always greater than that without dividing into subsamples, if ratios of the signal to the background are different. This relation also holds for the effective tagging efficiency and the Δt resolution and for the case of more than one subsamples. The maximum statistical sensitivity is realized when these dilutions are determined event-by-event.

To maximize the statistical sensitivity by using event-by-event information, we use the unbinned maximum likelihood method to extract CP asymmetry parameters.

Chapter 3

Experimental Apparatus

The Belle experiment is performed in the KEK (High Energy Accelerator Research Organization), Tsukuba, Japan. The main physics goal is to test the Kobayashi-Maskawa mechanism of CP violation in B decays. The experiment has started data taking in June, 1999 and has achieved many physics results until now [46]. In this chapter, we briefly explain the apparatus of the experiment: the KEKB e^+e^- collider and the Belle detector.

3.1 The KEKB Collider

The KEKB [47] is an asymmetric energy e^+e^- collider. The energy of electrons and positrons are 8 GeV and 3.5 GeV, respectively. The center of mass energy is 10.58 GeV, which corresponds to the mass of the $\Upsilon(4S)$ resonance that decays into a $B\overline{B}$ meson pair. The produced B meson is boosted due to the asymmetric energy with a Lorentz factor $\beta\gamma \simeq 0.425$ and fly about 200 μm on average along the electron beam direction.

Figure 3.1 illustrates the configuration of the KEKB. The electrons (positrons) are accelerated to their full energies by the linear accelerator (Linac) and are injected into the HER (LER) of about 3 km circumference. These rings are built side by side in a tunnel 11 m below the ground level. The KEKB has only one interaction point (IP) in the Tsukuba experimental hall, where the electron and positron beams collide at a finite angle of ± 11 mrad to avoid parasitic collisions. The design luminosity is $10 \times 10^{33}\mathrm{cm}^{-2}\mathrm{s}^{-1}$ which corresponds to 10^8 $B\overline{B}$ pairs a year. The main parameters of the KEKB are summarized in Table 3.1. Figure 3.1 shows the luminosity history of the KEKB. As of Octorber 2002, the KEKB has achieved a peak luminosity of $8.26 \times 10^{33}\mathrm{cm}^{-2}\mathrm{s}^{-1}$ and data recorded by the Belle detector correspond to the integrated luminosity of 102 fb^{-1}. These are the world records at the time.

3.2 The Belle Detector

The Belle detector surrounds the IP to catch particles produced by the e^+e^- collisions. As explained in the last chapter, study of the time-dependent CP asymmetry needs efficient reconstruction of $B^0 \to \eta' K_S$ decays, reconstruction of B meson vertices and

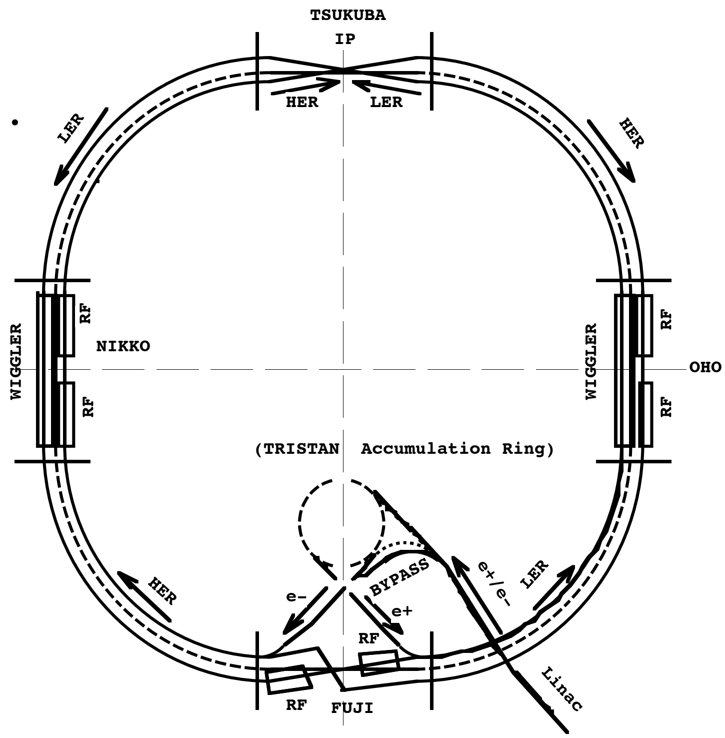

Figure 3.1: *Configuration of the KEKB collider*

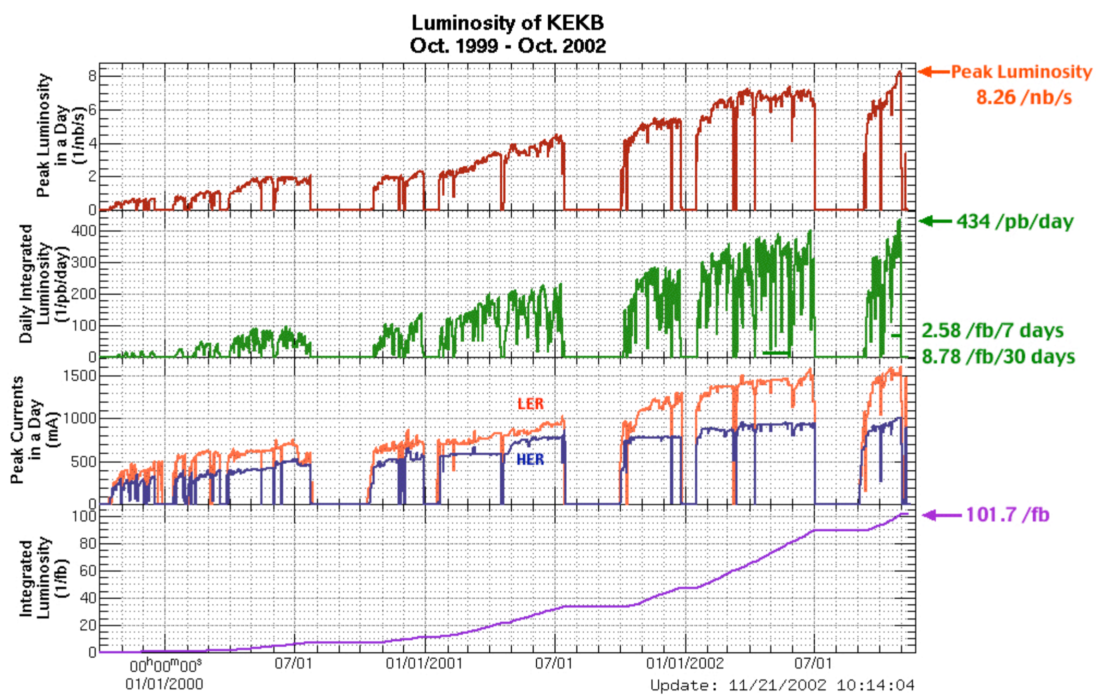

Figure 3.2: *Luminosity history of the KEKB collider*

Table 3.1: *Main parameters of KEKB.*

Ring		LER	HER	
Energy	E	3.5	8.0	GeV
Circumference	C	3016.26		m
Luminosity	$\mathcal{L}$	1×10^{34}		$\mathrm{cm}^{-2}\mathrm{s}^{-1}$
Crossing angle	θ_x	± 11		mrad
Tune shifts	ξ_x/ξ_y	0.039/0.052		
Beta function at IP	β_x^*/β_y^*	0.33/0.01		m
Beam current	I	2.6	1.1	A
Natural bunch length	σ_z	0.4		cm
Energy spread	σ_ε	7.1×10^{-4}	6.7×10^{-4}	
Bunch spacing	s_b	0.59		m
Particle/bunch	N	3.3×10^{10}	1.4×10^{10}	
Emittance	$\varepsilon_x/\varepsilon_y$	$1.8 \times 10^{-8}/3.6 \times 10^{-10}$		m
Synchrotron tune	ν_s	$0.01 \sim 0.02$		
Betatron tune	ν_x/ν_y	45.52/45.08	47.52/43.08	
Momentum compaction factor	α_p	$1 \times 10^{-4} \sim 2 \times 10^{-4}$		
Energy loss/turn	U_o	0.81†/1.5‡	3.5	MeV
RF voltage	V_c	$5 \sim 10$	$10 \sim 20$	MV
RF frequency	f_{RF}	508.887		MHz
Harmonic number	h	5120		
Longitudinal damping time	τ_ε	43†/23‡	23	ms
Total beam power	P_b	2.7†/4.5‡	4.0	MW
Radiation power	P_{SR}	2.1†/4.0‡	3.8	MW
HOM power	P_{HOM}	0.57	0.15	MW
Bending radius	ρ	16.3	104.5	m
Length of bending magnet	ℓ_B	0.915	5.86	m

†: without wigglers, ‡: with wigglers

identification of charged particle ($e^\pm, \mu^\pm, \pi^\pm$ and $K^\pm$) for the flavor tagging. The Belle detector is designed to detect and identify many charged and neutral particles and to detect B vertices by several sub-detectors.

Figure 3.3 and 3.4 shows the detector configuration. The B meson vertices are measured by the silicon vertex detector (SVD) situated just outside of a cylindrical beryllium beam pipe. Charged particle tracking is performed by the central drift chamber. Particle identification is provided by dE/dx measurements in CDC, aerogel Čherencov counter (ACC), and time-of-flight counter (TOF) placed radially outside of CDC. Electromagnetic showers, which are used to identify photons and electrons, are detected in an array of CsI(Tl) crystals (ECL) located inside the solenoid coil. The super-conducting solenoid provide a magnetic field of 1.5 T for momentum measurement of charged particles by CDC. Muons and K_L mesons are identified by arrays of resistive plate counters interspersed in the iron yoke (KLM). In addition to these sub-detectors, the Belle detector has extreme forward calorimeter (EFC) to improve the experimental sensitivity to some physics processes such as $B \to \tau\nu$. The detector performance is summarized in Table 3.2.

Figure 3.5 illustrates the Belle coordinate system which is defined as:

- x: horizontal, outward to the KEKB ring,
- y: vertical, upward,
- z: opposite of the positron beam direction,
- r: $\sqrt{x^2 + y^2}$,
- θ: the polar angle from z axis,
- and ϕ: the azimuth angle around z axis.

The detailed description of the Belle detector is found in the reference [48]. We give the brief description of the major detector subsystems and analysis software relevant to the measurement of CP asymmetry parameters.

3.2.1 Beam Pipe

The beam pipe is designed to minimize its thickness to reduce multiple coulomb scattering which deteoriate the vertex resolution. Figure 3.6 shows the cross section of the beryllium beam pipe at the interaction region. The beam pipe consists of two cylinders with different radii, the inner is 20.0 mm and the outer is 23.0 mm. Each cylinder have 0.5 mm thickness. A 2.5 mm gap between the cylinders provides a channel for cooling a beam-induced heating. Helium gas is used as a coolant in order to minimize the material in the beam pipe. Outside the outer beryllium cylinder, a 20 μm thick gold sheet is attached in order to reduce the low energy X-ray background from the HER. The total thickness of the beam pipe corresponds to 0.9% of a radiation length.

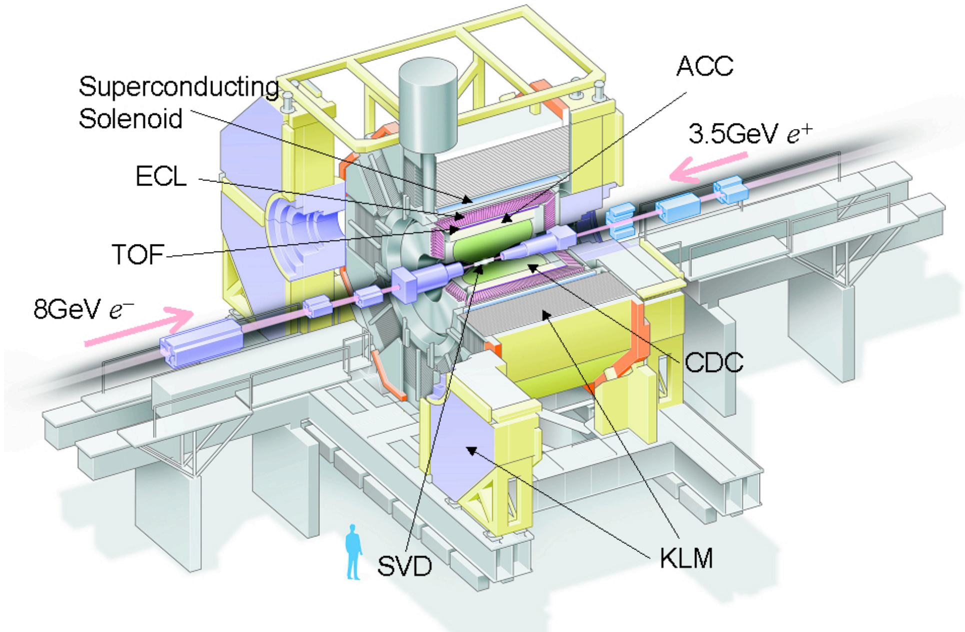

Figure 3.3: *Configuration of the Belle detector system.*

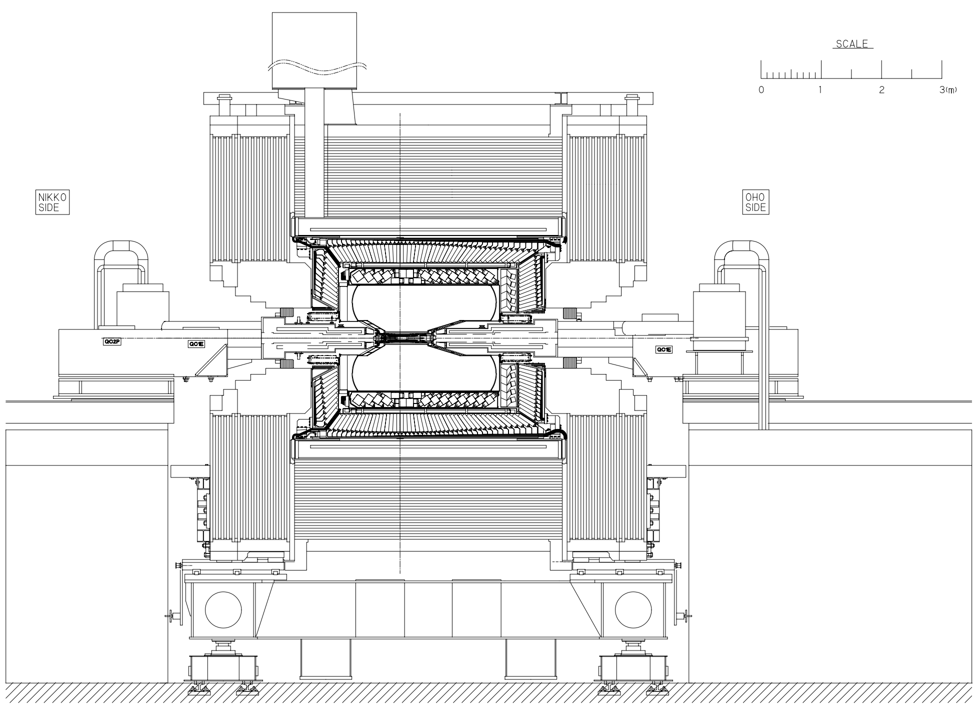

Figure 3.4: *Side view of the Belle detector.*

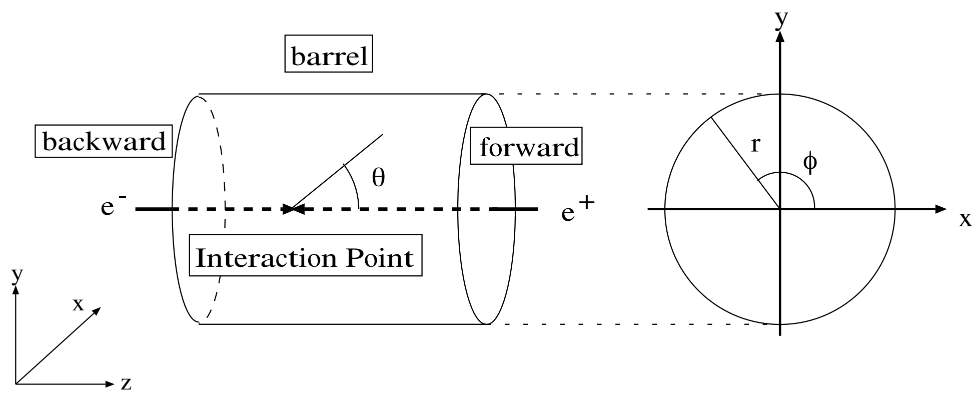

Figure 3.5: *Definition of the coordinate system.*

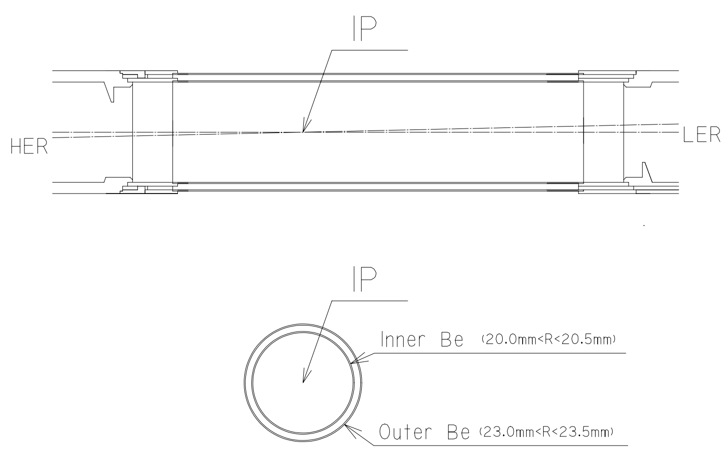

Figure 3.6: *The cross secton of the beryllium beam pipe at the interaction point.*

Detector	Type	Configuration	Readout	Performance
	Beryllium	Cylindrical, r=2.0 cm		He gas cooled
Beam pipe	double-wall	0.5/2.5/0.5(mm)=Be/He/Be		
	Double	300 μm-thick, 3 layers	ϕ : 40.96k	$\sigma_{\Delta z}$ ~200 μm
SVD	sided	r = 3.0 - 6.05 cm	z : 40.96k	
	Si strip	Length = 22 - 34 cm		
	Small cell	Anode: 50 layers	A: 8.4 K	$\sigma_{r\phi} = 130\ \mu$m
CDC	drift	Cathode: 3 layers	C: 1.5 K	$\sigma_z \lesssim 200 \sim 1,400\mu$m
	chamber	r = 8.3 - 86.3 cm		$\sigma_{p_t}/p_t = 0.3\%\sqrt{p_t^2+1}$
		-77$\leq z \leq$ 160 cm		$\sigma_{dE/dx} = 6\%$
	n : 1.01	~12x12x12 cm^3 blocks		$N_{p.e.} \geq 6$
ACC	$\sim$ 1.03	960 barrel		K/π separtation :
	Silica	/ 228 endcap		1.2<p<3.5GeV/c
	aerogel	FM-PMT readout	1,788	
TOF	Scintillator	128 ϕ segmentation	128$\times$2	σ_t = 100 ps
		r = 120 cm, 3 m-long		K/π separation :
TSC		64 ϕ segmentation	64	up to 1.2GeV/c
	CsI	Barrel : r = 125 - 162 cm	6,624	σ_E/E= 1.3 %/$\sqrt{E}$
ECL	(Towered-	End-cap : z =	1152 (F)	σ_{pos} = 0.5 cm/$\sqrt{E}$
	structure)	-102 cm and +196 cm	960 (B)	
Magnet	Super	inner radious = 170 cm		B = 1.5 T
	conducting			
	Resistive	14 layers	θ:16 K	$\Delta\phi$=$\Delta\theta$=30 mrad
KLM	plate	(5cm Fe+4cm gap)	ϕ:16 K	for K_L
	counters	2 RPCs in each gap		$\sim$ 1 % hadron fake
EFC	BGO	2x1.5x12 cm^3	θ:5	σ_E/E=
			ϕ:32	$(0.3 \sim 1)\%/\sqrt{E}$

Table 3.2: *Performance parameters expected (or achieved) for the Belle detectror (p_t in* GeV/c, *E in GeV).*

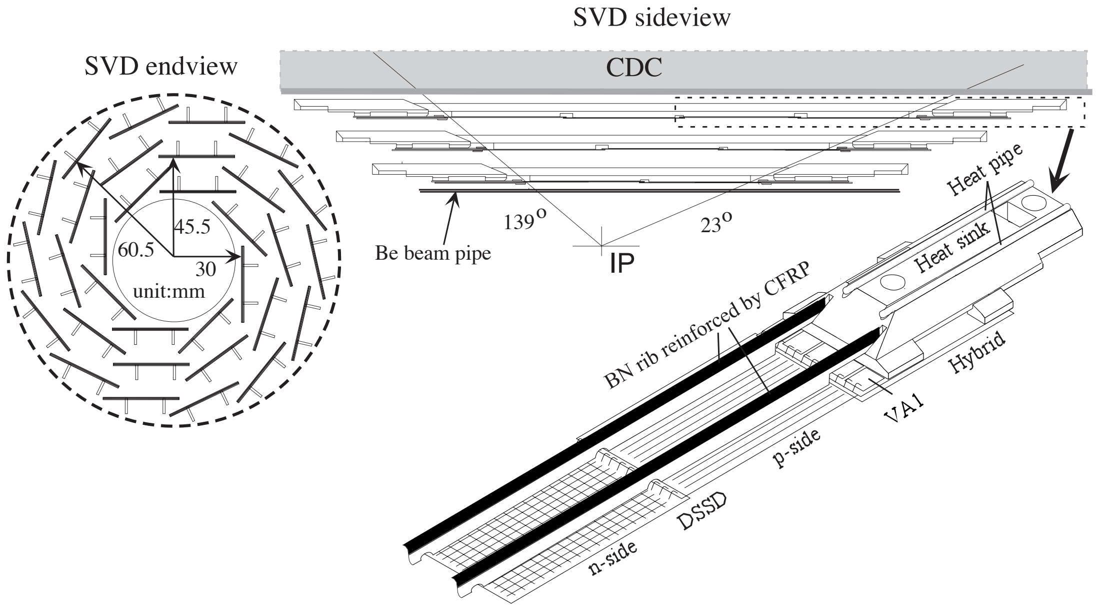

Figure 3.7: *Detector configuration of SVD.*

3.2.2 Silicon Vertex Detector(SVD)

SVD detect the B meson vertex position which is essential for the measurement of time-dependent CP asymmetry parameters.

Figure 3.7 shows the geometrical configuration of SVD. SVD consists of three concentric cylindrical layers of silicon sensors and covers a polar angle $23° < \theta < 139°$. This corresponds to 86% of the full solid angle. The radii of the three layers are 30, 45.5 and 60.5 mm. The three layers are constructed from 8, 10 and 14 ladders. Each ladder is made up of two long or short half ladders that are mechanically jointed by a support structure but electrically independent of each other. Each long half-ladder contains two double-sided silicon strip detectors (DSSDs) and a hybrid unit. Each short half-ladder contains a DSSD and a hybrid unit. The innermost layer ladder consists of two short half-ladders. The middle layer ladder consists of a short and a long half-ladder. The outermost layer ladder consists of two long half-ladders.

We use S6936 DSSDs fabricated by Hamamatsu Photonics, which were originally developed for the DELPHI [49]. The size of DSSD is 57.5×33.5 mm^2 with thickness of 300 μm . The schematic view of DSSD is shown in Figure 3.8. One side (n-side) of DSSD has n^+ strips oriented perpendicular to the beam direction to measure the z coordinate. The other side (p-side) with longitudinal p^+ strips allows the ϕ coordinate measurement. The n^+-strips are interleaved by p^+ implants, which are called p stops, to separatethe consecutive strips electrically. The bias voltage of 75V is supplied to the n-side, while p-side is grounded. A charged particle passing through the depletion region of the n bulk silicon generates pairs of electron and hole. The electrons and holes drift to each strip and make two dimensional hit signals. The strip pitch is 25 μm for p-side and

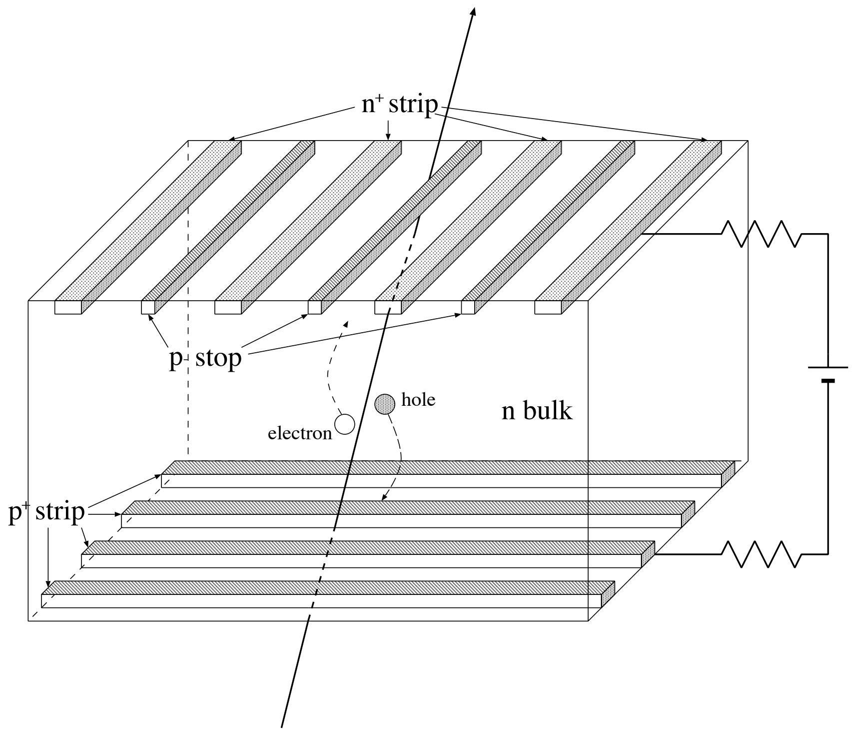

Figure 3.8: *Schematic drawing of the DSSD.*

42 μm for n-side. On the n-side, adjacent strips are read out by a single channel. This gives an effective strip pitch of 84 μm . On the p-side, every other strip is connected to a readout channel. Charge collected by the floating strips in between is read from adjacent strips by means of capacitive charge division. The signal of DSSDs are read out by VA1 chips [50, 51]. The VA1 chip is a 128 channel CMOS integrated circuit fabricated in the Austrian Micro Systems (AMS). Five VA1 chips are on both side of each hybrid unit. A total number of readout channels is 81,920.

The performance of SVD is parameterized by the SVD-CDC track matching efficiency and the impact parameter resolution of tracks with associated SVD hits. The SVD-CDC track matching efficiency is defined as the probability that a CDC track within the SVD acceptance has associated SVD hits in at least two layers, and in at least one layer with both the r-ϕ and r-z information. Figure 3.9 shows the SVD-CDC track matching efficiency for hadronic events as a function of time. The average matching efficiency is better than 98.7%, although we observe slight degradation after one year operation as a aresult of the gain loss of VA1 from radiation damage [52]. The momentum and angular dependence of the impact prameter resolution are shown in Figure 3.10. They are well represented by the following formula: $\sigma_{xy} = 19 \oplus 50/(p\beta \sin^{3/2}\theta)$ μm and $\sigma_z = 36 \oplus 42/(p\beta \sin^{5/2}\theta)$ μm , where "$\oplus$" indicates a quadratic sum.

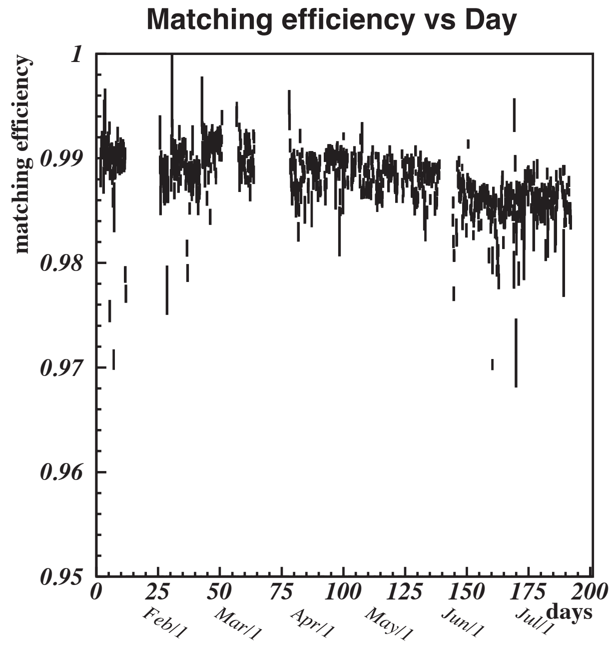

Figure 3.9: *SVD-CDC track matching efficiency as a function of the date of data taking.*

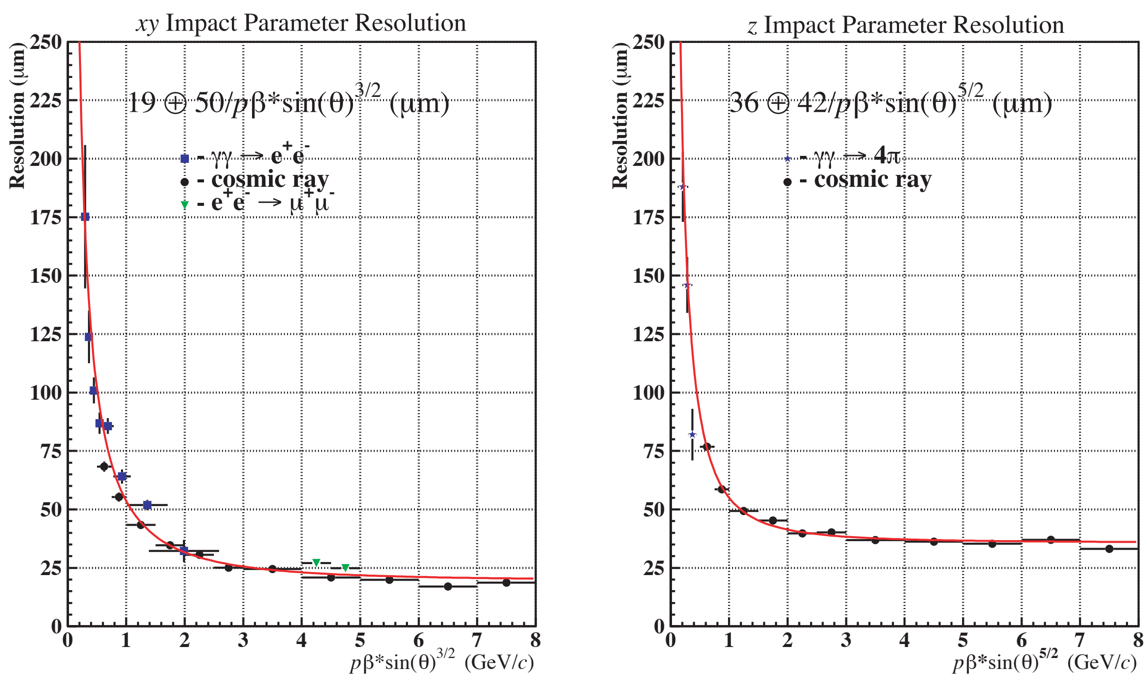

Figure 3.10: *Impact parameter resolution of charged tracks with associated SVD hits.*

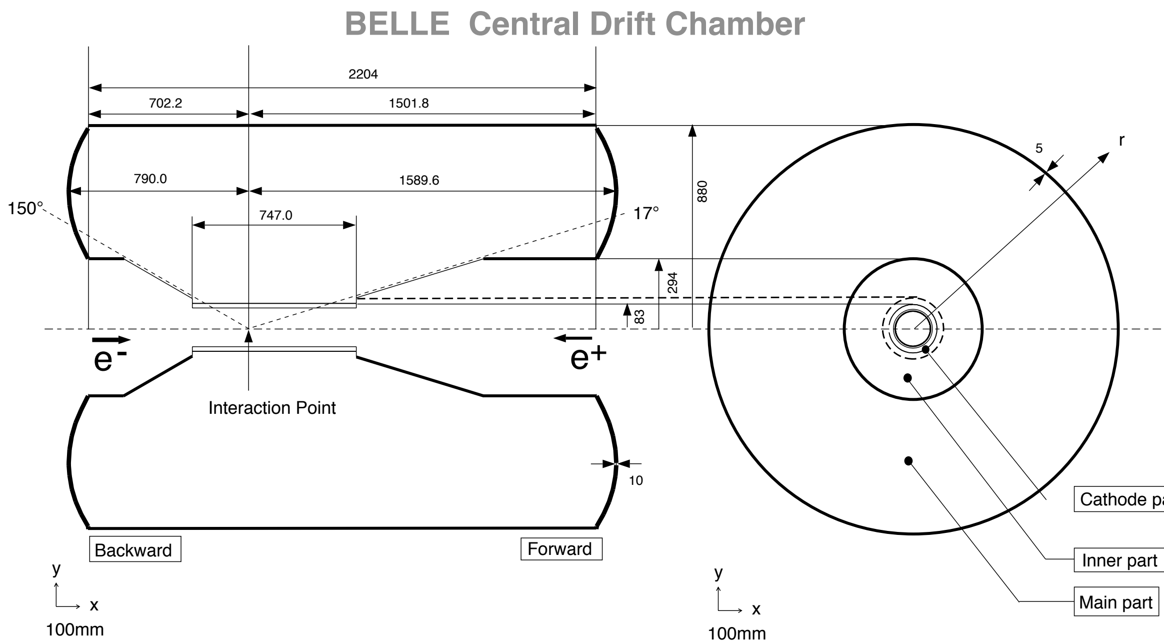

Figure 3.11: *Overview of the CDC structure. The lengths in the figure are in units of mm.*

3.2.3 Central Drift Chamber(CDC)

The main role of Central Drift Chamber(CDC) is detection of charged particle tracks and reconstruction of their momenta from their curvature in the magnetic field of 1.5 T provided by the superconducting solenoid. CDC also provides particle identification information in the form of dE/dx measurements for charged particles.

The structure of CDC is shown in Figure 3.11. The length is 2,400 mm, and the inner and outer radii are 83 and 874 mm, respectively. The polar angle coverage is $17° \leq \theta \leq 150°$. CDC is a small cell drift chamber containing a total of 50 anode sense wire layers (32 axial wire layers and 18 stereo wire layers) and 3 cathode strip layers. The axial wires are configured to be parallel to z axis, while the stereo wires are slanted by approximately ± 50 mrad. The three dimensional information is provided by this wire configuration. Eight field wires providing drift electric field surround a sense wire, and the field wires and a sense wire form a drift cell. The cell structure is shown in Figure 3.12. CDC has 8,400 drift cells. A mixture of helium (50%) and ethane (50%) gas is filled in the chamber. A charged particle passing through CDC ionizes the gas. A charge avalanche is caused by the ionized gas and drifts to a sense wire with a specific drift velocity, then the measured signal height and drift the time provides information of the energy deposit and distance from the sense wire. In the innermost radii, the three cathode strip layers are installed to provide the z position measurements of tracks for the trigger system. The number of readout channel is 8,400 for anode sence wires and 1,792 for cathode strips.

Figure 3.13 shows the transverse momentum resolution (p_t) resolution as a function of

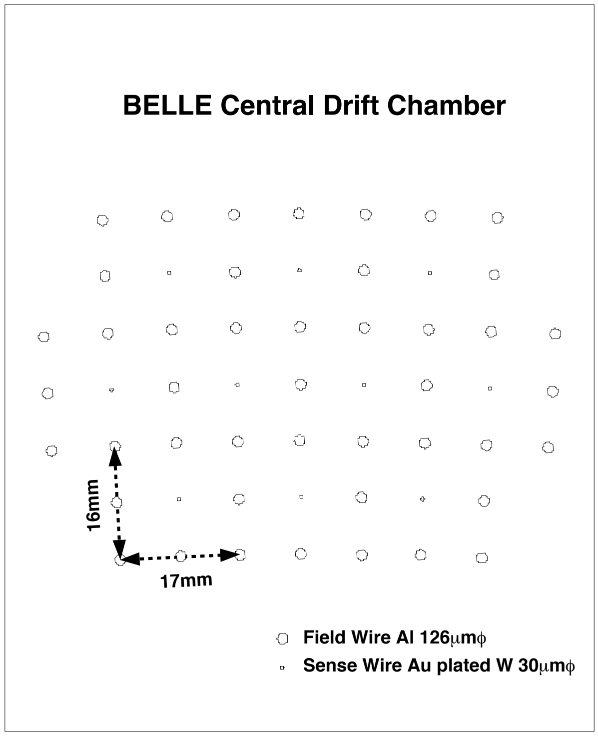

Figure 3.12: *Cell structure of CDC.*

p_t. The p_t resolution is $(0.20p_t \oplus 0.29)\%$, where p_t is in unit of GeV/c. Figure 3.14 shows a scatter plot of measured dE/dx and particle momentum. Populations of pions, kaons, protons and electrons are clearly seen. Figure 3.15 shows the distribution of dE/dx for minimum ionizing particles measured with pions from K_S decays. The dE/dx resolution is measured to be 7.8%

3.2.4 Aerogel Čherenkov Counter(ACC)

The aerogel Čherenkov counter (ACC) provides separation between $K^{\pm}$ and $\pi^{\pm}$ with momentum ranged from 1.2 GeV/c to 3.5 GeV/c.

ACC detects if the particle emit Čherenkov light or not and distinguishes particle species. A charged particle passing through a matter emit Čherenkov light if its velocity is larger than the light velocity in the matter. The condition to emit Čhrenkov light is written as

$$m < p\sqrt{n^2 - 1}, \tag{3.1}$$

where m and p are the particle mass and the momentum and n is the refractive index of the matter.

Figure 3.16 shows the configuration of ACC. ACC consists of 960 counter modules segmented into 60 cells in the ϕ direction for the barrel part and 228 modules arranged in 5 concentric layers for the forward endcap part of the detector. Each counter mod-

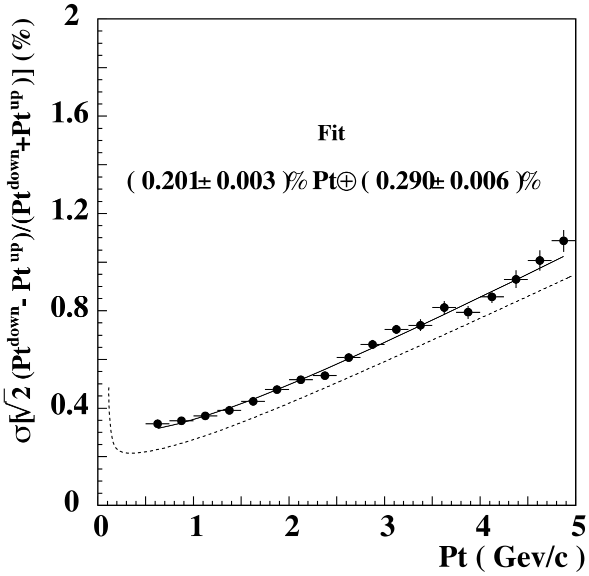

Figure 3.13: *The p_t resolution is a function of p_t itself. The solid curve shows the fitted result (0.201%$p_t \oplus 0.290\%/\beta$) and the dotted curve shows the ideal expectation for $\beta = 1$ particles.*

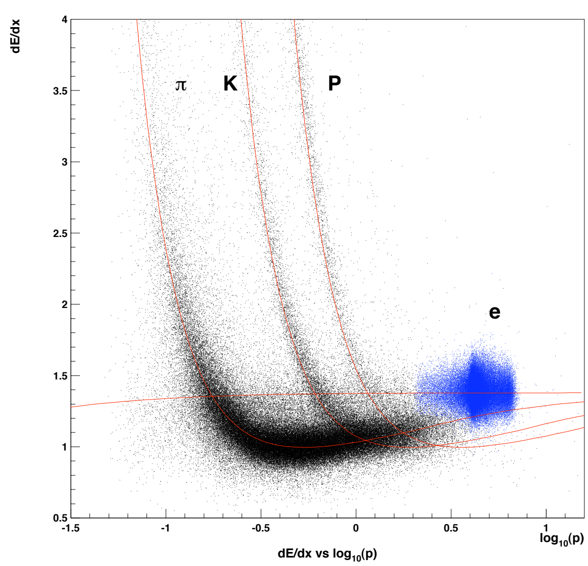

Figure 3.14: *The measured dE/dx versus momentum observed in collision data.*

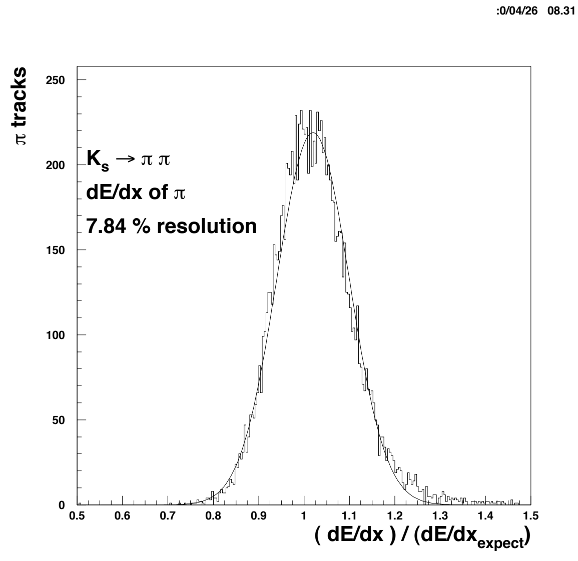

Figure 3.15: *Distribution of* $(dE/dx)/(dE/dx_{exp})$ *for pions from* K_S^0 *decays.*

ule consists of a block of silica aerogel in an aluminum box of 0.2 mm thickness and one or two fine mesh-type photomultiplier tubes (FM-PMTs) which can work in the 1.5 T magnetic field. The silica aerogel with five different refractive indices, namely, $n = 1.010, 1.013, 1.015, 1.020$ and 1.028 are used for the barrel modules depending on the polar angle. The refractive indices are selected to cover up to the maximum momentum of two body B decays. For the endcap module, the silica aerogel with $n = 1.030$ is used for low momentum particles, which is necessary for flavor tagging, to cover lack of TOF in the endcap. The number of readout channel is 1,560 for the barrel modules and 228 for the endcap modules.

Figure 3.17 shows measured pulse height distributions for barrel ACC for $e^{\pm}$ tracks in Bhabha events and $K^{\pm}$ candidates in hadronic events, where $K^{\pm}$ candidates are selected by TOF and dE/dx measurements, together with the expectations from Monte Carlo simulation. Clear separation between $K^{\pm}$ and $e^{\pm}$ is seen.

3.2.5 Time of Flight Counter(TOF)

Time of flight counter (TOF) detector system using plastic scintillation counters is used to distinguish $K^{\pm}$ from $\pi^{\pm}$ up to 1.2 GeV/c. TOF measure the elapsed time between a collision at the interaction point and the time when the particle hits the TOF layer. A relation between measured time T and the particle mass m is expressed as

$$m = p\sqrt{\frac{c^2T^2}{L^2} - 1}, \tag{3.2}$$

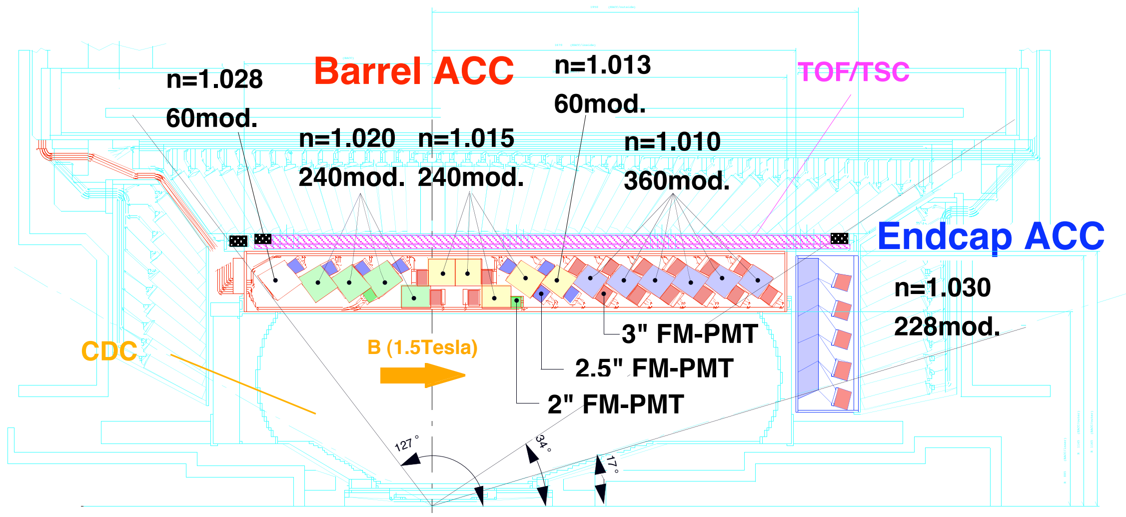

Figure 3.16: *The arrangement of ACC.*

where p is the particle momentum and L is the flight path length. For $K^{\pm}$ and $\pi^{\pm}$ with a momentum of 1.2 GeV/c and a flight path length of 1.2 m, which is the distance between the interaction point and TOF, give T of 4.3 ns and 4.0 ns, respectively. TOF is designed to have 100 ps time resolution which separate these $K^{\pm}$ and $\pi^{\pm}$ by 3 σ significance. In addition to particle identification, TOF provide fast timing signals for the trigger system. To sustain the fast trigger rate in any beam background condition, the thin trigger scintillation counters (TSC) is appended just inside the TOF counter.

TOF system consists of 128 counters and 64 TSCs. Two trapezoidally shaped TOF counters and one TSC counter form one module. Figure 3.18 shows the configuration of a TOF/TSC module. In total 64 TOF/TSC modules located at a radius of 1.2 m from the interaction point cover a polar angle ranged from 34° to 120°. Each TOF counter is read out by a FM-PMT at each end. Each TSC counter is read out by only one FM-PMT from the backward end. The total number of readout channels is 256 for TOF and 64 for TSC.

Figure 3.19 shows TOF time resolution for forward and backward PMTs and for the weighted average as a function of z position in TOF module measured by μ-pair events. The resolution for the weighted average time is about 100 ps with a small z dependence. Figure 3.20 shows the mass distribution obtained from TOF measurement. Clear peaks corresponding to $\pi^{\pm}$, $K^{\pm}$ and protons are seen. The data points are in good agreement with the expectation assuming time resolution of 100 ps (histogram).

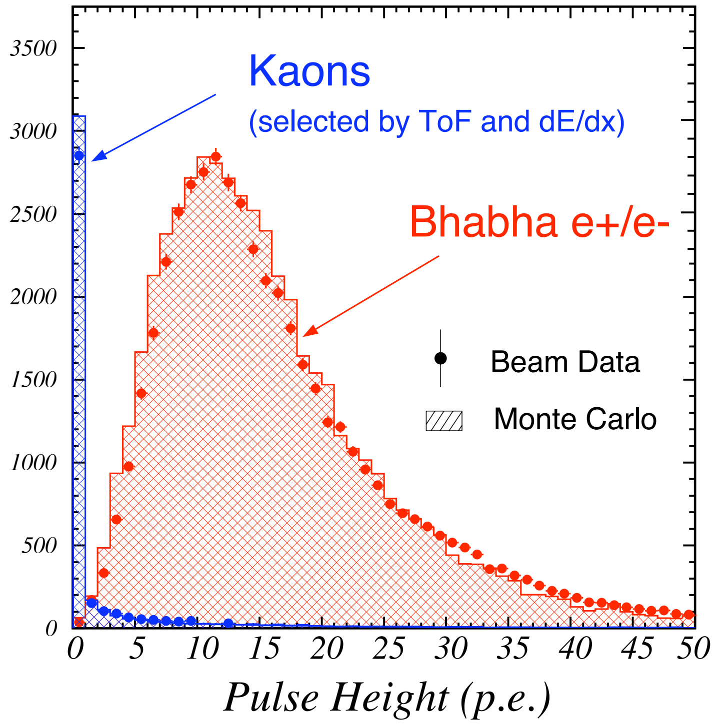

Figure 3.17: *Pulse-height spectra in units of photoelectrons observed by barrel ACC for electrons and kaons.*

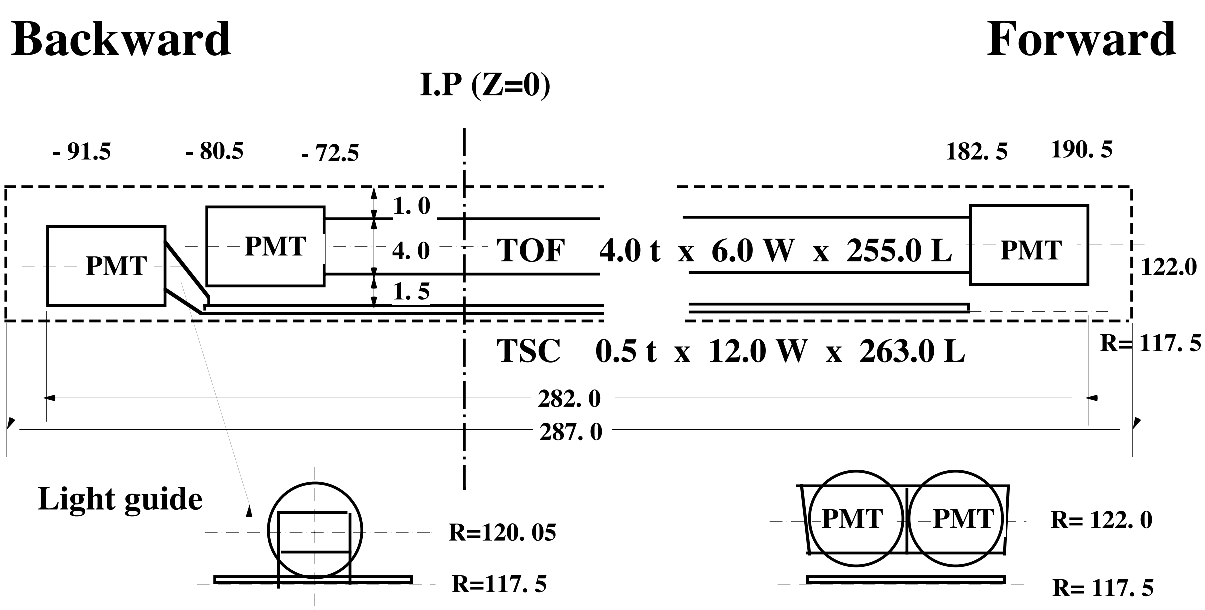

Figure 3.18: *Dimensions of a TOF/TSC module.*

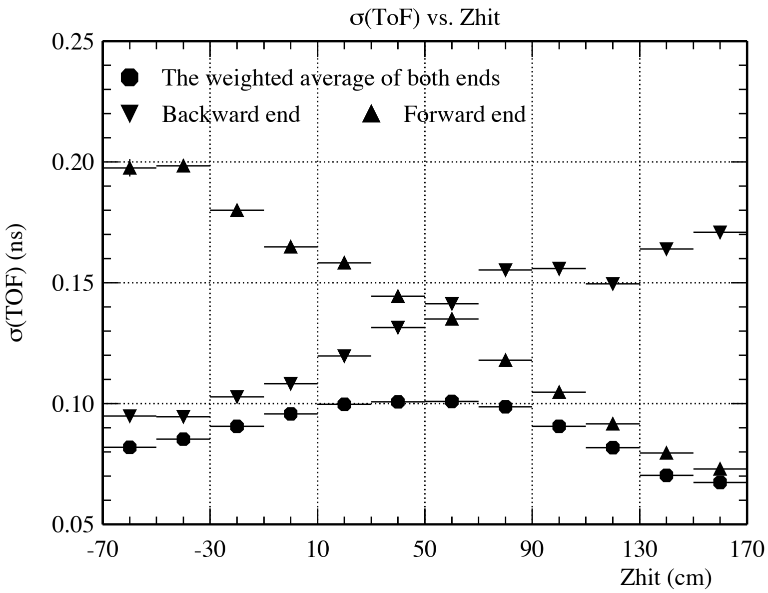

Figure 3.19: *Time resolution for μ-pair events.*

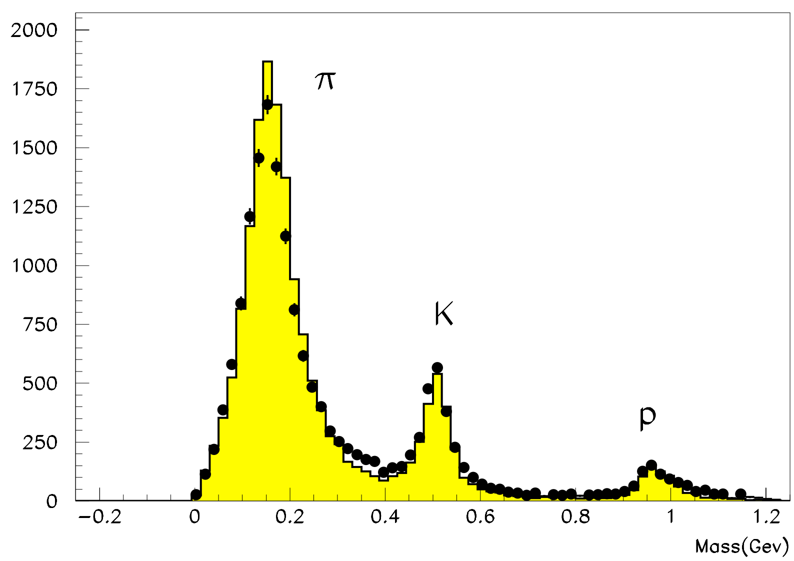

Figure 3.20: *Mass distribution from TOF measurement for particle momenta below 1.2GeV/c. Histogram shows the expectation assuming time resolution of 100 ps. The points with error bars are data.*

3.2.6 $K^\pm/\pi^\pm$ Identification

As explained in the previous chapter, $K^\pm/\pi^\pm$ identification is crucial for flavor tagging. The $K^\pm/\pi^\pm$ identification is carried out by combining information from three nearly independent measurements: dE/dx measurement by CDC, TOF measurement, and measurement of the number of photoelectrons in the ACC. For each charged track, we calculate probability with kaon and pion hypothesis for each subdetector. The probabilities of each subdetector is combined to form a likelihood ratio defined as $PID(K) \equiv P_K/(P_K + P_\pi)$, where P_K and P_π are product of subdetectors' probabilities for $K^\pm$ and $\pi^\pm$, respectively. The $K^\pm/\pi^\pm$ identification is performed with the $PID(K)$. The $K^\pm$ identification efficiency and wrong identification probability of $\pi^\pm$ as $K^\pm$ measured with $D^{*\pm} \to D^0(\to K^\mp\pi^\pm)\pi^\pm$ decays are shown in Figure 3.21. For most of the momentum region, the measured $K^\pm$ identification efficiency exceeds 80%, while the π fake rate is kept below 10%.

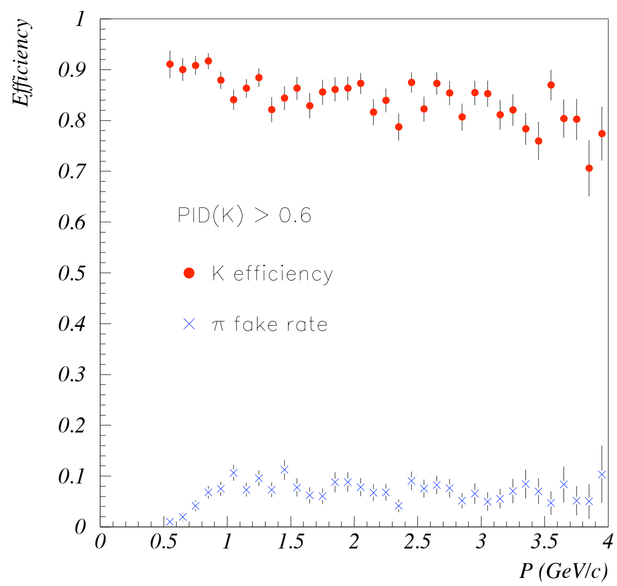

Figure 3.21: *K efficiency and π fake rate as a function of momentum.*

3.2.7 Electromagnetic Calorimeter(ECL)

The main purpose of the electromagnetic calorimeter (ECL) is the detection of electrons and photons from B meson decays with high efficiency and good energy and position resolutions. For our measurement, the photon reconstruction is necessary for η' reconstruction and electrons are used for flavor tagging.

The overall configuration of the ECL is shown in Figure 3.22. ECL consists of 8,736 thallium doped CsI crystal counters. The barrel part has 6,624 crystals segmented 46 in θ and 144 in ϕ. The forward (backward) endcap has 1,152 (960) crystals segmented 13 (10) in θ and 48-144 (64-144) in ϕ depending on θ. Each CsI(Tl) crystal has tower shape of 30 cm long, which corresponds to 16.2 radiation lengths, and is arranged so that it points to the interaction point. A signal from each crystal is read out by two 10 mm $\times$ 20 mm photodiodes. The total number of readout channels is 17,472.

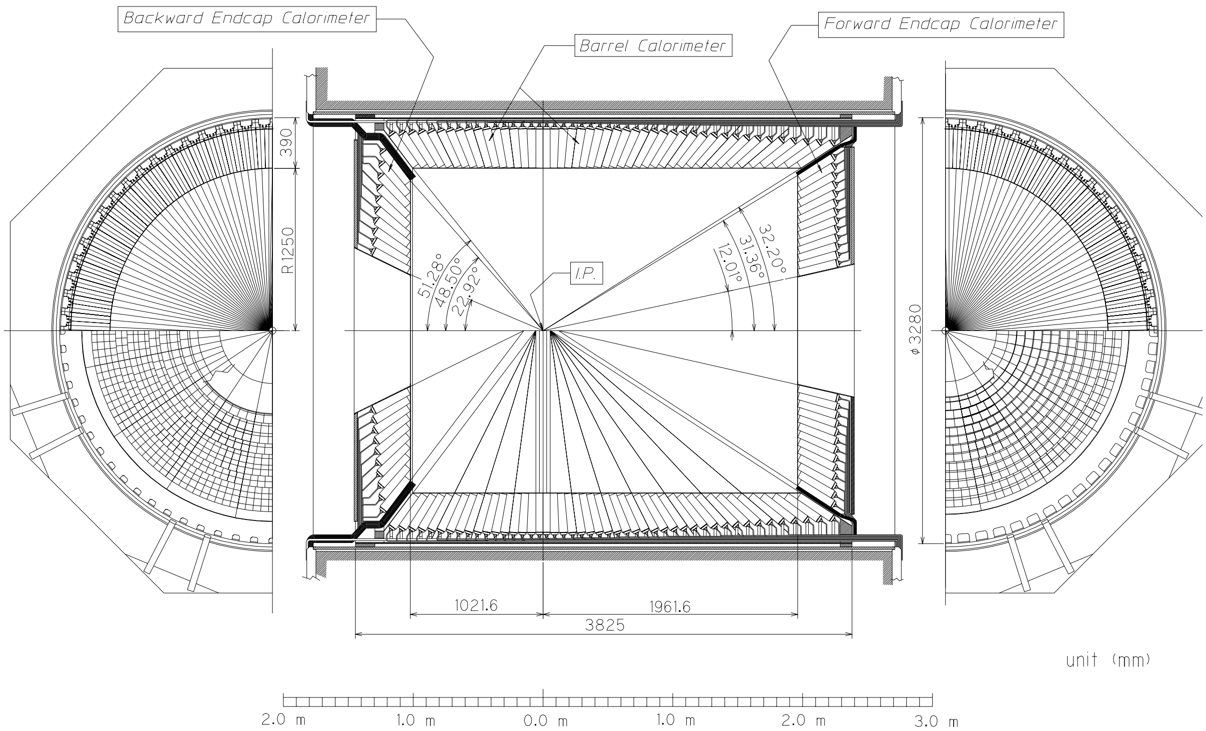

Figure 3.22: *Configuration of ECL.*

The energy resolution is measured with the beam test before installation into the Belle structure to be $\sigma_E/E = 1.34 \oplus 0.066/E \oplus 0.81/E^{1/4}$, where E in GeV. The position resolution is $0.27 + 3.4/E^{1/2} + 1.8/E^{1/4}$. Figure 3.23 show the energy resolution and the position resolution.

The electron identification primarily relies on a comparison of the charged particle momentum measured by the CDC and the energy deposit in ECL. Electrons lose all their energy in ECL crystals by electromagnetic showers, while hadrons and muons do not make electromagnetic shower and deposit only a part of their energy in ECL. The ratio of cluster energy measured by ECL and charged track momentum measured by CDC, E/p, is, therefore, close to unity for electrons and lower for other particles. The lateral spread of ECL cluster is also used to distinguish electrons from hadrons. Because the radiation

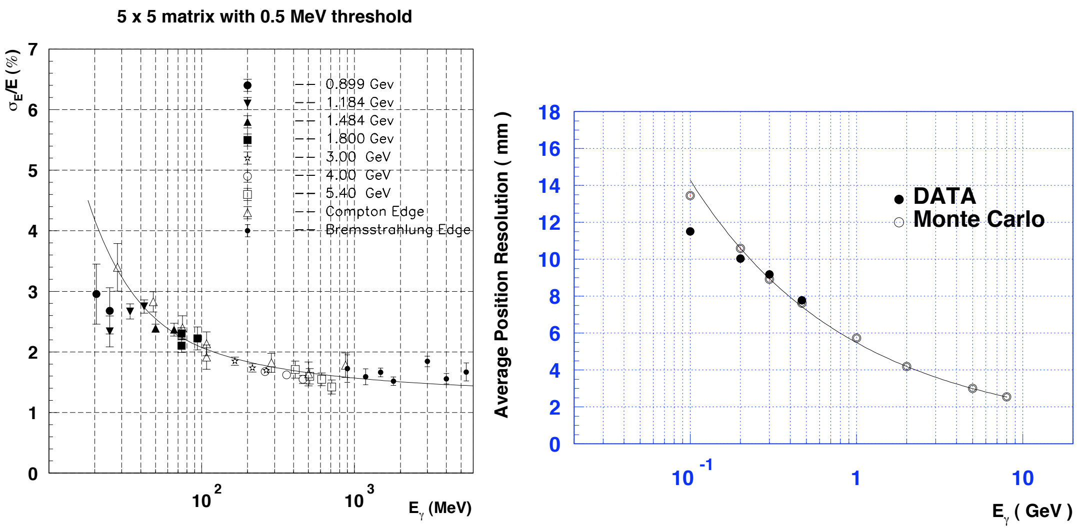

Figure 3.23: *The energy resolution (left) and the position resolution (right) of ECL as a function of incident photon energy.*

length of electrons is smaller than the interaction length of hadrons, clusters made by hadrons tend to be wider than those of electrons. In addition to these ECL information, dE/dx measured by CDC and light yield of ACC are incorporated. Figure 3.24 shows the electron identification efficiency measured with $e^+e^- \to e^+e^-e^+e^-$ data and the fake rate for charged pions from $K_S \to \pi^+\pi^-$ decays as a function of momentum. The efficiency of electron identification is greater than 90 % and the hadron fake rate is about 0.3 % for $p > 1$ GeV/c. The details of electron identification are given in [53].

3.2.8 Solenoid Magnet

The super-conducting solenoid provides a magnetic field of 1.5 T over the tracking volume for measurement of charged particle momentum. The super-conducting coil consists of a single layer of niobium-titanium-copper alloy embedded in a high purity aluminum stabilizer. It is wound around the inner surface of an aluminum support cylinder with 3.4 m in diameter and 4.4 m length. Indirect cooling is provided by liquid helium circulating through a tube on the inner surface of the aluminum cylinder. Figure 3.25 shows the structure of the solenoid.

3.2.9 K_L and Muon Detector(KLM)

KLM detects K_L and muons. For our measurement, KLM provides muons for flavor tagging.

KLM consists of alternating layers of charged particle detectors and 4.7 cm thick iron plates. There are 15 resistive plate counter (RPC) superlayers and 14 iron layers in the octagonal barrel region and 14 RPC superlayers in each of the forward and backward

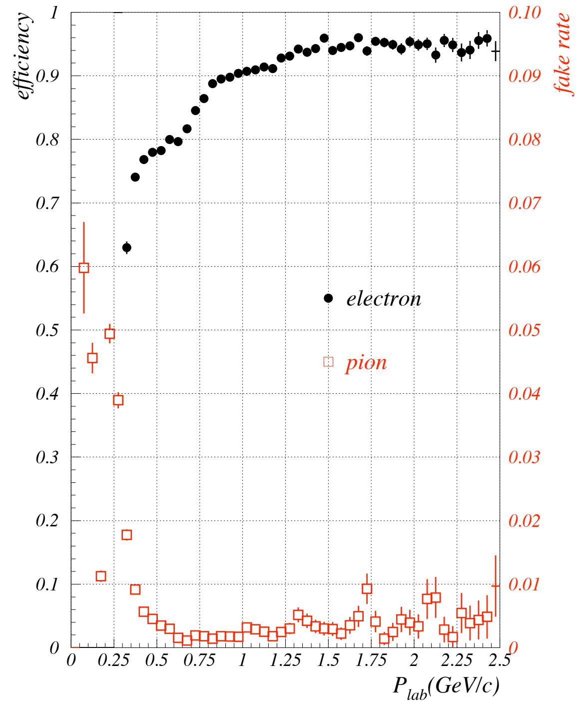

Figure 3.24: *Electron identification efficiency (circles) and fake rate for charged pions (squares). Note the different scales for the efficiency and fake rate.*

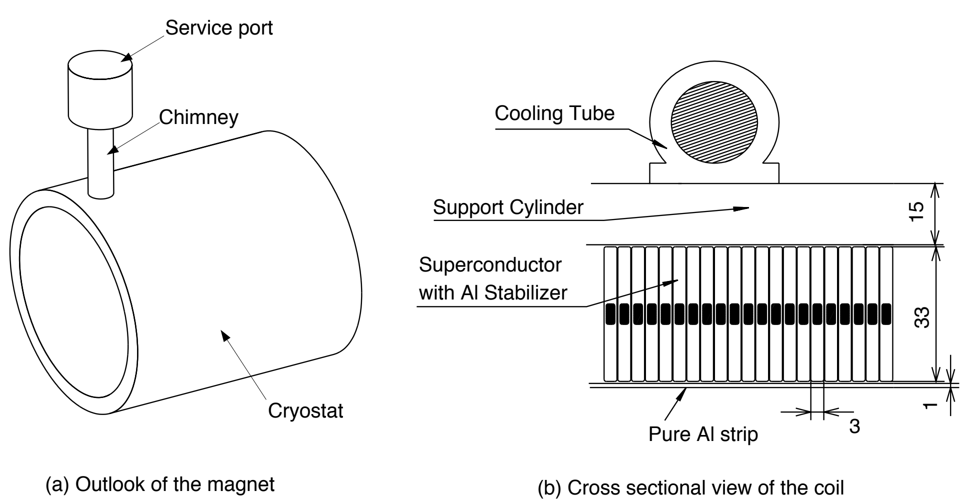

Figure 3.25: *An outlook of the solenoid and the cross-sectional view of the coil. The unit is mm.*

endcaps. The iron layers also serve as a return yoke of the magnetic flux provided by the super-conducting solenoid. Figure 3.26 shows the barrel part of the iron yoke. A cross section of a RPC superlayers is shown in Figure 3.27. Each RPC superlayer consists of two RPC modules and provides θ-ϕ two dimensional information. A charged particle traversing the gas gap ionizes the gas and initiates a streamer in the gas. The streamer results in a local discharge of the glass plates. This discharge is limited by the high resistivity of the plates and induces a signal on external pickup strips. The iron plates provide a total of 3.9 hadronic interaction lengths for a particle traveling normal to the detector planes. K_L interacting with the iron produces a shower of ionizing particles and is detected by RPC layers.

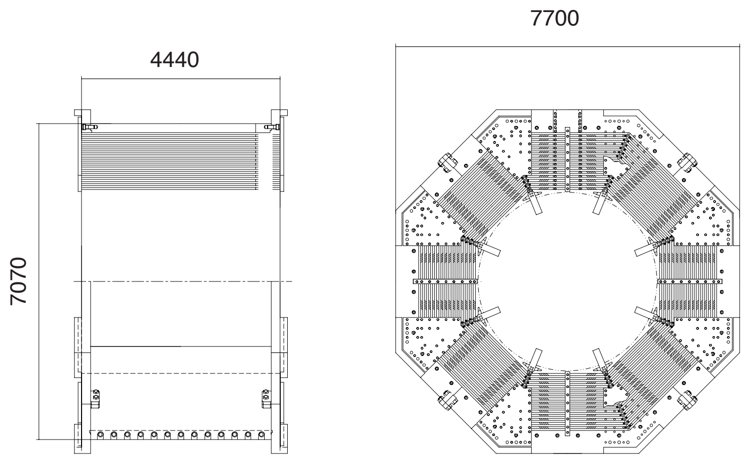

Figure 3.26: *Barrel part of the iron yoke. The unit is mm.*

KLM provides muon identification for charged particles with momenta greater than 0.6 GeV/c. Charged particles with momenta less than 0.6 GeV/c cannot reach KLM. The muon identification is performed based on the range and the transverse scattering in KLM. Muons pass through KLM with small deflections, while hadrons, which are dominated by pions, are deflected by the strong interaction with iron and then stop within less iron layers than muons. These information is parametrized by the number of penetrated iron plates and the reduced χ^2 calculated with the extrapolated charged track and the position of KLM hits. A likelihood ratio of the muon hypothesis and the pion hypothesis is made combining these two information and is used to separate muons from hadrons. Figure 3.28 shows the muon identification efficiency measured with cosmic muons as a function of momentum and the fake rate for $\pi^{\pm}$ measured with $K_S \to \pi^+\pi^-$ decays. Typical efficiency for momentum grater than 1 GeV/c is better than 90%, while fake rate for $\pi^{\pm}$

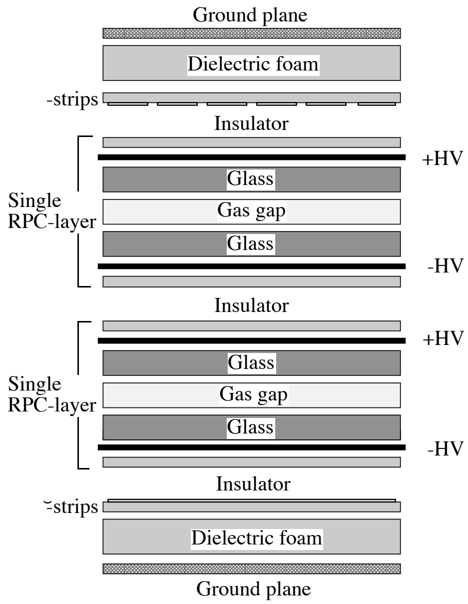

Figure 3.27: *Cross section of a KLM super-layer.*

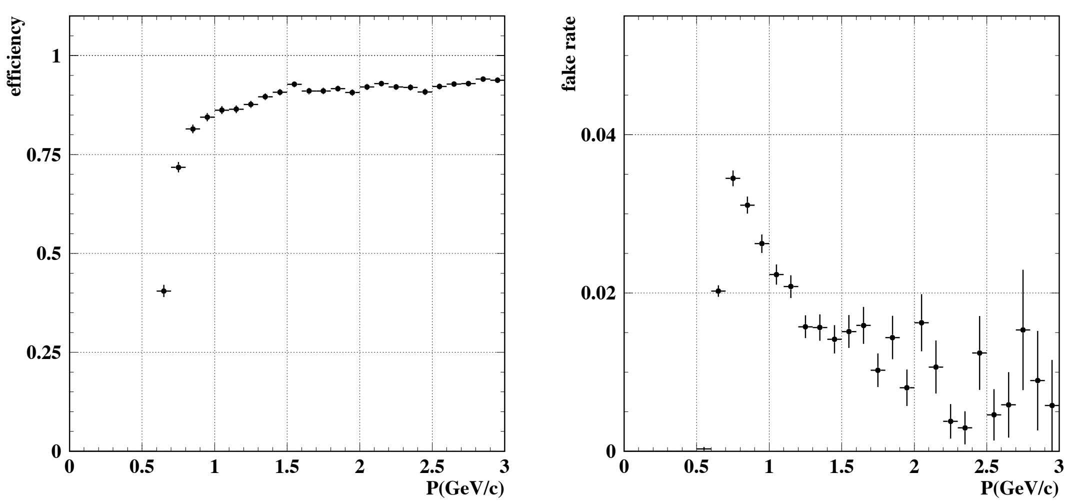

Figure 3.28: *Muon identification efficiency versus momentum in KLM (left). Fake rate for charged pions versus momentum in KLM (right).*

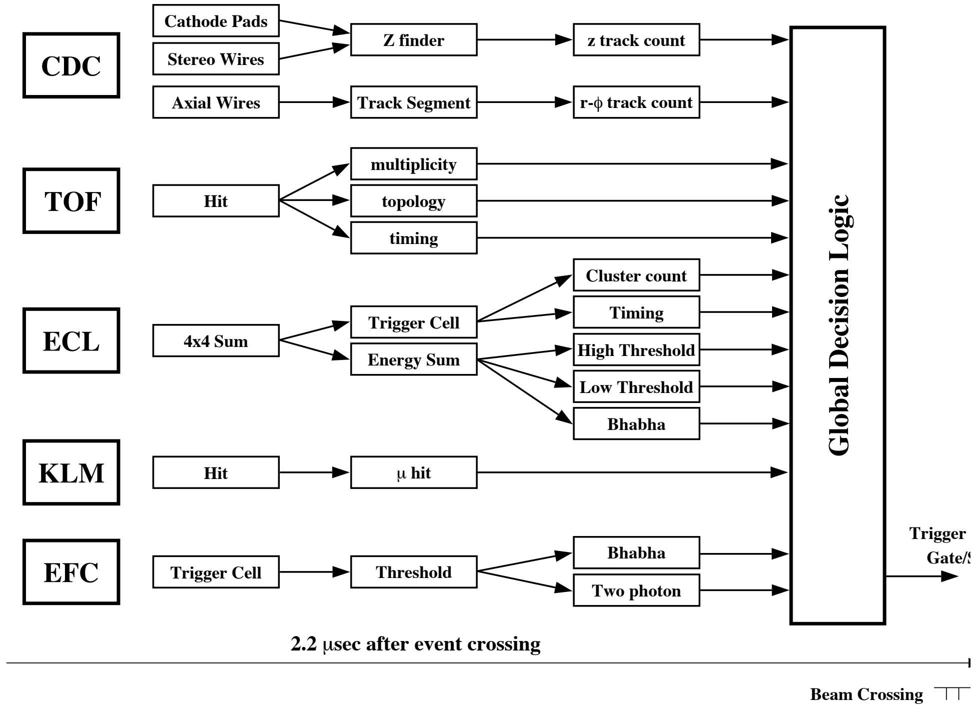

Figure 3.29: *The Level-1 trigger system for the Belle detector.*

is smaller than 2 %. The details of muon identification are given in [54].

3.2.10 Trigger and Data acquisition

The trigger system is required to catch $B\overline{B}$ event by ~ 100 % efficiency, while it is needed to suppress the trigger rate for uninteresting events. Because of the high beam current of KEKB, the trigger suffers from severe beam background. Since the beam background rates are very sensitive to actual accelerator conditions, it is difficult to make a reliable estimate. Therefore, the trigger system is required to be flexible so that background rates are kept within the tolerance of the data acquisition system and is also needed to have redundant triggers to keep the high trigger efficiency for physics events of interest.

Figure 3.29 shows a schematic view of the Belle Level 1 trigger system. It consists of the sub-detector trigger systems and the central trigger system called the global decision logic (GDL). The GDL combines the sub-detector trigger signals and make a final decision to initiate a Belle wide data acquisition within 2.2 μs from beam crossing. There are two major types of triggers prepared for the hadronic events. One is based on the charged track information from CDC. The other is provided by the energy information from ECL. These two redundant triggers provide more than 99.5 % trigger efficiency for $B\overline{B}$ events. The typical trigger rate is 200-250 Hz.

A schematic view of the Belle data acquisition system is shown in Figure 3.30. In order to keep DAQ dead time fraction less than 10 % up to a maximum trigger rate of 500Hz, the entire system is segmented into 7 subsystems running in parallel. The signals

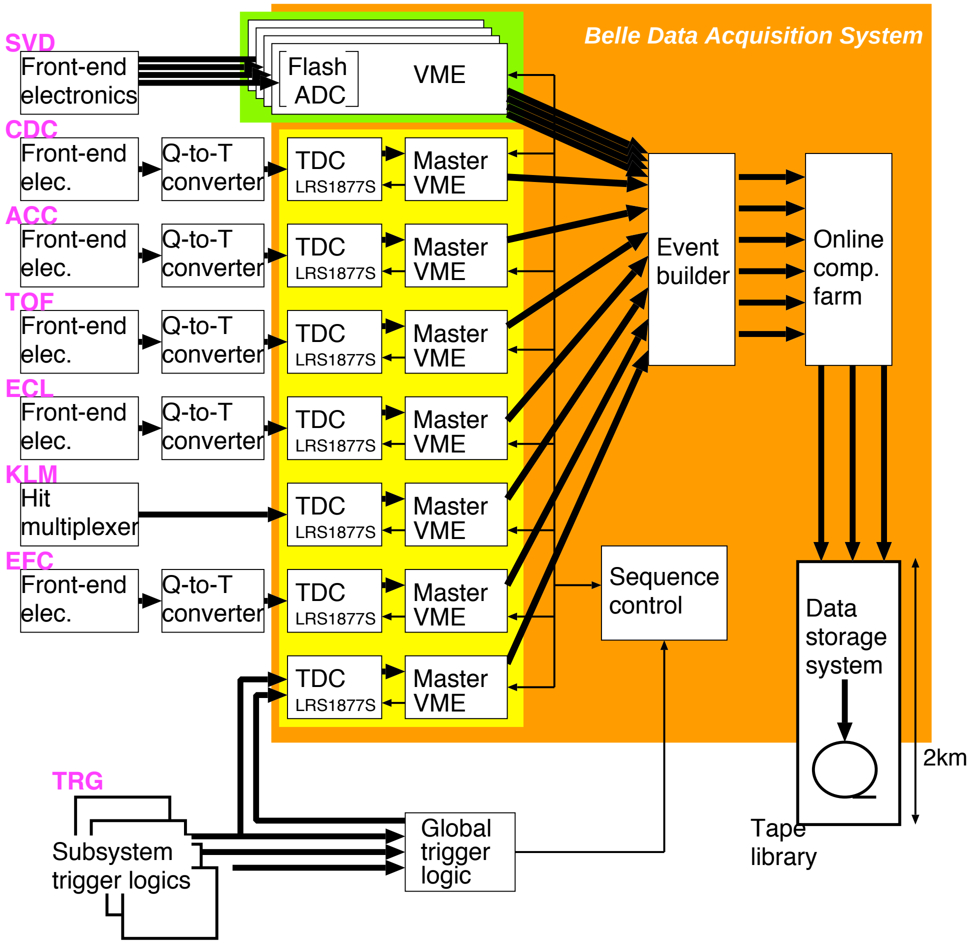

Figure 3.30: *Belle DAQ system overview.*

from sub-detectors are converted to timing signals by the Q-to-T converters except for KLM and SVD and are sent to the event builder. The event builder converts "detector-by-detector" parallel data streams to an "event-by-event" data river and sent the data to an online computer farm. The online computer formats an event data into an offline event format and performs a background reduction (the Level 3 trigger) after a fast event reconstruction. The data are then sent to a mass storage system located at the computer center 2 km away via optical fibers. A typical event data size is about 30 kB, which corresponds to the maximum data rate of 15 MB/s.

3.2.11 Offline Software and Computing

Collected data by the Belle detector are analyzed at the offline computer farm. To cope with large data which accumulate at a rate of 400 GB a day, the parallel processing scheme by multi-CPU-servers is developed. Belle has a pc farm equivalent to 650 GHz Pentium III for data analysis. The pc farm is capable of processing ~ 2 fb^{-1} data a day.

All software for the data acquisition and the data analysis except for a few HEP specific and non HEP specific free software packages has been developed by the members of the Belle collaboration. In particular, the mechanisms to process events in parallel on large SMP (Symmetric Multiple Processor) computer servers have been developed locally using C and C++ programming languages. The users' reconstruction and analysis codes run on the event processing framework, called BASF (Belle analysis framework), as modules and are linked dynamically at the run time. The BASF takes care of input/output of event data, parallel processing and HBOOK [55] output.

The Monte Carlo simulation (MC) generation is also an important task of the computing. Using the MC sample, we study the detector response to the physics events and determine the analysis procedure. The physical process of production and decay is simulated by event generator softwares. We use two event generator softwares: QQ [56] and EvtGen [57, 58]. QQ event generator was originally developed by CLEO and modified for the use of the Belle analysis [59]. We use QQ to generate large number of $\Upsilon(4S)$ decays to study background for $B^0 \to \eta' K_S$ decays. EvtGen is developed by CLEO and BaBar. It is designed so that the extension of the generator can be done easily by adding a new decay as a module. The B decay sample generated by EvtGen is used to study signal event selection criteria and the flavor tagging algorithm. The detector response is simulated with the Belle full detector simulator called GSIM based on GEANT [60]. GEANT is a library developed at CERN to simulate reactions between particles and matters. The simulator takes the data from the event generator and traces the behavior of each particle in the detector, generating detector response which simulates the real detector output.

Chapter 4

Event Selection

In this chapter, we describe the reconstruction of B^0 decays into $\eta' K_S$.

4.1 Data Sample

We use data taken between January 2000 and July 2002. The total integrated luminosity of 78.2 fb^{-1} has been accumulated on the $\Upsilon(4S)$ resonance in this period. It corresponds to 85×10^6 $B\overline{B}$ pairs.

4.2 Hadronic Event Selection

The collected data include hadronic events ($B\overline{B}$ pairs or continuum events) and other processes with cross sections that are comparable to or larger than those for hadronic events. The cross sections are shown in Table 4.1. To select hadronic events, we require the following criteria [61]:

- At least three "good" charged tracks must exist, where a "good" track is defined by (i) $|r| < 2.0$ cm and $|z| < 4.0$ cm at the closest approach to the beam axis, (ii) transverse momentum greater than 0.1 GeV/c.

- More than one "good" cluster must be observed in the barrel region of the calorimeter, where a "good" cluster is defined in such a way that it is detected in the polar angle range of $-0.7 < \cos\theta < 0.9$ with an energy deposit greater than 0.1 GeV and no track is associated with the cluster.

- The absolute value of the momentum balance in the z-component calculated in the rest frame of the $\Upsilon(4S)$ resonance should be less than 50% of the energy in the center of mass system (cms).

- The event vertex, which is reconstructed from the "good" tracks defined above, must be within 1.5 cm and 3.5 cm from the nominal interaction point (IP) in r and z, respectively.

Process	cross section (nb)
$B\overline{B}$	1.1
$q\overline{q}(q = u, d, s, c)$	3.3
$\tau^+\tau^-$	0.93
$QED(25.551^\circ < \theta < 159.94^\circ)$	37.8
$\gamma\gamma \to q\overline{q}(W_{\gamma\gamma} > 500\text{MeV})$	1.1

Table 4.1: *Cross sections for various processes in e^+e^- collisions at $\sqrt{s} = 10.58$ GeV. QED refers to Bhabha and radiative Bhabha processes. The $W_{\gamma\gamma}$ is the two-photon invariant mass.*

- The total visible energy, which is computed as a sum of the energy of "good" tracks assuming the pion mass and that of the "good" clusters, in the rest frame of $\Upsilon(4S)$ should exceed 18% of the center of mass energy.
- A sum of all cluster energies, after boosted back into the rest frame of the $\Upsilon(4S)$ resonance, should be between 10% and 80% of the cms energy.
- The invariant mass of particles found in hemispheres perpendicular to the event thrust axis is required to be greater than 1.8 GeV/c^2.

These selection criteria retain more than 99% of $B\overline{B}$ events, while keeping the contamination of non-hadronic processes smaller than 5%.

4.3 $B^0 \to \eta' K_S$ Reconstruction

4.3.1 Reconstruction of η'

We reconstruct η' candidates using decays into $\rho^0\gamma$ or $\eta\pi^+\pi^-$, where ρ^0 and η candidates are reconstructed using decays into $\pi^+\pi^-$ and two γ, respectively.

Charged Pion Selection

For pions, we use charged tracks that are not identified as kaons by combined information of ACC, TOF and dE/dx in CDC. In order to remove poorly-reconstructed tracks, we require charged tracks to be within 0.1 cm from the IP in the r-ϕ plane.

Photon Selection

Photon candidates are selected from ECL clusters that do not have associated charged tracks. We use photon candidates with energy greater than 50 MeV for the $\eta\pi^+\pi^-$ mode and 100 MeV for the $\rho^0\gamma$ mode. Since the $\rho^0\gamma$ mode has a larger background than the $\eta\pi^+\pi^-$ mode due to the wide ρ^0 width, we apply more stringent requirements on the $\rho^0\gamma$ mode.

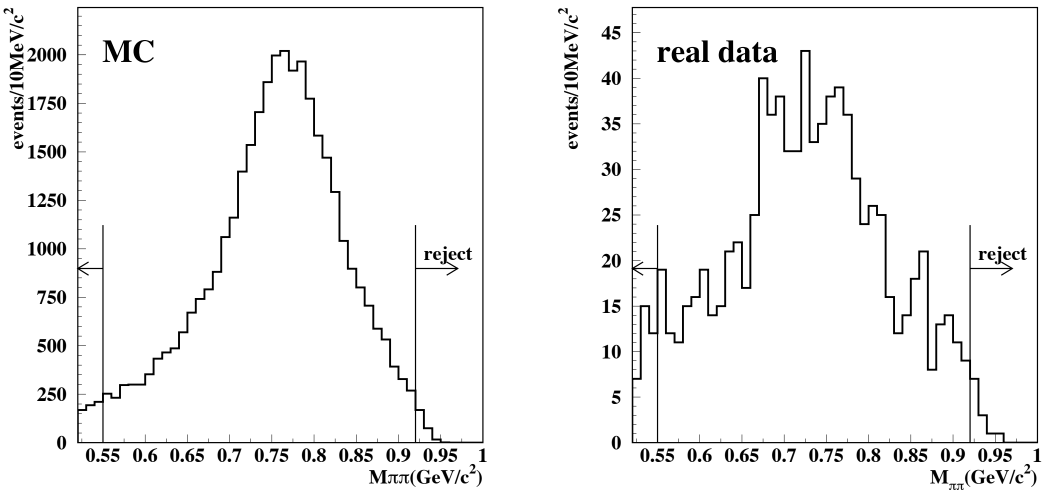

Figure 4.1: *The ρ^0 invariant mass distribution. The left figure is the signal MC and the right figure is the reconstructed $B^0 \to \eta' K_S$ decay candidates in the real data. For the data, selection criteria other than ρ^0 mass are applied.*

Reconstruction of ρ^0

Candidate ρ^0 mesons are selected from pairs of two oppositely-charged pions. We calculate an invariant mass of each pion pair $M_{\pi^+\pi^-}$, using the reconstructed pion momenta $\vec{P}_{\pi^+}$ and $\vec{P}_{\pi^-}$ and the nominal pion mass $M_\pi = 139.57$ MeV/c^2 as

$$M^2_{\pi^+\pi^-} = \left(\sqrt{M^2_\pi + |\vec{P}_{\pi^+}|^2} + \sqrt{M^2_\pi + |\vec{P}_{\pi^-}|^2}\right)^2 - |\vec{P}_{\pi^+} + \vec{P}_{\pi^-}|^2. \quad (4.1)$$

We select pion pairs that satisfy $0.55 < M_{\pi^+\pi^-} < 0.92$GeV/$c^2$ as ρ^0 candidates, which retains 93% of the signal events. Figure 4.1 shows the invariant mass distribution of ρ^0 candidates in the signal MC and the real data with selection criteria other than ρ^0 mass applied.

Reconstruction of η

Candidate η mesons are selected from pairs of two photons. We calculate invariant mass of each two photon pair assuming that they come from the nominal IP.

$$M^2_{\gamma\gamma} = |\sum_{i=1}^{2} E_{\gamma_i}|^2 - |\sum_{i=1}^{2} \vec{P}_{\gamma_i}|^2, \quad (4.2)$$

where E_{γ_i} and $\vec{P}_{\gamma_i}$ are the energy and momentum of the i-th photon, respectively. Figure 4.2 shows the two photon invariant mass distribution of η candidates in the signal MC and the real data with selection criteria other than η mass are applied. Due to the shower

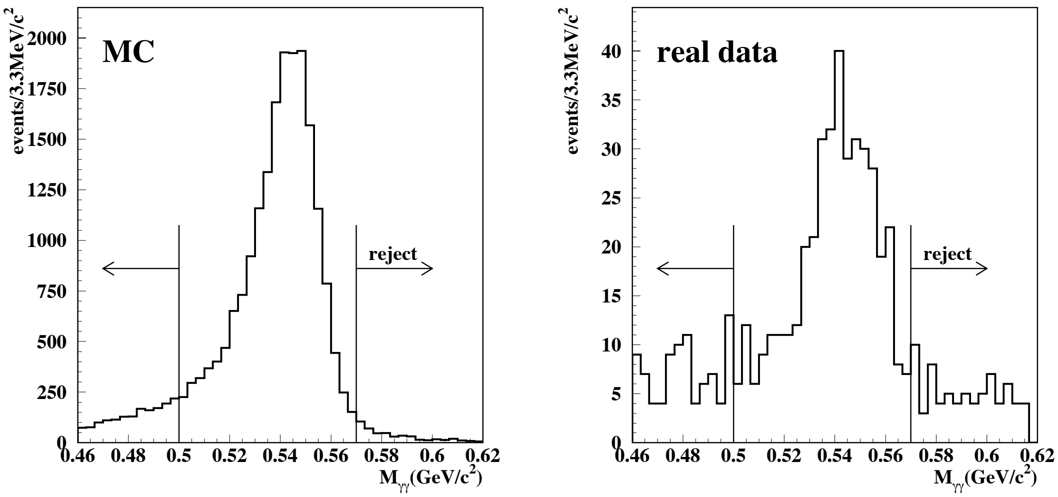

Figure 4.2: *The η invariant mass distribution. The left figure is the signal MC and the right figure is the reconstructed $B^0 \to \eta' K_S$ decay candidates in the real data. For the data, selection criteria other than η mass are applied.*

leakage of photons in the ECL, the invariant mass distribution has a longer tail in the lower side. We select η candidates that satisfy $0.50 < M_{\gamma\gamma} < 0.57\mathrm{GeV}/c^2$. About 87% of the signal falls in this signal range. To improve the resolution of the η candidates, a kinematic fit with a mass constraint is performed.

Reconstruction of η'

To form an η' candidate, ρ^0 and η candidates are combined with a photon and two oppositely-charged pions, respectively. The invariant masses are calculated as:

$$\begin{aligned} M_{\rho\gamma}^2 &= (E_\rho + E_\gamma)^2 - |\vec{P}_\rho + \vec{P}_\gamma|^2, \\ M_{\eta\pi\pi}^2 &= \left(E_\eta + \sqrt{M_\pi^2 + |\vec{P}_{\pi^+}|^2} + \sqrt{M_\pi^2 + |\vec{P}_{\pi^-}|^2}\right)^2 - |\vec{P}_\eta + \vec{P}_{\pi^+} + \vec{P}_{\pi^-}|^2, \end{aligned} \tag{4.3}$$

where $E_{\rho(\gamma)}$ and $\vec{P}_{\rho(\gamma)}$ are the energy and momentum of the ρ^0 (photon) candidate, respectively, and E_η and $\vec{P}_\eta$ are the energy and momentum of the η candidate after the mass-constrained fit. Figure 4.3 shows the invariant mass distribution of reconstructed η' candidates. The invariant mass of the η' candidate is required to be in the range of $0.935 < M_{\rho\gamma} < 0.975\mathrm{GeV}/c^2$ or $0.94 < M_{\eta\pi^+\pi^-} < 0.97\mathrm{GeV}/c^2$. Due to the shower leakage of photons in the ECL, the mass distribution has a longer tail in the lower side. The mass range retains 86% of the $\eta' \to \rho^0\gamma$ signal and 96% of the $\eta' \to \eta\pi^+\pi^-$ signal. A kinematical fit with a mass constraint is performed for selected η' candidates at the decay vertex. The method of the decay vertex reconstruction is explained in Section 4.4. The χ^2 of the mass-constrained fit is required to be less than 40.

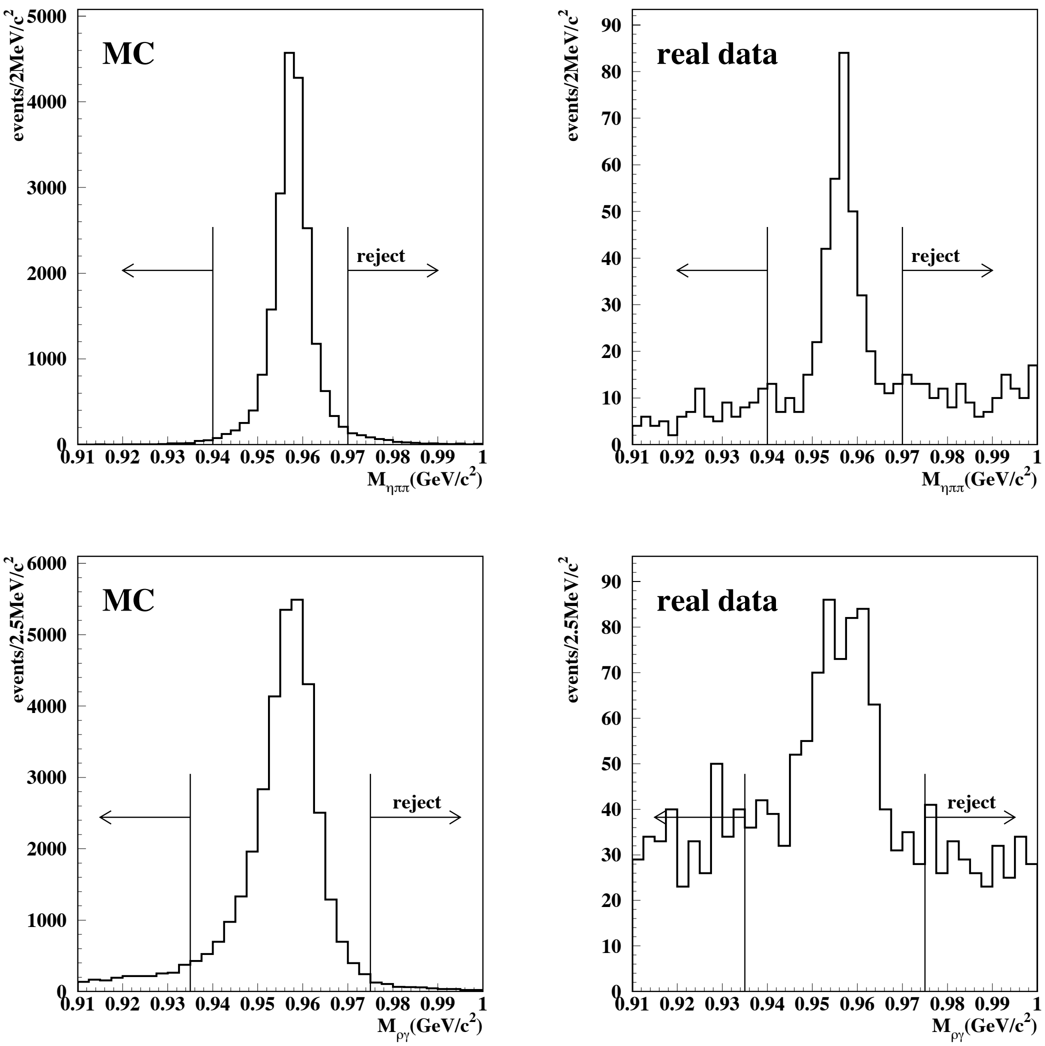

Figure 4.3: *The η' invariant mass distributions. The upper figures are for the $\eta' \rightarrow \eta\pi^+\pi^-$ decays and the lower figures are for the $\eta' \rightarrow \rho^0\gamma$ decays. The left figures are the signal MC and the right figures are the reconstructed $B^0 \rightarrow \eta' K_S$ decay candidates in the real data. For the data, selection criteria other than η' mass are applied.*

4.3.2 Reconstruction of K_S

K_S candidates are reconstructed using decays into $\pi^+\pi^-$. Since a K_S meson travels several cm on average before it decays ($c\tau \simeq 2.7$ cm), we can obtain a clean signal by rejecting candidates that have short decay lengths.

We first reconstruct a K_S vertex with oppositely charged track pairs. The vertex is reconstructed by the following procedure:

1. We define a temporary decay vertex of K_S as the crossing point of two tracks. The z position of the temporary decay vertex is defined as the middle point of two helices at the cross point in the r-ϕ plane.

2. Two tracks are interpolated to the temporary decay point by taking into account the multiple scattering and energy loss.

3. The vertex is then re-fitted with the recalculated track momenta. If the fitting succeeds, the temporary decay vertex is replaced by the fitted one.

We then require following conditions depending on the number of tracks having associated SVD hits:

1. If none of the two pions has associated SVD hits, which indicates that the K_S decays outside of SVD, we require the direction of the K_S momentum point to the nominal IP: the ϕ coordinate of the $\pi^+\pi^-$ vertex point and the ϕ direction of the $\pi^+\pi^-$ candidate's three momentum vector should agree within 0.1 radian.

2. If one of the two pions has associated SVD hits, the closest distances of both pion tracks to the IP in the r-ϕ plane are required to be larger than 250 μm to suppress tracks from the IP.

3. In case both pions have associated SVD hits, we require the distance of the two tracks in z to be smaller than 1 cm rather than the flight length, because those tracks have much better resolution in z direction than other cases.

Finally, the invariant mass is calculated for K_S candidates which pass above criteria as

$$M^2_{K_S\to\pi\pi} = \left(\sqrt{M_\pi^2 + |\vec{P}_{\pi^+}|^2} + \sqrt{M_\pi^2 + |\vec{P}_{\pi^-}|^2}\right)^2 - |\vec{P}_{\pi^+} + \vec{P}_{\pi^-}|^2. \qquad (4.4)$$

We require the invariant mass to be within 482 and 514 MeV/c^2, which corresponds to three standard deviations from the nominal K_S mass. The invariant mass distribution of the K_S candidates is shown in Figure 4.4.

4.3.3 Reconstruction of B^0

B^0 candidates are reconstructed by combining reconstructed η' and K_S candidates. We use two variables to select signal candidate: the energy difference (ΔE) and the beam

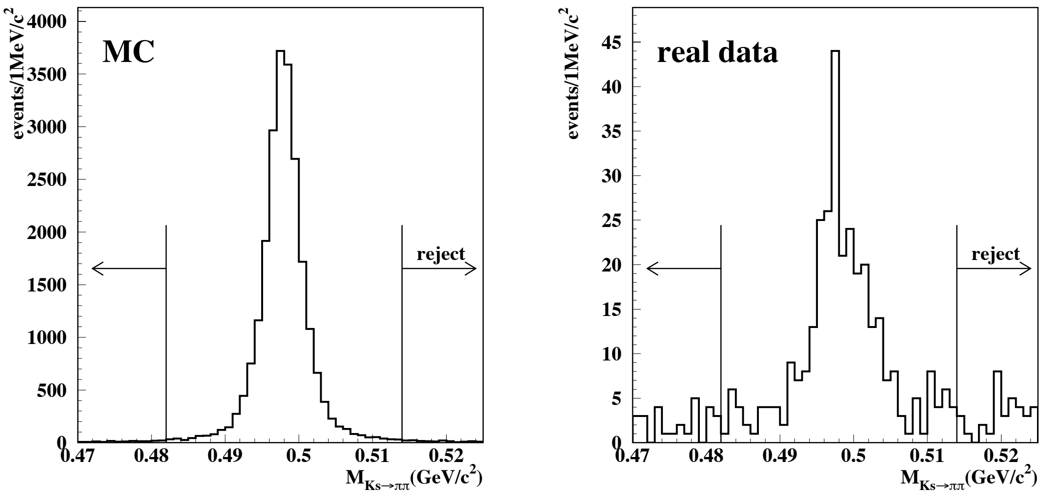

Figure 4.4: *The K_S invariant mass distribution. The left figure is the signal MC and the right figure is the reconstructed $B^0 \to \eta' K_S$ decay candidates in the real data. For the data, selection criteria other than K_S mass are applied.*

constraint mass ($M_{\rm bc}$) defined as;

$$\begin{aligned} \Delta E &\equiv E_B - E_{beam}, \\ M_{\rm bc} &\equiv \sqrt{E_{beam}^2 - p_B^2}, \end{aligned} \tag{4.5}$$

where E_B and p_B are energy and momentum of the B^0 candidate in the center of mass system, respectively, and E_{beam} is the beam energy in the center of mass system. Since only a B meson pair is created by the beam collision, the ΔE equals 0 for the signal. We use E_{beam} instead of E_B for the mass calculation because the resolution of E_{beam} ($\sim$ 3MeV) is much better than the resolution of E_B (20 $\sim$ 30MeV) and the mass resolution is dominated by the energy resolution due to the small p_B value (~ 0.3GeV/c). Figure 4.5 shows the $M_{\rm bc}$ and ΔE distribution of the signal MC sample. We define signal regions to be $5.27 < M_{\rm bc}$ and $|\Delta E| < 0.06$ for $\eta' \to \rho^0\gamma$ mode, and $5.27 < M_{\rm bc}$ and $-0.1 < \Delta E < 0.08$ for the $\eta' \to \eta\pi^+\pi^-$ mode. They correspond to three standard deviations.

4.3.4 Continuum Background Suppression

As explained in Section 2.2, the dominant background comes from the continuum $e^+e^- \to q\bar{q}$ events. MC studies shows that the ratio of the signal to the background is about 1/10 for the $\eta' \to \rho^0\gamma$ mode and 1/2 for the $\eta' \to \eta\pi^+\pi^-$ mode, if we select signal candidates only with the selection criteria described above. We suppress the continuum background with the criteria [45] that utilize the event shape difference between the signal and the continuum background. In the following, all values are calculated in the $\Upsilon(4S)$ center of mass system unless explicitly stated otherwise.

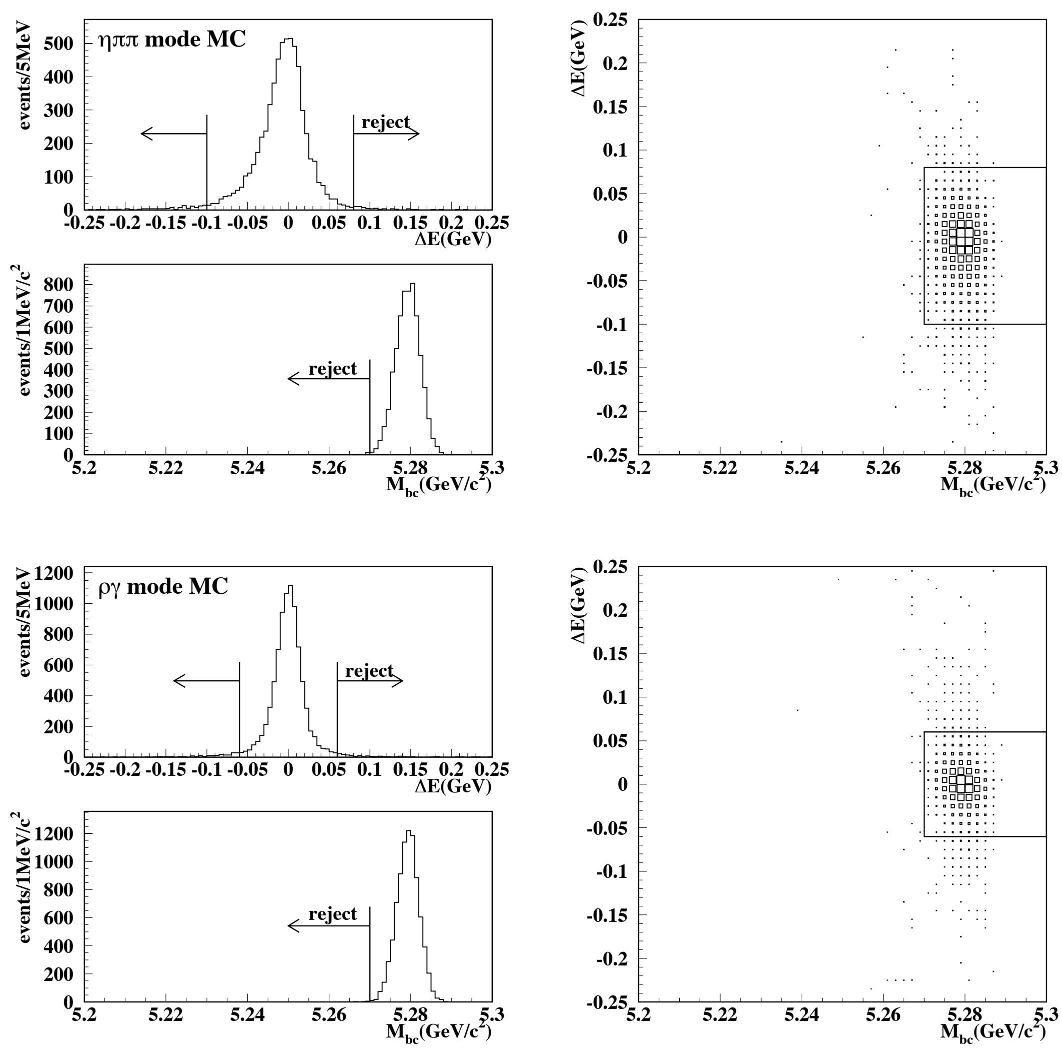

Figure 4.5: *ΔE and M_{bc} distributions of the signal MC sample. The upper figures are $\eta' \to \eta\pi^+\pi^-$ mode and the lower figures are $\eta' \to \rho^0\gamma$ mode. The box in the ΔE-M_{bc} two dimensional plot shows the signal region.*

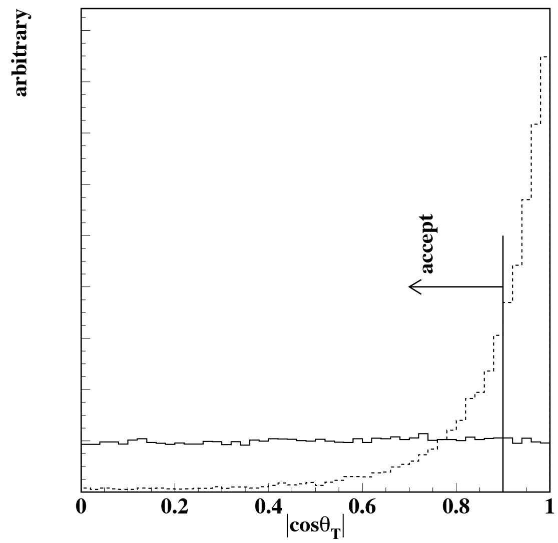

Figure 4.6: *The $|\cos\theta_T|$ distribution of the signal MC (solid line) and the ΔE-M_{bc} sideband data (dashed line).*

First, we calculate the thrust angle θ_T that is defined as an angle between the candidate η' direction and the thrust axis calculated from the momenta of all other particles than those belonging to the $B^0 \to \eta' K_S$ decay candidate. Figure 4.6 shows $|\cos\theta_T|$ distribution of the signal MC and the ΔE-$M_{\rm bc}$ sideband data defined as $5.2 < M_{bc} < 5.26$ and $0.15 < \Delta E < 0.25$ for the $\eta' \to \rho^0\gamma$ mode, and $5.2 < M_{bc} < 5.26$ and $-0.25 < \Delta E < -0.15$ or $0.15 < \Delta E < 0.25$ for the $\eta' \to \eta\pi^+\pi^-$ mode. The continuum background accumulates near $|\cos\theta_T| = 1$, while signal events distribute uniformly. We reject events with $|\cos\theta_T| > 0.9$. This reduces the continuum background by 60% but keeps 90% of the signal.

We then introduce the Fisher discriminant [62] F that is made of the following seven variables:

- $\cos\theta_T$,
- $S_\perp$, which is the scalar sum of the transverse momenta of all particles outside a 45° cone around the η' direction divided by the scalar sum of their momenta,
- five variables R_2^{SO}, R_4^{SO}, R_2^{OO}, R_3^{OO} and R_4^{OO}, which are modified Fox-Wolfram moments [63].

The Fisher discriminant F is defined as

$$F \equiv \sum_{n=2,4} \alpha_n R_n^{SO} + \sum_{n=2,3,4} \beta_n R_n^{OO} + c_1|cos\theta_T| + c_2 S_\perp, \tag{4.6}$$

where coefficients α_n, β_n, c_1 and c_2 are determined by optimizing the separation between the signal and the continuum background. The modified Fox-Wolfram moments are made by dividing the normal Fox-Wolfram moments into three components: a component including only particles belonging to the the signal candidate, a component including other particles than the signal candidate, and a component including both the signal candidate and the other particles. They are defined as

$$\begin{aligned}
R_n^{SS} &\equiv \frac{\sum_{k,l} |\vec{p}_k||\vec{p}_l| P_n(\cos\theta_{kl})}{\sum_{k,l} |\vec{p}_k||\vec{p}_l|}, \\
R_n^{SO} &\equiv \frac{\sum_{i,k} |\vec{p}_i||\vec{p}_k| P_n(\cos\theta_{ik})}{\sum_{i,k} |\vec{p}_i||\vec{p}_k|}, \\
R_n^{OO} &\equiv \frac{\sum_{i,j} |\vec{p}_i||\vec{p}_j| P_n(\cos\theta_{ij})}{\sum_{i,j} |\vec{p}_i||\vec{p}_j|},
\end{aligned} \tag{4.7}$$

where $|\vec{p}|$ indicates particle momentum, P_n is the Legendre polynomial of nth order, k, l are either η' or K_S from the B candidates, and i,j enumerate all remaining photons and charged particles in the event, and $\theta_{ij(ik,kl)}$ is the angle between the momentum vectors of the particles. We do not use R_n^{SS} because they are strongly correlated with M_{bc} and ΔE. The R_1^{SO}, R_3^{SO} and R_1^{OO} are also not used because they are correlated with M_{bc} [64]. Figure 4.7 shows these event shape variables and the Fisher discriminant F. In addition, we utilize characteristic angular distribution of the decay of a vector meson into a pair of pseudoscalar mesons. We use the cosine of the polar angle of the B candidate ($\cos\theta_B$) and the cosine of the angle between the ρ^0 direction in the η' rest frame and the daughter π^+ direction in the ρ^0 rest frame ($\cos\theta_\pi$) for the $\eta' \to \rho^0\gamma$ mode. Figure 4.8 shows the distribution of $\cos\theta_B$ and $\cos\theta_\pi$. The signal follows $(1 - \cos^2\theta)$, while the background distribute uniformly. These three variables: F, $\cos\theta_B$ and $\cos\theta_\pi$ are combined to a likelihood ratio LR defined as

$$\begin{aligned}
LR &\equiv \frac{L_{sig}}{L_{sig} + L_{bg}}, \\
L_{sig} &\equiv P_{sig}^{F} \times P_{sig}^{\cos\theta_B} \times P_{sig}^{\cos\theta_\pi}, \\
L_{bg} &\equiv P_{bg}^{F} \times P_{bg}^{\cos\theta_B} \times P_{bg}^{\cos\theta_\pi},
\end{aligned} \tag{4.8}$$

where $P_{sig(bg)}$ is a probability density function of the signal (background) for F, $\cos\theta_B$ and $\cos\theta_\pi$ obtained from their distributions in Figure 4.7 and 4.8. The LR distributions are shown in Figure 4.9. We use the LR to classify events into subsamples. As explained in Section 2.4, the sensitivity to CP asymmetry improves by increasing the figure of merit of signals, and the figure of merit is increased by dividing events into subsamples that have different background levels. We divide events into two LR bins for each η' decay mode: $0 < LR \leq 0.5$ and $0.5 < LR \leq 1.0$ for the $\eta' \to \eta\pi^+\pi^-$ mode, and $0.5 < LR \leq 0.75$ and $0.75 < LR \leq 1.0$ for the $\eta' \to \rho^0\gamma$ mode. Events with $LR < 0.5$ for the $\eta' \to \rho^0\gamma$ mode are discarded because their background levels are high. The improvement of the total figure of merit by dividing into subsamples is estimated to be about 4%.

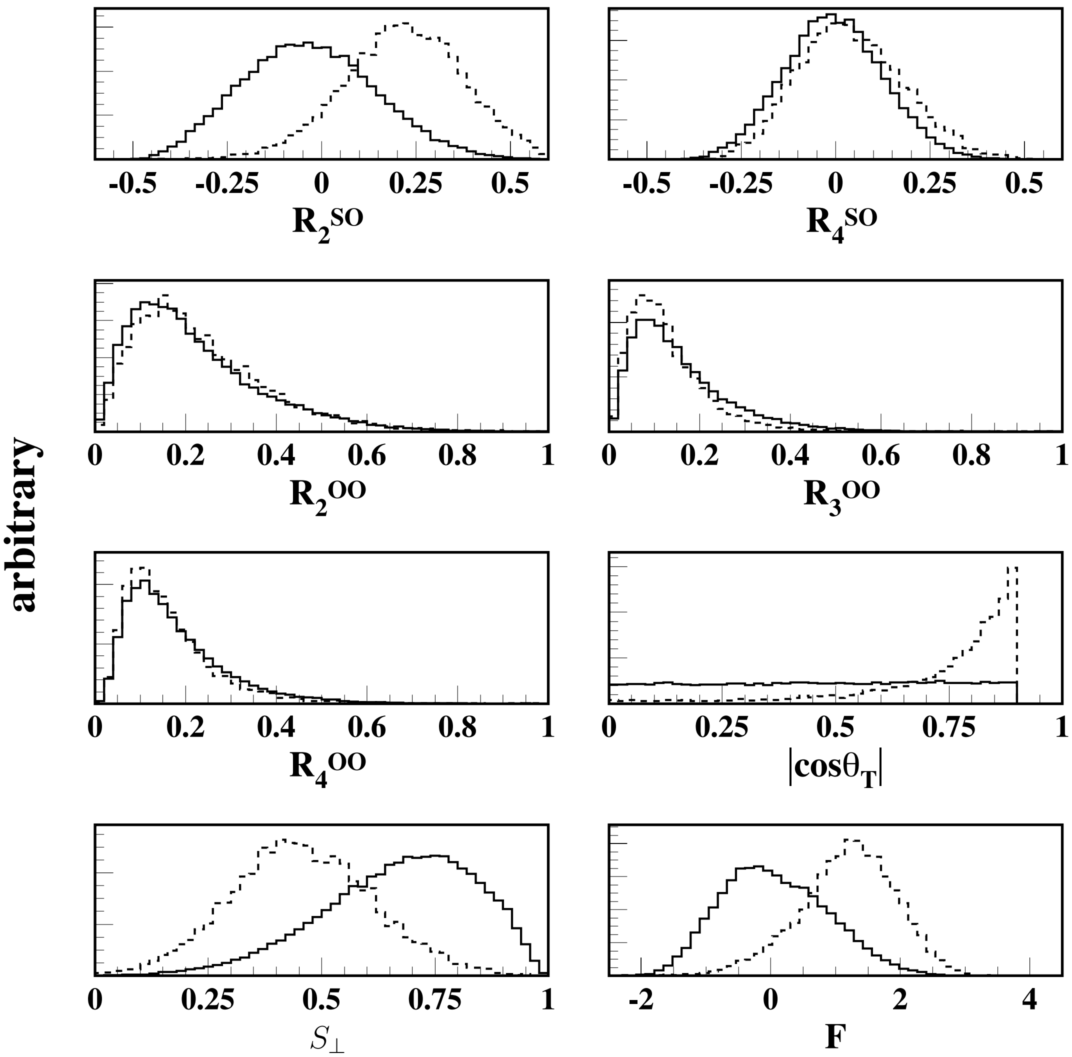

Figure 4.7: *Distributions of event shape variables and the Fisher discriminant F made with them. The solid line shows the distribution of the signal MC and the dotted line shows the ΔE-M_{bc} sideband data.*

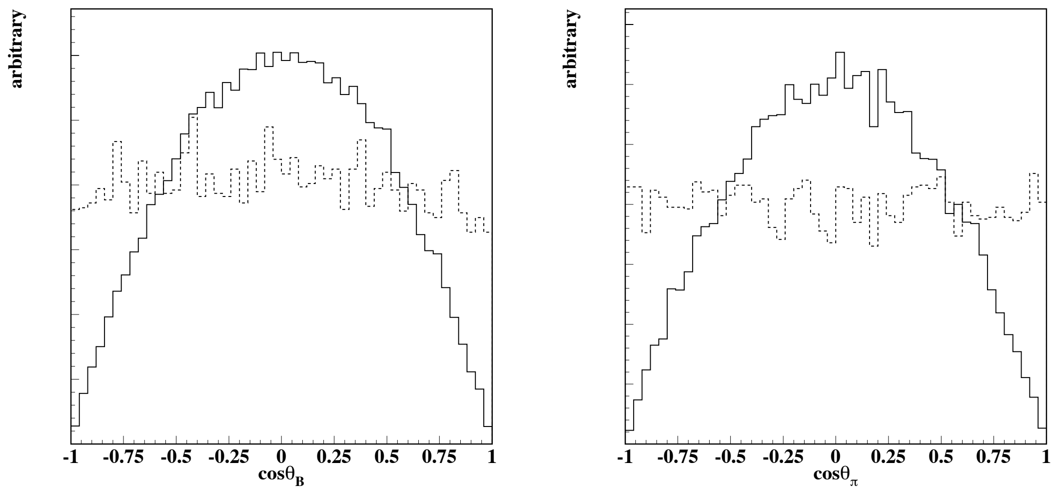

Figure 4.8: *The* $\cos\theta_B$ *distribution (left) and the* $\cos\theta_\pi$ *distribution (right). The solid line is the signal MC and the dashed line is the* ΔE*-*M_{bc} *sideband data.*

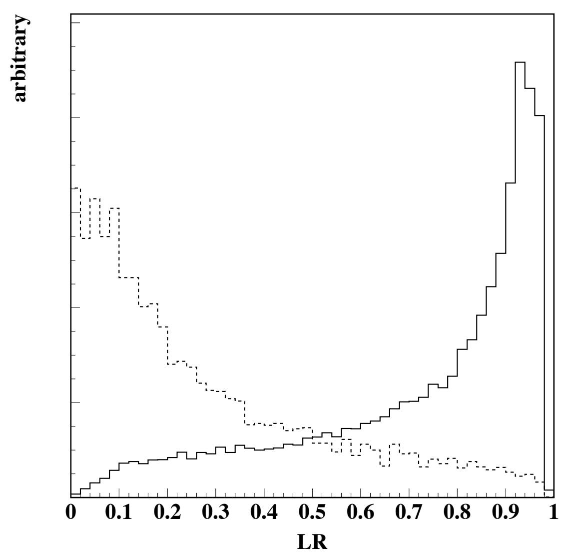

Figure 4.9: *The likelihood ratio made with* F*,* $\cos\theta_B$ *and* $\cos\theta_\pi$*. The solid line is the signal MC and the dashed line is the* ΔE*-*M_{bc} *sideband data.*

4.3.5 Multiple Candidates

The 12% of remaining events have multiple signal candidates due to combinatorial background of η' which mainly originate from photons. We select the best candidate that has the smallest χ^2 in the η' mass-constrained fit.

4.3.6 Summary of $B^0 \to \eta' K_S$ Candidates

The reconstruction efficiency is estimated with the signal MC to be 20% for the $\eta' \to \eta\pi^+\pi^-$ mode and 16% for the $\eta' \to \rho^0\gamma$ mode. Figure 4.10 and 4.11 show the ΔE and M_{bc} distribution of reconstructed candidates for each LR bin and each η' decay mode. We find 213 events for the $\eta' \to \rho^0\gamma$ mode and 99 events for the $\eta' \to \eta\pi^+\pi^-$ mode in the signal boxes.

4.4 Vertex Reconstruction

The decay time difference Δt is calculated from the distance between the B_{CP} and B_{tag} vertices as

$$\Delta t \simeq \frac{z_{CP} - z_{tag}}{\beta\gamma c}, \tag{4.9}$$

where $z_{CP(tag)}$ is the z position of the $B_{CP(tag)}$ decay vertex and $\beta\gamma = 0.425$ is the Lorentz boost factor of the B meson pair.

Figure 4.12 shows the schematic picture of the vertex reconstruction. We reconstruct vertices using primary tracks from the B meson and the constraint to the IP profile. The IP profile is calculated for every 10000 events using hadronic events. The typical size of the IP profile is 100 μm in x, 3-5 μm in y and 3-4 mm in z. To take into account the B^0 flight length in the x-y plane, the IP profile is smeared by a Gaussian function with rms of 21 μm .

4.4.1 Vertex Reconstruction of B_{CP}

Since the decay lengths of η' and ρ^0 mesons are negligible, we can reconstruct the decay vertex using two charged pions from $\eta' \to \eta\pi^+\pi^-$ or $\rho^0 \to \pi^+\pi^-$ for $\eta' \to \rho^0\gamma$ mode.

To reconstruct the vertex, we only use tracks that have sufficient numbers of associated SVD hits, i.e. with both r-ϕ and z hits in at least one layer and with two or more z hits in total. We call such a track "SVD track" hereafter. We use a constraint to the IP profile to improve vertex resolution. The IP constraint also enables us to reconstruct the vertex even when only one SVD track is available. Approximately 11% of events have vertices reconstructed with just one SVD track.

We reject poorly-reconstructed vertices. The vertex quality is represented by a reduced χ^2 projected onto the z axis defined as

$$\xi \equiv \frac{1}{2n} \sum_{i=1}^{n} \left[\frac{z^i_{after} - z^i_{before}}{e^i_{before}} \right], \tag{4.10}$$

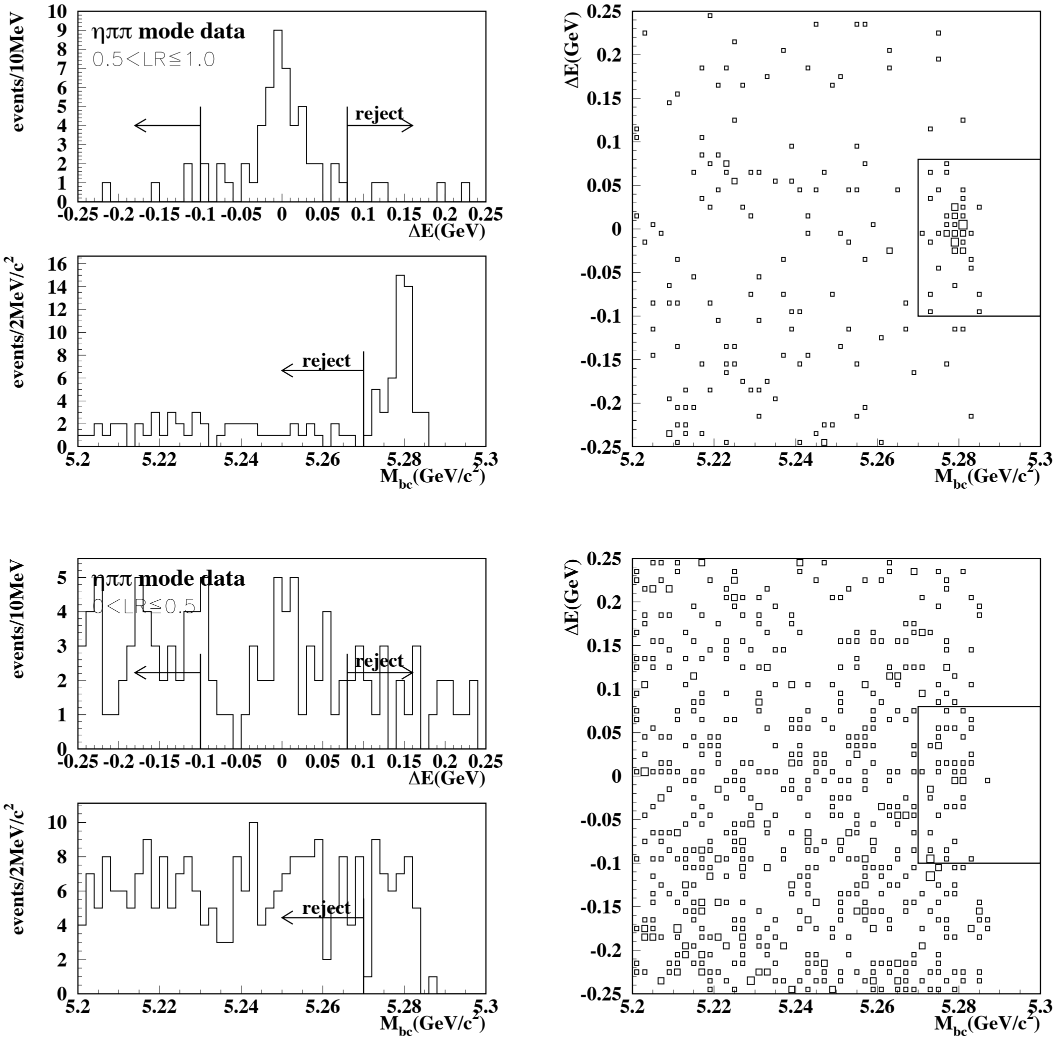

Figure 4.10: ΔE *and* M_{bc} *distributions of the* $B^0 \to \eta' K_S$ *candidates of the* $\eta' \to \eta\pi^+\pi^-$ *mode in the data. The box in the* ΔE-M_{bc} *two dimensional plot shows the signal region. The upper figures are for higher LR candidates* ($0.5 < LR \leq 1.0$) *and the lower figures are for lower LR candidates* ($0.0 < LR \leq 0.5$).

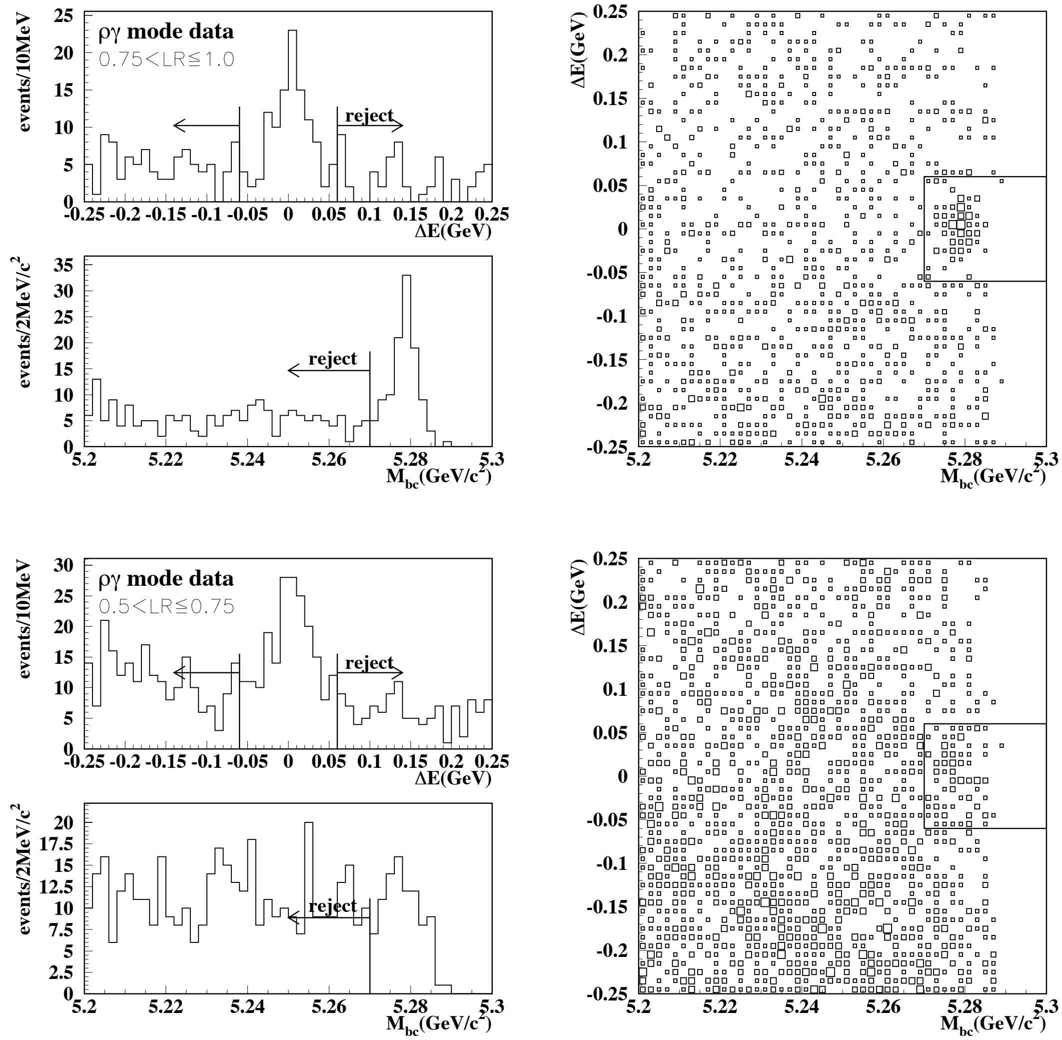

Figure 4.11: ΔE *and* M_{bc} *distributions of* $B^0 \to \eta' K_S$ *candidates of the* $\eta' \to \rho^0\gamma$ *mode in the data. The box in the* ΔE*-*M_{bc} *two dimensional plot shows the signal region. The upper figures are for higher LR candidates* $(0.75 < LR \leq 1.0)$ *and the lower figures are for lower LR candidates* $(0.5 < LR \leq 0.75)$*.*

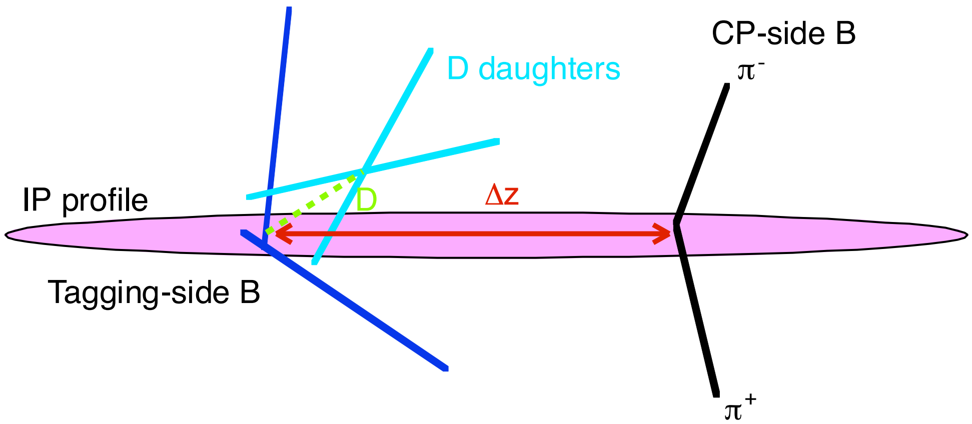

Figure 4.12: *The schematic picture of the vertex reconstruction.*

where z^i_{before} and z^i_{after} are the z positions of each track before and after the vertex fit, respectively, and e^i_{before} is the error of z^i_{before}. We do not use the normal χ^2 because it is correlated with the vertex z position due to the IP constraint in the x-y plane. We require $\xi < 100$.

The typical z resolution estimated by the signal MC is 90 μm (rms) for the $\eta' \to \rho^0\gamma$ mode and 140 μm (rms) for the $\eta' \to \eta\pi^+\pi^-$ mode. Resolution of the $\eta' \to \eta\pi^+\pi^-$ mode is larger than the $\eta' \to \rho^0\gamma$ mode because of the lower pion momenta.

4.4.2 Vertex Reconstruction of B_{tag}

The B_{tag} vertex is reconstructed with remaining charged tracks in an event after removing charged tracks belonging to B_{CP}. We only use well-reconstructed tracks, which are tracks with enough SVD hits in the same way as the B_{CP} vertex reconstruction and with a position error in the z direction less than 0.5 mm. We also require that the impact parameter dr with respect to the B_{CP} vertex be less than 0.5 mm in the r-ϕ plane. We use a constraint to the IP profile to improve vertex resolution.

Charged tracks from secondary particles with a finite lifetime such as D and K_S dilute and bias the reconstructed vertex. The vertex reconstruction algorithm, therefore, must be carefully chosen to minimize the effect of secondary particles. We use the same vertex reconstruction algorithm as that used for the $\sin 2\phi_1$ analysis [10]. At first, we remove tracks that form a K_S candidate which has an invariant mass within 15 MeV from the nominal K_S. The B_{tag} vertex is then reconstructed with remaining tracks and the IP constraint. If the reduced χ^2 of the vertex is less than 20, we accept the vertex. Otherwise we remove the track that gives the largest contribution to the χ^2 and repeat the vertex reconstruction. If the track to be removed is a lepton with $p^* > 1.1$ GeV/c, however, we keep the lepton and remove the track with the second largest χ^2 contribution because high momentum leptons are likely to come from primary semi-leptonic B decays. We repeat this trimming procedure until we obtain a reduced χ^2 less than 20. We accept the vertex if the vertex quality parameter ξ is less than 100. We also apply the selection of $|\Delta t| < 70$ ps to reject badly reconstructed events.

After the reconstruction of vertices, 295 events out of 312 events remain.

4.5 Flavor Tagging

We identify the flavor of B_{tag} with the same method that has been used for the previous $\sin 2\phi_1$ measurement [10]. The details of the method are given in Appendix A. We explain the essence here.

Initially, the b-flavor determination is performed at the track level. Several categories of well measured tracks that have a charge correlated with the b flavor are selected:

- high-momentum leptons from $B^0 \to X\ell^+\nu$,
- kaons from the $\overline{b} \to \overline{c} \to \overline{s}$ cascade decay,
- intermediate momentum leptons coming from $\overline{b} \to \overline{c} \to \overline{s}\ell^-\overline{\nu}$,
- high momentum pions from $B^0 \to D^{(*)}\pi^+X$ decay,
- slow pions from $B^0 \to D^{*-}X, D^{*-} \to \overline{D}^0\pi^-$ decay, and
- Λ baryons from the cascade decay $\overline{b} \to \overline{c} \to \overline{s}$.

The results from the separate track categories are then combined for the final b-flavor determination, taking into account correlations in the case of multiple track-level tags. The flavor tagging result is expressed by a flavor charge q and a tagging quality variable r. The q indicates the determined flavor: $q = +1$ for B^0 and $q = -1$ for $\overline{B}^0$. The r is a MC-determined flavor-tagging dilution factor that ranges from $r = 0$ for no flavor discrimination to $r = 1$ for unambiguous flavor assignment. It is used only to sort data into six intervals of r, according to estimated flavor purity.

The wrong tag probability in each interval, w_l ($l = 1, 6$), is determined from the B^0-$\overline{B}^0$ mixing analysis using self-tagged $B^0 \to D^{*-}\ell^+\nu, D^{(*)-}\pi^+, D^{*-}\rho^+$ and $J/\psi K^{*0}(K^{*0} \to K^+\pi^-)$ decays. The detail of the wrong tag probability determination is explained in Appendix C. Table 4.2 summarizes the number of remaining events, w_l, event fraction of the signal ϵ_l and effective efficiency $\epsilon^l_{eff} = \epsilon_l(1 - 2w_l)^2$ in each r interval. The total effective efficiency is estimated to be $\sum_l \epsilon^l_{eff} = (31.2 \pm 0.7)\%$. 294 events out of 295 events are assigned a non-zero value of r.

l	r interval	N_l	w_l	ϵ_l	ϵ_{eff}^l
1	$0.000 - 0.250$	143	0.457 ± 0.006	0.369	0.003 ± 0.001
2	$0.250 - 0.500$	50	0.332 ± 0.009	0.154	0.017 ± 0.002
3	$0.500 - 0.625$	29	0.224 ± 0.010	0.107	0.033 ± 0.002
4	$0.625 - 0.750$	30	$0.156^{+0.009}_{-0.008}$	0.116	0.055 ± 0.003
5	$0.750 - 0.875$	18	0.108 ± 0.009	0.100	0.062 ± 0.003
6	$0.875 - 1.000$	24	$0.016^{+0.006}_{-0.005}$	0.152	0.142 ± 0.004

Table 4.2: *Number of flavor-tagged candidates N_l, wrong tag probability w_l, event fraction of the signal ϵ_l and effective efficiency $\epsilon_{eff}^l = \epsilon_l(1-2w_l)^2$ for each r interval. The errors of w_l and ϵ_{eff}^l include both statistical and systematic. Event fractions are obtained from the signal MC.*

Chapter 5

Extraction of CP Asymmetry Parameters

In this chapter, we extract the CP asymmetry parameters from the Δt distribution of 294 candidate events selected in the previous chapter. In order to make maximal use of the available statistics, we apply a maximum likelihood method. At first, we introduce the maximum likelihood method briefly, and then we describe how we apply it to our measurement. Finally, we present the fit result.

5.1 Maximum Likelihood Method

The principle of a maximum likelihood method is simple. Assume that we have a set of variables x_i as a result of N independent measurements and that we know the probability density function (PDF) $P(\alpha, x_i)$ to observe x_i, where α is a set of parameters to be obtained. The likelihood function $\mathcal{L}$ is defined as

$$\mathcal{L}(\alpha) = \prod_{i=1}^{N} P_i(\alpha, x_i). \tag{5.1}$$

This likelihood function can be considered as a joint probability density of getting the result. The most probable values of α are then the ones which maximize $\mathcal{L}$.

The maximum likelihood method has an advantage over the least squares method on binned histogram because it can take into account event-by-event difference, such as background probability or experimental resolution. Therefore, the maximum likelihood method is the best method to squeeze as much sensitivity as possible from data.

In the limit of large number of events, the likelihood becomes a Gaussian, and the error on the estimated parameter is given by difference between the value at the likelihood maximum and the value at which the likelihood becomes $e^{-1/2}$ of the maximum. In practical use, we minimize $-2\ln\mathcal{L}$ instead of maximizing $\mathcal{L}$ itself, because $\mathcal{L}$ gets too small to be treated by computer. In this case, an error is calculated to be a difference between the value at the minimum and the value at which the $-2\ln\mathcal{L}$ increases by one.

5.2 Probability Density Function

To apply the maximum likelihood method to our measurement, we need to construct PDF. Although we already know the theoretical PDF given by equation (2.2), we can not use it alone because measured quantity is smeared by experimental dilution.

There are three experimental dilution effects in our measurement: background contamination, wrong flavor tagging and resolution of Δt reconstruction. We define the PDF as

$$P = (1 - f_{ol}) \left(f_{sig} P_{sig} + f_{cont} P_{cont} + f_{B\overline{B}} P_{B\overline{B}} \right) + f_{ol} P_{ol} \tag{5.2}$$

where f_X is a fraction of the signal, the continuum background and the $B\overline{B}$ background, P_{sig} is the signal PDF smeared by wrong flavor tagging and Δt resolution and $P_{cont(B\overline{B})}$ is the Δt PDF of the continuum ($B\overline{B}$) background. The small number of signal and background events that have large Δt are accommodated by the outlier PDF, P_{ol}, with fraction f_{ol}. In this section, we describe these components.

5.2.1 Signal PDF

The P_{sig} is made by adding dilution of wrong flavor tagging and Δt resolution to the theoretical function $\mathcal{P}$ given in equation (2.2).

Due to the wrong tagging probability w_l, the probability to observe the true flavor is reduced by $1 - w_l$, while the opposite flavor contaminates by w_l. The effect of Δt resolution is expressed by introducing a resolution function $R(\Delta t - \Delta t')$ which is the probability density to observe Δt for a true value of $\Delta t'$. The P_{sig} is then given by a function of flavor q, Δt, w_l, CP asymmetry parameters $\mathcal{A}_{\eta' K_S}$ and $\mathcal{S}_{\eta' K_S}$:

$$P_{sig}(q, \Delta t, w_l; \mathcal{A}_{\eta' K_S}, \mathcal{S}_{\eta' K_S}) = \int \mathcal{P}_{sig}(q, \Delta t', w_l; \mathcal{A}_{\eta' K_S}, \mathcal{S}_{\eta' K_S}) R_{sig}(\Delta t - \Delta t') d\Delta t', \tag{5.3}$$

where

$$\begin{aligned} \mathcal{P}_{sig}(q, \Delta t', w_l; \mathcal{A}_{\eta' K_S}, \mathcal{S}_{\eta' K_S}) &= (1 - w_l)\mathcal{P}(q, \Delta t') + w_l \mathcal{P}(-q, \Delta t') \\ &= \frac{e^{-\frac{|\Delta t'|}{\tau_{B^0}}}}{4\tau_{B^0}} [1 + (1 - 2w_l) q (\mathcal{A}_{\eta' K_S} \cos \Delta m_d \Delta t' \\ &\qquad\qquad + \mathcal{S}_{\eta' K_S} \sin \Delta m_d \Delta t')] \,. \end{aligned} \tag{5.4}$$

We use the event-by-event resolution function depending on errors of reconstructed vertices. The resolution function is defined as convolution of three component

$$R_{sig} = R_{det} \otimes R_{np} \otimes R_k, \tag{5.5}$$

where R_{det} is the detector resolution, R_{np} takes care of contamination of non-primary tracks to the B_{tag} vertex, and R_k is the dilution due to the kinematic approximation that we neglect B motion in the center of mass system in the Δt calculation. We use the same parameterization as that used for the previous $\sin 2\phi_1$ measurement [10]. The details are given in Appendix B. The R_{np} is determined with MC. The R_k is calculated

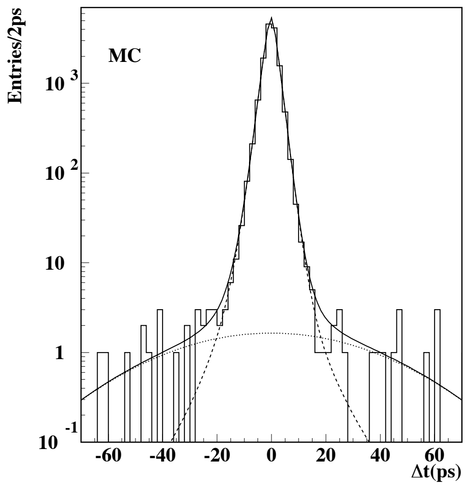

Figure 5.1: *The Δt distribution of the $B^0 \to \eta' K_S$ signal MC. The dashed line shows the signal PDF. The dotted line shows the outlier term. The solid line shows the sum of them.*

analytically. Parameters of the R_{det} are determined from the lifetime analysis of B^0 and B^+ using $B^0 \to J/\psi K_S, J/\psi K^{*0}(K^{*0} \to K^+\pi^-), D^{*-}\ell^+\nu, D^{(*)-}\pi^+, D^{*-}\rho^+$ and $B^+ \to J/\psi K^+, \overline{D}^0\pi^+$ decays. The Δt resolution for the $B^0 \to \eta' K_S$ decays is estimated to be 1.8 ps (rms).

For the wrong tagging probability w_l, we use values obtained from the B^0-$\overline{B}^0$ mixing analysis using self-tagged $B^0 \to J/\psi K^{*0}(K^{*0} \to K^+\pi^-), D^{*-}\ell^+\nu, D^{(*)-}\pi^+, D^{*-}\rho^+$ decays.

The lifetime and the B^0-$\overline{B}^0$ mixing analysis is described in Appendix C. From the analysis, we obtain $\tau_{B^0} = (1.538 \pm 0.016)$ ps, $\tau_{B^+} = (1.661^{+0.017}_{-0.021})$ ps and $\Delta m_d = 0.509^{+0.007}_{-0.008}$ ps^{-1}, where errors include both statistical and systematic. They are consistent with world average values [16]: $\tau_{B^0} = (1.542 \pm 0.016)$ ps, $\tau_{B^+} = (1.674 \pm 0.018)$ ps and $\Delta m_d = (0.489 \pm 0.008)$ ps^{-1} within two standard deviations. These results verify the validity of the resolution function and the flavor tagging method we use. We use the obtained values of τ_{B^0} and Δm_d for the signal PDF.

5.2.2 Outlier PDF

There are small fraction ($\sim 0.5\%$) of events that have very long tail in Δt distribution that cannot be described by the PDF explained above. Figure 5.1 shows the Δt distribution of the signal MC. The dashed line shows the signal PDF. There are small number of events that have large Δt outside of the dashed line. The outlier term shown by the dotted line is introduced to describe the long tail. The outlier events also exist in the background. Since the outlier is considered to be caused by the mis-reconstruction of tracks and independent of whether the event is the signal or the background, we assign the same fraction f_{ol} and the shape of the outlier to the signal and the background. The

parameter	value
f_{ol}^{mult}	$(1.8^{+1.6}_{-1.1}) \times 10^{-4}$
f_{ol}^{single}	$(2.7^{+0.2}_{-0.5}) \times 10^{-2}$
σ_{ol} (ps)	$39.0^{+2.8}_{-11.0}$

Table 5.1: *Parameters of the outlier PDF. Errors include both statistical and systematic.*

PDF is given by a Gaussian with large width (~ 40 ps) as,

$$P_{ol}(q, \Delta t) = [f_{sig} f_q^{sig} + (1 - f_{sig}) f_q^{bg}] \times G(\Delta t; 0, \sigma_{ol}), \tag{5.6}$$

where the terms in a square bracket indicate the fraction of events with flavor q: f_{sig} is the signal fraction explained in Section 5.2.3, and $f_q^{sig(bg)}$ is the fraction of the signal (background) events with flavor q. The f_q^{bg} is set to 0.5 by assuming the background is CP conserving, and f_q^{sig} is calculated as the integral of $\mathcal{P}_{sig}$ in equation (5.4). The fraction of the outlier f_{ol} and the width σ_{ol} in the data are determined from the lifetime analysis described in Appendix C. We use different f_{ol} values depending on whether both vertices are reconstructed with multiple tracks or not. Their values are shown in Table 5.1.

5.2.3 Signal and Background Fraction

The signal and background fractions are determined event-by-event depending on its ΔE and M_{bc}, i.e. an event near the signal peak has a higher probability to be the signal than an event at the boundary of the signal region. The fraction is defined as

$$f_X(\Delta E, M_{bc}) = \frac{f_X^{ave} F_X(\Delta E, M_{bc})}{f_{sig}^{ave} F_{sig}(\Delta E, M_{bc}) + f_{cont}^{ave} F_{cont}(\Delta E, M_{bc}) + f_{B\overline{B}}^{ave} F_{B\overline{B}}(\Delta E, M_{bc})}, \tag{5.7}$$

where X is signal, continuum or $B\overline{B}$ background, $f_X^{ave.}$ is the average fraction defined to be $f_{sig}^{ave} + f_{cont}^{ave} + f_{B\overline{B}}^{ave} = 1$, and F_X is a ΔE-M_{bc} probability density function. In the following, we describe each ΔE-M_{bc} PDF and average fraction.

Signal ΔE-M_{bc} PDF

The signal probability density function are defined as a Gaussian function for M_{bc} and sum of a main Gaussian function and a bifurcated Gaussian which account for a tail part for ΔE due to photon energy leakage from the ECL. The F_{sig} is written as

$$\begin{aligned} F_{sig}(\Delta E, M_{bc}) \equiv {} & G(M_{bc}; \mu_{M_{bc}}, \sigma_{M_{bc}}) \\ & \times [f_g G(\Delta E; \mu_{\Delta E}, \sigma_{M_{bc}}) + (1 - f_g) G_{bif}(\Delta E; \mu_{bif}^{\Delta E}, \sigma_h^{\Delta E}, \sigma_l^{\Delta E})], \end{aligned} \tag{5.8}$$

where f_g is the fraction of a main Gaussian for ΔE. Gaussian G and bifurcated Gaussian G_{bif} are defined as:

$$G(x; \mu, \sigma) \equiv \frac{1}{\sqrt{2\pi}\sigma} \exp\left(-\frac{(x-\mu)^2}{2\sigma^2}\right), \tag{5.9}$$

parameter	$\eta' \to \eta\pi^+\pi^-$ mode	$\eta' \to \rho^0\gamma$ mode
$\mu_{M_{bc}}(\mathrm{MeV}/c^2)$	5279.4 ± 0.2	5279.4 ± 0.2
$\sigma_{M_{bc}}(\mathrm{MeV}/c^2)$	2.8 ± 0.2	2.7 ± 0.2
$\mu_{\Delta E}(\mathrm{MeV})$	$-2.8^{+2.3}_{-2.5}$	-3.6 ± 1.3
$\sigma_{\Delta E}(\mathrm{MeV})$	$21.0^{+2.4}_{-2.3}$	15.9 ± 1.2
f_g	0.76 ± 0.02	0.82 ± 0.01
$\mu^{\Delta E}_{bif}(\mathrm{MeV})$	$-27.5 \pm^{+6.2}_{-6.5}$	-10.2 ± 3.8
$\sigma^{\Delta E}_{h}(\mathrm{MeV})$	$60.3^{+7.9}_{-7.5}$	$55.0^{+4.7}_{-4.6}$
$\sigma^{\Delta E}_{l}(\mathrm{MeV})$	$54.0^{+6.7}_{-6.4}$	51.2 ± 4.3

Table 5.2: *Parameters of the signal ΔE-M_{bc} shape.*

parameter	$\eta' \to \eta\pi^+\pi^-$ mode	$\eta' \to \rho^0\gamma$ mode
c	-1.7 ± 0.2	-1.4 ± 0.1
N	-22.5 ± 4.2	-22.5 ± 2.3

Table 5.3: *Parameters of the continuum background ΔE-M_{bc} shape. The c is the ΔE slope and N is the parameter of the ARGUS function.*

$$G_{bif}(x;\mu,\sigma_h,\sigma_l) \equiv \begin{cases} \dfrac{2}{\sqrt{2\pi}(\sigma_h+\sigma_l)} \exp\left(-\dfrac{(x-\mu)^2}{2\sigma_h^2}\right) & (x \geq \mu), \\ \dfrac{2}{\sqrt{2\pi}(\sigma_h+\sigma_l)} \exp\left(-\dfrac{(x-\mu)^2}{2\sigma_l^2}\right) & (x < \mu). \end{cases} \tag{5.10}$$

The means, widths and the main Gaussian fraction f_g are determined separately for $\eta' \to \eta\pi^+\pi^-$ and $\eta' \to \rho^0\gamma$ modes from the signal MC sample. Figure 5.2 shows the ΔE and M_{bc} distributions of the signal MC with the the fit result overlaid. Possible difference of means and widths between the real data and the MC are determined with $B^+ \to \eta' K^+$ decays. The event selection for $B^+ \to \eta' K^+$ decays and the determination of correction factors are described in Appendix E. Obtained parameters are summarized in Table 5.2.

ΔE-M_{bc} PDF of Continuum Background

The distribution of continuum background is parametrized by a first order polynomial for ΔE and the ARGUS function [65] for M_{bc} distribution.

$$F_{cont}(\Delta E, M_{bc}) = a(1+c\Delta E) \times M_{bc}\sqrt{1-\left(\frac{M_{bc}}{E_{beam}}\right)^2} \exp\left(N\left[1-\left(\frac{M_{bc}}{E_{beam}}\right)^2\right]\right), \tag{5.11}$$

where a is a normalization factor, c is a slope of ΔE and N determines a curvature of the M_{bc} shape. Different values of c and N are used between $\eta' \to \eta\pi^+\pi^-$ and $\eta' \to \rho^0\gamma$ modes. We determine their values from the fit to the real data simultaneously with average fractions. The fit is described later. We list obtained c and N in Table 5.3.

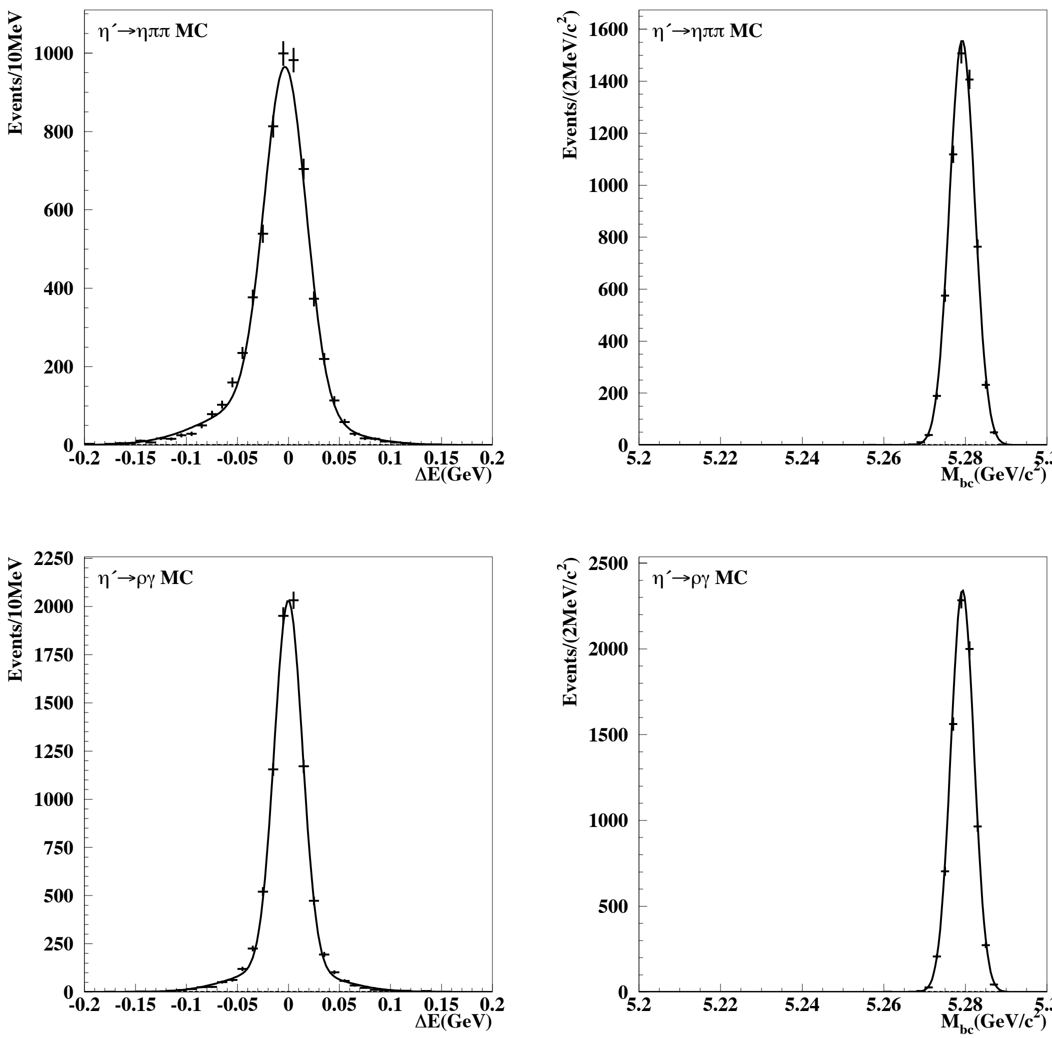

Figure 5.2: The ΔE and M_{bc} distributions of the $B^0 \to \eta' K_S$ MC. Upper figures are for the $\eta' \to \eta\pi^+\pi^-$ mode, and lower figures are for the $\eta' \to \rho^0\gamma$ mode. Solid lines show the obtained PDF by the unbinned maximum likelihood fit.

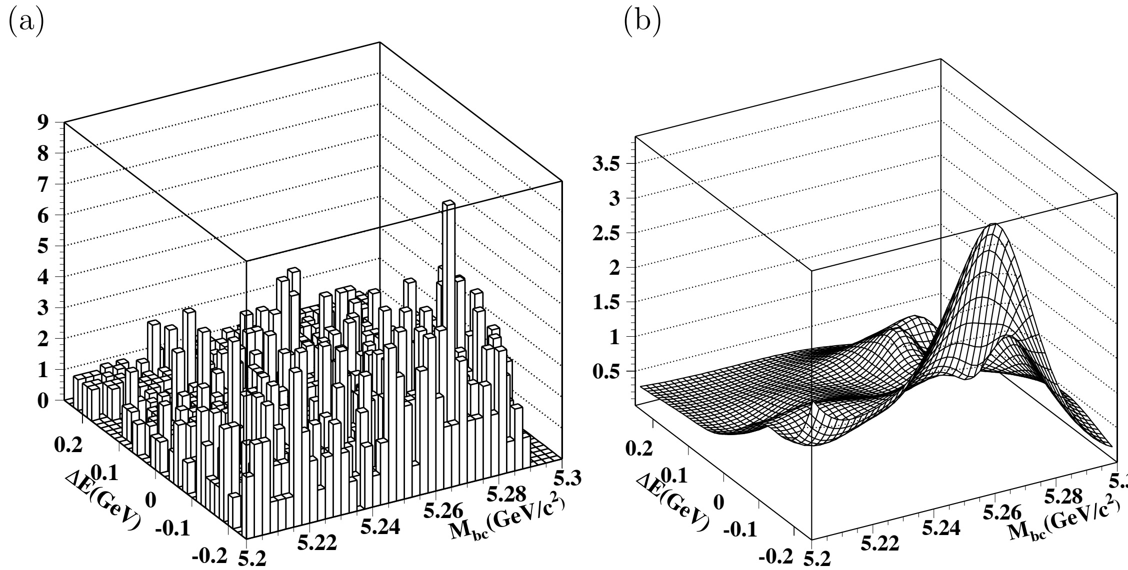

Figure 5.3: *The ΔE-M_{bc} distribution of the $B\overline{B}$ background: (a) the ΔE-M_{bc} distribution obtained from the $B\overline{B}$ MC, (b) the $B\overline{B}$ background PDF made from the MC distribution by smoothing.*

$B\overline{B}$ Background Shape

The PDF for $B\overline{B}$ background are determined with MC sample. Figure 5.3 shows the ΔE-M_{bc} distribution obtained from the MC sample of 157×10^6 $B\overline{B}$ pairs. Because of the small statistics of the MC sample, we do not separate the remaining events into submode of η' and also use the events reconstructed as $B^+ \to \eta' K^+$. We obtain the PDF by smoothing the ΔE-M_{bc} distribution. The obtained function is shown in Figure 5.3 (b).

Average Signal and Background Fraction Determination

The $B\overline{B}$ background fractions are obtained from MC sample of 157×10^6 $B\overline{B}$ pairs. We count the number of events in the MC and scale it to the real data.

Signal fractions are determined by the unbinned maximum likelihood fit to ΔE and M_{bc} distributions of events in $|\Delta E| < 0.25$ GeV and $5.2\text{GeV}/c^2 < M_{bc}$ using PDFs explained above. Continuum background parameters, c and N, are also determined in the fit simultaneously.

To maximize the sensitivity, different signal and background fractions are used for each of two LR bins and six flavor tagging quality r bins. We use same signal and background ΔE-M_{bc} shapes for all LR and r bins. The detailed result of the ΔE-M_{bc} fit is given in Appendix D. Figure 5.4 show the ΔE and M_{bc} distribution for each η' decay mode with all LR and r bins combined. Estimated signal yield and fraction in the signal region are shown in Table 5.4.

η' Mode	N_{cand}	N_{sig}	f_{sig}	$f_{B\overline{B}}$	f_{cont}
$\eta' \to \eta\pi^+\pi^-$	93	52.5 ± 8.5	0.57	0.01	0.42
$\eta' \to \rho^0\gamma$	201	94.6 ± 11.7	0.48	0.06	0.46

Table 5.4: *Signal yields and average signal and background fractions in the signal region for the $B^0 \to \eta' K_S$ candidates. The N_{cand} is the number of candidates in the signal region. The N_{sig} is the signal yield in the signal region obtained by the ΔE-M_{bc} fit. Each f_X shows fraction of signal, $B\overline{B}$ or continuum background calculated as the ratio of the integral of their PDFs in the signal region.*

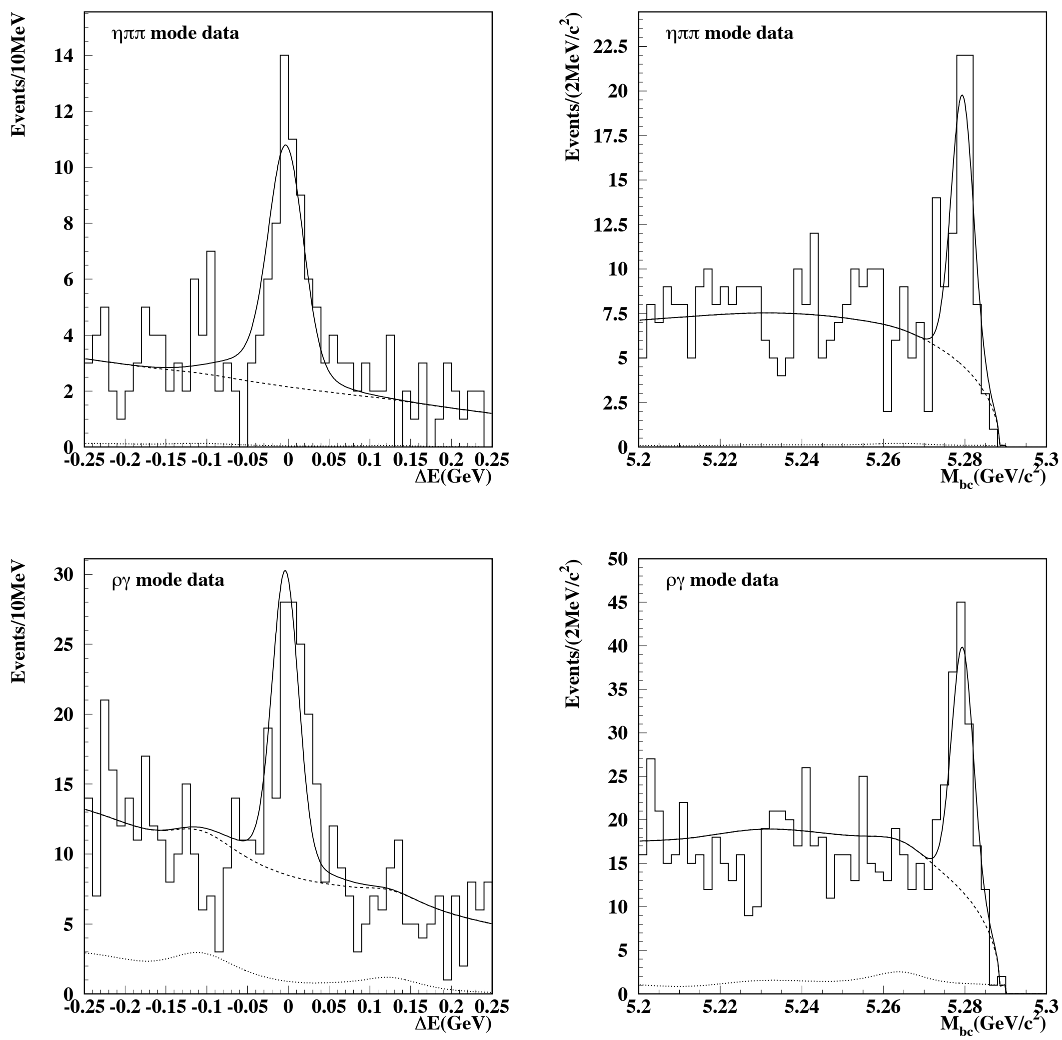

Figure 5.4: *ΔE and M_{bc} distributions of the reconstructed $B^0 \to \eta' K_S$ candidates for the $\eta' \to \eta\pi^+\pi^-$ (upper) mode and the $\eta' \to \rho^0\gamma$ mode (lower). Solid lines show the fit results. Dotted lines show the $B\overline{B}$ background component. Dashed lines show the sum of the $B\overline{B}$ background and the continuum background.*

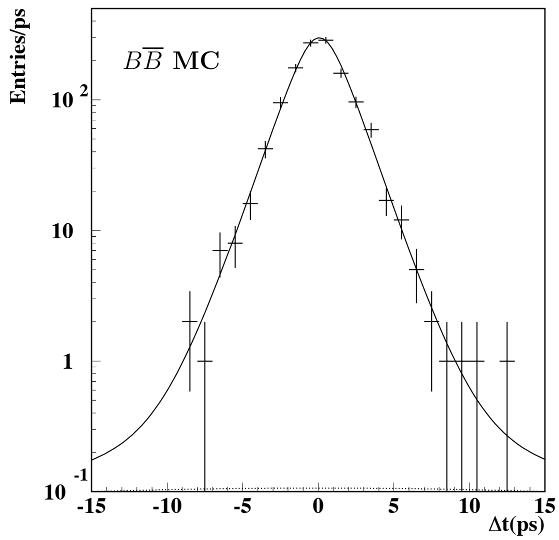

Figure 5.5: *The Δt distribution of the $B\overline{B}$ background MC sample. The solid line shows the fit result. The dotted line shows the outlier component.*

5.2.4 Background Δt PDF

$B\overline{B}$ Background Δt PDF

The Δt PDF of the $B\overline{B}$ background is obtained from the $B\overline{B}$ MC. Figure 5.5 shows the Δt distribution obtained with the Monte Carlo sample of 157×10^6 $B\overline{B}$ pairs. Due to the limited statistics, we use events in wider region ($|\Delta E| < 0.25$GeV and 5.2GeV$/c^2 < M_{bc}$) and also use events reconstructed as $B^+ \to \eta' K^+$. The same function is used for both $\eta' \to \rho^0\gamma$ and $\eta' \to \eta\pi^+\pi^-$ modes. The solid line in Figure 5.5 shows the obtained PDF. The dotted line is the outlier PDF, which is described in Section 5.2.2. We parameterize the PDF as an exponential smeared by a Gaussian,

$$P_{B\overline{B}}(\Delta t) \equiv \int d\Delta t' \frac{1}{2\tau} \exp\left(-\frac{|\Delta t'|}{\tau_{B\overline{B}}}\right) G(\Delta t - \Delta t'; \mu_{B\overline{B}}, s_{B\overline{B}}\sigma), \tag{5.12}$$

where σ is the error of Δt calculated from errors of vertices and $s_{B\overline{B}}$ is the global scaling factor of the error. We use different $s_{B\overline{B}}$ depending on whether both vertices are reconstructed with multiple tracks or not. The obtained parameter values are shown in Table 5.5.

Continuum Δt PDF

The Δt PDF of the continuum background is expressed as the sum of a exponential component with the effective lifetime τ_{cont} and a prompt component expressed by Dirac's

parameter	value
$\tau_{B\overline{B}}$(ps)	1.16 ± 0.06
$\mu_{B\overline{B}}$(ps)	0.07 ± 0.05
$(s_{B\overline{B}})_{multiple}$	1.30 ± 0.12
$(s_{B\overline{B}})_{single}$	1.15 ± 0.11

Table 5.5: *The Δt PDF parameters of the $B\overline{B}$ background obtained from the Monte Carlo sample.*

delta function smeared by double Gaussian,

$$P_{cont}(\Delta t) \equiv \int d\Delta t' \left[(1-f_\delta)\frac{1}{2\tau_{cont}}\exp\left(-\frac{|\Delta t' - \mu_\tau^{cont}|}{\tau_{cont}}\right) + f_\delta \delta(\Delta t' - \mu_\delta^{cont})\right] \times R_{cont}(\Delta t - \Delta t'), \quad (5.13)$$

where f_δ is the fraction of the prompt component, μ_τ^{cont} and μ_δ^{cont} are offsets of the Δt distribution, and R_{cont} is defined as,

$$R_{cont}(\Delta t) \equiv (1 - f_{tail}^{cont})G(\Delta t; 0, s_{main}^{cont}\sigma) + f_{tail}^{cont}G(\Delta t; 0, s_{tail}^{cont}\sigma), \quad (5.14)$$

where f_{tail} is the fraction of the second Gaussian. Different values of s_{main}^{cont}, s_{tail}^{cont} and f_{tail}^{cont} are used depending on whether both vertices are reconstructed with multiple tracks or not. Parameters of P_{cont} are determined by fitting to the Δt distribution of the M_{bc} sideband events defined as $5.2 < M_{bc} < 5.26$ GeV/c^2 and $|\Delta E| < 0.25$ GeV. To increase statistics, we also use events reconstructed as $B^+ \to \eta' K^+$ candidates together. We use different parameter values between the $\eta' \to \eta\pi^+\pi^-$ mode and the $\eta' \to \rho^0\gamma$ mode. Figure 5.6 shows the Δt distribution of the M_{bc} sideband events with the obtained Δt PDF function. The dotted and the dashed lines in Figure 5.6 are the outlier component and the sum of the $B\overline{B}$ background component and the outlier component. The obtained PDF parameters are summarized in Table 5.6. Since the lifetime component of $\eta' \to \eta\pi + \pi^-$ mode is measured to be consistent with 0, we fix f_δ of the $\eta' \to \eta\pi^+\pi^-$ mode to 1.

We assume backgrounds are CP conserving, i.e. the probability to observe $q = +1$ or $q = -1$ is set to 0.5.

5.3 Fitting Result

CP asymmetry parameters are obtained from the Δt distribution of 294 $B^0 \to \eta' K_S$ candidate events. Using results of previous sections, the PDF is written as

$$P(q, w_l, \Delta t; \mathcal{A}_{\eta' K_S}, \mathcal{S}_{\eta' K_S}) = (1 - f_{ol})[f_{sig}P_{sig}(q, \Delta t, w_l; \mathcal{A}_{\eta' K_S}, \mathcal{S}_{\eta' K_S}) + \frac{1}{2}f_{B\overline{B}}P_{B\overline{B}}(\Delta t) + \frac{1}{2}f_{cont}P_{cont}(\Delta t)] + f_{ol}P_{ol}(q, \Delta t) \quad (5.15)$$

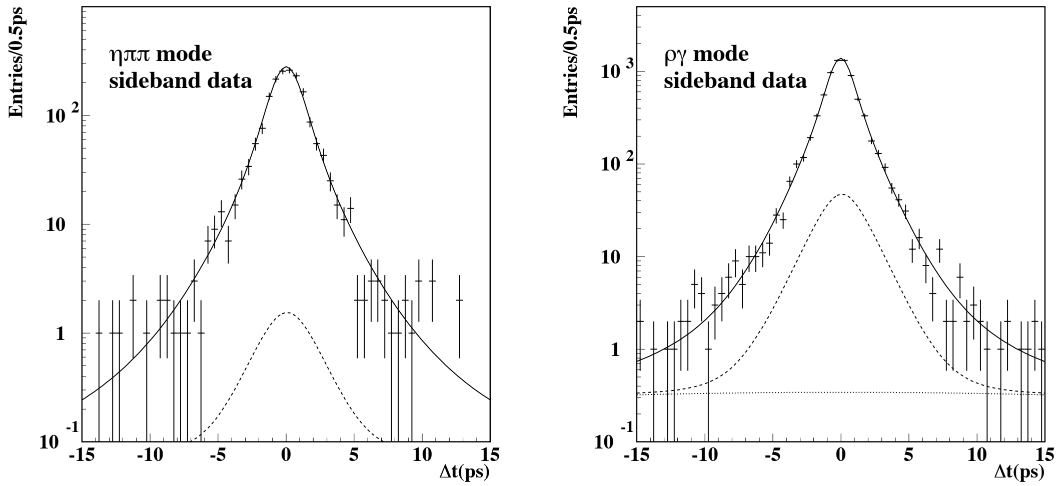

Figure 5.6: *The Δt distribution of the M_{bc} sideband data for the $\eta' \to \eta\pi^+\pi^-$ mode (left) and for the $\eta' \to \rho^0\gamma$ mode (right). The solid lines show the fit results. The dotted lines show the outlier component and the dashed lines show the sum of the $B\overline{B}$ background component and the outlier component.*

	$\eta' \to \eta\pi^+\pi^-$	$\eta' \to \rho^0\gamma$
$(s^{cont}_{main})_{multiple}$	1.17 ± 0.05	$1.05^{+0.04}_{-0.05}$
$(s^{cont}_{tail})_{multiple}$	$2.50^{+0.19}_{-0.16}$	2.22 ± 0.20
$(f^{cont}_{tail})_{multiple}$	$0.20^{+0.05}_{-0.04}$	$0.20^{+0.07}_{-0.05}$
$(f^{cont}_{\delta})_{multiple}$	1	$0.89^{+0.05}_{-0.08}$
$(s^{cont}_{main})_{single}$	1.10 ± 0.06	0.97 ± 0.06
$(s^{cont}_{tail})_{single}$	$2.81^{+0.58}_{-0.45}$	$2.73^{+0.44}_{-0.45}$
$(f^{cont}_{tail})_{single}$	$0.11^{+0.06}_{-0.04}$	$0.13^{+0.05}_{-0.04}$
$(f^{cont}_{\delta})_{single}$	1	$0.60^{+0.19}_{-0.25}$
τ_{cont}(ps)	$-$	$0.96^{+0.41}_{-0.29}$
μ^{cont}_{δ}(ps)	0.01 ± -0.02	-0.02 ± 0.02
μ^{cont}_{τ}(ps)	$-$	$-0.02^{+0.11}_{-0.12}$

Table 5.6: *Parameters of the continuum background Δt PDF.*

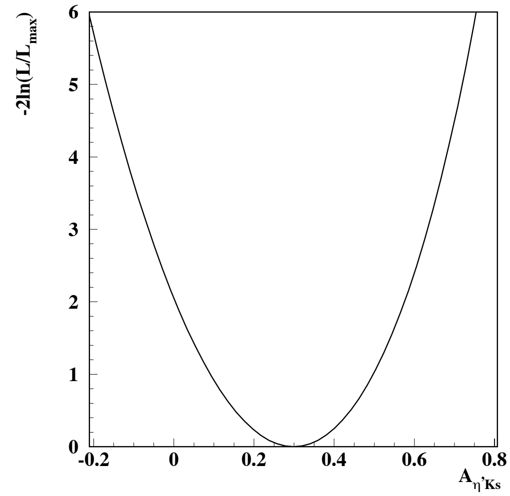

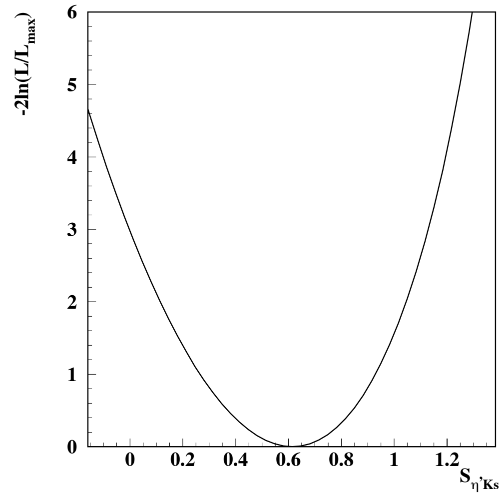

Figure 5.7: $-2\ln(\mathcal{L}/\mathcal{L}_{max})$ *as a function of* $\mathcal{A}_{\eta' K_S}$ *(left) and* $\mathcal{S}_{\eta' K_S}$ *(right).*

The likelihood function is given by

$$\mathcal{L}(\mathcal{A}_{\eta' K_S}, \mathcal{S}_{\eta' K_S}) = \prod_i P(q_i, \Delta t_i; \mathcal{A}_{\eta' K_S}, \mathcal{S}_{\eta' K_S}), \tag{5.16}$$

where i runs over all candidate events. We determine the most probable CP asymmetry parameters by minimizing $-2\ln\mathcal{L}$. We obtain

$$\begin{array}{l} 0.30^{+0.20}_{-0.21}, \\ 0.61^{+0.31}_{-0.35}. \end{array} \tag{5.17}$$

Figure 5.7 shows the $-2\ln(\mathcal{L}/\mathcal{L}_{max})$ as a function of $\mathcal{A}_{\eta' K_S}$ or $\mathcal{S}_{\eta' K_S}$. Figure 5.8 shows the Δt distribution of 157 B^0-tagged events and 137 $\overline{B}^0$-tagged events together with the fit results. We test the goodness of fit from a χ^2 comparison of the results of the unbinned fit and the Δt distributions of Figure 5.8[1]. We obtain $\chi^2 = 13.7/16$ DOF (13.3/16 DOF) for the Δt distribution of the $B^0(\overline{B}^0)$ tags. Figure 5.9 shows asymmetry between the B^0- and $\overline{B}^0$-tagged without background subtraction as a function of Δt. In figure 5.10, we show the background-subtracted CP asymmetry.

5.4 Systematic Uncertainties

We consider following sources for systematic errors. The results are summarized in Table 5.7.

[1]We use Eq. (31.12) in Particle Data Group, K. Hagiwara *et al.*, Phys. Rev. **D66**, 010001 (2002) p.230.

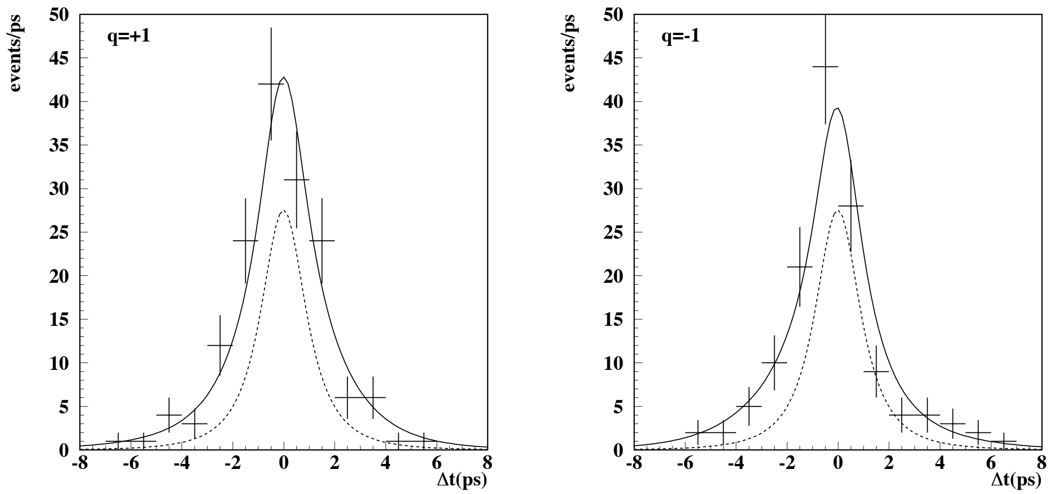

Figure 5.8: *The* Δt *distribution of 157* B^0*-tagged (left) and 137* $\overline{B}^0$*-tagged (right)* $B^0 \to \eta' K_S$ *candidates. Solid lines show the fit result. Dashed lines show the background component.*

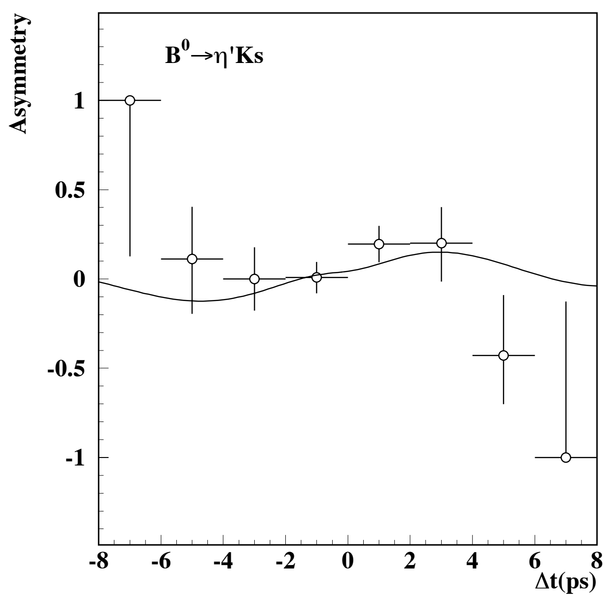

Figure 5.9: CP *asymmetry of* $B^0 \to \eta' K_S$ *candidate events. The solid line show the fit result.*

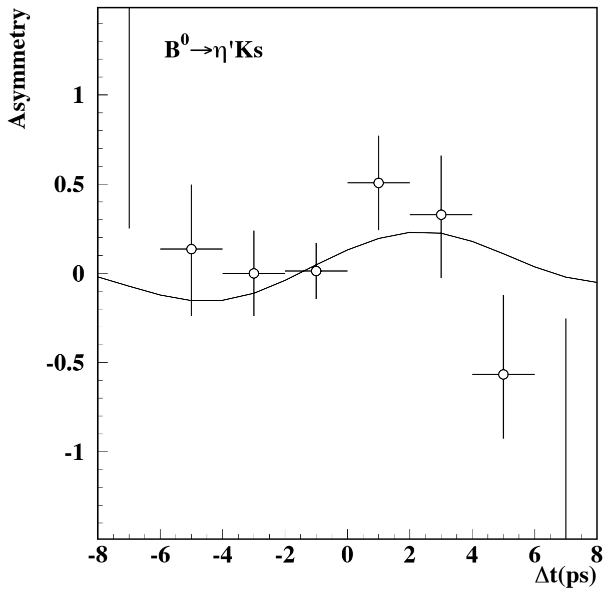

Figure 5.10: *CP asymmetry of $B^0 \to \eta' K_S$ after background subtraction.*

Source	Error on $\mathcal{A}_{\eta' K_S}$	Error on $\mathcal{S}_{\eta' K_S}$
Background Fractions	$^{+0.031}_{-0.034}$	$^{+0.054}_{-0.040}$
Vertex Reconstruction	$^{+0.046}_{-0.016}$	$^{+0.006}_{-0.044}$
Resolution Function	$^{+0.003}_{-0.004}$	$^{+0.023}_{-0.028}$
Wrong Tag Probability	$^{+0.014}_{-0.005}$	$^{+0.011}_{-0.016}$
Physics Parameter	± 0.001	$^{+0.006}_{-0.007}$
Bakground Δt PDF	$^{+0.002}_{-0.003}$	± 0.006
Total	$^{+0.057}_{-0.039}$	$^{+0.061}_{-0.069}$

Table 5.7: *Sources of systematic errors for the CP asymmetry parameter measurement.*

5.4.1 Signal and Background Fractions

Signal

Each parameter describing signal ΔE-M_{bc} shape is varied and the fit is repeated. The systematic error due to the average signal fraction is evaluated by varying each average fraction by its error and repeating the fit. We add each deviation from the nominal fit in quadrature. The errors are estimated to be $^{+0.030}_{-0.033}$ for $\mathcal{A}_{\eta' K_S}$ and $^{+0.053}_{-0.040}$ for $\mathcal{S}_{\eta' K_S}$.

$B\overline{B}$ Background

We estimated the $B\overline{B}$ fraction with the MC sample. The systematic error due to uncertainty of the MC is evaluated by setting all $B\overline{B}$ background fractions to zero or double. The difference from the nominal analysis is taken to be the systematic error. The errors are estimated to be $^{+0.003}_{-0.008}$ for $\mathcal{A}_{\eta' K_S}$ and $^{+0.011}_{-0.006}$ for $\mathcal{S}_{\eta' K_S}$.

Continuum Background ΔE-M_{bc} Shape

We change each parameter describing the ΔE and M_{bc} shape of the continuum background by its errors and repeat the analysis. Each deviation from the nominal fit is added in quadrature. The errors are estimated to be ± 0.001 for $\mathcal{A}_{\eta' K_S}$ and ± 0.002 for $\mathcal{S}_{\eta' K_S}$.

Asymmetry of Background

We assumed the background events are CP conserving. From the ΔE-M_{bc} sideband data and the $B\overline{B}$ MC sample, the fraction with $q = +1$ is measured to be $50.3 \pm 0.5\%$ for the continuum background and $48.9 \pm 1.4\%$ for the $B\overline{B}$ background. We estimate the systematic error due to the assumption by varying the fraction of $q = +1$ by $\pm 0.8\%$ for the continuum background and $\pm 2.5\%$ for the $B\overline{B}$ background. The errors are estimated to be ± 0.005 for $\mathcal{A}_{\eta' K_S}$ and ± 0.002 for $\mathcal{S}_{\eta' K_S}$.

5.4.2 Vertex Reconstruction

Vertex Selection Dependence

We have required $\xi < 100$ for CP and tagging side vertices. We change the ξ requirement to $\xi < 50$ and $\xi < 200$. Difference from the nominal fit is treated as the systematic error. The errors are estimated to be $^{+0.045}_{-0.015}$ for $\mathcal{A}_{\eta' K_S}$ and $^{+0.000}_{-0.041}$ for $\mathcal{S}_{\eta' K_S}$.

Track Selection for Tagging Side Vertex

The systematic error due to the track selection criteria for the tagging side vertexing is estimated by varying the requirement for $|dr|$ and error of z by $\pm 10\%$. The errors are estimated to be $^{+0.006}_{-0.001}$ for $\mathcal{A}_{\eta' K_S}$ and $^{+0.006}_{-0.015}$ for $\mathcal{S}_{\eta' K_S}$.

Δt Selection

The reconstructed Δt has been required to satisfy $|\Delta t| < 70$ ps. The rejection criterion is varied by ± 30 ps to check the validity of the tail treatment of our resolution function, and the difference from the nominal analysis is treated as systematic error. The errors are estimated to be less than 0.001 for both of $\mathcal{A}_{\eta' K_S}$ and $\mathcal{S}_{\eta' K_S}$.

Flight Length of B Meson

The IP constraint vertex fit includes the uncertainty of the B meson decay point due to the flight length of B meson in the r-ϕ plane. The uncertainty is estimated to be 21 μm by assuming a Gaussian function although it is actually an exponential function. We estimated the systematic error by varying the smearing by ± 10 μm. The errors are estimated to be $^{+0.001}_{-0.005}$ for $\mathcal{A}_{\eta' K_S}$ and $^{+0.000}_{-0.002}$ for $\mathcal{S}_{\eta' K_S}$.

5.4.3 Resolution Function

We estimate the contribution due to the uncertainty in the resolution function by varying the parameters by their errors. Each contribution is added in quadrature. The difference of the detector resolution between the $B^0 \to \eta' K_S$ decays and the control samples are studied with MC. The systematic error due to the modeling of the resolution function is estimated by comparing the results with different parametrization. For this study, we use double Gaussian form for the detector resolution instead of single Gaussian in the nominal analysis. The errors are estimated to be $^{+0.003}_{-0.004}$ for $\mathcal{A}_{\eta' K_S}$ and $^{+0.023}_{-0.028}$ for $\mathcal{S}_{\eta' K_S}$.

5.4.4 Wrong Tagging Probability

The systematic errors due to uncertainty in the wrong tagging probability are estimated by varying wrong tagging probability individually for each r region, and adding them in quadrature. The possible differences of wrong tagging probability between $q = +1$ and $q = -1$ is estimated with wrong tagging probabilities measured separately for $q = \pm 1$. The errors are estimated to be $^{+0.014}_{-0.005}$ for $\mathcal{A}_{\eta' K_S}$ and $^{+0.011}_{-0.016}$ for $\mathcal{S}_{\eta' K_S}$.

5.4.5 Physics Parameter

We used τ_{B^0} and Δm_d obtained from the semileptonic and hadronic B^0 decays. We estimate the systematic error by repeating the fit varying them by their errors. The errors are estimated to be ± 0.001 for $\mathcal{A}_{\eta' K_S}$ and $^{+0.006}_{-0.007}$ for $\mathcal{S}_{\eta' K_S}$.

5.4.6 Background $|\Delta t|$ Shape

Parameters describing Δt distribution of backgrounds are varied individually by their errors and the fit is repeated. We add each contribution in quadrature. The errors are estimated to be $^{+0.002}_{-0.003}$ for $\mathcal{A}_{\eta' K_S}$ and ± 0.006 for $\mathcal{S}_{\eta' K_S}$.

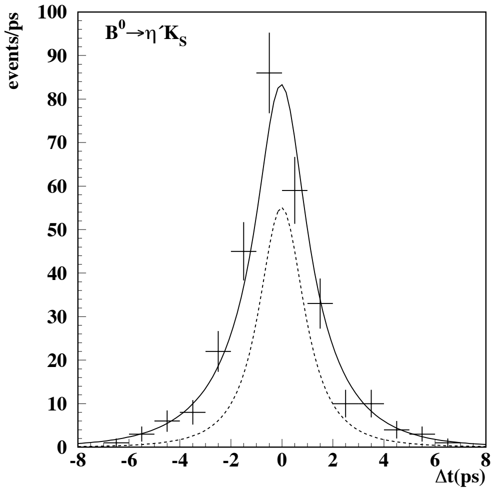

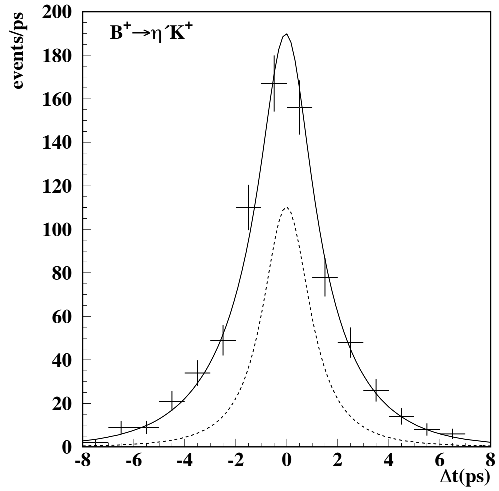

Figure 5.11: *The reconstructed Δt distribution of $B^0 \to \eta' K_S$ candidates (left) and $B^+ \to \eta' K^+$ candidates (right). Solid lines show the result of the lifetime fit. Dashed lines show the background component.*

5.5 Validity Check

To check the validity of the analysis, several tests are performed.

5.5.1 Lifetime Fit

The validity of the Δt reconstruction, the parametrization of the resolution function and background shapes are checked by the lifetime fit to $B^0 \to \eta' K_S$ and $B^+ \to \eta' K_S$ candidates. The reconstructed Δt distributions are shown in Figure 5.11. We obtain B^0 and B^+ lifetime as:

$$\begin{aligned} \tau_{B^0} &= (1.42^{+0.19}_{-0.17})\ \text{ps}, \\ \tau_{B^+} &= (1.59 \pm 0.10)\ \text{ps}, \end{aligned} \tag{5.18}$$

where errors are statistical only. They are consistent with the world average [16] and prove the validity of the Δt reconstruction, the background shapes and application of our resolution to $B \to \eta' K$ decays.

5.5.2 Asymmetry of non-CP Eigenstate Sample

The reconstruction bias to CP asymmetry are checked by the CP asymmetry analysis on B^0 samples that are not CP eigenstate: $D^{*-}\ell^+\nu$, $D^{*-}\pi^+$, $D^-\pi^+$, $D^{*-}\rho^+$ and $J/\psi K^{*0}(K^{*0} \to K^+\pi^-)$. These are the samples used for the lifetime and the mixing analysis in Appendix C. The unbinned maximum likelihood fit is performed assuming them to be $CP = -1$. The fit result are summarized in Table 5.8. Combining all non-CP

mode	$\mathcal{A}$	$\mathcal{S}$
$B^0 \to D^{*-}\ell^+\nu$	0.030 ± 0.013	-0.001 ± 0.017
$B^0 \to D^{(*)-}\pi^+, D^{*-}\rho^+$	-0.019 ± 0.021	0.032 ± 0.031
$B^0 \to J/\psi K^{*0}(K^{*0} \to K^+\pi^-)$	0.022 ± 0.060	-0.021 ± 0.090

Table 5.8: *The result of CP asymmetry analysis on non-CP eigenstate samples.*

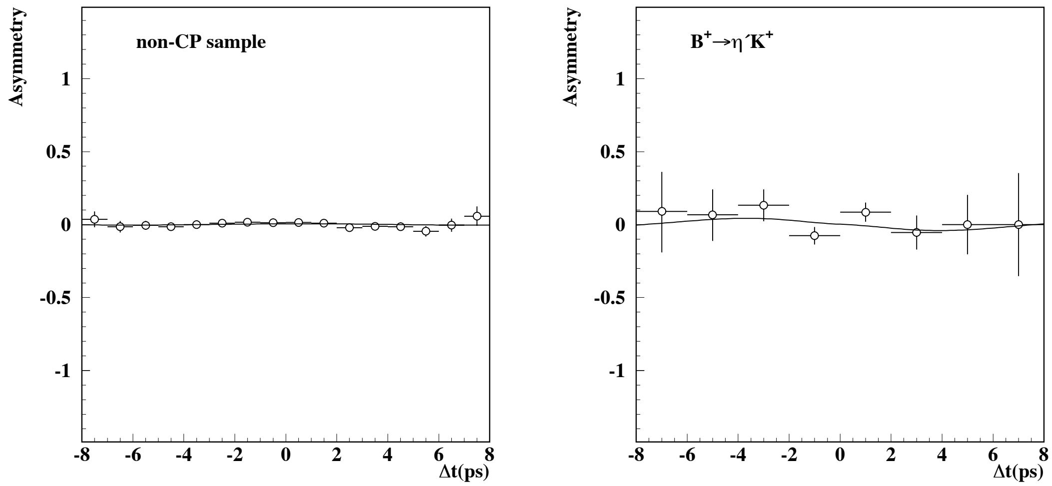

Figure 5.12: *Asymmetry of non-CP eigenstate B^0 samples (right) and asymmetry of $B^+ \to \eta' K^+$ candidates (left) as a function Δt. The solid line shows the fit result.*

eigenstate samples, we obtain

$$\begin{aligned} \mathcal{A}_{non-CP} &= 0.016 \pm 0.011, \\ \mathcal{S}_{non-CP} &= 0.006 \pm 0.014, \end{aligned} \tag{5.19}$$

where errors are statistical only. They are consistent with zero. Asymmetry of non-CP eigenstate samples as a function of Δt is shown in Figure 5.12 (left).

We also fit $B^+ \to \eta' K^+$ candidates which expected not to show time dependent CP asymmetry. The fit result is

$$\begin{aligned} \mathcal{A}_{\eta' K^+} &= 0.02 \pm 0.13, \\ \mathcal{S}_{\eta' K^+} &= -0.18 \pm 0.20, \end{aligned} \tag{5.20}$$

where errors are statistical only. The time-dependent asymmetry is shown in Figure 5.12 (right). They are consistent with no time dependent CP asymmetry.

These results prove that there are no statistical significant bias to CP asymmetry in our reconstruction procedure.

5.5.3 Ensemble Test

To check the fit procedure and the validity of estimated errors, we study the parameterized Monte Carlo samples which are generated exactly following the probability density function. In this way, expected values of fit parameters are known exactly and we can determine directly whether values returned by the fit are unbiased estimation or not.

We generate 1000 sets of Monte Carlo samples based on the PDF we use. Number of events in each sample follows the Poisson statistics having the mean value of the real data. Input values of CP asymmetry parameters are $\mathcal{A}_{\eta' K_S} = 0.30$ and $\mathcal{S}_{\eta' K_S} = 0.61$. Figure 5.13 and 5.14 shows the distributions of the output value of the fit, (output-input)/(error of the fit), positive and negative errors. The mean of output values is consistent with the input and thus it proves the fit is not biased. Distribution of (output-input)/(error of the fit) follows a Gaussian of $\mu = 0$ and $\sigma = 1$. It indicates our error estimation is correct. Errors obtained by the fit to the real data shown by vertical lines resides within the Monte Carlo prediction. Therefore, we conclude the fit procedure and the error estimation are valid.

5.6 Result

Using 294 $B^0 \to \eta' K_S$ decay candidates, we obtain CP asymmetry parameters to be

$$\begin{aligned} \mathcal{A}_{\eta' K_S} &= 0.30^{+0.20}_{-0.21}(\text{stat})^{+0.06}_{-0.04}(\text{syst}), \text{ and} \\ \mathcal{S}_{\eta' K_S} &= 0.61^{+0.31}_{-0.35}(\text{stat})^{+0.06}_{-0.07}(\text{syst}). \end{aligned} \tag{5.21}$$

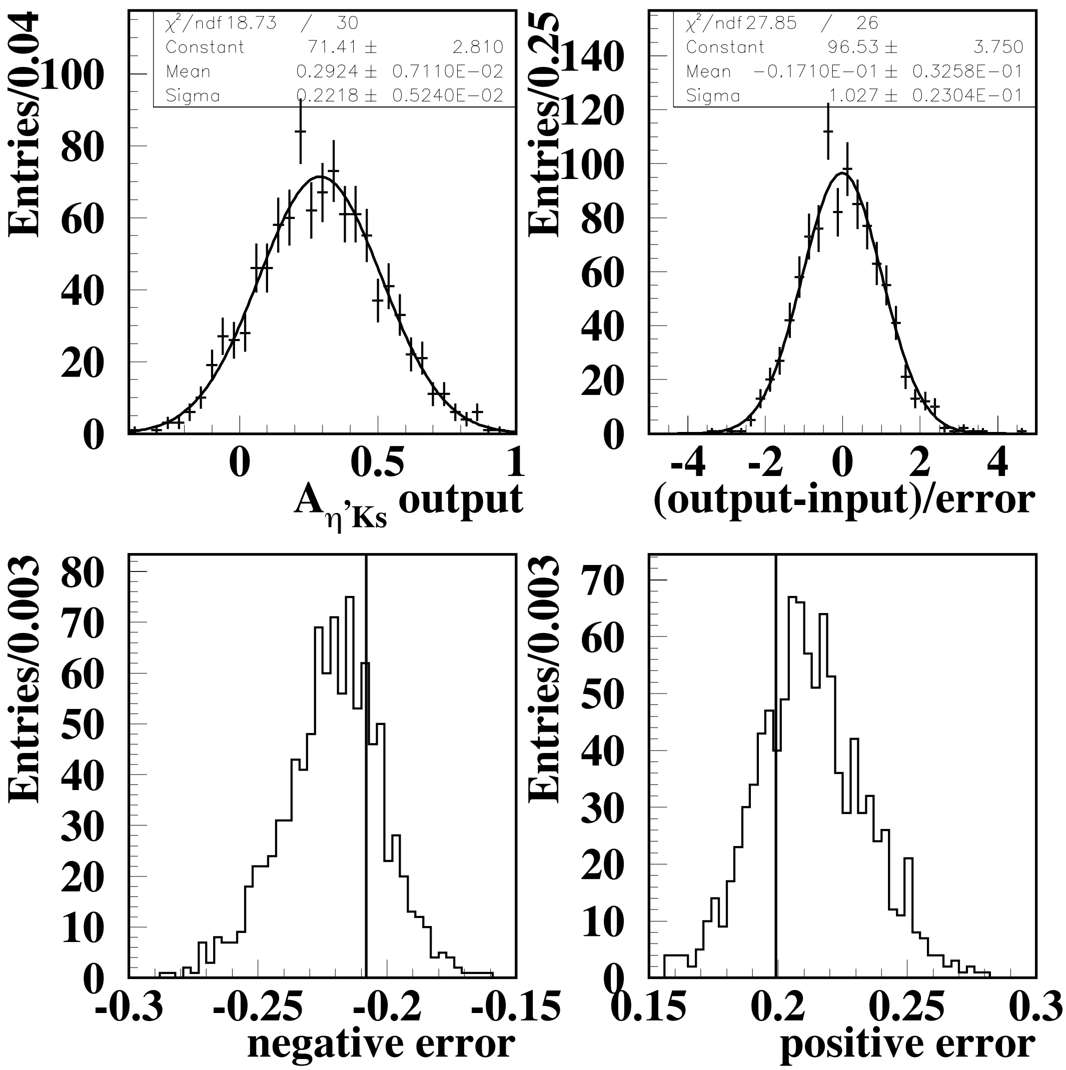

Figure 5.13: *Results of the ensemble test for* $\mathcal{A}_{\eta' K_S}$*. Each distribution shows* $\mathcal{A}_{\eta' K_S}$ *output of the fit (upper left), (output-input)/error (upper right), negative error (lower left) and positive error (lower right). Vertical lines show the errors obtained by the fit to the real data.*

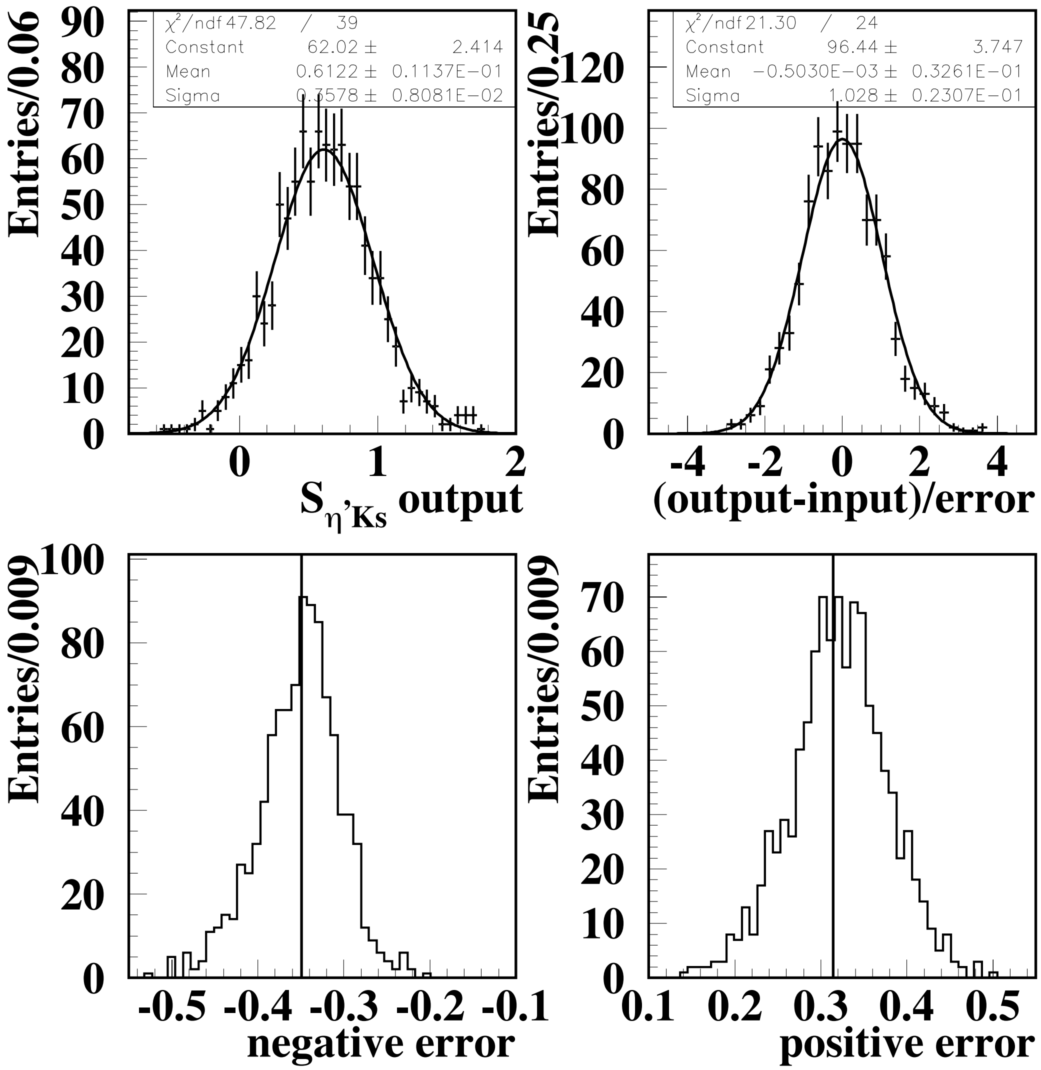

Figure 5.14: *Results of the ensemble test for $\mathcal{S}_{\eta' K_S}$. Each distribution shows $\mathcal{S}_{\eta' K_S}$ output of the fit (upper left), (output-input)/error (upper right), negative error (lower left) and positive error (lower right). Vertical lines show the errors obtained by the fit to the real data.*

Chapter 6

Discussion

6.1 Significance of the Measurement

Figure 6.1 shows the 68.27%, the 95.45% and the 99.73% confidence regions for the CP asymmetry parameters $\mathcal{A}_{\eta' K_S}$ and $\mathcal{S}_{\eta' K_S}$ based on the method proposed by Feldman and Cousins [66]. These confidence levels correspond to 1 sigma, 2 sigma and 3 sigma intervals of a one-dimensional Gaussian, respectively. In the calculation of the confidence level, we assume that the likelihood function is a two-dimensional Gaussian of symmetric errors of $\sigma_{\mathcal{A}_{\eta' K_S}} = 0.21$ and $\sigma_{\mathcal{S}_{\eta' K_S}} = 0.36$. As for the errors, we added statistical and systematic errors of our result in quadrature. To use the symmetric errors, we compare the absolute values of the positive and negative errors and take the larger value.

6.1.1 Comparison with the Standard Model

The SM expectation of CP asymmetry parameters are $\mathcal{A}_{\eta' K_S} = 0$ and $\mathcal{S}_{\eta' K_S} = \sin 2\phi_1$ when we neglect the small contribution from the $b \to u\overline{u}s$ transition. The open circle in Figure 6.1 shows the world average value of $\sin 2\phi_1$ obtained by $B^0 \to J/\psi K_S$ and other $c\overline{c}K^{(*)0}$ decays. Our measurement is consistent with the SM expectation at the 68% confidence level.

6.1.2 Model Independent Constraint on New Physics Beyond the Standard Model

Although our measurement shows no evidence for new physics, we can provide a constraint on new physics in a model-independent manner as we mentioned in Section 1.2.3. Our 95.45% confidence region in Figure 6.1 is about 1/4 of the physically-allowed region and exclude large negative values of CP asymmetry parameters. We extract a three dimensional allowed region for $|A_{NP}|/|A_{SM}|$, δ_{12} and ϕ_{NP} by using equations (1.32) and the confidence regions in Figure 6.1. We use $\sin 2\phi_1 = 0.734$ and neglect the error of $\sin 2\phi_1$ and the uncertainties of the SM expectation of CP asymmetry parameters that are estimated to be a few %. Figure 6.2 and 6.3 show the allowed regions in slices.

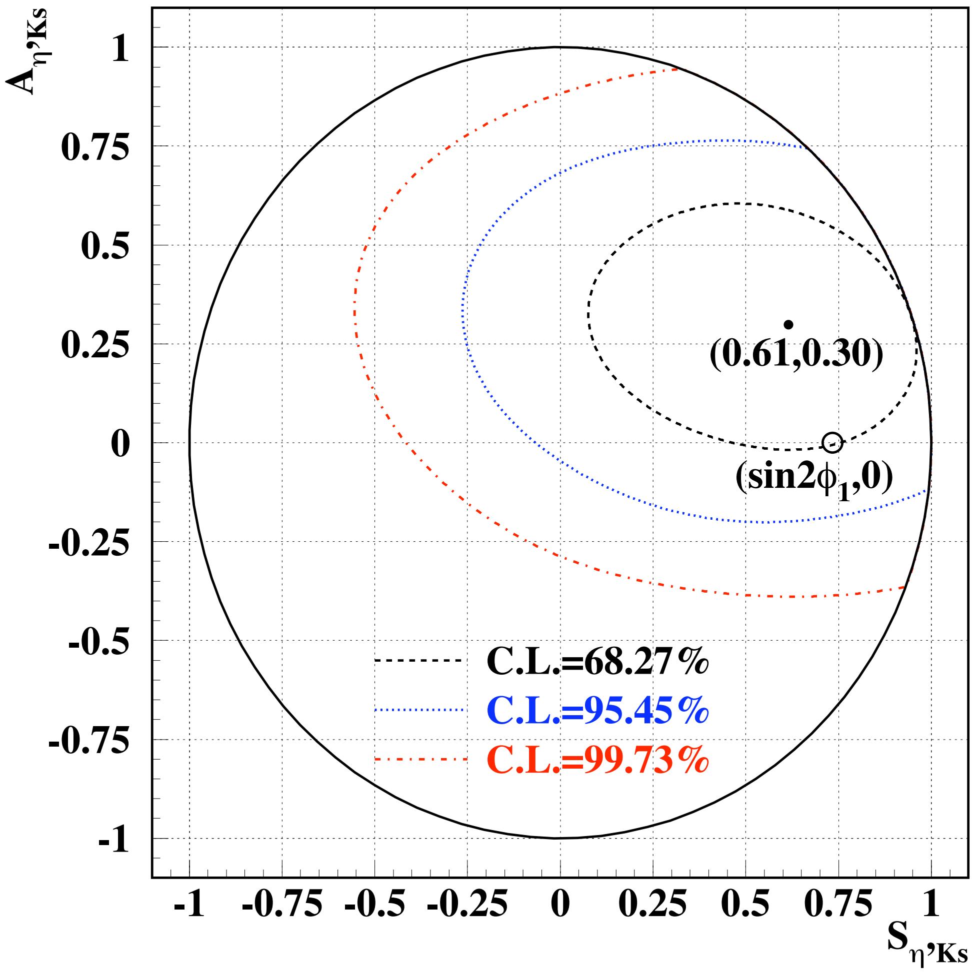

Figure 6.1: *Confidence regions at the level of 68.27%, 95.45%, and 99.73% for* $\mathcal{A}_{\eta' K_S}$ *and* $\mathcal{S}_{\eta' K_S}$. *A solid circle is the physical boundary* $\mathcal{A}^2_{\eta' K_S} + \mathcal{S}^2_{\eta' K_S} = 1$. *The open circle shows the SM expectation* $\mathcal{A}_{\eta' K_S} = 0$ *and* $\mathcal{S}_{\eta' K_S} = \sin 2\phi_1$ *where* $\sin 2\phi_1$ *is the world average obtained from* $B^0 \to c\bar{c}K^{(*)0}$ *decays.*

This is the first measurement of CP violating phases in the $b \to sq\overline{q}$ transition that provides model independent constraints on physics beyond the SM with negligibly small hadronic uncertainties.

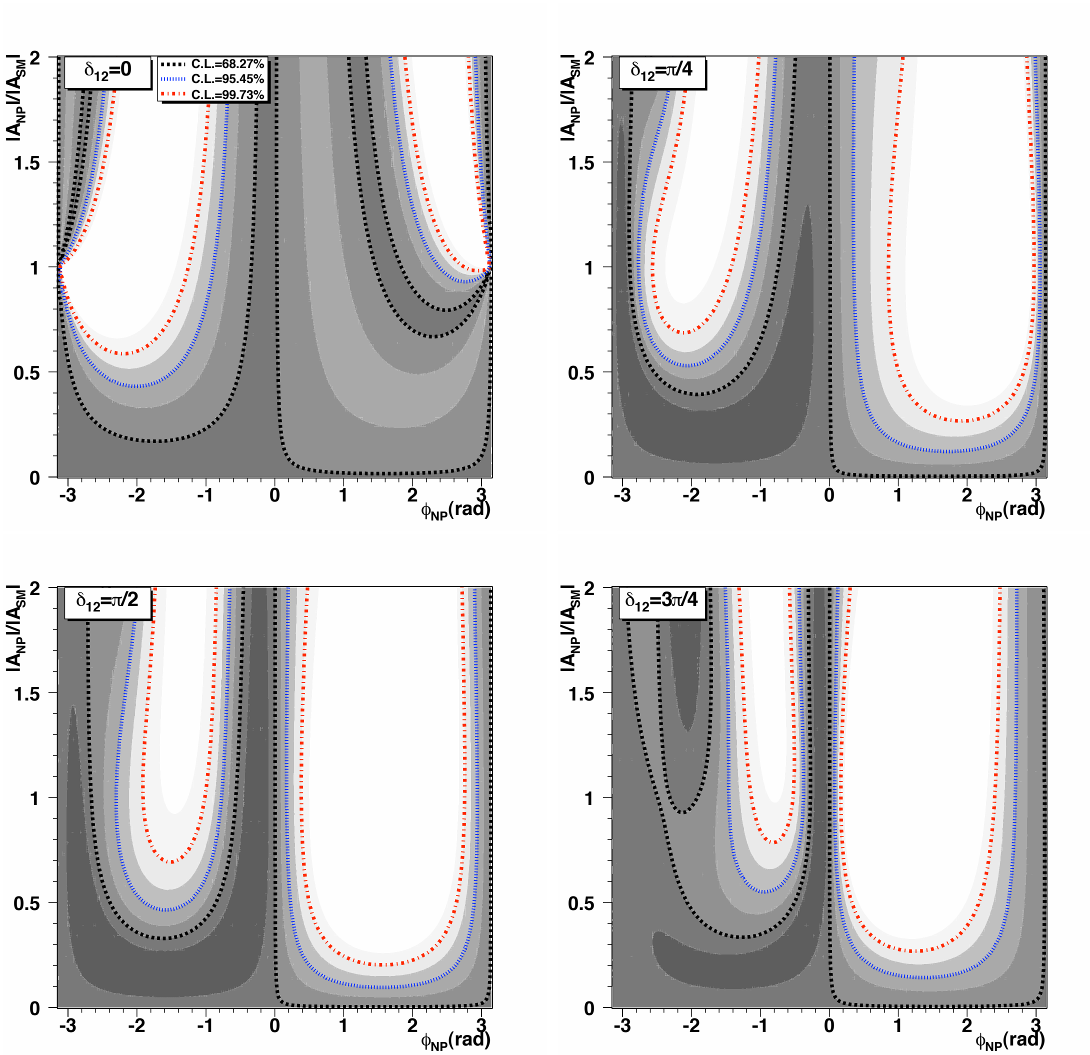

Figure 6.2: *The confidence level contour plot on the* $|A_{NP}|/|A_{SM}|$*-*ϕ_{NP} *plane for* $\delta_{12} = 0, \pi/4, \pi/2$ *and* $3\pi/4$*. The confidence level decreases from dark region to light region. The dashed, dotted, and dot-dashed lines show 68.27%, 95.45% and 99.73% confidence level boundaries, respectively.*

6.1.3 Constraint on SUSY Models

Recently, Khalil and Kou calculated the decay amplitude of a general SUSY model for the squark mass and gluino mass of 500 GeV/c^2 [67]. They give the amplitude ratio between

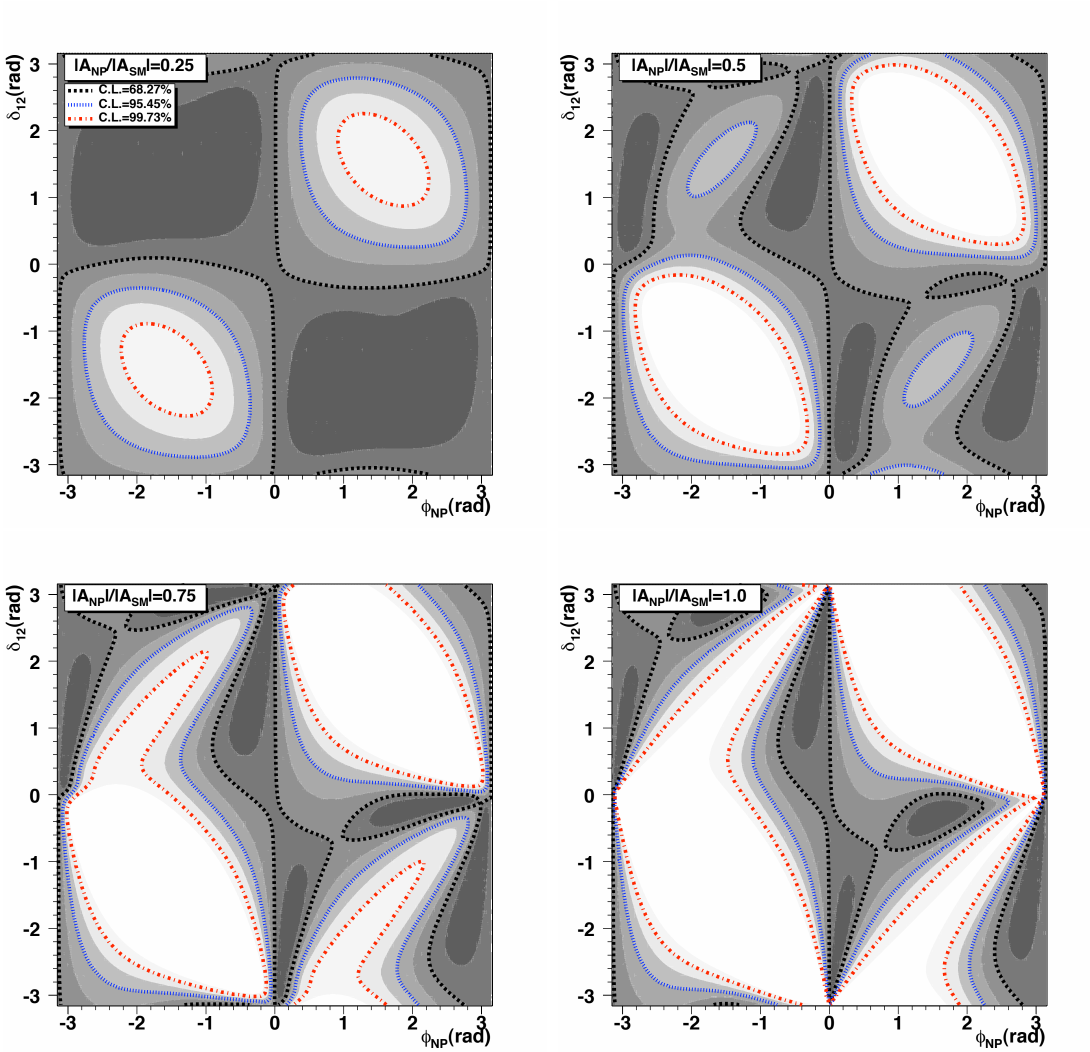

Figure 6.3: *The confidence level contour plot on the* δ_{NP}-ϕ_{NP} *plane for* $|A_{NP}|/|A_{SM}|$*=0.25, 0.5, 0.75 and 1.0. The confidence level decreases from dark region to light region. The dashed, dotted, and dot-dashed lines show 68.27%, 95.45% and 99.73% confidence level boundaries, respectively.*

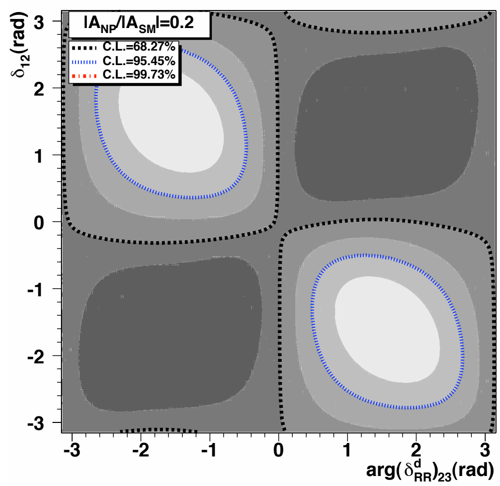

Figure 6.4: *The confidence level contour plot on the* δ_{12}-$\arg(\delta^d_{RR})_{23}$ *plane for* $|(\delta^d_{RR})_{23}| \simeq 1$ *that corresponds to* $|A_{NP}|/|A_{SM}| \sim 0.2$. *The confidence level decreases from dark region to light region. The dashed and dotted lines show 68.27%, 95.45% confidence level boundaries, respectively.*

the SUSY and the SM as

$$\frac{A_{SUSY}}{A_{SM}} \simeq 0.23(\delta^d_{LL})_{23} + 101(\delta^d_{LR})_{23} - 101(\delta^d_{RL})_{23} - 0.23(\delta^d_{RR})_{23}, \tag{6.1}$$

where CP-violating phases in the $\tilde{b} \to \tilde{s}$ transition are introduced by the mass insertion $(\delta^d_{LL})_{23}$, $(\delta^d_{LR})_{23}$, $(\delta^d_{RL})_{23}$ and $(\delta^d_{RR})_{23}$. In some specific SUSY models, the flavor structure of the model determines the relative size of the CP-violating phases. For instance, in SUSY GUT with right-handed neutrinos [38, 39] and SUSY with abelian horizontal symmetry [35, 36], $(\delta^d_{RR})_{23}$ is dominant. For $|(\delta^d_{RR})_{23}| \simeq 1$, the constraint on $\arg(\delta^d_{RR})_{23}$ is obtained from the constraint on our ϕ_{NP} for $|A_{NP}|/|A_{SM}| \sim 0.2$ and is shown in Figure 6.4.

Although the $(\delta^d_{LR})_{23}$ and $(\delta^d_{RL})_{23}$ are constrained to be $\mathcal{O}(10^{-2})$ by the $B \to X_s\gamma$ branching fraction measurement [33, 34], $(\delta^d_{RL})_{23}$ and $(\delta^d_{LR})_{23}$ are enhanced by the ratio of the gluino mass to the b quark mass and they can make considerable contribution to the amplitude. In case $(\delta^d_{LR})_{23}$ ($(\delta^d_{RL})_{23}$) is dominant, our ϕ_{NP} corresponds to $\arg(\delta^d_{LR})_{23}$ ($\arg(\delta^d_{RL})_{23} + \pi$).

6.2 Future Prospect

The uncertainty of our measurement is dominated by statistical errors, and thus it will be reduced with more data. The Belle experiment plans to accumulate more than 300 fb^{-1} integrated luminosity, which is about 4 times as large sample as now, in a coming few years. Furthermore, the Super KEKB [68] upgrade is being planned to accumulate 10000 fb^{-1} of data. Concerning the systematic errors, the main contribution comes from background fractions, the vertex reconstruction algorithm and wrong tag probabilities. Since the uncertainties of background fractions and wrong tag probabilities depend on statistics of control samples, they will decrease with more data. The systematic error due to the vertex reconstruction algorithm is dominated by the variation of the ξ requirement, which changes the number of candidates and causes the statistical fluctuation. The size of the current systematic error due to the variation of the ξ requirement is consistent with the statistical fluctuation and will be reduced with more data. Figure 6.5 shows expected errors as a function of the integrated luminosity.

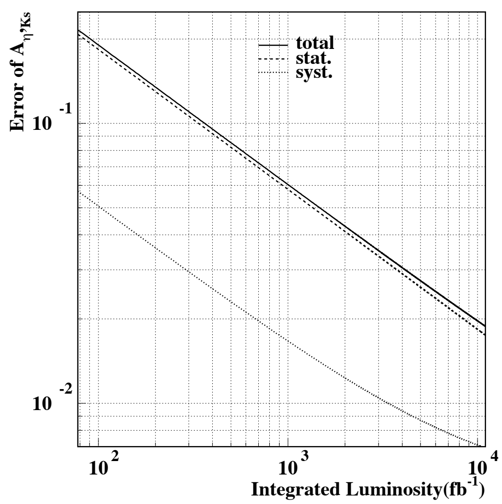

Figure 6.5: *Expected errors of CP asymmetry parameters in $B^0 \to \eta' K_S$ decays as a function of the integrated luminosity. Dashed and dotted lines are statistical and systematic error, respectively. The solid line shows the quadratic sum of statistical and systematic.*

At an integrated luminosity of 300 fb^{-1}, the errors of $\mathcal{A}_{\eta' K_S}$ and $\mathcal{S}_{\eta' K_S}$ become 0.11 and 0.18, respectively. Figure 6.6 shows the 68.27%, the 95.45% and the 99.73% confidence level regions for the SM expectation of CP asymmetry parameters assuming $\sin 2\phi_1 = 0.734$. Figure 6.7 and 6.8 show the sensitive regions in ϕ_{NP}, δ_{12} and $|A_{NP}|/|A_{SM}|$ space. The measurement at 300 fb^{-1} covers 83% of the full physical region of $\mathcal{A}_{\eta' K_S}$-$\mathcal{S}_{\eta' K_S}$ plane at the 99.73% confidence level. At 10000 fb^{-1} integrated luminosity, errors of $\mathcal{A}_{\eta' K_S}$ and $\mathcal{S}_{\eta' K_S}$ will be 0.02 and 0.03, respectively. The 68.27%, the 95.45% and the 99.73% confidence level regions for the SM expectation of CP asymmetry parameters assuming $\sin 2\phi_1 = 0.734$ is shown in Figure 6.9. Figure 6.10 and 6.11 show the sensitive regions in ϕ_{NP}, δ_{12} and $|A_{NP}|/|A_{SM}|$ space. More than 99% of the full physical region of the $\mathcal{A}_{\eta' K_S}$-$\mathcal{S}_{\eta' K_S}$ plane will be explored at the 99.73% confidence level with 10000 fb^{-1} data.

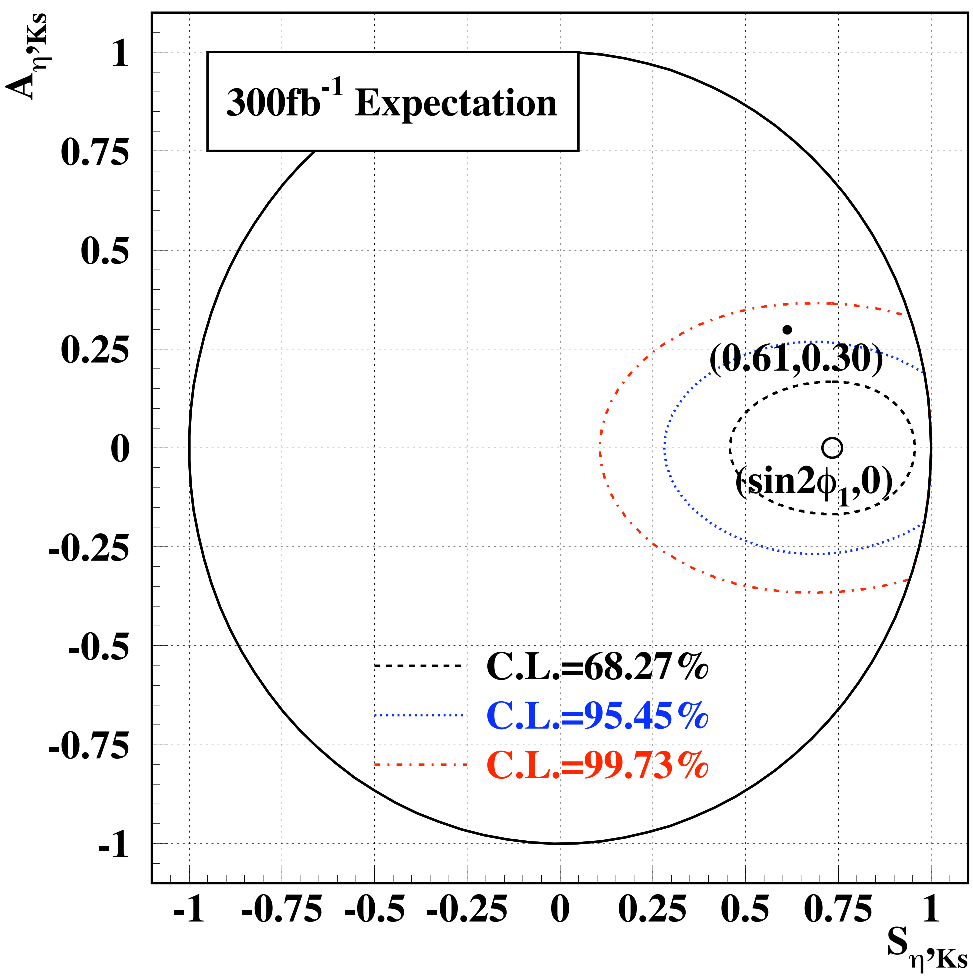

Figure 6.6: *The expected 68.27%, 95.45% and 99.73% confidence level allowed regions for the SM expectation of CP asymmetry parameters at 300* fb^{-1} *integrated luminosity assuming* $\sin 2\phi_1 = 0.734$.

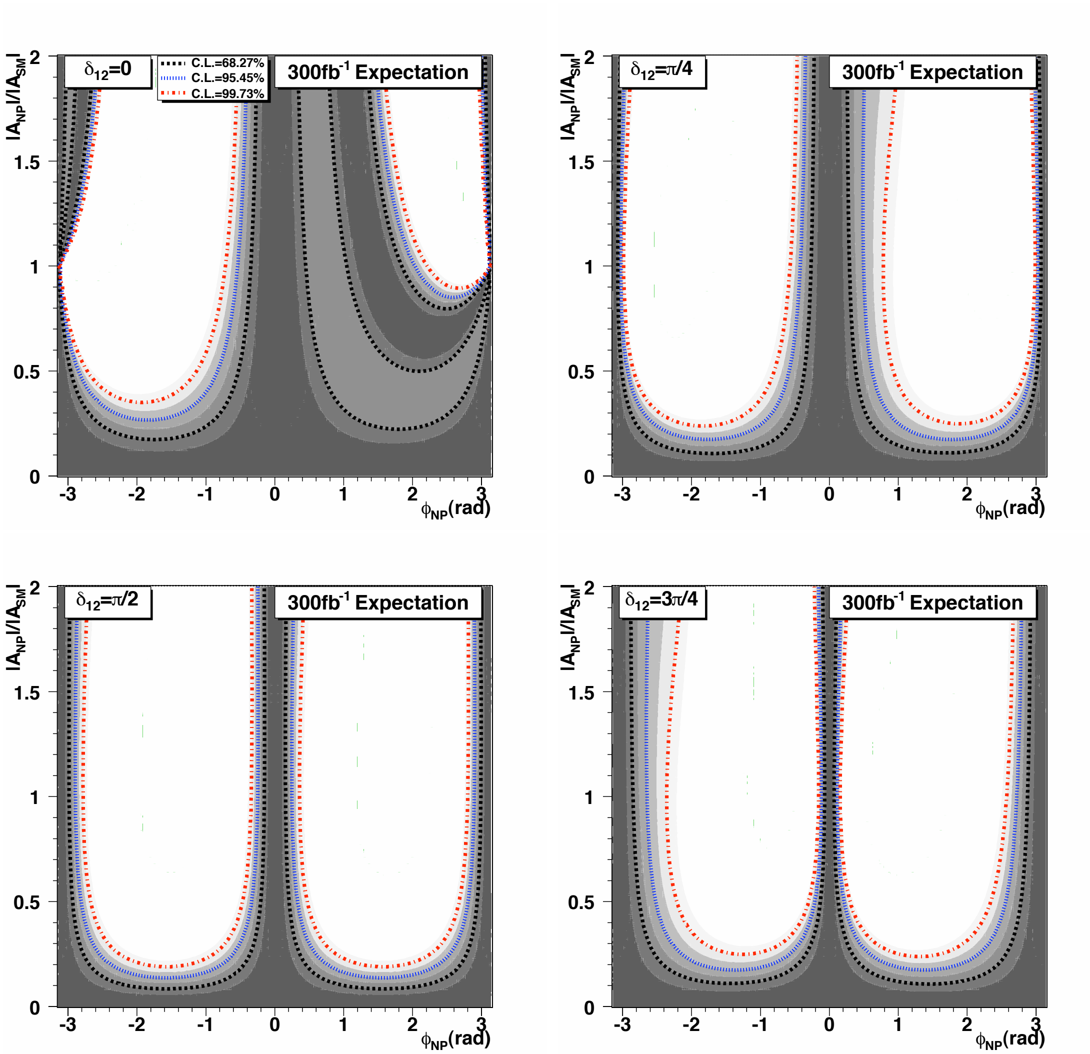

Figure 6.7: *The 300* fb^{-1} *expected confidence level contour plot on the* $|A_{NP}|/|A_{SM}|$-ϕ_{NP} *plane for* $\delta_{12} = 0, \pi/4, \pi/2$ *and* $3\pi/4$ *assuming the SM* CP *asymmetry parameters. The confidence level decreases from dark region to light region. The dashed, dotted, and dot-dashed lines show 68.27%, 95.45% and 99.73% confidence level boundaries, respectively. New physics out of these regions can be detected at the corresponding confidence level.*

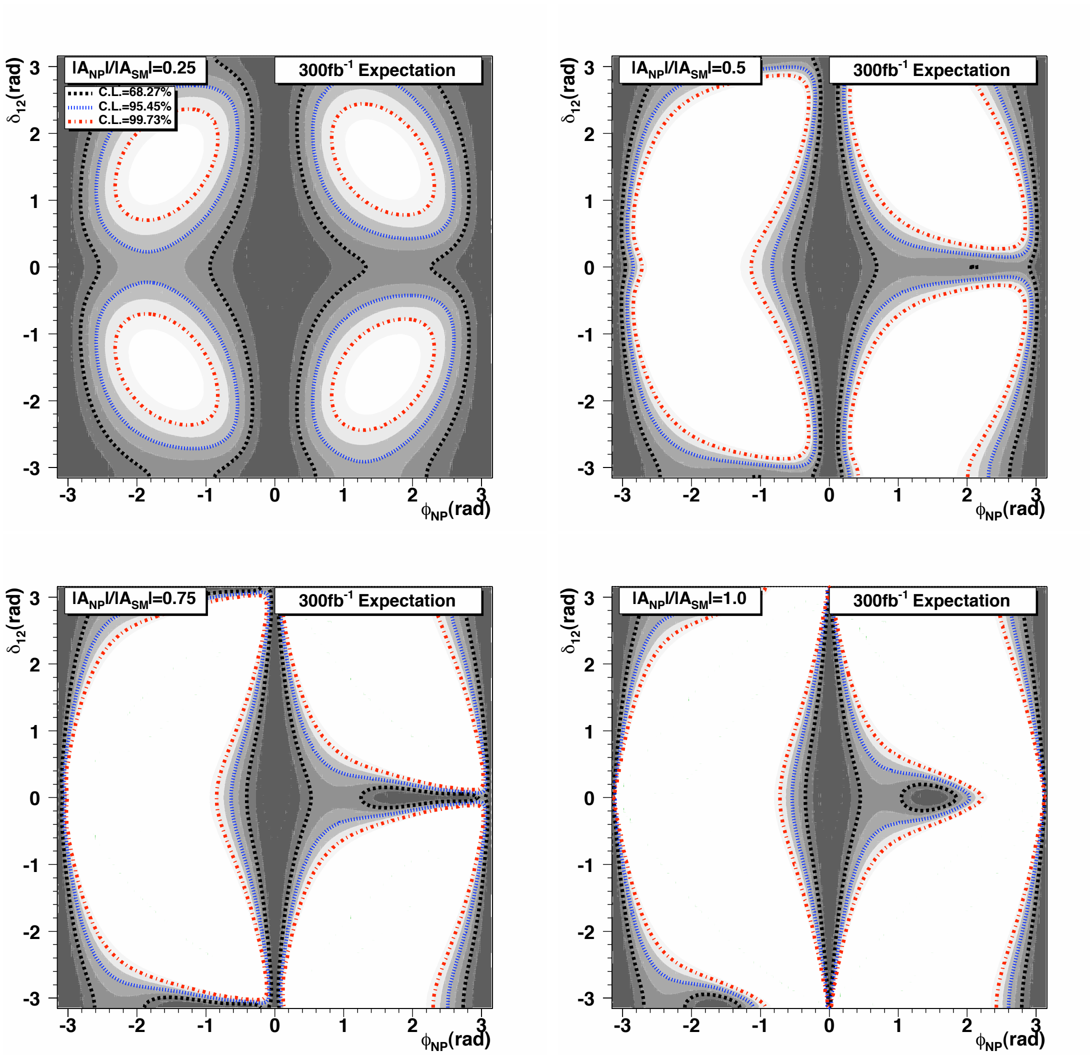

Figure 6.8: *The 300* fb^{-1} *expected confidence level contour plot on the* δ_{NP}-ϕ_{NP} *plane for* $|A_{NP}|/|A_{SM}|$*=0.25, 0.5, 0.75 and 1.0 assuming the SM* CP *asymmetry parameters. The confidence level decreases from dark region to light region. The dashed, dotted, and dot-dashed lines show 68.27%, 95.45% and 99.73% confidence level boundaries, respectively. New physics out of these regions can be detected at the corresponding confidence level.*

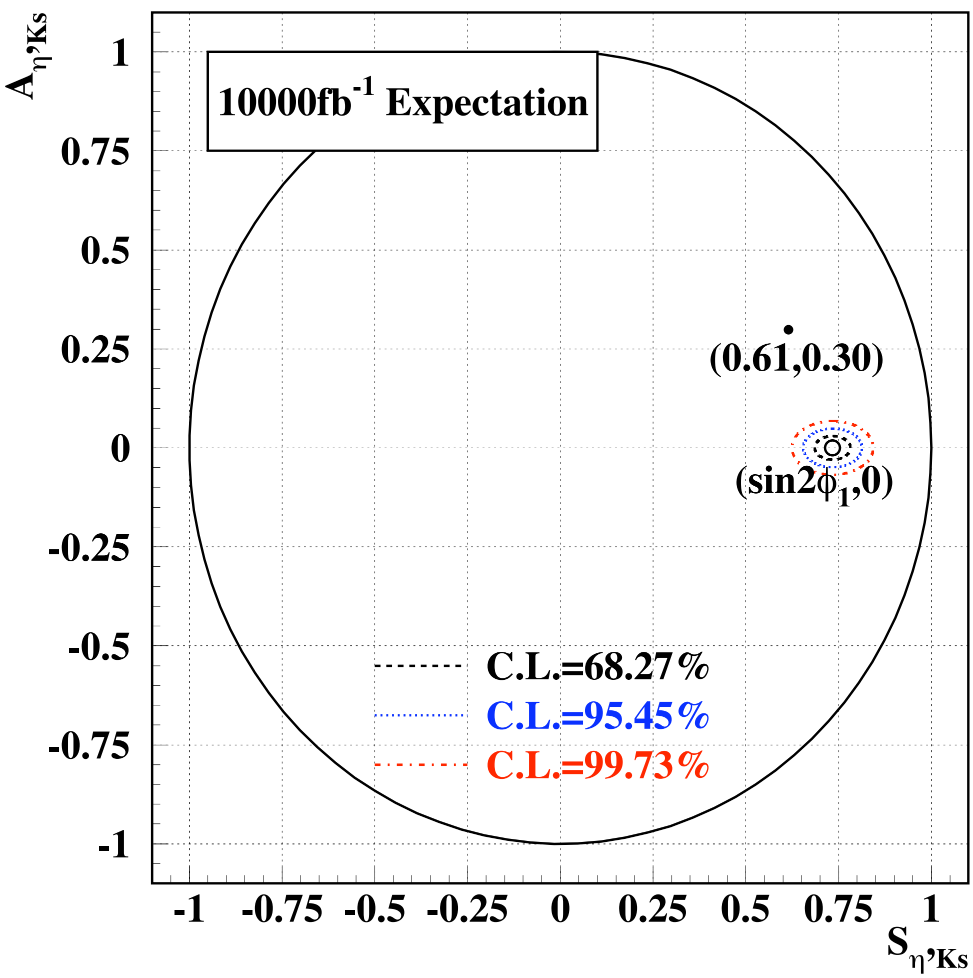

Figure 6.9: *The expected 68.27%, 95.45% and 99.73% confidence level allowed regions for the SM expectation of CP asymmetry parameters at 10000* fb^{-1} *integrated luminosity assuming* $\sin 2\phi_1 = 0.734$.

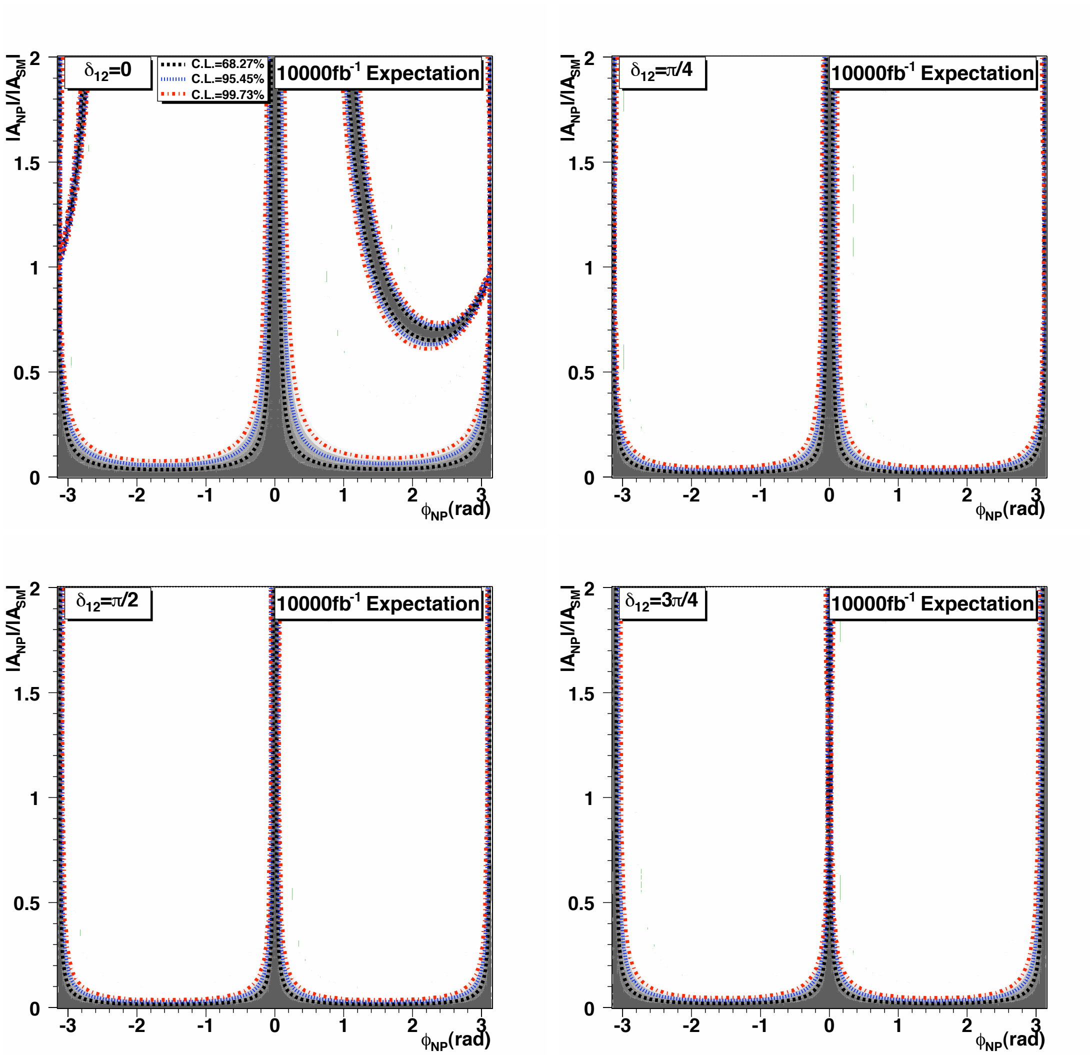

Figure 6.10: *The 10000* fb^{-1} *expected confidence level contour plot on the* $|A_{NP}|/|A_{SM}|$-ϕ_{NP} *plane for* $\delta_{12} = 0, \pi/4, \pi/2$ *and* $3\pi/4$ *assuming the SM* CP *asymmetry parameters. The confidence level decreases from dark region to light region. The dashed, dotted, and dot-dashed lines show 68.27%, 95.45% and 99.73% confidence level boundaries, respectively. New physics out of these regions can be detected at the corresponding confidence level.*

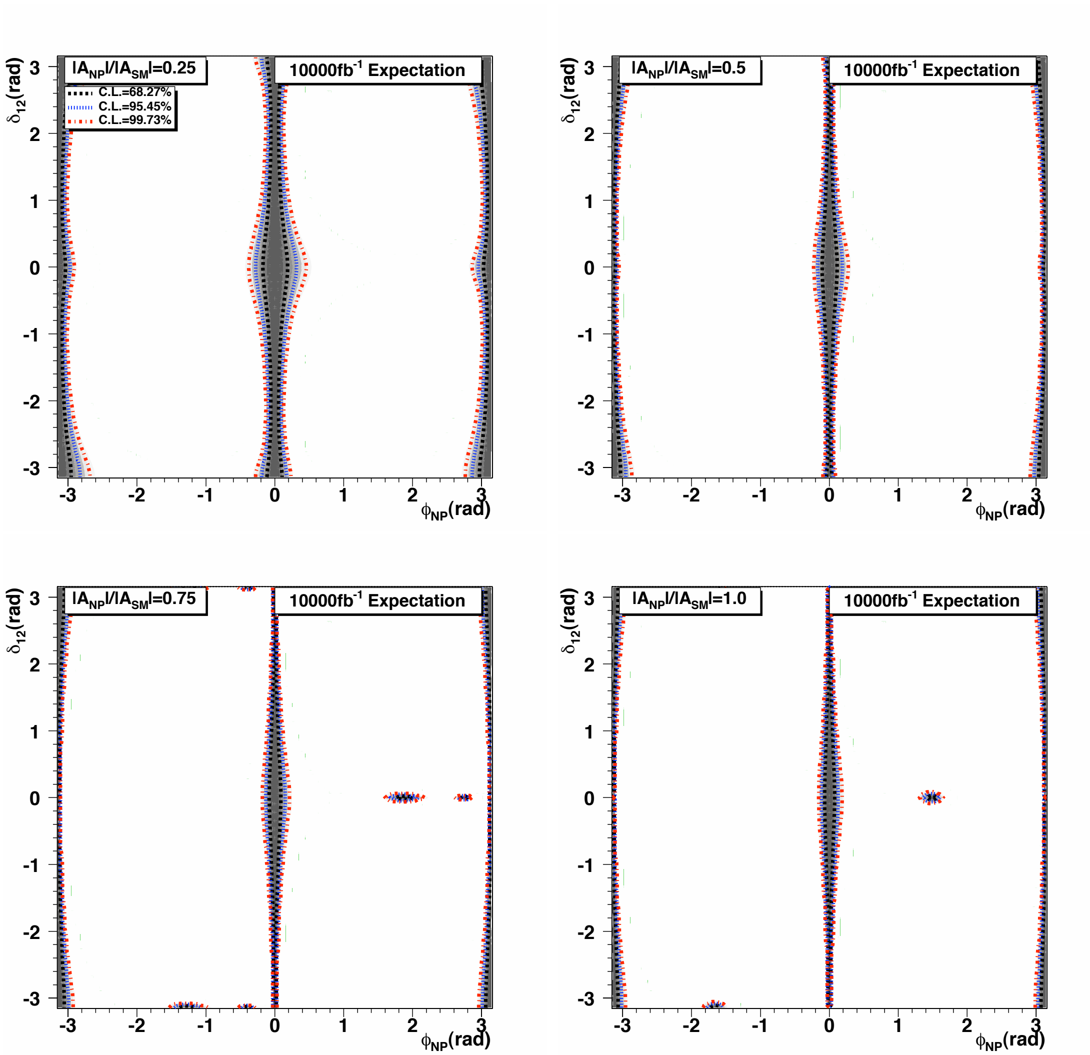

Figure 6.11: *The 10000* fb^{-1} *expected confidence level contour plot on the* δ_{NP}-ϕ_{NP} *plane for* $|A_{NP}|/|A_{SM}|$*=0.25, 0.5, 0.75 and 1.0 assuming the SM* CP *asymmetry parameters. The confidence level decreases from dark region to light region. The dashed, dotted, and dot-dashed lines show 68.27%, 95.45% and 99.73% confidence level boundaries, respectively. New physics out of these regions can be detected at the corresponding confidence level.*

Chapter 7

Conclusion

We have measured time-dependent CP asymmetry parameters in $B^0 \to \eta' K_S$ decays. Since the $B^0 \to \eta' K_S$ decays are caused by the $b \to sq\overline{q}$ hadronic penguin process, it is sensitive to new physics beyond the Standard Model. In the Standard Model, this CP asymmetry is equal to a parameter of the Cabibbo-Kobayashi-Maskawa matrix, $\sin 2\phi_1$, with a small theoretical uncertainty. The $\sin 2\phi_1$ has already been measured with the $B^0 \to J/\psi K_S$ and other $c\overline{c}K^{(*)0}$ decays with an uncertainty less than 10%. Therefore, by measuring the CP asymmetry parameters in $B^0 \to \eta' K_S$ decays, and by comparing it with $\sin 2\phi_1$, we can test the Standard Model strictly and can search for an existence of physics beyond the Standard Model.

We use a data sample of 78 fb^{-1} recorded on the $\Upsilon(4S)$ resonance that contains 85×10^6 B meson pairs collected with the Belle detector at the KEKB asymmetric e^+e^- collider. From 294 candidate $B^0 \to \eta' K_S$ events, we extract the CP asymmetry parameters $\mathcal{A}_{\eta' K_S}$ and $\mathcal{S}_{\eta' K_S}$ with an unbinned maximum likelihood fit.We obtain:

$$\begin{aligned}\mathcal{A}_{\eta' K_S} &= 0.30^{+0.20}_{-0.21}(\mathrm{stat})^{+0.06}_{-0.04}(\mathrm{syst}),\\ \mathcal{S}_{\eta' K_S} &= 0.61^{+0.31}_{-0.35}(\mathrm{stat})^{+0.06}_{-0.07}(\mathrm{syst}).\end{aligned}$$

This is an improved measurement from the previous Belle result and is the only measurement of CP asymmetry parameters in the $b \to sq\overline{q}$ hadronic penguin process. The result is consistent with the Standard Model expectation at the 68% confidence level. We set model-independent constraints on the CP phases and the size of the new physics decay amplitude. This is the first measurement of CP-violating phases in the $b \to sq\overline{q}$ transition that provides model independent constraints on new physics beyond the Standard Model with negligibly small theoretical uncertainties.

The uncertainties of our result are dominated by statistical errors. Therefore, high statistics measurements using the $B^0 \to \eta' K_S$ decays in the near future at the Belle experiment will be very important to search for new physics beyond the Standard Model.

Appendix A

Flavor Tagging Method

The flavor of B_{tag} is determined by correlation with flavor of B_{tag} and charged particles remaining in the event after reconstructing B_{CP} candidate. We apply the same method used for the Belle $\sin 2\phi_1$ measurement [10]. We explain the method in this Appendix.

A.1 Flavor Tagging Algorithm

We use following particles that have a charge correlated with the b flavor:

- high-momentum leptons from $B^0 \to X\ell^+\nu$,
- kaons from the $\overline{b} \to \overline{c} \to \overline{s}$ cascade decay,
- intermediate momentum leptons coming from $\overline{b} \to \overline{c} \to \overline{s}\ell^-\overline{\nu}$,
- high momentum pions from $B^0 \to D^{(*)}\pi^+ X$ decay,
- slow pions from $B^0 \to D^{*-}X, D^{*-} \to \overline{D}^0\pi^-$ decay, and
- Λ baryons from the cascade decay $\overline{b} \to \overline{c} \to \overline{s}$.

To maximize the effective tagging efficiency, we need to know the properties of these particles and take into account correlation between them. We use a large statistics Monte Carlo (MC) sample to evaluate the properties of the particles and correlations. We use GEANT3 [60] to fully simulate the detector. Either of two event generators, QQ [56] or EvtGen [57] is used to simulate the tag-side B-meson decays. We use QQ-generated MC for early measurement of $\sin 2\phi_1$ [8] and EvtGen-generated MC for latter $\sin 2\phi_1$ measurement [10] and the CP asymmetry parameter measurement in $B^0 \to \eta' K_S$ decays. The correlations and variables representing the particle property are expressed by look-up tables. We assign each cell of look-up tables a flavor q and flavor tagging quality r. The flavor q takes a 1 or -1 and indicates that the flavor is B^0 (q=1) or $\overline{B}^0$ (q=-1). The flavor tagging quality r ranges from 0 for no flavor discrimination to $r = 1$ for unambiguous flavor assignment. The q and r are calculated by

$$q \cdot r \equiv \frac{N(B^0) - N(\overline{B}^0)}{N(B^0) + N(\overline{B}^0)}, \tag{A.1}$$

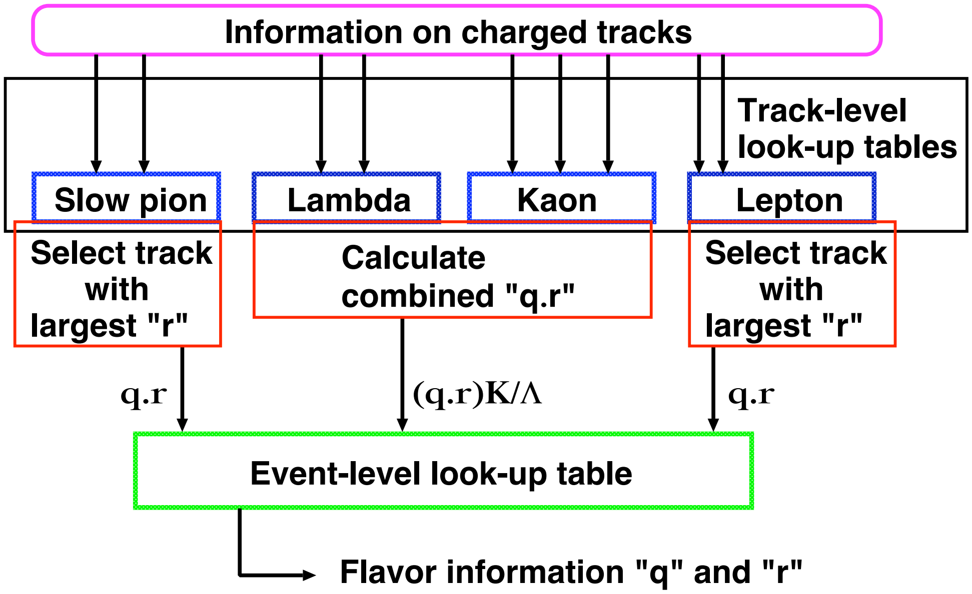

Figure A.1: A schematic diagram of the two-stage flavor tagging.

where $N(B^0)$ and $N(\overline{B}^0)$ are the numbers of B^0 and $\overline{B}^0$ in the cell determined by Monte Carlo sample.

Since the number of particles in an event is not limited, it is practically difficult to consider all the correlations at once. The flavor tagging procedure is, therefore, divided in two stages: the track stage and the event stage. Figure A.1 shows the schematic diagram of the flavor tagging. At first, each charged track is classified into four categories depending on the particle species: lepton class; kaons class; Λ baryon and slow pions, and each track is then assigned $q \cdot r$ by a look-up table of specific variables in each category. An event level look-up table is made of output of each track class and the final flavor information is determined. In the following, we explain each stage.

A.2 Track Level Flavor Tagging

Reconstructed tracks that do not belong to B_{CP} are examined and passed to one of track classes. We use only well-reconstructed tracks satisfying $|dr| < 2$ cm and $|dz| < 10$ cm, where dr and dz are distances from the nominal interaction point in r-ϕ plane and z direction, respectively. We do not use a track if it forms photon conversion candidate with any opposite charged track. If tracks form K_S and Λ candidates, the tracks are not also used, but the Λ candidates themselves are assigned into the Λ category and the existence of K_S is used as one of discriminant.

A.2.1 Lepton Track Class

The lepton track class consists of electron-like track class and muon-like track class. If the momentum in the center of mass system (cms), p^*, of a track is larger than 0.4 GeV/c and the ratio of its electron and kaon likelihoods is larger than 0.8, the track is assigned to the electron-like track class. If a track has p^* larger than 0.8 GeV/c and the ratio of its muon and kaon likelihoods is larger than 0.95, it is passed to the muon-like track class. The likelihoods is calculated by combining the ACC, TOF, dE/dx in CDC, and ECL or KLM information.

In the lepton track class, leptons from semileptonic B decays yield the largest effective efficiency. Leptons from semileptonic decays of D mesons which originate from $B \to D$ cascade decays and high momentum pions from $B^0 \to D^{(*)-}\pi^+X$ also make a small contribution to this class. A look-up table of following six variables are prepared to determine $q \cdot r$ for each track:

- magnitude of the momentum in cms (p^*);
- recoil mass M_{recoil}, which is an invariant mass of the tagging side tracks except for the lepton track;
- magnitude of the missing momentum in cms, p^*_{miss};
- polar angle in the laboratory frame (θ_{lab});
- lepton identification likelihood value,L_{lep};
- charge of the lepton track.

The p^*, M_{recoil} and p^*_{miss} are used to discriminate between the leptons from primary B decays and from secondary D decays. The p^*, θ_{lab} and L_{lep} are used to take into account the momentum and the angular dependence of lepton identification performance. Figure A.2 shows the p^*, M_{recoil} and p^*_{miss} distributions for the MC and the data of control samples:$B^0 \to D^{*-}\ell^+\nu$, $D^{*-}\pi^+$, $D^-\pi^+$ and $D^{*-}\rho^+$ decays and their charge conjugates. Although the agreement between the data and the MC is not so good, an experimental bias due to this disagreement is found to be negligible since we evaluate wrong tagging probability from the control samples as is described in Appendix C. These discriminant variables are divided into bins: 11 for p^*; 10 for M_{recoil}; 6 for p^*_{miss}; 6 for θ_{lab}; 4 for L_{lep} and 2 for track charge, and form a look-up table of 31680 bins in total.

Among lepton tracks, one lepton track with the highest r is selected, and the $q \cdot r$ value of the track is passed to the event level flavor tagging.

A.2.2 Slow Pion Track Class

If p^* of a track is less than 0.25 GeV/c and it is not identified as a kaon, the track is assigned to the slow-pion track class.

This class is intended to utilize the charge of low momentum pions from $D^{*\pm}$. Due to the low momentum which is 39 MeV/c in the $D^{*\pm}$ rest frame, the direction of the slow

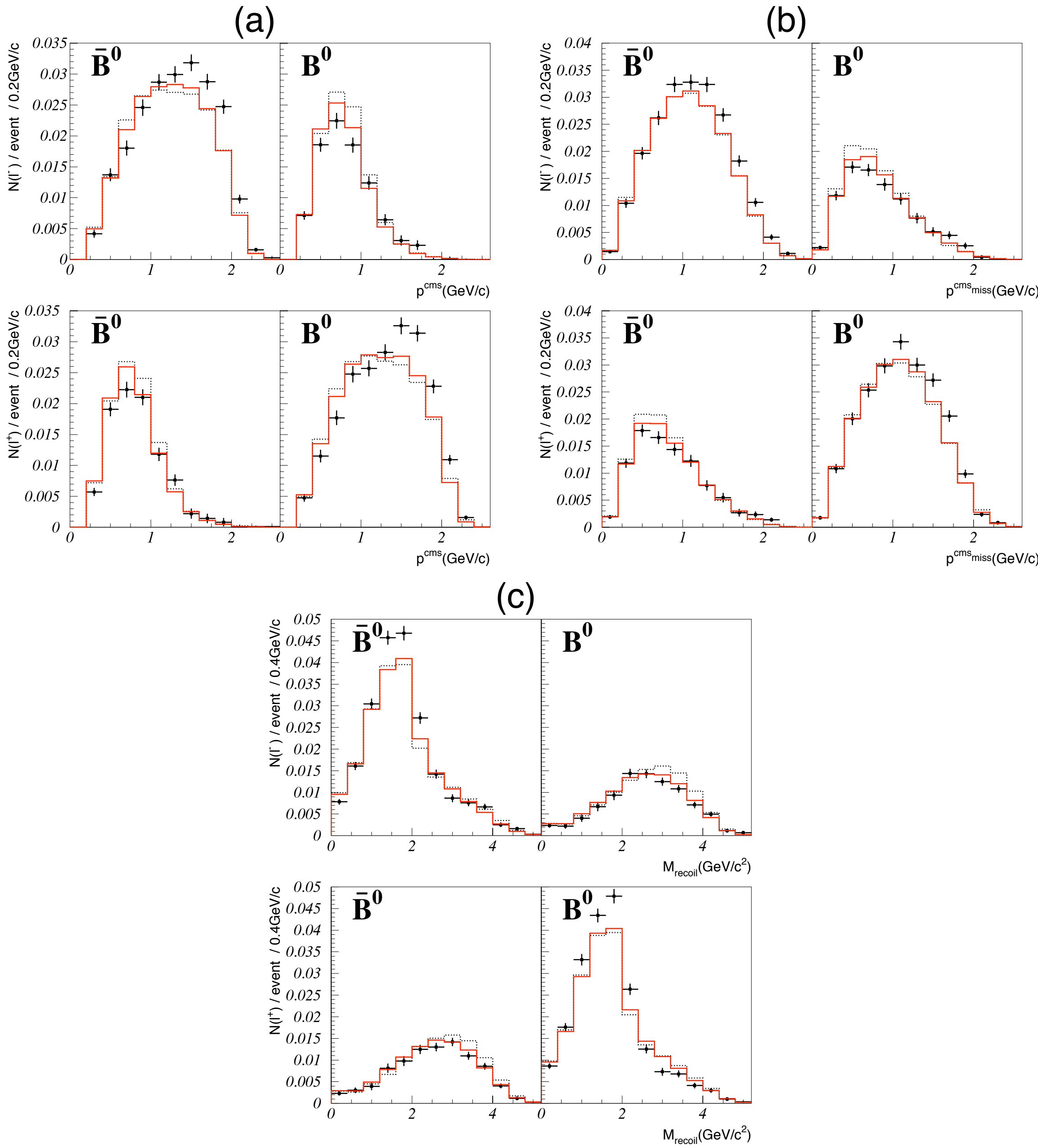

Figure A.2: *Distributions of (a) p^*, (b) p^*_{miss} and (c) M_{recoil} for $\overline{B}^0$ and B^0. The points are for the data of control samples:$B^0 \to D^{*-}\ell^+\nu$, $D^{*-}\pi^+$, $D^-\pi^+$ and $D^{*-}\rho^+$ decays and their charge conjugates. while the histograms with solid line and dotted line are for the EvtGen-MC and QQ-MC, respectively. All distributions are made with a requirement on lepton ID to exclude the dominating pion component. Upper two figures and lower two figures in each of (a), (b) or (c) are for ℓ^--like tracks and for ℓ^+-like tracks, respectively. Upper left and lower right figures in each (a), (b) or (c) contain primary leptons from B decay, while upper right and lower left figures in each (a), (b) or (c) contain secondary leptons from D decay.*

pions follow the direction of $D^{*\pm}$. The direction of $D^{*\pm}$ is approximated by the thrust axis of tagging side tracks, and the angle between the pion and the thrust axis can be used to discriminate the slow pion. The main background in this class comes from low momentum pions from other decays and electrons from photon conversions or π^0 Dalitz decays. The electrons can be separated by dE/dx measured with CDC. The discriminant variables in this class are summarized as:

- magnitude of the momentum in the laboratory flame (p_{lab});
- polar angle in the laboratory frame (θ_{lab});
- cosine of the angle between the slow pion candidate and the thrust axis of the tagging side particles in cms. ($\cos\alpha_{thr}$);
- pion likelihood value by dE/dx ($L_{dE/dx}$);
- charge of the track,

where p_{lab} is used instead of p^* because e/π separation of dE/dx strongly depend on the momentum in the laboratory frame. The p^* is then determined uniquely by θ_{lab} and p_{lab}. Figure A.3 shows the distribution of $\cos\alpha_{thr}$ and the momenta of the slow pion candidates in the laboratory frame. The number of bins for each variable in the look-up table is 10 for p_{lab}, 10 for θ_{lab}, 7 for $\cos\alpha_{thr}$, 5 for $L_{dE/dx}$ and 2 for charge of the track (7000 bins in total).

Among tracks of this class, one pion track with the highest r is selected, and the $q \cdot r$ value of the track is passed to the event level flavor tagging.

A.2.3 Kaon and Λ Track Class

This track class is intended to utilize the information of strangeness from $b \to c \to s$ cascade decays.

If a track is not fall into any of lepton and slow pion class and is not identified as a proton, it is classified as a kaon. Discriminant variables are:

- kaon likelihood value (L_K);
- momentum in cms (p^*);
- polar angle in the laboratory frame (θ_{lab});
- existence of K_S candidates;
- charge of the track.

The L_K is used to discriminate kaons from pions and determined by combined information of ACC, TOF and dE/dx measured with CDC. The p^* and θ_{lab} are used to take into account the momentum and polar angle dependence of the kaon identification performance. If there are K_S candidates, correlation of the kaon charge and the flavor of B is diluted.

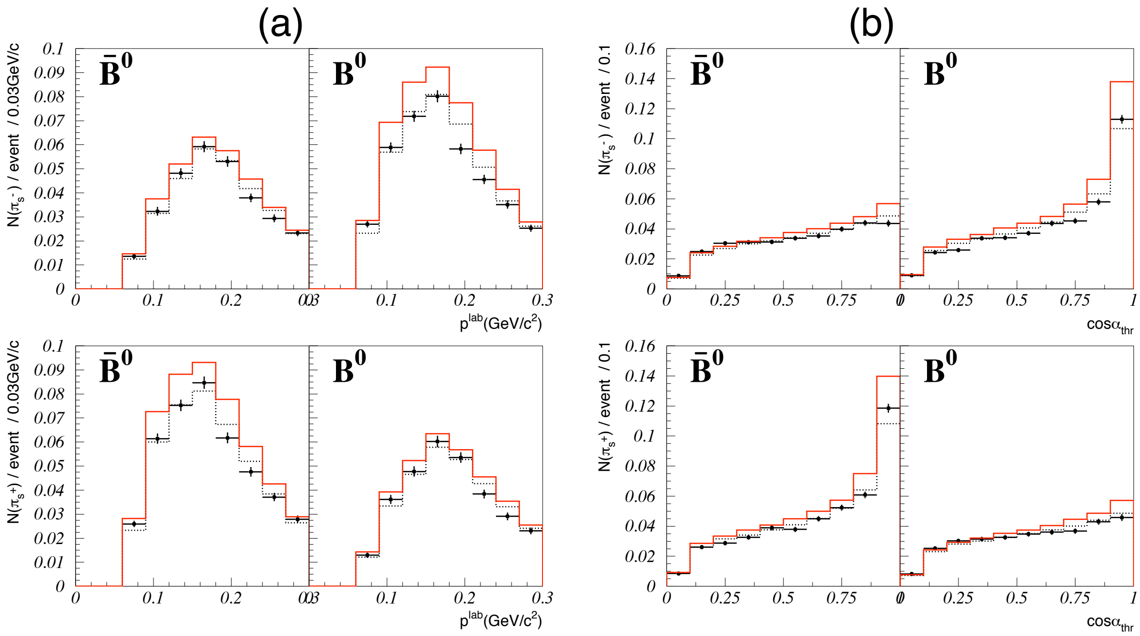

Figure A.3: *Distributions of (a) the lab. momentum and (b)* $\cos\alpha_{thr}$ *of slow pion for* $\overline{B}^0$ *and* B^0*. The points are for the data of control samples, while the histograms with solid line and dotted line are for the EvtGen-MC and QQ-MC, respectively. All distributions are made with a requirement on* π/e *ID to exclude the soft electrons originating from photon conversions and* π^0 *Dalitz decays. Upper two figures and lower two figures in each (a) or (b) are for* π_s^-*-like tracks and for* π_s^+*-like tracks, respectively. Upper right and lower left figures in each (a) or (b) contain slow pions from* $D^{*\pm}$ *decay.*

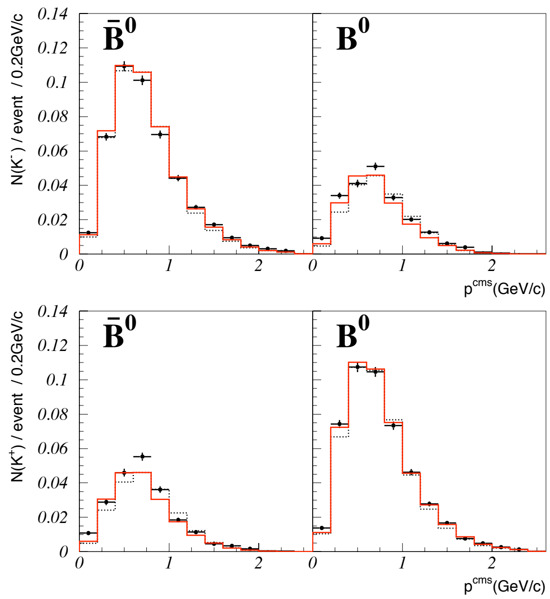

Figure A.4: *The cms momentum distributions of kaon candidates for* $\overline{B}^0$ *and* B^0*. The points are for the data of control samples, while the histograms with solid line and dotted line are for the EvtGen-MC and QQ-MC, respectively. The distribution of kaon cms momentum is made with a requirement on* K/π *ID to exclude the dominating pion component. Upper two figures and lower two figures are for* K^-*-like tracks and for* K^+*-like tracks, respectively. Upper right and lower left figures contain kaons from cascade* $b \to c \to s$ *transition.*

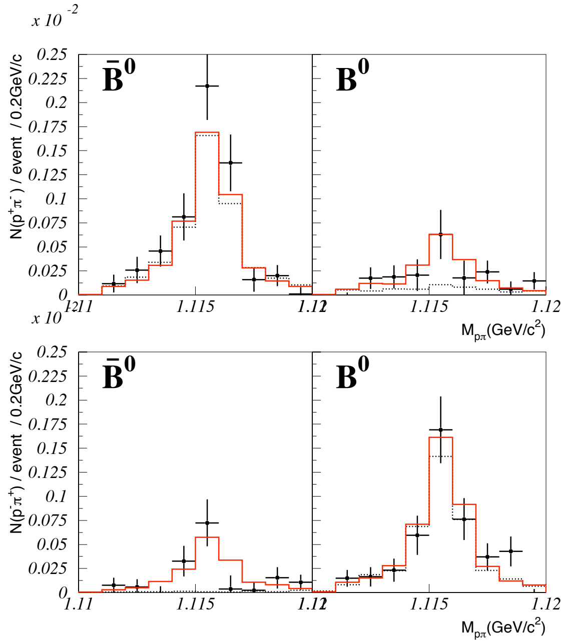

Figure A.5: *$M_{p\pi}$ distributions of Λ candidates for $\overline{B}^0$ and B^0. The points are for the data of control samples. Histograms with solid line and dotted line are for the EvtGen-MC and QQ-MC, respectively. Upper two figures and lower two figures are for Λ candidates and for $\overline{\Lambda}$ candidates, respectively. Upper left figure and lower right figure contain Λ particle from cascade $b \to c \to s$ transition.*

Figure A.4 shows cms momentum distribution of kaon-like track candidates compared to those in MC. The number of bins for each variable in the look-up table is 13 for L_K, 21 for p^*, 18 for θ_{lab}, 2 for K_S existence (with or without) and 2 for charge of the track (19656 bins in total).

If a track is identified as a proton and forms a Λ candidate with a pion track, the Λ candidate is assigned to Λ track class. The discriminant variables are:

- flavor of the Λ candidate (Λ or $\overline{\Lambda}$);
- existence of K_S candidates;
- invariant mass $M_{P\pi}$ of the Λ candidate;
- angle difference between the Λ momentum vector and the direction of the Λ vertex from IP;
- a distance in z direction between two tracks at the Λ vertex.

Figure A.5 shows $M_{P\pi}$ distributions for the data and the MC. Each discriminant variables are divided into two bins, and a look-up table of 32 total bins are made.

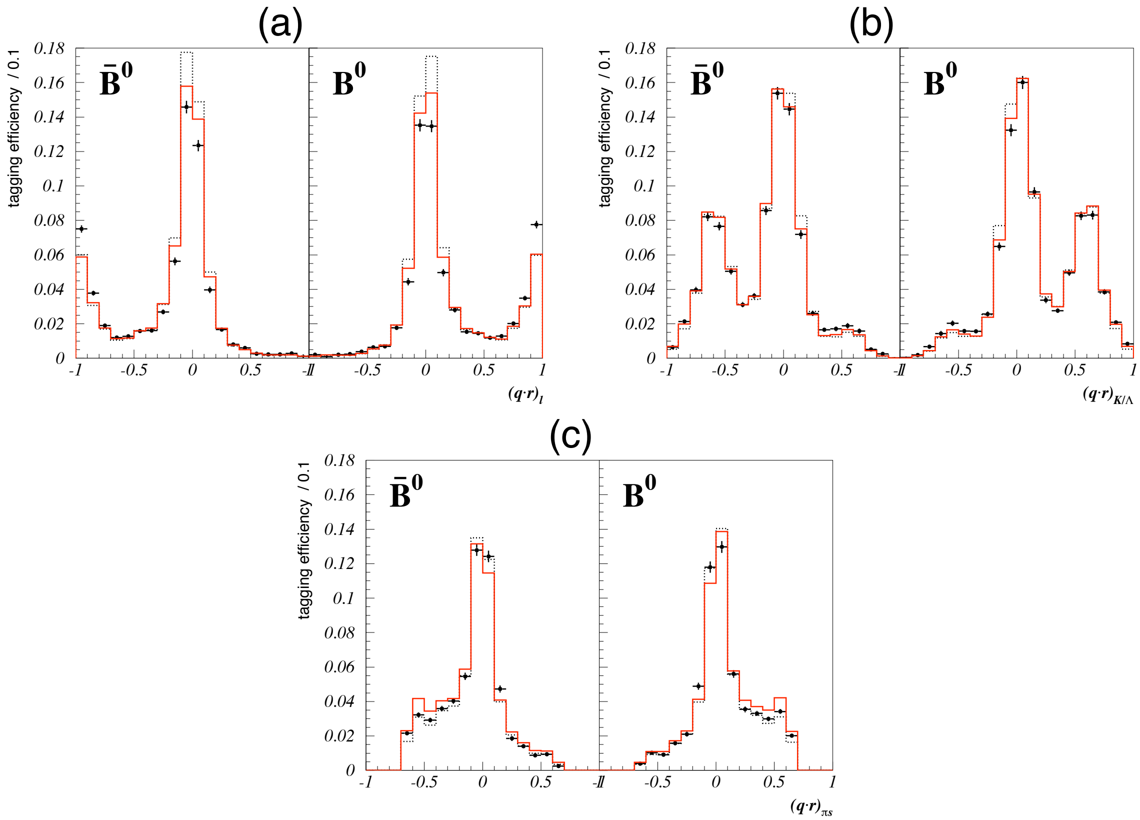

Figure A.6: *Distributions of input variables of event layer (a) $(q \cdot r)_l$, (b) $(q \cdot r)_{K/\Lambda}$ and (c) $(q \cdot r)_{\pi_s}$ for $\overline{B}^0$ and B^0. The points are for the data of control samples. The histograms with solid line and dotted line are for the EvtGen-MC and QQ-MC, respectively. For these distribution, the $(q \cdot r)$ values of corresponding track-layer outputs are obtained with EvtGen-MC lookup table. Events which have $r = 0$ due to no input tracks are excluded from each plots. The fractions of $r = 0$ are 36% for lepton category, 10% for Kaon/Λ category and 41% for slow pion category.*

The output of the kaon and Λ track class is given by the product of $q \cdot r$ for all kaon/Λ tracks assigned to this class:

$$(q \cdot r)_{K/\Lambda} \equiv \frac{\prod_i (1 + (q \cdot r)_i) - \prod_i (1 - (q \cdot r)_i)}{\prod_i (1 + (q \cdot r)_i) + \prod_i (1 - (q \cdot r)_i)}. \tag{A.2}$$

A.3 Event Level Flavor Tagging

The event level stage combines the track-level tagging results using $q \cdot r$ of three track classes as input. Figure A.6 shows the distribution of the track level $q \cdot r$. The $q \cdot r$ variables are divided into 25 for lepton class, 19 for slow pion class and 35 for kaon/Λ class and form a look-up table of 16625 total bins. The final $q \cdot r$ output of the event-level flavor

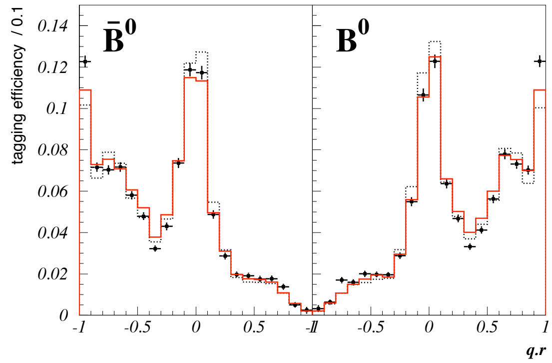

Figure A.7: *The $q \cdot r$ distribution for $\overline{B}^0$ and B^0. The points are for the data of control samples, while the histograms with solid line and dotted line are for the EvtGen-MC and the QQ-MC, respectively.*

tagging of the data and MC is shown in Figure A.7. In the figure, separation between $\overline{B}^0$ and B^0 sample is clearly seen and distributions of the data and the MC show good agreement.

A.4 Performance

We utilized the flavor quality value r to categorize the candidate events into six groups: $0.0 < r \leq 0.25$, $0.25 < r \leq 0.5$, $0.5 < r \leq 0.625$, $0.625 < r \leq 0.75$, $0.75 < r \leq 0.875$ and $0.875 < r$. The wrong tagging probabilities of these six tagging categories are measured with the self-tagged B^0 decays to $D^{*-}\ell^+\nu$, $D^-\pi^+$, $D^{*-}\pi^+$, $D^{*-}\rho^+$ and $J/\psi K^{*0}(K^{*0} \to K^+\pi^-)$. The detail of the wrong tagging probability determination is described in Appendix C. Table A.1 shows the measured wrong tagging probability (w_l), event fractions (ϵ_l) and effective tagging efficiency (ϵ^l_{eff}) for each r interval ($l = 1, 6$). The overall tagging efficiency is found to be 99.8%. The effective tagging efficiency for the $B^0 \to \eta' K_S$ decay are estimated to be (31.2 ± 0.7)%.

l	r interval	w_l	ϵ_l	ϵ^l_{eff}
1	$0.000 - 0.250$	0.457 ± 0.006	0.369	0.003 ± 0.001
2	$0.250 - 0.500$	0.332 ± 0.009	0.154	0.017 ± 0.002
3	$0.500 - 0.625$	0.224 ± 0.010	0.107	0.033 ± 0.002
4	$0.625 - 0.750$	$0.156^{+0.009}_{-0.008}$	0.116	0.055 ± 0.003
5	$0.750 - 0.875$	0.108 ± 0.009	0.100	0.062 ± 0.003
6	$0.875 - 1.000$	$0.016^{+0.006}_{-0.005}$	0.152	0.142 ± 0.004

Table A.1: *Wrong tag probability w_l, event fraction ϵ_l and effective efficiency $\epsilon^l_{eff} = \epsilon_l(1-2w_l)^2$ for each r interval. The errors of w_l and ϵ^l_{eff} include both statistical and systematic. Event fractions are obtained from the $B^0 \to \eta' K_S$ MC.*

Appendix B

Δt Resolution Function

We use the same resolution function as that used in the previous $\sin 2\phi_1$ measurement [10]. The details of the resolution function is found in the reference [69]. Here, we describe the resolution function briefly.

The Δt resolution consists of four components: detector resolution of vertices of a full reconstructed side, R_{ful}, and an associated B meson, R_{asc}, smearing due to contamination of non-primary tracks to the associated B vertex, R_{np}, and the kinematic approximation that we calculate $\Delta t \simeq \Delta z/\beta\gamma c$ neglecting motion of B mesons in the center of mass system (cms), R_k. The overall resolution function is expressed as

$$\begin{aligned} R_{sig}(\Delta t) = \iiint_{-\infty}^{\infty} d(\Delta t')d(\Delta t'')d(\Delta t''')R_{ful}(\Delta t - \Delta t')R_{asc}(\Delta t' - \Delta t'') \\ \times R_{np}(\Delta t'' - \Delta t''')R_k(\Delta t''') \end{aligned} \quad \text{(B.1)}$$

B.1 Detector Resolution

The detector resolution is parametrized as Gaussians of event-by-event determined sigma. For vertices reconstructed with two or more tracks, the event-by-event sigma is given by vertex errors calculated from track errors with correction factors depending on the quality of the vertex. The vertex quality is represented by a reduced χ^2 projected onto z axis defined as

$$\xi \equiv \frac{1}{2n} \sum_{i=1}^{n} \left[\frac{z^i_{after} - z^i_{before}}{e^i_{before}} \right], \quad \text{(B.2)}$$

where z^i_{before} and z^i_{after} are the z positions of each track before and after the vertex fit, respectively, and e^i_{before} is the error of z^i_{before}. We do not use normal χ^2 because it correlate with vertex z position due to tight IP constraint in the x-y plane. We require $\xi < 100$ to eliminate poorly reconstructed vertices. Using ξ, the correction factor of errors are expressed as a first order polynomial of ξ:

$$\begin{aligned} s_{ful} &\equiv (s^0_{ful} + s^1_{ful}\xi), \\ s_{asc} &\equiv (s^0_{asc} + s^1_{asc}\xi). \end{aligned} \quad \text{(B.3)}$$

The detector resolution function is then given by

$$R_{ful}^{multiple}(\delta z_{ful}) = G(\delta z_{ful}; s_{ful}\sigma_{asc}),$$
$$R_{asc}^{multiple}(\delta z_{asc}) = G(\delta z_{asc}; s_{asc}\sigma_{asc}), \tag{B.4}$$

where δz is defined as difference between a reconstructed z and the true z, $\delta z \equiv z - z_{true}$, $\sigma_{ful(asc)}$ is a vertex errors calculated from track errors for $B_{ful(asc)}$ vertex and G is a Gaussian function,

$$G(x;\sigma) \equiv \frac{1}{\sqrt{2\pi}\sigma} \exp\left(-\frac{x^2}{2\sigma^2}\right). \tag{B.5}$$

For a vertex reconstructed with single track, the vertex quality can not be defined. Therefore, we use a global correction factor and define the resolution function as

$$R_{single}(\delta z) = G(\delta z; s_{single}\sigma) \tag{B.6}$$

where s_{single} is the global correction factor which are common to all the single track vertices. Since vertex reconstruction situation is expected to be exactly same for full reconstructed and associated B meson, we use the same shape for both vertices.

The correction factor, s, depend on real detector performance and must be determined with real data. We describe the determination in Appendix C.

B.2 Smearing due to Non-Primary Tracks

The resolution function representing the smearing of associated side vertex due to contamination of non-primary tracks, R_{np}, consists of a prompt component expressed by Dirac's δ function which represents vertices without the contamination, and components which account for the smearing due to the contamination.

The R_{np} shape is studied by comparing two MC samples. One is normal $B\overline{B}$ MC sample. In another special MC sample, all secondary short-lived ($\tau < 10^{-9}$ s) particles are forced to decay with zero lifetime at the B meson decay point. We reconstruct associated side vertices in two MC sample and compare differences of reconstructed z positions between two samples. Figure B.1 shows distribution of $z_{asc} - z_{asc}^{noNP}$, where z_{asc} is the z position of the associated side vertex in normal MC and z_{asc}^{noNP} is the z vertex position in the special MC. From the figure, the functional form is determined to be

$$R_{np}(\delta z_{asc}) = f_\delta \times \delta(\delta z_{asc})$$
$$+ (1 - f_\delta) \times [f_p E_p(\delta z_{asc}/c(\beta\gamma)_\Upsilon; \tau_{np}^p) + (1 - f_p) E_n(\delta z_{asc}/c(\beta\gamma)_\Upsilon; \tau_{np}^n)], \tag{B.7}$$

where f_δ is a fraction of the prompt component, f_p is a fraction of the $\delta z_{asc} > 0$ component and E_p and E_n are:

$$E_p(x;\tau) \equiv \frac{1}{\tau} \exp\left(-\frac{x}{\tau}\right) \text{ for } x > 0, \text{ otherwise } 0,$$
$$E_n(x;\tau) \equiv \frac{1}{\tau} \exp\left(-\frac{x}{\tau}\right) \text{ for } x \leq 0, \text{ otherwise } 0. \tag{B.8}$$

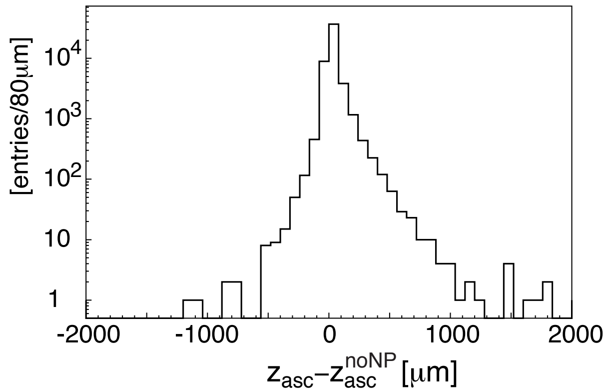

Figure B.1: *Distribution of $z_{asc} - z^{n}_{asc}oNP$ for vertices reconstructed with two or more tracks. In making this plot the events in which $z_{asc} = z^{noNP}_{asc}$ are removed.*

Introduction of exponential components is natural because of lifetime of secondary particles. The τ^{p}_{np} and τ^{n}_{np} are related with the vertex quality ξ and error σ_{asc}, because non-primary particles from longer lived particles are farther from the primary vertex and deteriorate the vertex quality and the error. For vertices reconstructed with two or more tracks, τ^{p}_{np} and τ^{n}_{np} are parametrized as:

$$\begin{aligned} \tau^{p}_{np} &= \tau^{0}_{p} + \tau^{1}_{p}(s^{0}_{asc} + s^{1}_{asc}\xi) \times \sigma_{asc}/c(\beta\gamma)_{\Upsilon}, \\ \tau^{n}_{np} &= \tau^{0}_{n} + \tau^{1}_{n}(s^{0}_{asc} + s^{1}_{asc}\xi) \times \sigma_{asc}/c(\beta\gamma)_{\Upsilon}. \end{aligned} \tag{B.9}$$

For vertices reconstructed with single track, they are given by:

$$\begin{cases} (\tau^{p}_{np}) = \tau^{0}_{p} + \tau^{1}_{p} \times s_{single} \times \sigma_{asc} \\ (\tau^{n}_{np}) = \tau^{0}_{n} + \tau^{1}_{p} \times s_{single} \times \sigma_{asc} \end{cases} \tag{B.10}$$

The parameters of R_{np} are determined with a MC study. Since the distribution shown in Figure B.1 includes detector resolution effect of additional tracks as well, we do not use it to determine the parameters but fit the δz_{asc} distribution with the convolution of R_{asc} and R_{np}. Because of the difference between neutral D lifetime (0.412 ps) and charged D lifetime (1.051 ps), the parameters are determined separately for neutral and charged B mesons. Figure B.2 shows the δz_{asc} distributions with fitted curves. The R_{asc} and R_{np} reproduce the distribution well. Table B.1 shows the determined parameters.

B.3 Kinematic Approximation

The smearing due to the kinematic approximation that we calculate $\Delta t \simeq \Delta z/\beta\gamma c$ neglecting motion of B mesons in cms is calculated analytically. From the kinematics of the $\Upsilon(4S)$ two body decay, the difference between measured Δt and the $\delta t_{true} = t_{ful} - t_{asc}$ is

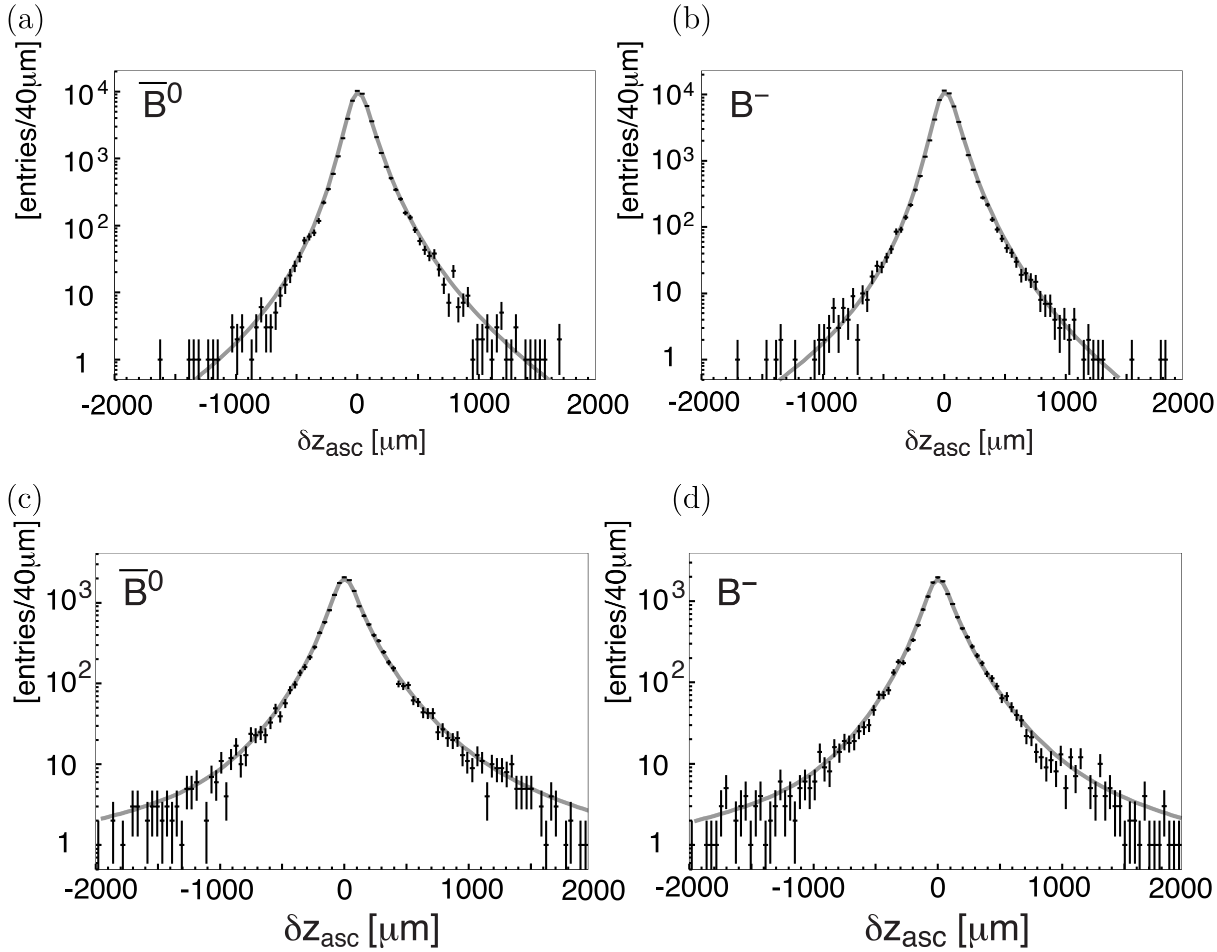

Figure B.2: *The δz_{asc} distributions of (a) multiple-track vertices for neutral B, (b) multiple-track vertices for charged B, (c) single-track vertices for neutral B (d) single-track vertices for charged B. The full reconstructed side B mesons decay into $J/\psi K_S$ or $J/\psi K^-$.*

	neutral B		charged B	
	multiple	single	multiple	single
f_p	0.959 ± 0.003	0.785 ± 0.013	0.971 ± 0.003	$0.804^{+0.016}_{-0.017}$
τ_p^0 (ps)	-0.049 ± 0.010	$0.374^{+0.084}_{-0.082}$	0.015 ± 0.009	$0.214^{+0.070}_{-0.069}$
τ_p^1	$1.008^{+0.023}_{-0.022}$	$1.472^{+0.105}_{-0.102}$	0.736 ± 0.020	$1.234^{+0.104}_{-0.099}$
τ_n^0 (ps)	$-0.138^{+0.083}_{-0.082}$	$0.193^{+0.146}_{-0.141}$	$-0.070^{+0.099}_{-0.100}$	$-0.148^{+0.193}_{-0.189}$
τ_n^1	$2.057^{+0.188}_{-0.176}$	$1.811^{+0.221}_{-0.205}$	$1.927^{+0.231}_{-0.212}$	$2.086^{+0.318}_{-0.286}$

Table B.1: *List of R_{np} parameters determined with the Monte Carlo simulation.*

calculated to be:

$$
\begin{aligned}
x \equiv \Delta t - \Delta t_{true} &= (z_{ful} - z_{asc})/c(\beta\gamma)_\Upsilon - (t_{ful} - t_{asc}) \\
&= [t_{ful} c(\beta\gamma)_{ful} - t_{asc} c(\beta\gamma)_{asc}]/c(\beta\gamma)_\Upsilon - (t_{ful} - t_{asc}) \\
&= [(\beta\gamma)_{ful}/(\beta_\gamma)_\Upsilon - 1]t_{ful} - [(\beta\gamma)_{asc}/(\beta_\gamma)_\Upsilon - 1]t_{asc},
\end{aligned}
\tag{B.11}
$$

where $(\beta\gamma)_{ful}$ and $(\beta\gamma)_{asc}$ are Lorentz boost factors of the fully reconstructed and associated B mesons, respectively. Their ratio to $(\beta\gamma)_\Upsilon$ are given by:

$$
\begin{aligned}
(\beta\gamma)_{ful}/(\beta\gamma)_\Upsilon &= \frac{E_B^{cms}}{m_B} + \frac{p_B^{cms}\cos\theta_B^{cms}}{\beta_\Upsilon m_B}, \\
(\beta\gamma)_{asc}/(\beta\gamma)_\Upsilon &= \frac{E_B^{cms}}{m_B} - \frac{p_B^{cms}\cos\theta_B^{cms}}{\beta_\Upsilon m_B},
\end{aligned}
\tag{B.12}
$$

where E_B^{cms} is the energy of B meson which corresponds to the beam energy ~ 5.29GeV, m_B is the B meson mass, $p_B^{cms} \sim 0.34$ GeV/c is the B momentum in the cms and θ_B^{cms} is the polar angle of the fully reconstructed B in the cms.

Since t_{ful} and t_{asc} distributions follow $E_p(t_{ful};\tau_B) = 1/\tau_B \exp(-t_{ful}\tau_B)$ and $E_p(t_{asc};\tau_B) = 1/\tau_B \exp(-t_{asc}\tau_B)$, respectively, the probability density of obtaining x and Δt true simultaneously is given by

$$
\begin{aligned}
F(x, \Delta t) = &\int_0^\infty \int_0^\infty dt_{ful} dt_{asc} E_p(t_{ful};\tau_B) E_p(t_{asc};\tau_B) \delta(\Delta t_{true} - (t_{ful} - t_{asc})) \\
&\times \delta(x - \{[(\beta\gamma)_{ful}/(\beta\gamma)_\Upsilon - 1]t_{ful} - [(\beta\gamma)_{asc}/(\beta\gamma)_\Upsilon - 1]t_{asc}\}),
\end{aligned}
\tag{B.13}
$$

and the probability density of obtaining Δt_{true} is given by

$$
F(\Delta t) = \int_0^\infty \int_0^\infty dt_{ful} dt_{asc} E_p(t_{ful};\tau_B) E_p(t_{asc};\tau_B) \delta(\Delta t_{true} - (t_{ful} - t_{asc})). \tag{B.14}
$$

The $R_k(x)$ is then defined as the conditional probability density of obtaining x given Δt_{true}. It is expressed as $R_k(x) = F(x, \Delta t_{true})/F(\Delta t_{true})$ which gives:

$$
R_k(x) = \begin{cases}
E_p\left(x - \left[(\frac{E_B^{cms}}{m_B} - 1)\Delta t_{true} + \frac{p_B^{cms}\cos\theta_B^{cms}}{\beta_\Upsilon m_B}|\Delta t_true|\right]; |\frac{p_B^{cms}\cos\theta_B^{cms}}{\beta_\Upsilon m_B}|\tau_B\right) & (\cos\theta_B^{cms} > 0) \\
\delta\left(x - (\frac{E_B^{cms}}{m_B} - 1)\Delta t_{true}\right) & (\cos\theta_B^{cms} = 0) \\
E_n\left(x - \left[(\frac{E_B^{cms}}{m_B} - 1)\Delta t_{true} + \frac{p_B^{cms}\cos\theta_B^{cms}}{\beta_\Upsilon m_B}|\Delta t_true|\right]; |\frac{p_B^{cms}\cos\theta_B^{cms}}{\beta_\Upsilon m_B}|\tau_B\right) & (\cos\theta_B^{cms} < 0)
\end{cases}
\tag{B.15}
$$

Figure B.3 shows the x distribution for B^0 MC sample with the function $R_k(x)$. The $R_k(x)$ function represents the distribution correctly.

B.4 Outlier

We find that there still exists a small component with a very long tail, which is order of several tens ps, that cannot be described by the resolution functions above. The outlier

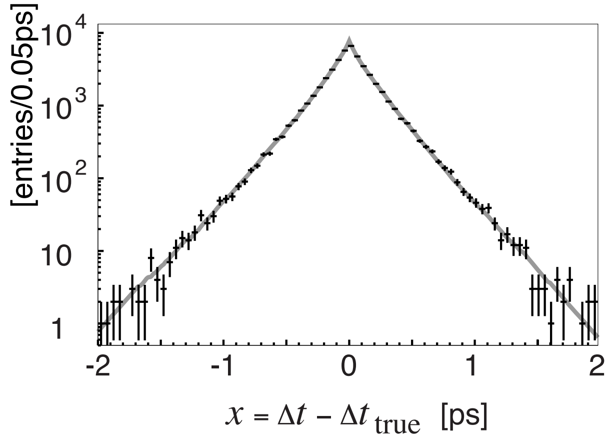

Figure B.3: *The $x = \Delta t - \Delta t_{true}$ distribution for neutral B meson MC sample together with the function $R_k(x)$.*

term is introduced to describe this long tail and represented by a Gaussian with zero mean and event-independent width,

$$P_{ol}(\Delta t) = G(\Delta t, \sigma_{ol}). \tag{B.16}$$

The fraction of outlier f_{ol} is typically less than 10^{-3} for multiple-track vertices and $\sim 10^{-2}$ for single-track vertices.

Appendix C

Wrong Tagging Probability and Detector Resolution Determination

The wrong tagging probability are determined with the self-tagged neutral B meson: $B^0 \to D^{*-}\ell^+\nu$, $D^{*-}\pi^+$, $D^-\pi^+$, $D^{*-}\rho^+$, and $J/\psi K^{*0}(K^* \to K + \pi^-)$. To determine the parameters of the Δt resolution function related to the detector resolution, we use the $B^0 \to J/\psi K_S$, $B^+ \to J/\psi K^+$, $B^+ \to \overline{D}^0 K^+$ and the self-tagged B decays. In this Appendix, we describe the reconstruction of these decays and the determination.

C.1 Event Reconstruction

C.1.1 $B^0 \to D^{*-}\ell^+\nu$ Reconstruction

To reconstruct $B^0 \to D^{*-}\ell^+\nu$ decays, we use the decay chain $B^0 \to D^{*-}\ell^+\nu$, $D^{*-} \to \overline{D}^0\pi^-$, and $\overline{D}^0 \to K^+\pi^-$, $K^+\pi^-\pi^0$ or $K^+\pi^-\pi^+\pi^-$. We require associated SVD hits and radial impact parameters $|dr| < 0.2$ cm for all tracks. Track momenta in the laboratory frame for $\overline{D}^0 \to K^+\pi^-\pi^0$ decays are required to be larger than 0.2 GeV/c, while no additional requirements are applied for the other modes. Charged kaons are identified by combining information from the TOF, ACC and dE/dx measurements in the CDC. For $\pi^0 \to \gamma\gamma$ candidates, we use pairs of photons with energies greater than 0.08 GeV that have an invariant mass within 0.011 GeV/c^2 of m_{π^0} and a total momentum greater than 0.2 GeV/c. For $\overline{D}^0 \to K^+\pi^-$ and $K^+\pi^-\pi^+\pi^-$ candidates, we use daughter combinations that are within 0.013 GeV/c^2 of m_{D^0}; for $\overline{D}^0 \to K^+\pi^-\pi^0$ we expand the mass window to -0.037 and $+0.023$ GeV/c^2. For $D^{*-} \to \overline{D}^0\pi^-$ decays, we combine $\overline{D}^0$ candidates with a low-momentum π^- (slow pion) that is reconstructed using a vertex constraint and require the mass difference between the D^{*-} and $\overline{D}^0$ candidates to be within 1 MeV/c^2 of the nominal value. We reject D^{*-} candidates with cms momentum greater than 2.6 GeV/c, which is beyond the kinematic limit for B meson decays.

For the associated lepton, we use electrons or muons that have an opposite charge to the D^{*-} candidate. Electron identification is based on a combination of CDC dE/dx information, the ACC response, and energy deposit of the associated ECL shower. Muons are identified by comparing information from the KLM to extrapolated charged particle trajectories. We require $1.4 < p_\ell^{\rm cms} < 2.4$ GeV/c, where $p_\ell^{\rm cms}$ is the cms momentum of the lepton. The cms angle of the lepton with respect to the direction of the D^{*-} candidate is also required to be greater than 90 degrees. For $B^0 \to D^{*-}\ell^+\nu$ decays, the energies and momenta of the B meson and the $D^*\ell$ system in the cms satisfy $M_\nu^2 = (E_B^{\rm cms} - E_{D^*\ell}^{\rm cms})^2 - |\vec{p}_B^{\,\rm cms}|^2 - |\vec{p}_{D^*\ell}^{\,\rm cms}|^2 + 2|\vec{p}_B^{\,\rm cms}|\,|\vec{p}_{D^*\ell}^{\,\rm cms}|\cos\theta_{B,D^*\ell}$, where M_ν is the neutrino mass and $\theta_{B,D^*\ell}$ is the angle between $\vec{p}_B^{\,\rm cms}$ and $\vec{p}_{D^*\ell}^{\,\rm cms}$. We calculate $\cos\theta_{B,D^*\ell}$ setting $M_\nu = 0$. Figure C.1 shows the $\cos\theta_{B,D^*\ell}$ distribution. The signal region is defined as $|\cos\theta_{B,D^*\ell}| < 1.1$. We find 47317 candidates in the signal region. The purity is estimated to be 79.2%. The background consists of $B \to D^{**}\ell\nu$ events (7.9%), fake D^* (7.4%), continuum events (2.9%) and combination of lepton B and D^* from the other B (2.6%).

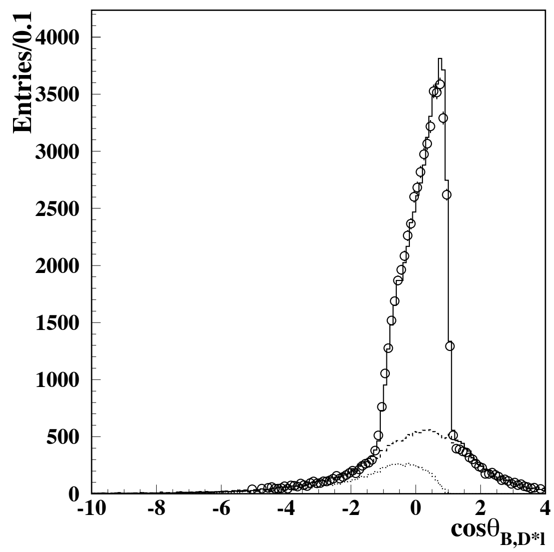

Figure C.1: *The $\cos\theta_{B,D^*\ell}$ distribution for the $D^{*-}\ell^+\nu$ candidates. The circles with errors show the data. The solid histograms show the fit result. The total background and the $D^{**}\ell\nu$ component are shown by the dashed line and the dotted line, respectively.*

C.1.2 $B^0 \to D^{(*)-}\pi^+$, $B^0 \to D^{*-}\rho^+$ and $B^+ \to \overline{D}^0\pi^+$ Reconstruction

$B \to D^{(*)}\pi^+$ and $B^0 \to D^{*-}\rho^+$ decays are reconstructed using D^{*-} and $\overline{D}^0$ decay chains which are same as the $D^{*-}\ell^+\nu$ reconstruction, $D^- \to K^+\pi^-\pi^-$, and $\rho^+ \to \pi^+\pi^0$. For D reconstruction, we require that at least two charged tracks have associated SVD hits. We require that the reconstructed D mass lies within the decay-mode dependent range from the nominal D mass: from ± 15 to ± 60 MeV/c^2 for D and from 3 to 12 MeV/c^2 for the $D^* - D$ mass difference. The ρ^+ candidates are selected from π^+ and π^0 pairs by requiring the invariant mass to be within 150 MeV/c^2 from the nominal ρ^+ mass. The B candidates are formed by combining the reconstructed $D^{(*)}$ candidates and the charged π or ρ candidates. The associated charge pion tracks including π^+ from ρ^+ are required to

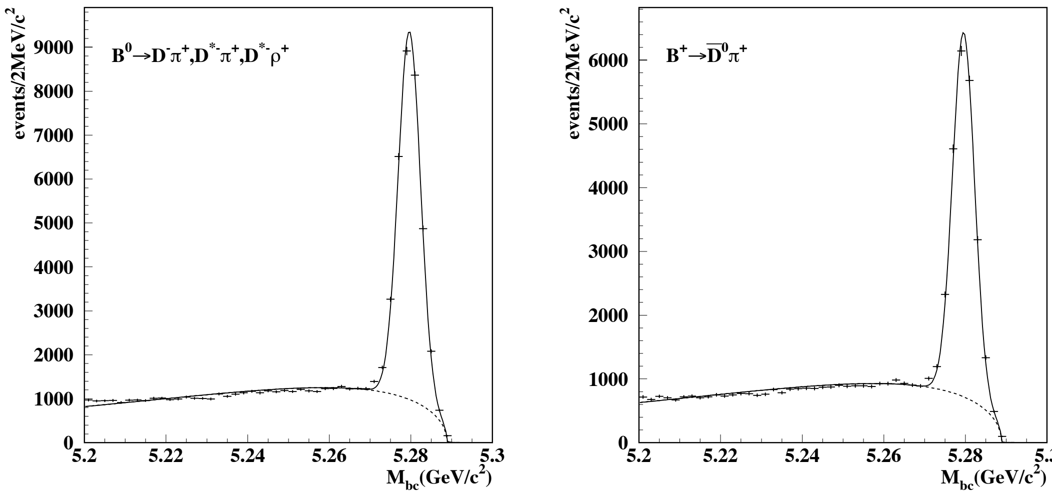

Figure C.2: *M_{bc} distribution of $B^0 \to D^-\pi^+, D^{*-}\pi^+, D^{*-}\rho^+$ candidates (left) and $B^+ \to D^0\pi^+$ candidates (right). The solid lines show the fit result. The dashed lines show the background component.*

have associated SVD hits. In order to suppress continuum background, we impose mode dependent requirements on the ratio of the second order Fox-Wolfram moments to the zero-th order Fox-Wolfram moments and on the cosine of the angle between the thrust axis of the daughter particles of the reconstructed B candidates and the thrust axis of the remaining particles. We select B candidates by requiring $5.27 < M_{bc} < 5.29$ GeV/c^2 and ΔE to be within the mode-dependent region from 0 MeV, which range from 45 to 80 MeV.

Figure C.2 shows the M_{bc} distribution for reconstructed B^0 and B^+ candidates. We find 6080 $B^0 \to D^-\pi^+$, 6782 $B^0 \to D^{*-}\pi^+$, 5153 $B^0 \to D^{*-}\rho^+$ and 26066 $B^+ \to \overline{D}^0\pi^+$ candidates in the signal region. The purity is estimated to be 87.9% for $B^0 \to D^-\pi^-$, 84.3% for $B^0 \to D^{*-}\pi^+$, 72.6% for $B^0 \to D^{*-}\rho^+$ and 74.1% for $B^+ \to \overline{D}^0\pi^+$.

C.1.3 $B \to J/\psi K^{(*)}$ Reconstruction

We reconstruct J/ψ using the decay into e^+e^- or $\mu^+\mu^+$. We use oppositely charged track pairs identified as leptons by the similar method as $D^*\ell\nu$ reconstruction. Since $B^0 \to J/\psi K_S$ and $B^+ \to J/\psi K^+$ decays are clean enough , we loosen the lepton id requirement for one of the track pairs. We require at least one of a track pair constructing a J/ψ candidate has associated SVD hits and the impact parameter $|dz| < 5$ cm for both tracks. In order to account partially for final-state radiation and bremsstrahlung, the invariant mass calculation of the e^+e^- pairs is corrected by adding photons found within 50 mrad of the e^+ or e^- direction. Nevertheless, a radiative tail remains and we use an asymmetric invariant mass requirement. For $B^0 \to J/\psi K_S$ and $B^+ \to J/\psi K^+$, we require e^+e^- invariant mass to be within $-150 \leq M_{e^+e^-} - M_{J/\psi} \leq 36$ MeV/c^2, where $M_{J/\psi}$ is the nominal J/ψ mass. For $B^0 \to J/\psi K^{*0}$, we require $-147 \leq M_{e^+e^-} - M_{J/\psi} \leq 53$. Since the $\mu^+\mu^-$ radiative tail is smaller, the lower limit of mass window is set to be higher than e^+e^-. We select $-60 \leq M_{\mu^+\mu^-} - M_{J/\psi} \leq 36$ MeV/c^2 for $B \to J/\psi K_S(K^+)$, and $-47 \leq M_{\mu^+\mu^-} - M_{J/\psi} \leq 53$ for $J/\psi K^{*0}$. The K_S are selected with the same criteria described in Section 4.3.2. The K^{*0} candidates are selected from oppositely charged track pairs in which one track is identified as kaon and the other is not. We require the invariant mass must be within ± 75 MeV/c^2 from the nominal K^{*0} mass. The reconstructed J/ψ are paired with K_S, K^+ or K^{*0}. We select B candidates by requiring the beam constraint mass to be within $5.2694 < M_{bc} < 5.2894$ GeV/c^2 for $B^0 \to J/\psi K_S$ and $5.27 < M_{bc} < 5.29$ GeV/c^2 for $B^0 \to J/\psi K^{*0}$ and $B^+ \to J/\psi K^+$. The ΔE is required to be within ± 40 MeV for $B^+ \to J/\psi K^+$ and $B^0 \to J/\psi K_S$ and ± 30 MeV for $B^0 \to J/\psi K^{*0}$.

Figure C.3 shows the M_{bc} distribution. We find 1116 $B^0 \to J/\psi K_S$, 1860 $B^0 J/\psi K^{*0}$ and 4810 $B^+ \to J/\psi K^+$ candidates. The purity is estimated to be 97.6% for $B^0 \to J/\psi K_S$, 93.0% for $B^0 \to J/\psi K^{*0}$ and 94.2% for $B^+ \to J/\psi K^+$.

C.2 Vertex Reconstruction

The vertex of the reconstructed $B \to D^{(*)}X$ candidates is reconstructed with the D track and the accompanying π track or lepton track except for slow pion from D^*. The IP constraint is also used to make the resolution better. The D track is made with the momentum of the daughter particles at the D vertex which is reconstructed with the daughter tracks with associated SVD hits.

The vertex of the $B \to J/\psi K$ candidate is reconstructed with the one or two lepton tracks from $J/\psi \to \ell^+\ell^-$ decay and IP constraint, where we use only lepton tracks having associated SVD hits.

The vertex of the associated B meson is reconstructed with the remaining tracks with associated SVD hits in the event. We use the same reconstruction algorithm described in Section 4.4.2.

C.3 Flavor Tagging

The flavor of the associated B meson with the self-tagged B^0 candidate is determined with the flavor tagging method described in Appendix A.

C.4 Lifetime and B^0-$\overline{B}^0$ Mixing Fit

The reconstructed B meson candidates are summarized in Table C.1. The parameters of detector resolution function are calibrated by fitting the Δt distribution of these candidates with the convolution of the Δt resolution function and the exponential function of the B lifetime. The wrong tagging probabilities are determined by comparing the flavor determined with the self-tagged B^0 decays and the flavor determined by the flavor tagging.

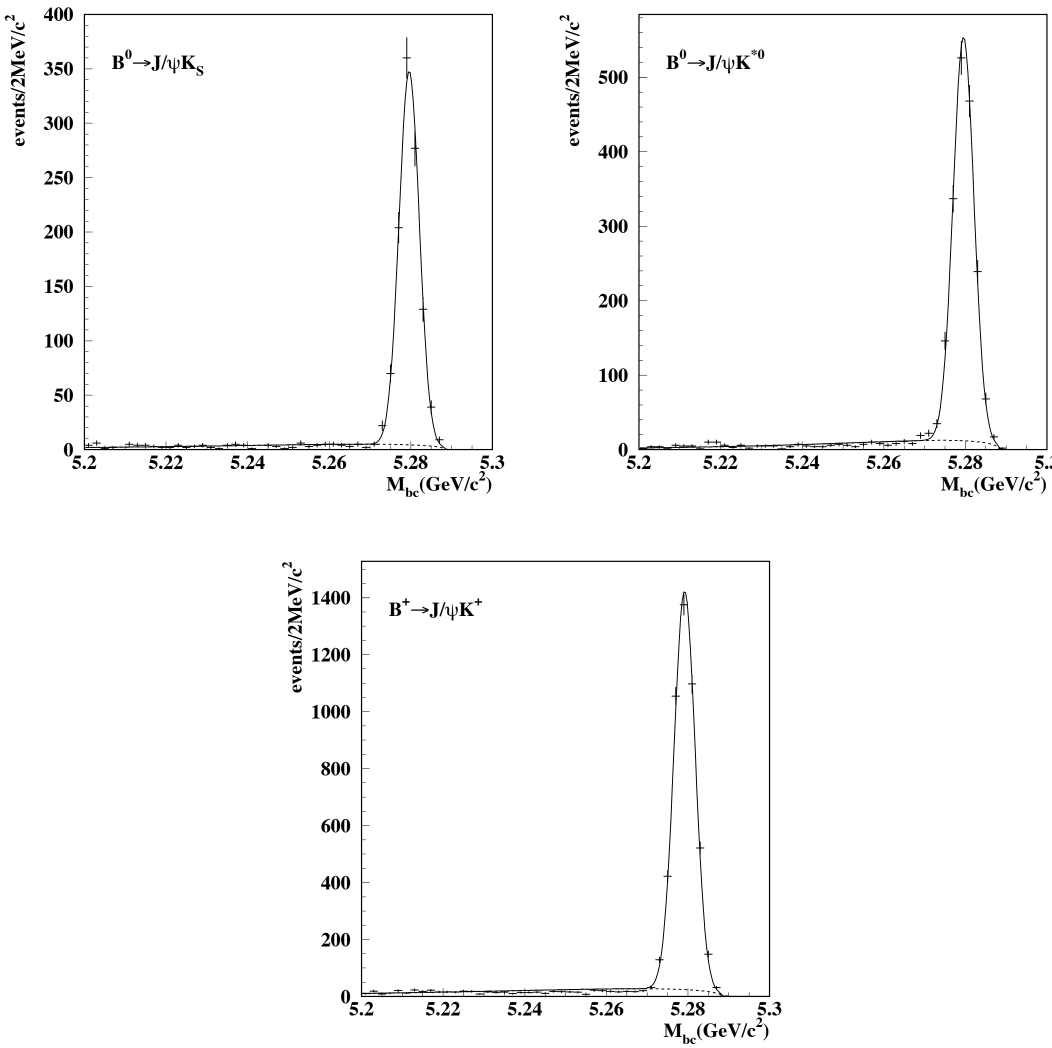

Figure C.3: M_{bc} *distribution of* $B^0 \to J/\psi K_S$ *(upper left),* $B^0 \to J/\psi K^*0$ *(upper right) and* $B^+ \to J/\psi K^+$ *(lower). The solid line shows the fit result. The dashed line shows the background component.*

mode	Number of candidates	purity
$B^0 \to D^{*-}\ell^+\nu$	47317	79.2%
$B^0 \to D^-\pi^+$	6080	87.9%
$B^0 \to D^{*-}\pi^+$	6782	84.3%
$B^0 \to D^{*-}\rho^+$	5153	72.6%
$B^0 \to J/\psi K^{*0}(K^{*0} \to K^+\pi^-)$	1860	93.0%
$B^0 \to J/\psi K_S$	1116	97.6%
$B^+ \to J/\psi K^+$	4810	94.2%
$B^+ \to \overline{D}^0\pi^+$	26066	74.1%

Table C.1: *The number of reconstructed B meson candidates for the lifetime and the mixing analysis after the reconstruction of vertices and the flavor tagging.*

To obtain the wrong tagging probability, we need to take into account the B^0-$\overline{B}^0$ mixing. We correct the B^0-$\overline{B}^0$ mixing effect by fitting the time-dependent B^0-$\overline{B}^0$ oscillation.

The resolution parameters and the wrong tagging probabilities are determined simultaneously by the unbinned maximum likelihood fit. The PDF is defined as

$$P(\Delta t) = (1 - f_{ol})\left[f_{sig}P_{sig}(\Delta t) + (f_{sig}P_{BG}(\Delta t)\right] + f_{ol}P_{ol}(\Delta t), \tag{C.1}$$

where f_{sig} is the signal probability, P_{sig} and P_{BG} are the Δt PDF of the signal and the background, respectively, and f_{ol} and P_{ol} are the outlier fraction and PDF. The f_{sig} and P_{BG} are determined separately for each B decay mode. The details of the f_{sig} and P_{BG} are described in references [70–72]. The P_{sig} is defined as a convolution of the Δt resolution function R_{sig} and a root function $\mathcal{P}_{sig}$ depending on B decay modes,

$$P_{sig} = \int d\Delta t' \mathcal{P}_{sig}(\Delta t') R_{sig}(\Delta t - \Delta t'). \tag{C.2}$$

For the self-tagged B^0 decays, the $\mathcal{P}_{sig}$ is defined as

$$\mathcal{P}_{sig} = \begin{cases} \dfrac{1}{4\tau_{B^0}} \exp\left(-\dfrac{|\Delta t|}{\tau_{B^0}}\right)[1 + (1 - 2w_l)\cos\Delta m_d \Delta t] & \text{For opposite flavor (OF) events} \\ \dfrac{1}{4\tau_{B^0}} \exp\left(-\dfrac{|\Delta t|}{\tau_{B^0}}\right)[1 - (1 - 2w_l)\cos\Delta m_d \Delta t] & \text{For same flavor (SF) events ,} \end{cases} \tag{C.3}$$

where w_l is the wrong tagging probability of each r region ($l = 1, 6$) and "OF (SF)" means that the flavor of the reconstructed B^0 is opposite (same) to the flavor of the associated B meson. For other B decays, the $\mathcal{P}_{sig}$ is given by

$$\mathcal{P}_{sig} = \frac{1}{2\tau_B} \exp\left(-\frac{|\Delta t|}{\tau_B}\right), \tag{C.4}$$

where τ_B is the lifetime of B^0 or B^+.

The lifetimes, Δm_d, wrong tagging probabilities, the detector resolution parameters are fitted simultaneously. We also determine the fraction of the prompt component in the

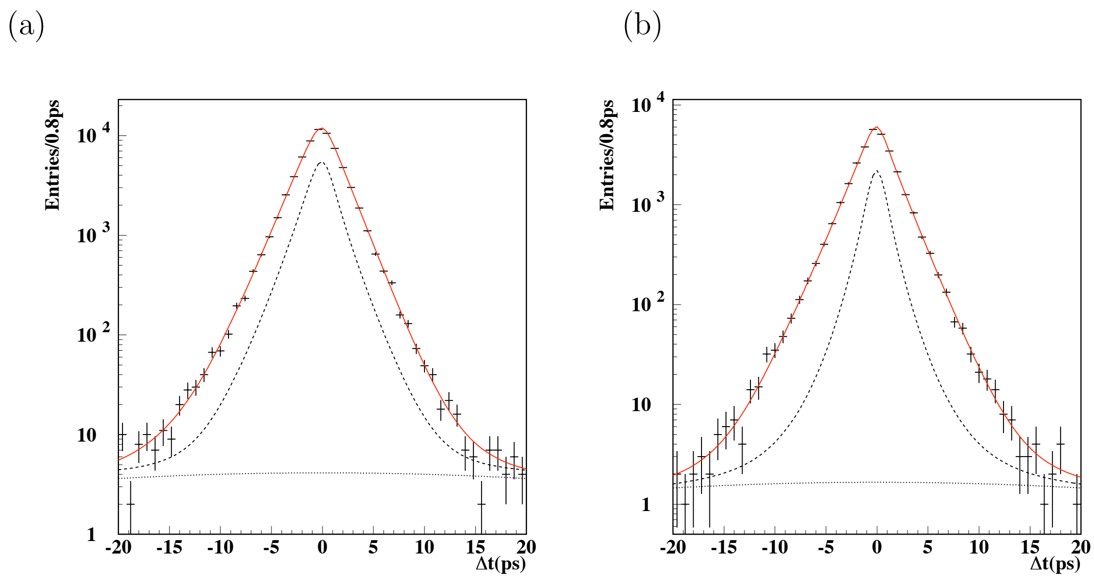

Figure C.4: *The Δt distribution of (a) neutral B and (b) charged B mesons with fitted curves overlaid. The dotted lines show the outlier component. The dashed lines show the sum of the outlier and the background component.*

R_{np}, f_δ, and the outlier fraction and width in the fit. Results are shown in Table C.2. The figure C.4 shows the Δt distribution with fitted curve overlaid. The figure C.5 shows the $(OF - SF)/(OF + SF)$ distribution of the self-tagged B^0 decays. The fit results agree with the Δt distribution well.

C.5 Systematic Errors

We consider the following sources of the systematic errors. In principle, we change value of each parameter by its error and repeat the analysis, and each difference from the default analysis is added in quadrature. As the error of each parameter, we use one σ for parameters obtained from the real data and two σ for parameters obtained from MC study. Results are summarized in Table C.3, C.4, C.5 and C.7.

C.5.1 Background Fraction

We vary each background fraction or each parameters describing the background fraction by its error and repeat the fit. The ΔE-M_{bc} signal region are varied by $\pm$10MeV for ΔE and $\pm 3\text{MeV}/c^2$ for M_{bc}. The difference between the nominal result is treated as systematic error.

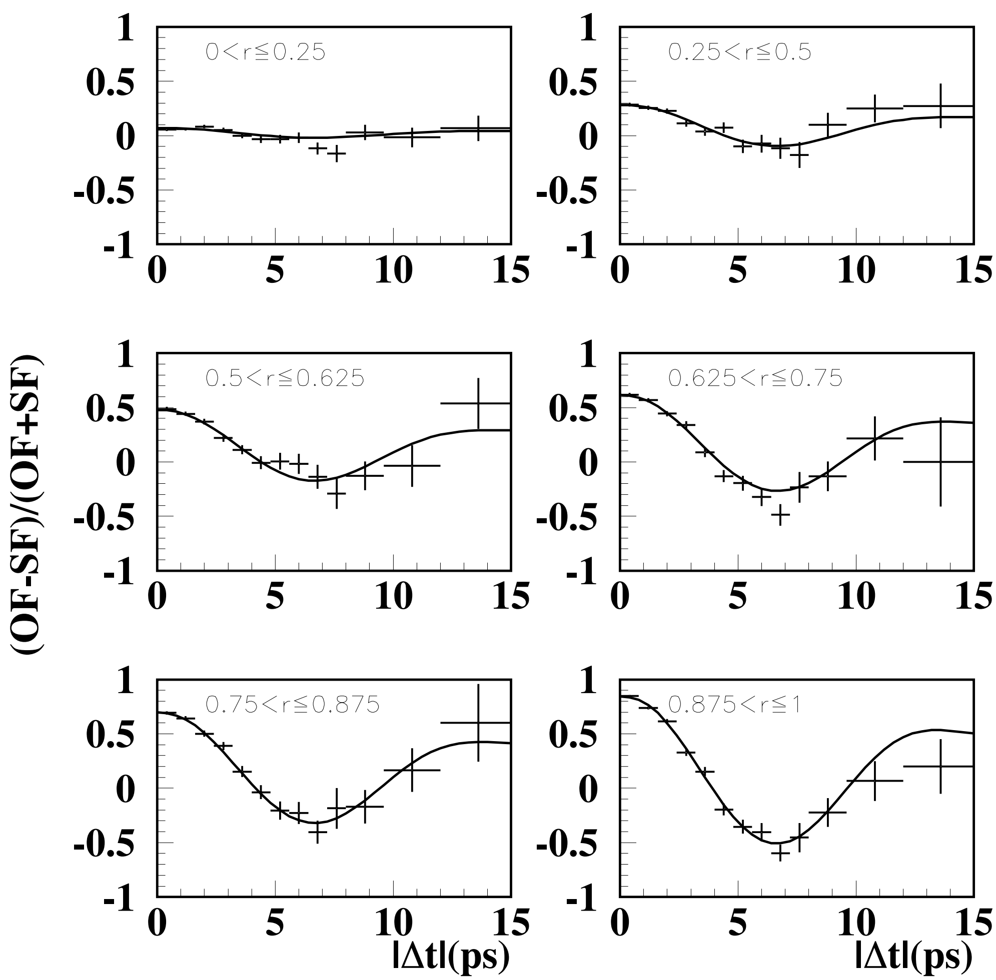

Figure C.5: *Time dependent* A_{charge} *distribution of* $B^0 \to D^{*-}\ell^+\nu$, $D^{*-}\pi^+$, $D^-\pi^+$, $D^-\pi^+$, $D^{*-}\rho^+$ *and* $J/\psi K^{*0}$ $(K^{*0} \to K^+\pi-)$ *for six tagging quality categories. Solid lines show the mixing fit result.*

Parameter	Value
τ_{B^0}(ps)	1.538 ± 0.011
τ_{B^+}(ps)	1.661 ± 0.015
Δm_d(ps^{-1})	0.509 ± 0.006
w_1	0.457 ± 0.005
w_2	0.332 ± 0.008
w_3	0.224 ± 0.009
w_4	$0.156^{+0.008}_{-0.007}$
w_5	0.108 ± 0.008
w_6	0.016 ± 0.005
s^0_{ful}	$0.969^{+0.074}_{-0.077}$
s^1_{ful}	$0.085^{+0.005}_{-0.004}$
s^0_{asc}	0.799 ± 0.032
s^1_{asc}	0.043 ± 0.002
s_{single}	0.913 ± 0.032
$(f^{mult}_{\delta})_{B^0}$	0.555 ± 0.025
$(f^{single}_{\delta})_{B^0}$	$0.666^{+0.026}_{-0.027}$
$(f^{mult}_{\delta})_{B^+}$	0.450 ± 0.040
$(f^{single}_{\delta})_{B^+}$	$0.731^{+0.040}_{-0.042}$
f^{mult}_{ol}	$(1.8 \pm 0.8) \times 10^{-4}$
f^{single}_{ol}	$(2.7 \pm 0.1) \times 10^{-2}$
σ_{ol}(ps)	$39.0^{+2.5}_{-2.1}$

Table C.2: *Results of the lifetime and B^0-$\overline{B}^0$ mixing fit.*

C.5.2 Background Δt shape

The systematic errors due to the uncertainty of the background Δt shape are estimated by changing the parameters of the background Δt PDF individually and repeating the analysis.

We have neglected mixing component in the background of the hadronic mode in the nominal fit. We repeat the analysis by including the mixing component and the difference is treated as systematic error.

C.5.3 D^{**} Composition

We assumed the theoretical prediction of the D^{**} branching fractions [73, 74] in the MC which we used to estimate the $B \to D^{**}\ell\nu$ background to the $B^0 \to D^{*-}\ell^+\nu$ decays. The systematic error due to the uncertainty of the D^{**} composition is estimated by setting each such branching fraction to unity in the MC (with all others set to zero), and repeating the analysis. We take the largest variation as the systematic error.

C.5.4 Wrong Tagging Probability of B^+ Background

Wrong tagging probabilities of the $B^+ \to D^{**0}\ell^+\nu$ background of the $B^0 \to D^{*-}\ell^+\nu$ is changed by their errors.

C.5.5 Resolution function

Each of the parameters of R_{np} determined with the MC is varied by two σ and the fit is repeated.

The systematic error due to the modeling of the resolution function is estimated by comparing the results with different parametrization. For this study, we use double Gaussian form for R_{det}.

C.5.6 Vertex Reconstruction

Vertex Selection Dependence

We have required $\xi < 100$ for vertices. We estimated the systematic error by repeating the fit for $\xi < 50$ and $\xi < 200$.

Track Selection of Tagging Side Vertex

The systematic error due to the track selection criteria for tagging side vertexing is estimated by varying the requirement for $|dr|$ and error of z by $\pm 10\%$.

Δt Selection

The reconstructed Δt has been required to satisfy $|\Delta t| < 70$ ps. The rejection criterion is varied by ± 30 ps to check the validity of the tail treatment of our resolution function, and the difference from the default analysis is treated as systematic error.

Flight Length of B Meson

The IP constraint fit includes the uncertainty of the B meson decay point due to flight length of B meson in the r-ϕ plane. The uncertainty is estimated to be assuming a Gaussian function although it is actually an exponential function. We estimated the systematic error by repeating the fit varying the uncertainty by ± 10 μm.

C.6 Result

The determined parameters and their errors are summarized in Table C.8

Source	τ_{B^0}(ps)	τ_{B^+}(ps)	Δm_d(ps^{-1})
Semileptonic background fraction	$^{+0.0017}_{-0.0018}$	±0.0007	$^{+0.0006}_{-0.0007}$
Semileptonic background shape	±0.0041	$^{+0.0012}_{-0.0019}$	$^{+0.0015}_{-0.0016}$
Semileptonic D^{**} composition	$^{+0.0075}_{-0.0038}$	$^{+0.0000}_{-0.0017}$	$^{+0.0012}_{-0.0030}$
Semileptonic B^+ background w	$^{+0.0003}_{-0.0004}$	$^{+0.0000}_{-0.0001}$	$^{+0.0001}_{-0.0003}$
Hadronic background fraction	$^{+0.0003}_{-0.0011}$	$^{+0.0015}_{+0.0086}$	$^{+0.0006}_{-0.0005}$
Hadronic background shape	±0.0022	$^{+0.0038}_{-0.0040}$	$^{+0.0005}_{-0.0004}$
Hadronic background mixing	-0.0005	-0.0003	-0.0006
Vertex reconstruction	$^{+0.0025}_{-0.0040}$	$^{+0.0027}_{-0.0041}$	$^{+0.0009}_{-0.0036}$
Resolution function	$^{+0.0053}_{-0.0080}$	$^{+0.0051}_{-0.0097}$	$^{+0.0025}_{-0.0018}$
Total	±0.011	$^{+0.007}_{-0.014}$	$^{+0.003}_{-0.005}$

Table C.3: *Summary of systematic errors for τ_{B^0}, τ_{B^+} and Δm_d.*

Souce	w_1	w_2	w_3	w_4	w_5	w_6
Semileptonic background fraction	±0.0018	±0.0027	$^{+0.0033}_{-0.0032}$	±0.0028	$^{+0.0032}_{-0.0031}$	$^{+0.0020}_{-0.0019}$
Semileptonic background shape	±0.0007	±0.0012	±0.0015	±0.0014	±0.0016	$^{+0.0032}_{-0.0013}$
Semileptonic D^{**} composition	$^{+0.0020}_{-0.0014}$	$^{+0.0009}_{-0.0000}$	$^{+0.0006}_{-0.0009}$	$^{+0.0014}_{-0.0007}$	$^{+0.0010}_{-0.0007}$	$^{+0.0009}_{-0.0001}$
Semileptonic B^+ background w	±0.0013	±0.0009	±0.0010	±0.0007	±0.0008	±0.0003
Hadronic background fraction	$^{+0.0004}_{-0.0003}$	$^{+0.0004}_{-0.0005}$	$^{+0.0008}_{-0.0004}$	$^{+0.0011}_{-0.0003}$	$^{+0.0015}_{-0.0003}$	$^{+0.0005}_{-0.0002}$
Hadronic background shape	±0.0001	$^{+0.0002}_{-0.0001}$	±0.0002	±0.0001	±0.0002	$^{+0.0003}_{-0.0002}$
Hadronic background mixing	$+0.0003$	$+0.0001$	$+0.0007$	$+0.0004$	$+0.0009$	$+0.0006$
Vertex reconstruction	$^{+0.0008}_{-0.0009}$	±0.0008	$^{+0.0006}_{-0.0037}$	$^{+0.0012}_{-0.0009}$	±0.0006	$^{+0.0005}_{-0.0011}$
Resolution function	$^{+0.0002}_{-0.0001}$	$^{+0.0004}_{-0.0006}$	$^{+0.0005}_{-0.0010}$	$^{+0.0006}_{-0.0009}$	$^{+0.0006}_{-0.0008}$	$^{+0.0006}_{-0.0009}$
Total	±0.003	±0.003	$^{+0.004}_{-0.005}$	$^{+0.004}_{-0.003}$	±0.004	$^{+0.004}_{-0.003}$

Table C.4: *Summary of systematic errors for wrong tag probabilities.*

Souce	s^0_{ful}	s^1_{ful}	s^0_{asc}	s^1_{asc}	s_{single}
Semileptonic background fraction	$^{+0.0066}_{-0.0076}$	$^{+0.0002}_{-0.0003}$	$^{+0.0021}_{-0.0019}$	±0.0001	±0.0008
Semileptonic background shape	$^{+0.0193}_{-0.0137}$	$^{+0.0002}_{-0.0003}$	$^{+0.0054}_{-0.0042}$	±0.0001	$^{+0.0054}_{-0.0048}$
Semileptonic D^{**} composition	$^{+0.0152}_{-0.0015}$	$^{+0.0000}_{-0.0002}$	$^{+0.0036}_{-0.0002}$	±0.0000	$^{+0.0009}_{-0.0000}$
Semileptonic B^+ background w	$^{+0.0006}_{-0.0007}$	±0.0000	$^{+0.0003}_{-0.0000}$	±0.0000	±0.0001
Hadronic background fraction	$^{+0.0046}_{-0.0039}$	$^{+0.0006}_{-0.0018}$	$^{+0.0064}_{-0.0003}$	$^{+0.0001}_{-0.0003}$	$^{+0.0040}_{-0.0020}$
Hadronic background shape	$^{+0.0136}_{-0.0132}$	±0.0003	$^{+0.0041}_{-0.0035}$	±0.0001	±0.0033
Hadronic background mixing	$+0.0015$	±0.0000	$+0.0007$	±0.0000	$+0.0004$
Vertex reconstruction	$^{+0.0232}_{-0.0643}$	$^{+0.0173}_{-0.0031}$	$^{+0.0182}_{-0.0246}$	$^{+0.0028}_{-0.0018}$	$^{+0.0068}_{-0.0102}$
Resolution function	$^{+0.0090}_{-0.0087}$	±0.0002	$^{+0.0012}_{-0.0113}$	±0.0005	$^{+0.0445}_{-0.0302}$
Total	$^{+0.038}_{-0.068}$	$^{+0.017}_{-0.004}$	$^{+0.021}_{-0.028}$	$^{+0.003}_{-0.002}$	$^{+0.046}_{-0.032}$

Table C.5: *Summary of systematic errors for detector resolution parameters.*

Souce	$(f_\delta^{mult})_{B^0}$	$(f_\delta^{single})_{B^0}$	$(f_\delta^{mult})_{B^+}$	$(f_\delta^{single})_{B^+}$
Semileptonic background fraction	$^{+0.0013}_{-0.0011}$	±0.0014	$^{+0.0025}_{-0.0020}$	$^{+0.0013}_{-0.0012}$
Semileptonic background shape	±0.0059	$^{+0.0036}_{-0.0034}$	±0.0044	$^{+0.0033}_{-0.0030}$
Semileptonic D^{**} composition	$^{+0.0015}_{-0.0001}$	±0.0011	$^{+0.0026}_{-0.0006}$	$^{+0.0003}_{-0.0002}$
Semileptonic B^+ background w	$^{+0.0001}_{-0.0000}$	$^{+0.0002}_{-0.0000}$	±0.0001	±0.0001
Hadronic background fraction	$^{+0.0028}_{-0.0003}$	$^{+0.0087}_{-0.0007}$	$^{+0.0033}_{-0.0005}$	$^{+0.0011}_{-0.0007}$
Hadronic background shape	$^{+0.0027}_{-0.0023}$	$^{+0.0028}_{-0.030}$	$^{+0.0047}_{-0.0044}$	$^{+0.0053}_{-0.0055}$
Hadronic background mixing	$+0.0002$	$+0.0001$	$+0.0005$	$+0.0002$
Vertex reconstruction	$^{+0.0046}_{-0.0143}$	$^{+0.0103}_{-0.0041}$	$^{+0.0301}_{-0.0086}$	$^{+0.0131}_{-0.0121}$
Resolution function	$^{+0.0309}_{-0.0326}$	$^{+0.0563}_{-0.0573}$	$^{+0.0326}_{-0.0367}$	$^{+0.0540}_{-0.0543}$
Total	$^{+0.032}_{-0.036}$	±0.058	$^{+0.046}_{-0.046}$	±0.056

Table C.6: *Summary of systematic errors for prompt component fractions of R_{np}.*

Souce	f_{ol}^{mult}	f_{ol}^{single}	σ_{ol}(ps)
Semileptonic background fraction	$\binom{+0.22}{-0.37} \times 10^{-4}$	$\binom{+0.24}{-0.11} \times 10^{-4}$	$^{+0.02}_{-0.12}$
Semileptonic background shape	$\pm 0.01 \times 10^{-4}$	$\binom{+0.24}{-0.26} \times 10^{-4}$	$^{+0.04}_{-0.06}$
Semileptonic D^{**} composition	$\pm 0.01 \times^{-4}$	$\binom{+0.10}{-0.14} \times 10^{-4}$	± 0.02
Semileptonic B^+ background w	$\pm 0.00 \times 10^{-4}$	$\binom{+0.02}{-0.01} \times 10^{-4}$	$^{+0.00}_{-0.01}$
Hadronic background fraction	$\binom{+0.35}{-0.34} \times 10^{-4}$	$\binom{+5.6}{-4.2} \times 10^{-4}$	$^{+0.21}_{-1.36}$
Hadronic background shape	$\binom{+0.05}{-0.06} \times 10^{-4}$	$\binom{+1.3}{-1.7} \times 10^{-4}$	$^{+0.20}_{-0.21}$
Hadronic background mixing	$+0.02 \times 10^{-4}$	$+0.08 \times 10^{-4}$	-0.02
Vertex reconstruction	$\binom{+1.33}{-0.47} \times 10^{-4}$	$\binom{+1.8}{-5.4} \times 10^{-3}$	$^{+0.88}_{-10.7}$
Resolution function	$\pm 0.03 \times 10^{-4}$	$\binom{+5.1}{-6.3} \times 10^{-4}$	$^{+0.84}_{-0.67}$
Total	$\binom{+1.4}{-0.7} \times 10^{-4}$	$\binom{+2.0}{-5.4} \times 10^{-3}$	$^{+1.2}_{-10.8}$

Table C.7: *Summary of systematic errors for fractions and width of the outlier.*

Parameter	Value
τ_{B^0}(ps)	$1.538 \pm 0.011 \pm 0.011$
τ_{B^+}(ps)	$1.661 \pm 0.015^{+0.007}_{-0.014}$
Δm_d(ps^{-1})	$0.509 \pm 0.006^{+0.003}_{-0.005}$
w_1	$0.457 \pm 0.005 \pm 0.003$
w_2	$0.332 \pm 0.008 \pm 0.003$
w_3	$0.224 \pm 0.009^{+0.004}_{-0.005}$
w_4	$0.156^{+0.008+0.004}_{-0.007-0.003}$
w_5	$0.108 \pm 0.008 \pm 0.004$
w_6	$0.016 \pm 0.005^{+0.004}_{-0.003}$
s^0_{ful}	$0.969^{+0.074+0.038}_{-0.077-0.068}$
s^1_{ful}	$0.085^{+0.005+0.017}_{-0.004-0.004}$
s^0_{asc}	$0.799 \pm 0.032^{+0.003}_{-0.002}$
s^1_{asc}	$0.043 \pm 0.002^{+0.003}_{-0.002}$
s_{single}	$0.913 \pm 0.032^{+0.046}_{-0.032}$
$(f_\delta^{mult})_{B^0}$	$0.555 \pm 0.025^{+0.032}_{-0.036}$
$(f_\delta^{single})_{B^0}$	$0.666^{+0.026}_{-0.027} \pm 0.058$
$(f_\delta^{mult})_{B^+}$	$0.450 \pm 0.040^{+0.046}_{-0.038}$
$(f_\delta^{single})_{B^+}$	$0.731^{+0.040}_{-0.042} \pm 0.056$
f_{ol}^{mult}	$(1.8 \pm 0.8^{+1.4}_{-0.7}) \times 10^{-4}$
f_{ol}^{single}	$(2.7 \pm 0.1^{+0.2}_{-0.5}) \times 10^{-2}$
σ_{ol}(ps)	$39.0^{+2.5+1.2}_{-2.1-10.8}$

Table C.8: *Parameters determined by the lifetime and B^0-$\overline{B}^0$ mixing analysis. First errors are statistical and second are systematic.*

Appendix D

Signal Fraction Determination by ΔE-M_{bc} Fit

Signal fractions are determined by a fit to the ΔE-M_{bc} distribution of $B^0 \to \eta' K_S$ candidate events. We show the detailed fit result in this Appendix.

D.1 ΔE-M_{bc} Fit

The ΔE-M_{bc} distribution of $B^0 \to \eta' K_S$ candidate events are fitted by an unbinned maximum likelihood method using the following PDF

$$PDF(\Delta E, M_{bc}) = f_{sig}^{ave} F_{sig}(\Delta E, M_{bc}) + f_{B\overline{B}}^{ave} F_{B\overline{B}}(\Delta E, M_{bc}) + f_{cont}^{ave} F_{cont}(\Delta E, M_{bc}), \quad (D.1)$$

where f_X^{ave} and F_X are average fraction and PDF described in Section 5.2.3 for each of signal, $B\overline{B}$ and continuum background. These fractions are defined to be $\sum f_X^{ave} = 1$. To maximize the sensitivity for the CP analysis, different signal and background fractions are used for each of two LR bins and six flavor tagging quality r bins, while we use same signal and background ΔE-M_{bc} shapes for all LR and r bins. The fit are performed on 852 (3211) events in $|\Delta E| < 0.25$ GeV and $5.2\mathrm{GeV}/c^2 < M_{bc}$ for the $\eta' \to \eta\pi^+\pi^-$ ($\eta' \to \rho^0\gamma$) mode, and f_X^{ave} is defined as a fraction in this ΔE-M_{bc} region. In total, 12 signal fractions and 2 continuum PDF parameters are determined simultaneously in the fit for each η' decay mode.

D.2 Results

Table D.1 and D.2 show obtained f_{sig}^{ave} for each LR and r bins together with background fractions and projections of them on the signal region. Figure D.1 and D.1 show the ΔE-M_{bc} distribution with the fit result projected on two LR bins. The ΔE-M_{bc} distribution and the fit result projected on each LR and r bin is shown in Figure D.3, D.4, D.5 and D.6. Integrating PDFs, the signal yield and the average purity in the signal region is estimated to be 52 ± 9 (95 ± 12) and 57% (48%) for the $\eta' \to \eta\pi^+\pi^-$ ($\eta' \to \rho^0\gamma$) mode, respectively.

	r bin	N_{fit}	f^{ave}_{sig}	$f^{ave}_{B\overline{B}}$	f^{ave}_{cont}	N_{cand}	N_{sig}	$f^{s.r.}_{sig}$	$f^{s.r}_{B\overline{B}}$	$f^{s.r}_{cont}$
	$l=1$	379	$(2.8\pm1.1)\times10^{-2}$	$(0.7\pm0.4)\times10^{-2}$	0.97 ± 0.01	27	10.3 ± 4.1	0.36	0.01	0.63
	$l=2$	100	$(1.4\pm1.9)\times10^{-2}$	$(1.1\pm1.2)\times10^{-2}$	0.98 ± 0.02	9	1.3 ± 1.9	0.21	0.01	0.78
$\eta'\to\eta\pi^+\pi^-$	$l=3$	69	$(0.0\pm0.9)\times10^{-2}$	$(0.0\pm1.0)\times10^{-2}$	1.00 ± 0.01	3	0.0 ± 0.6	0.00	0.00	1.00
low LR	$l=4$	62	$(1.5\pm2.2)\times10^{-2}$	$(0.0\pm1.1)\times10^{-2}$	0.99 ± 0.02	3	0.9 ± 1.3	0.24	0.00	0.76
	$l=5$	45	$(0.0\pm3.1)\times10^{-2}$	$(1.2\pm2.1)\times10^{-2}$	0.99 ± 0.04	2	0.0 ± 1.4	0.00	0.02	0.98
	$l=6$	14	$(0.0\pm3.5)\times10^{-2}$	$(3.9\pm6.9)\times10^{-2}$	0.96 ± 0.08	0	0.0 ± 0.5	0.00	0.06	0.94
	$l=1$	100	0.16 ± 0.04	$(3.2\pm1.8)\times10^{-2}$	0.80 ± 0.04	21	16.0 ± 4.3	0.79	0.01	0.20
	$l=2$	26	0.12 ± 0.07	$(4.2\pm4.7)\times10^{-2}$	0.84 ± 0.09	5	2.9 ± 1.9	0.71	0.02	0.27
$\eta'\to\eta\pi^+\pi^-$	$l=3$	21	0.22 ± 0.09	$(2.6\pm4.5)\times10^{-2}$	0.75 ± 0.11	5	4.5 ± 2.2	0.85	0.01	0.14
high LR	$l=4$	16	0.31 ± 0.12	0.14 ± 0.10	0.55 ± 0.16	6	4.8 ± 2.4	0.89	0.03	0.08
	$l=5$	11	0.34 ± 0.15	0.10 ± 0.12	0.56 ± 0.19	4	3.7 ± 2.0	0.91	0.02	0.07
	$l=6$	9	0.92 ± 0.12	0.06 ± 0.11	0.02 ± 0.16	8	8.0 ± 3.5	0.99	0.01	0.00
Total		852				93	52.5 ± 8.5	0.57	0.01	0.42

Table D.1: *Signal, $B\overline{B}$ and continuum background fractions in each r and LR bin for the $\eta'\to\eta\pi^+\pi^-$ mode. The Signal fraction f^{ave}_{sig} is obtained from the ΔE-M_{bc} fit. The $B\overline{B}$ background fraction $f^{ave}_{B\overline{B}}$ is estimated from 157 million $B\overline{B}$ MC sample. The continuum background fraction f^{ave}_{cont} is calculated by $1-f^{ave}_{sig}-f^{ave}_{B\overline{B}}$. Each f^{ave}_X is defined as its fraction in $|\Delta E|<0.25GeV$ and $5.2GeV/c^2<M_{bc}<5.3GeV/c^2$. The N_{fit} is the number of events in $|\Delta E|<0.25GeV$ and $5.2GeV/c^2<M_{bc}<5.3GeV/c^2$ used for the ΔE-M_{bc} fit. The N_{cand} is the number of events in the signal region. The N_{sig} is the signal yield calculated by integrating the signal PDF in the signal region. The $f^{s.r}_X$ is the fraction of signal, $B\overline{B}$ and continuum background in the signal region calculated as the ratio of the integral of their PDFs in the signal region.*

	r bin	N_{fit}	f^{ave}_{sig}	$f^{ave}_{B\overline{B}}$	f^{ave}_{cont}	N_{cand}	N_{sig}	$f^{s.r}_{sig}$	$f^{s.r}_{B\overline{B}}$	$f^{s.r}_{cont}$
	$l=1$	1186	$(0.1\pm0.3)\times10^{-2}$	$(5.5\pm0.5)\times10^{-2}$	0.95 ± 0.01	44	0.9 ± 3.8	0.02	0.07	0.91
	$l=2$	305	$(2.9\pm1.2)\times10^{-2}$	$(7.8\pm1.3)\times10^{-2}$	0.89 ± 0.02	19	8.3 ± 3.6	0.46	0.05	0.49
$\eta'\to\rho^0\gamma$	$l=3$	194	$(1.6\pm1.2)\times10^{-2}$	$(8.4\pm1.6)\times10^{-2}$	0.90 ± 0.02	11	3.0 ± 2.3	0.32	0.07	0.61
low LR	$l=4$	177	$(2.7\pm1.7)\times10^{-2}$	$(8.5\pm1.7)\times10^{-2}$	0.89 ± 0.02	12	4.6 ± 2.9	0.44	0.06	0.50
	$l=5$	104	$(0.0\pm1.2)\times10^{-2}$	$(5.7\pm2.1)\times10^{-2}$	0.94 ± 0.02	3	0.0 ± 1.2	0.00	0.07	0.93
	$l=6$	29	$(3.8\pm4.2)\times10^{-2}$	0.26 ± 0.09	0.70 ± 0.10	2	1.0 ± 1.2	0.52	0.15	0.33
	$l=1$	729	$(4.6\pm0.9)\times10^{-2}$	0.12 ± 0.01	0.84 ± 0.01	51	31.7 ± 6.3	0.58	0.06	0.36
	$l=2$	181	$(7.1\pm2.2)\times10^{-2}$	0.16 ± 0.02	0.77 ± 0.03	17	12.2 ± 3.8	0.68	0.06	0.26
$\eta'\to\rho^0\gamma$	$l=3$	106	$(5.2\pm2.6)\times10^{-2}$	0.19 ± 0.04	0.76 ± 0.04	10	5.2 ± 2.7	0.61	0.09	0.30
high LR	$l=4$	105	$(6.3\pm3.0)\times10^{-2}$	0.17 ± 0.03	0.77 ± 0.04	9	6.3 ± 3.0	0.66	0.07	0.27
	$l=5$	68	0.13 ± 0.05	0.14 ± 0.04	0.73 ± 0.06	9	8.1 ± 3.1	0.80	0.04	0.16
	$l=6$	27	0.51 ± 0.10	0.30 ± 0.10	0.19 ± 0.15	14	13.2 ± 3.6	0.97	0.02	0.01
Total		3211				201	94.6 ± 11.7	0.48	0.06	0.46

Table D.2: *Signal, $B\overline{B}$ background and continuum background fractions in each r and LR bin for the $\eta'\to\rho^0\gamma$ mode. Parameter definitions are same as Table D.1.*

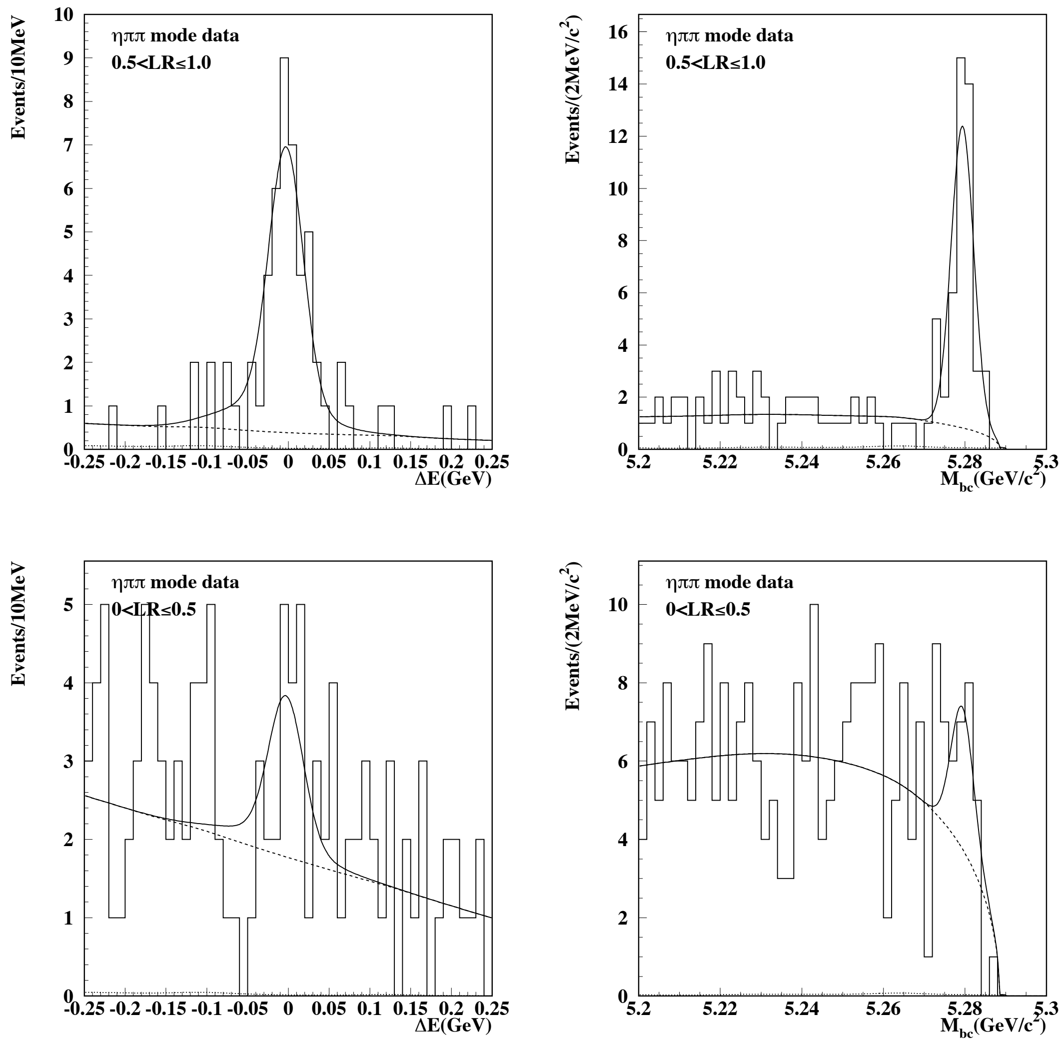

Figure D.1: ΔE and M_{bc} distributions of the reconstructed $B^0 \to \eta' K_S$ candidates for the $\eta' \to \eta\pi^+\pi^-$ mode. Solid lines are the fit result. Dotted lines are the $B\overline{B}$ background component. Dashed lines are the sum of the $B\overline{B}$ background and the continuum background. Upper figures are for $0.0 < LR \leq 0.5$ and lower figures are for $0.5 < LR \leq 1.0$.

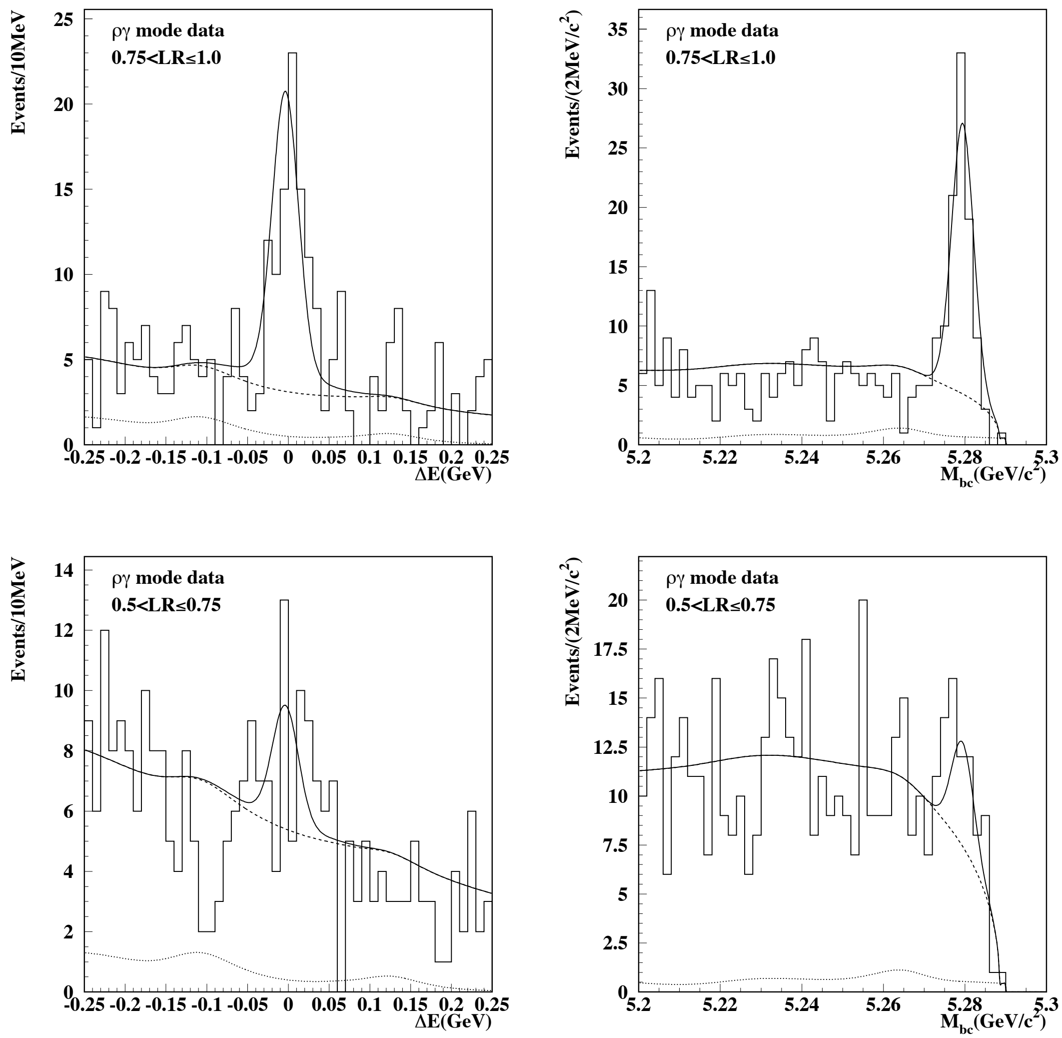

Figure D.2: ΔE and M_{bc} *distributions of the reconstructed* $B^0 \to \eta' K_S$ *candidates for the* $\eta' \to \rho^0\gamma$ *mode. Solid lines are the fit result. Dotted lines are the* $B\overline{B}$ *background component. Dashed lines are the sum of the* $B\overline{B}$ *background and the continuum background. Upper figures are for* $0.5 < LR \leq 0.75$ *and lower figures are for* $0.75 < LR \leq 0.5$.

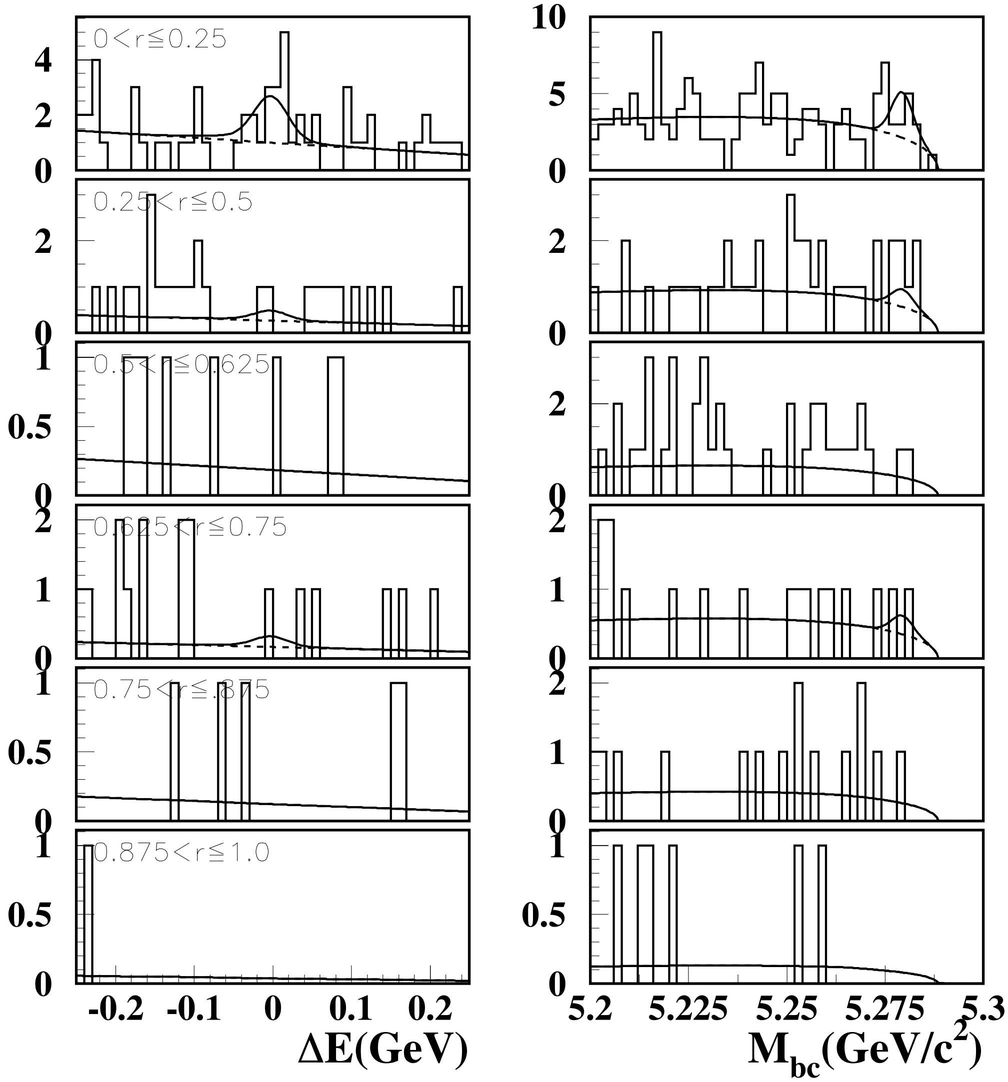

Figure D.3: *ΔE distributions (left) and M_{bc} distributions (right) of the reconstructed $B^0 \to \eta' K_S$ ($\eta' \to \eta\pi^+\pi^-$) candidates with $0. < LR \leq 0.5$ divided in six flavor tagging quality (r) bins. Solid lines show the fit result and dashed lines show the background component.*

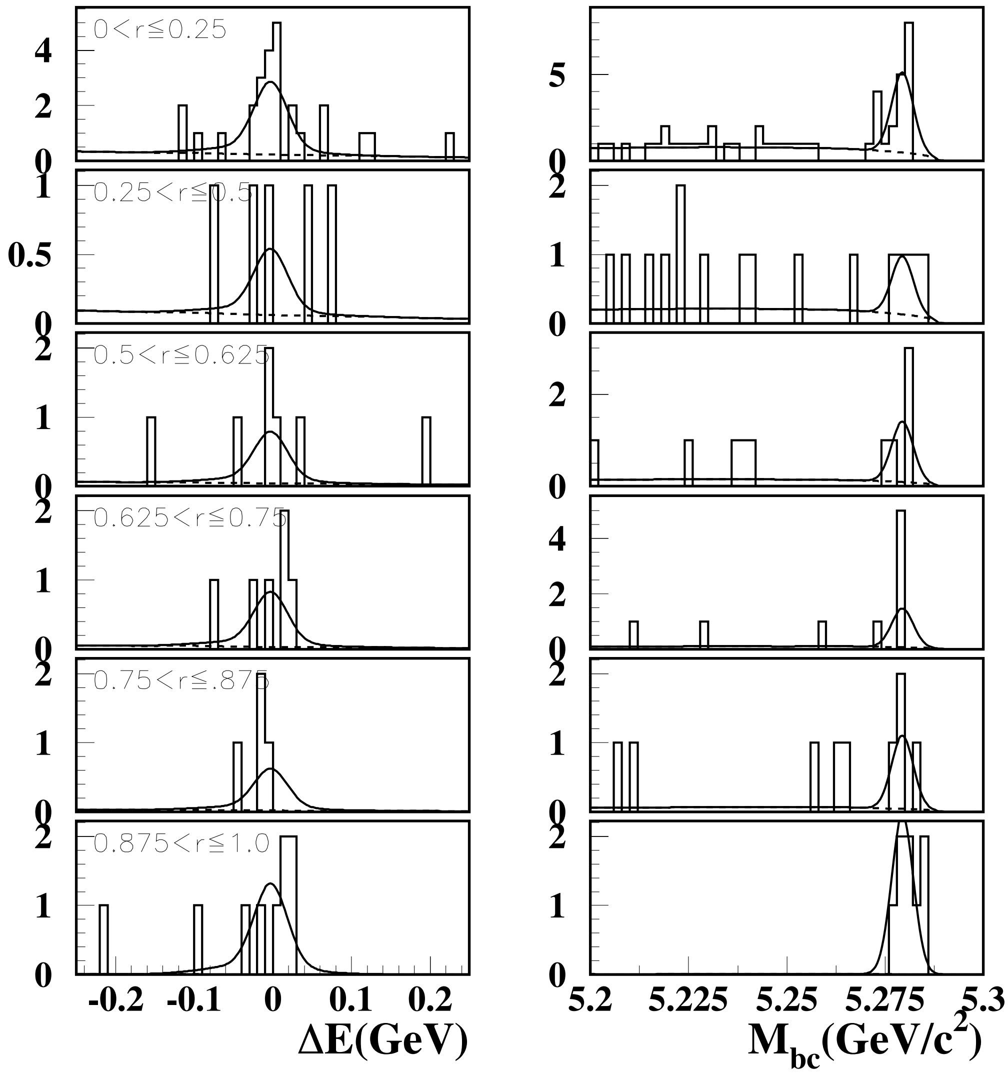

Figure D.4: ΔE *distributions (left) and* M_{bc} *distributions (right) of the reconstructed* $B^0 \to \eta' K_S$ ($\eta' \to \eta\pi^+\pi^-$) *candidates with* $0.5 < LR \leq 1.0$ *divided in six flavor tagging quality* (r) *bins. Solid lines show the fit result and dashed lines show the background component.*

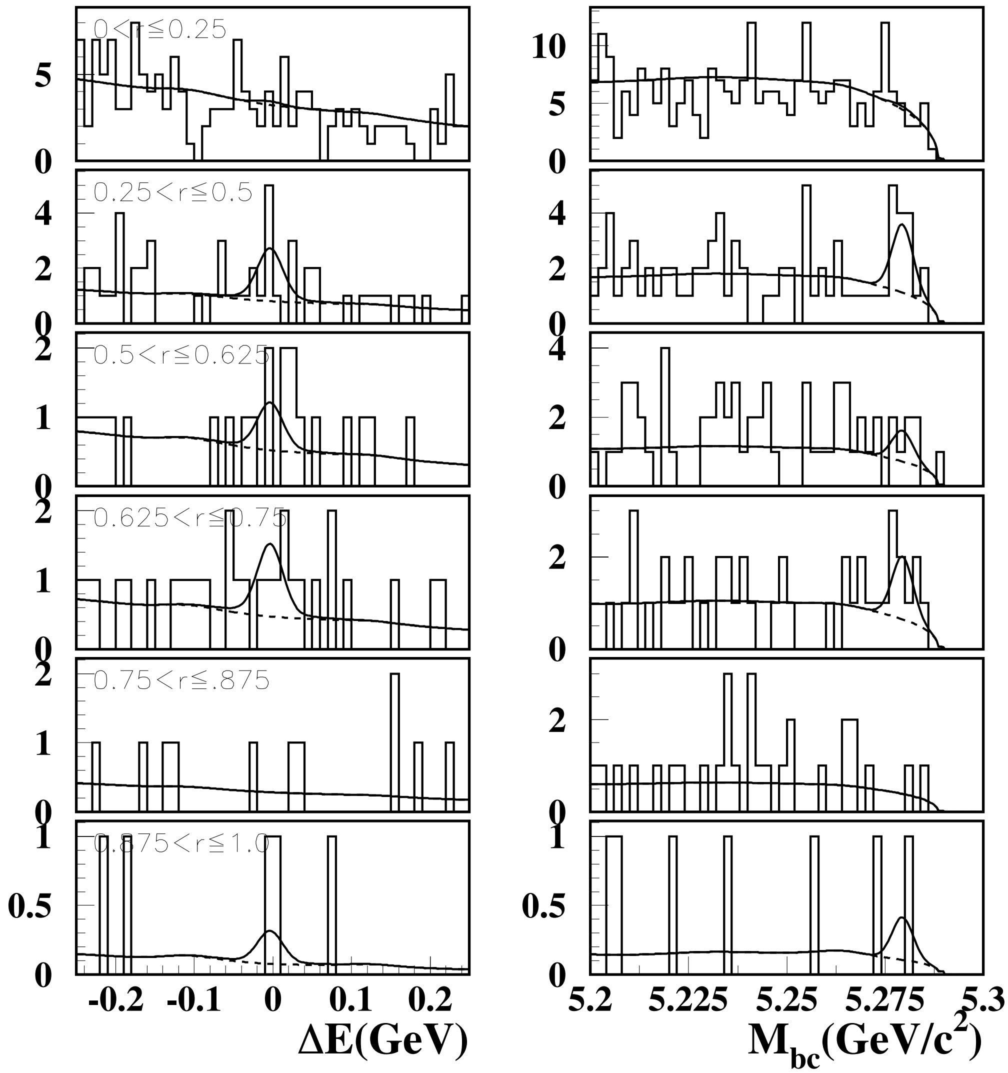

Figure D.5: ΔE *distributions (left) and* M_{bc} *distributions (right) of the reconstructed* $B^0 \to \eta' K_S$ $(\eta' \to \rho^0\gamma)$ *candidates with* $0.5 < LR \leq 0.75$ *divided in six flavor tagging quality (r) bins. Solid lines show the fit result and dashed lines show the background component.*

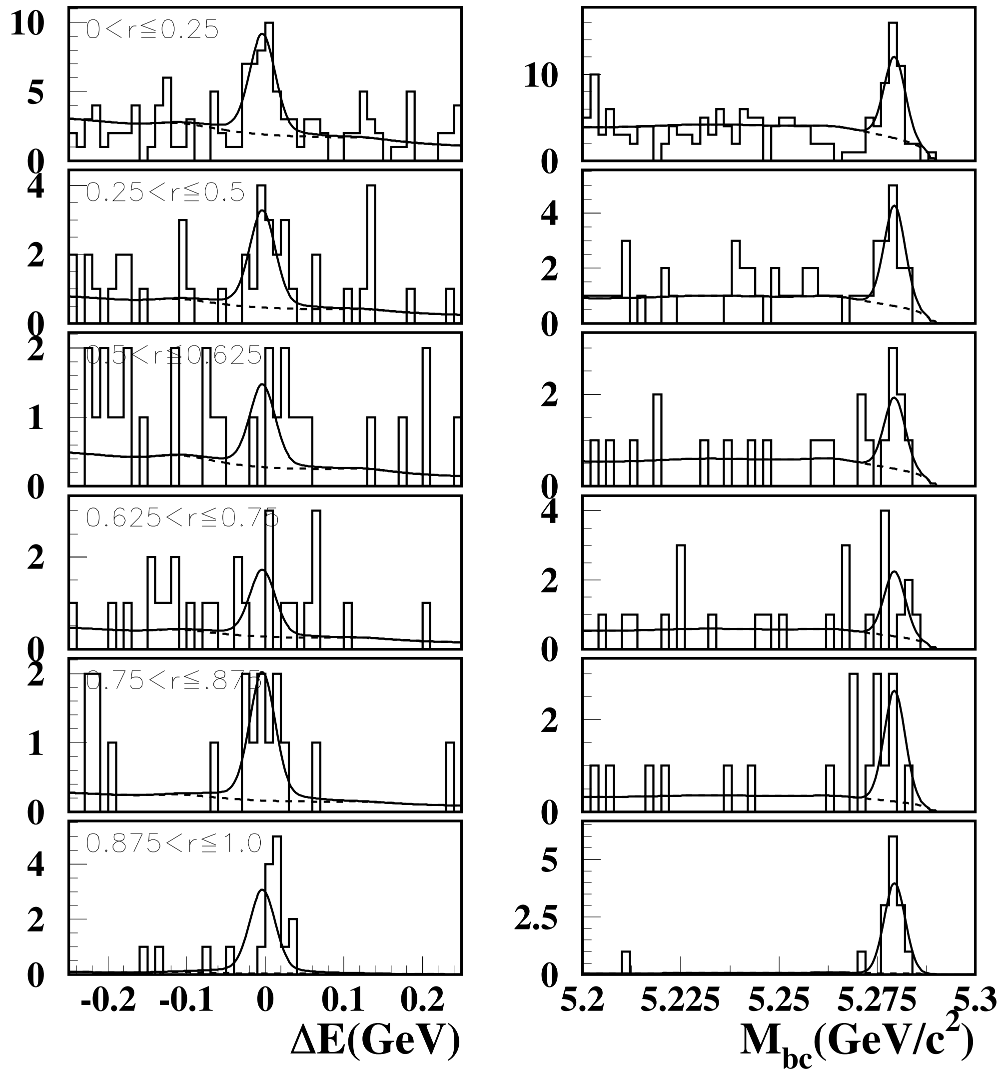

Figure D.6: ΔE *distributions (left) and* M_{bc} *distributions (right) of the reconstructed* $B^0 \to \eta' K_S$ $(\eta' \to \rho^0\gamma)$ *candidates with* $0.75 < LR \leq 1.0$ *divided in six flavor tagging quality (r) bins. Solid lines show the fit result and dashed lines show the background component.*

Appendix E

$B^+ \to \eta' K^+$ Analysis

ΔE and M_{bc} means and widths of $B^0 \to \eta' K_S$ decays are calibrated with $B^+ \to \eta' K^+$ decays. $B^+ \to \eta' K^+$ decays are also used for the validity check of the CP asymmetry analysis. In this appendix, we describe the reconstruction of $B^+ \to \eta' K^+$ decays and the procedure of the ΔE and M_{bc} correction factor determination.

E.1 Reconstruction of $B^+ \to \eta' K^+$

$B^+ \to \eta' K^+$ decays are reconstructed with the same criteria as the $B^0 \to \eta' K_S$ except for using charged track identified as Kaon instead of K_S. Figure E.1 shows M_{bc} and ΔE distribution of reconstructed $B^+ \to \eta' K^+$ candidates. 240 events for the $\eta' \to \eta\pi^+\pi^-$ mode and 509 events for the the $\eta' \to \rho^0\gamma$ mode remain in the signal region.

E.2 Determination of ΔE and M_{bc} Shape Correction

We obtained the mean shift and width corrections by fitting the ΔE and M_{bc} shape of $B^+ \to \eta' K^+$ candidates with the following signal PDF

$$\begin{aligned} F_{sig}(\Delta E, M_{bc}) \equiv\ & G(M_{bc}; \mu_{M_{bc}}+\delta_\mu^{M_{bc}}, (1+\delta_\sigma^{M_{bc}})\sigma_{M_{bc}}) \times [f_g G(\Delta E; \mu_{\Delta E}+\delta_\mu^{\Delta E}, (1+\delta_\sigma^{M_{bc}})\sigma_{M_{bc}}) \\ & + (1-f_g) G_{bif}(\Delta E; \mu_{bif}^{\Delta E} + \delta_\mu^{\Delta E}, (1+\delta_\sigma^{\Delta E})\sigma_h^{\Delta E}, (1+\delta_\sigma^{\Delta E})\sigma_l^{\Delta E})], \quad \text{(E.1)} \end{aligned}$$

where $\delta_\mu^{M_{bc}(\Delta E)}$ and $\delta_\sigma^{M_{bc}(\Delta E)}$ are the mean shift and the width correction for $M_{bc}(\Delta E)$, respectively, the means $\mu_{M_{bc}(\Delta E)}$ and widths $\sigma_{M_{bc}(\Delta E)}$ are determined with the $B^+ \to \eta' K^+$ MC. For background PDF, we use the same $B\overline{B}$ background PDF as that for $B^0 \to \eta' K_S$ and the same function with different parameter values for continuum background. We determine correction factors separately for the $\eta' \to \eta\pi^+\pi^-$ mode and the $\eta' \to \rho^0\gamma$ mode. Figure E.2 shows the ΔE and M_{bc} distributions for $B^+ \to \eta' K^+$ candidates with the fit result overlaid. Signal yield and purity in the signal region estimated by the fit are shown in Table E.1. Obtained mean shifts and width corrections are summarized in Table E.2.

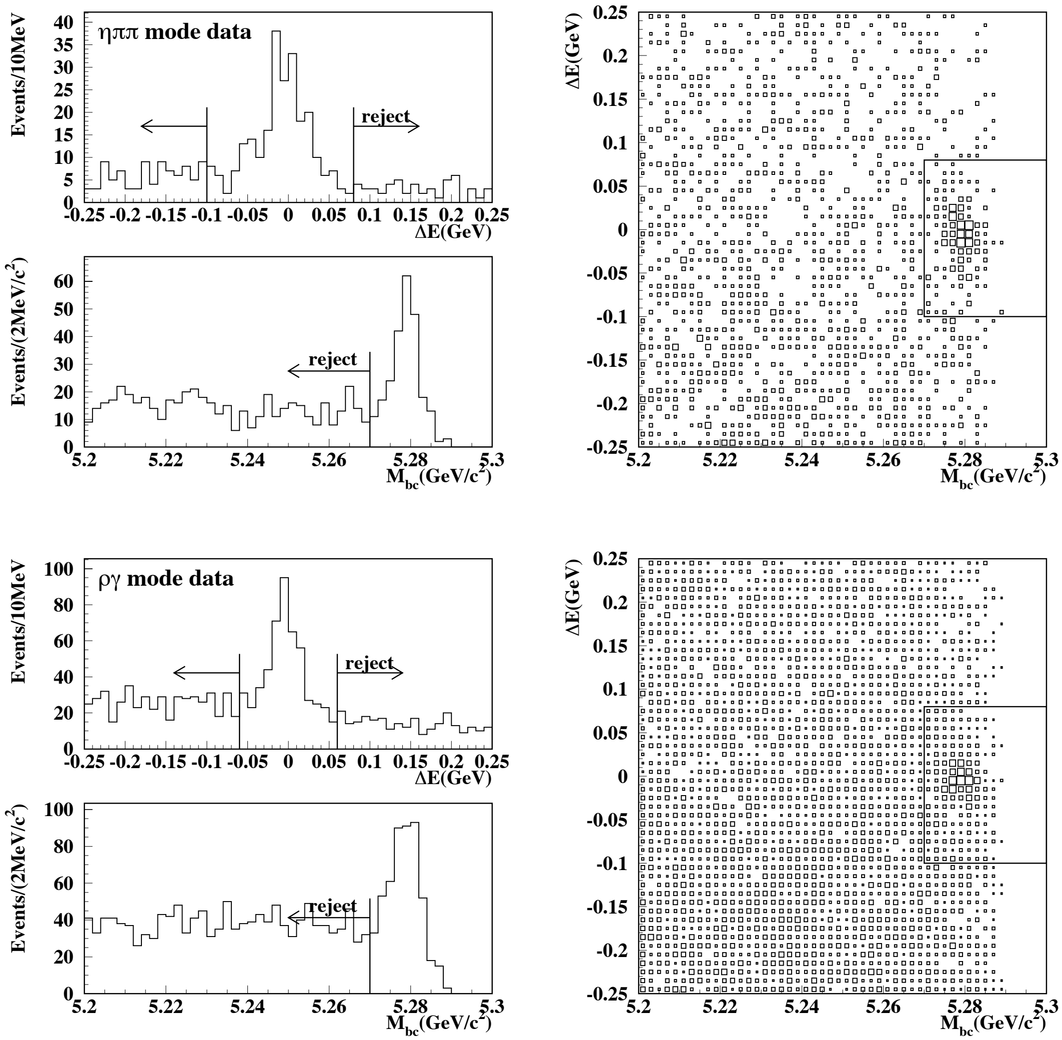

Figure E.1: ΔE *and* M_{bc} *distributions of* $B^+ \to \eta' K^+$ *candidates. The box in the* ΔE-M_{bc} *two dimensional plot shows the signal region. The upper figures are for the* $\eta' \to \eta\pi^+\pi^-$ *mode and the lower figures are for the* $\eta' \to \rho^0\gamma$ *mode.*

η' Mode	N_{cand}	N_{sig}	f_{sig}	$f_{B\overline{B}}$	f_{cont}
$\eta' \to \eta\pi^+\pi^-$	240	171.3 ± 14.1	0.69	0.00	0.31
$\eta' \to \rho^0\gamma$	508	272.2 ± 19.2	0.54	0.03	0.43

Table E.1: *Signal yields and signal and background fractions in the signal region for the* $B^+ \to \eta' K^+$ *candidates. The* N_{cand} *is the number of candidates in the signal region. The* N_{sig} *is the signal yield in the signal region obtained by the fit. Each* f_X *shows fraction of signal,* $B\overline{B}$ *or continuum background calculated as the ratio of the integral of the PDFs in the signal region.*

	ΔE		M_{bc}	
η' Mode	mean shift	width correction	mean shift	width correction
$\eta' \to \eta\pi^+\pi^-$	$(0.2^{+2.3}_{-2.5})$MeV	$(+2.8^{+11.5}_{-11.0})\%$	$(0.2 \pm 0.2)\mathrm{MeV}/c^2$	$(-10.9^{+6.3}_{-5.8})\%$
$\eta' \to \rho^0\gamma$	(-3.6 ± 1.3)MeV	$(+15.7^{+8.6}_{-8.3})\%$	$(0.1 \pm 0.2)\mathrm{MeV}/c^2$	$(-5.2^{+6.2}_{-5.9})\%$

Table E.2: ΔE and M_{bc} *width corrections and mean shifts obtained by study of* $B^+\eta' K_S$ *decays with real data and MC. The errors include both statistical and systematic.*

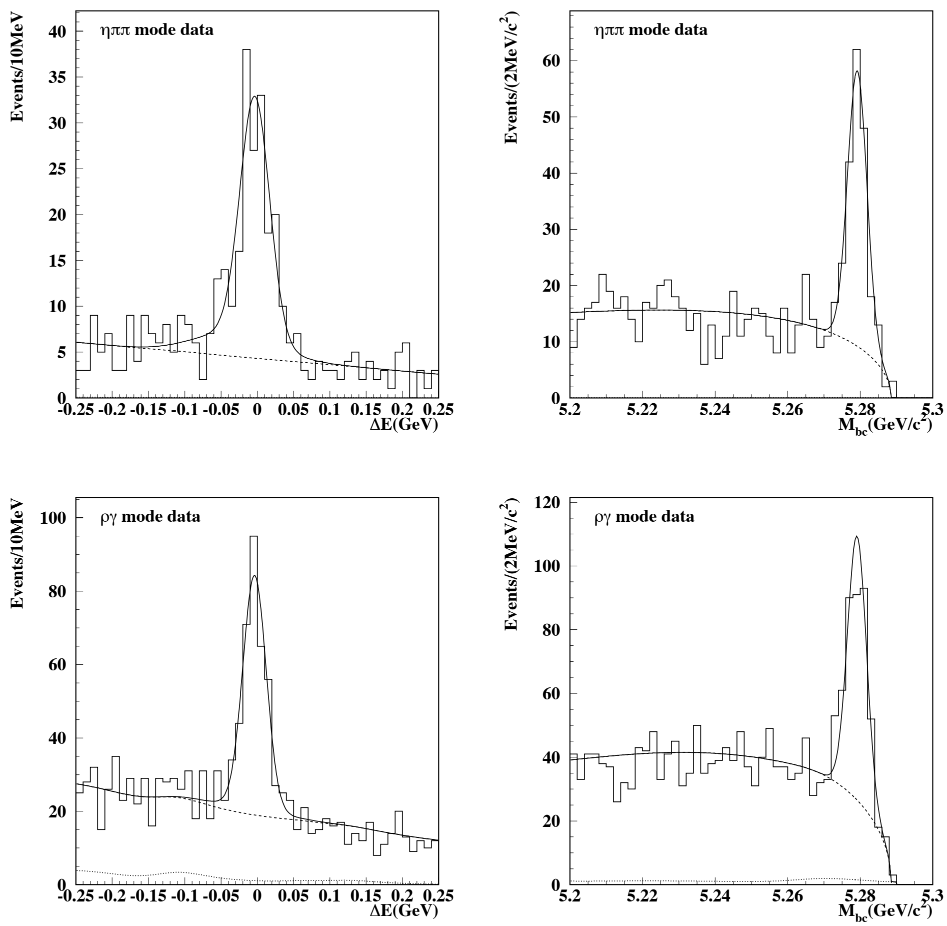

Figure E.2: *The* ΔE *and* M_{bc} *distributions of the reconstructed* $B^+ \to \eta' K^+$ *candidates. Upper figures are for the* $\eta' \to \eta\pi^+\pi^-$ *mode and lower figures are for* $\eta' \to \rho^0\gamma$ *mode. Solid lines are the result of the unbinned maximum likelihood fit. Dotted lines are the* $B\overline{B}$ *background component. Dashed lines are the sum of the* $B\overline{B}$ *background and the continuum background.*

Bibliography

[1] I. I. Bigi and A. I. Sanda, CP Violation, Cambridge University Press (2000).

[2] M. Neubert, Talk given at XX International Symposium on Lepton and Photon Interactions at High Energies (2001), http:www.lp01.infn.it/proceedings/neubert.pdf.

[3] L. H. Christenson, J. W. Cronin, V. L. Fitch, and R. Turlay, Phys. Rev. Lett. **13**, 138 (1964).

[4] Gaillard *et al.*, Phys. Rev. Lett. **18**, 20 (1967); Cronin *et al.*, Phys. Rev. Lett. **18**, 25 (1967).

[5] S. Bennett *et al.*, Phys. Rev. Lett. **19**, 993 (1967).

[6] D. Dorfan *et al.*, Phys. Lett. **19**, 983 (1967).

[7] A. Alavi-Hrati *et al.*, Phys. Rev. Lett. **83**, 22 (1999).

[8] K. Abe *et al.* (Belle Collaboration), Phys. Rev. Lett. **87**, 091802 (2001);
K. Abe *et al.* (Belle Collaboration), Phys. Rev. **D66**, 032007 (2002).

[9] B. Aubert *et al.* (BaBar Collaboration), Phys. Rev. Lett. **87**, 091801 (2001);
B. Aubert *et al.* (BaBar Collaboration) Phys. Rev. **D66** 032003 (2002).

[10] K. Abe *et al.* (Belle Collaboration), Phys. Rev. **D66**, 071102 (2002).

[11] B. Aubert *et al.* (BaBar Collaboration), Phys. Rev. Lett. **89**, 201802 (2002).

[12] B.H. Behrens *et al.*, Phys. Rev. Lett. **80**,3710 (1998).

[13] S. J. Richichi *et al.* (CLEO Collaboration), Phys. Rev. Lett. **85**, 520 (2000).

[14] B. Aubert *et al.* (BaBar Collaboration), Phys. Rev. Lett. **87**, 221802 (2001).

[15] K. Abe *et al.* (Belle Collaboration), Phys. Lett. **B517**, 309 (2001).

[16] K. Hagiwara *et al.* (Particle Data Group), Phys. Rev. **D66**, 010001 (2002).

[17] E. Kou and A. I. Sanda, Phys. Lett. **B525**, 240 (2002).

[18] A. Ali, G. Kramer, and C.-D. Lu, Phys. Rev. **D58**, 094009 (1998).

[19] Y.-H. Chen, H.-Y. Cheng, B.Tseng, and K.-C. Yang, Phys. Rev. **D60**, 094014.

[20] H.-Y. Cheng and K.C. Yang, Phys. Rev. **D62**, 054029.

[21] T. E. Browder *et al.* (CLEO Collaboration), Phys. Rev. Lett. **81**, 1786 (1998).

[22] X.-G.He A. Datta and S. Pakvasa, Phys. Lett. **B419**, 369 (1998).

[23] M. Kobayashi and T. Maskawa, Prog. Theor. Phys. **49**, 652 (1973).

[24] L. Wolfenstein, Phys. Rev. Lett. **51**, 1945 (1983).

[25] T. Inami and C.S. Lim, Prog. Theor. Phys., **65**,297(1981).

[26] F. Gilman and M. Wise, Phys. Rev. **D27**,1128 (1983).

[27] M. Jamin A. J. Buras and P. H. Weisz, Nucl. Phys. **B347**, 491 (1990).

[28] J. S. Hagelin, Nucl. Phys. **B193**,123 (1981).

[29] A. Ali, G. Kramer, and C.-D. Lu, Phys. Rev. **D59**, 014005 (1999).

[30] D. London and A. Soni, Phys. Lett. **B407**, 61 (1997).

[31] Y. Grossman, G. Isidori, and M. P. Worah, Phys. Rev. **D58**, 057504 (1998).

[32] S. Khalil and E. Kou, Phys. Rev. **D67**, 055009 (2003).

[33] M. B. Causse and J. Orloff, Eur. Phys. J. **C23** 749 (2002).

[34] F. Gabbiani, E. Gabrielli, A. Masiero, and L. Silvestrini, Nucl. Phys. **B477**, 321 (1996).

[35] M. Leurer, Y. Nir, and N. Seiberg, Nucl. Phys. **B420** 468 (1994).

[36] A. Arhrib, C. K. Chua, and W. S. Hou, Phys. Rev. **D65** 017701 (2002).

[37] Y. Nir, hep-ph/0208080 (2002).

[38] T. Moroi, Phys. Lett. **B493**, 366 (2000).

[39] D. Chang, A. Masiero, and H. Murayama, hep-ph/0205111 (2002).

[40] Y. Fukuda *et al.* (Super-Kamiokande Collabolation), Phys. Rev. Lett. **81**,1562 (1998).

[41] A. Hocker, H. Lacker, S. Laplace, and F. Le Diberder, Eur.Phys.J. **C21** 225 (2001) ;CKM fitter web page: `http://ckmfitter.in2p3.fr`.

[42] K. Ackerstaff *et al.* (OPAL Collaboration), Eur. Phys. J. **C5** 379 (1998).

[43] R. Barate *et al.* (ALEPH Collaboration), Phys. Lett. **B492**, 259 (2000).

[44] T. Affolder *et al.* (CDF Collaboration), Phys. Rev. **D61**, 072005 (2000).

[45] K.-F. Chen and K. Hara *et al.* (Belle Collaboration), Phys. Lett. **B546**, 196 (2002).

[46] Belle publications web page, http://belle.kek.jp/belle/publications.html.

[47] E. Kikutani ed., KEK Preprint 2001-157 (2001), to appear in Nucl. Instr. and Meth. A.

[48] A. Abashian *et al.* (Belle Collaboration), Nucl. Instr. and Meth. **A 479** (2002) 117.

[49] V. Chabaud *et al.*, Nucl. Instr. and Meth. **A368**, 314 (1996).

[50] E. Nygård *et al.*, Nucl. Instr. and Meth. **A301**, 506 (1991).

[51] O. Toker *et al.*, Nucl. Instr. and Meth. **A340**, 572 (1994).

[52] G. Alimonti *et al.*, Nucl. Instr. and Meth. **A453**, 71 (2000).

[53] K. Hanagaki *et al.*, Nucl. Instr. and Meth. **A485**, 490 (2002).

[54] A. Abashian *et al.*, Nucl. Instr. and Meth. **A491**, 69 (2002).

[55] HBOOK, CERN Program Library Long Writeup Y250 (1993).

[56] QQ event generator, `http://www.lns.cornell.edu/public/CLEO/soft/QQ`.

[57] The EvtGen package home page,`http://hep.ucsb.edu/people/lange/EvtGen/`.

[58] D. J. Lange, Nucl. Instr. and Meth. **A462**, 152 (2001).

[59] R. Itoh, "QQ quick reference for Belle": `http://belle.kek.jp/~software/qq/html/belle_qq.html` (1996).

[60] GEANT detector Description and Simulation Tool, CERN Program Library Long Writeup W5013 (1993).

[61] B. Casey, Belle note 296 and 390, unpublished.

[62] R.A. Fisher, Annals of Eugenics **7**, 179 (1936).

[63] G. Fox and S. Wolfram, Phys. Rev. Lett. **41**, 1581 (1978).

[64] K.-F. Chen *et al.*, Belle note 329, unpublished.

[65] H. Albrecht *et al.* (ARGUS Collaboration), Phys. Lett. **B241**, 278 (1990).

[66] G. J. Feldman and R. D. Cousins, Phys. Rev. **D57**, 3873 (1998).

[67] S. Khalil and E. Kou, hep-ph/0303214.

[68] I. Abe *et al.* Expression of Interest in A High Liminosity Upgrade of the KEKB Collider and the Belle Detector, `http://belle.kek.jp/~yamauchi/EoI.ps`.

[69] H. Tajima *et al.*, hep-ex/0301026 (2003).

[70] K. Abe *et al.* (Belle Collaboration), Phys. Rev. Lett. **88**, 171801 (2002).

[71] T. Tomura *et al.* (Belle Collaboration), Phys. Lett. **B542**, 207 (2002).

[72] K. Hara and M. Hazumi *et al.* (Belle Collaboration), Phys. Rev. Lett. **89**, 251803 (2002).

[73] J.L. Goity and W. Roberts, Phys. Rev. **D51** 3459 (1995).

[74] D. Scora and N. Isgur, Phys. Rev. **D52** 2783 (1995).